In Vivo Mapping of Tumor Microcirculation Parameters Using Dynamic Contrast Enhanced MR Imaging

by

Eli Stålsett

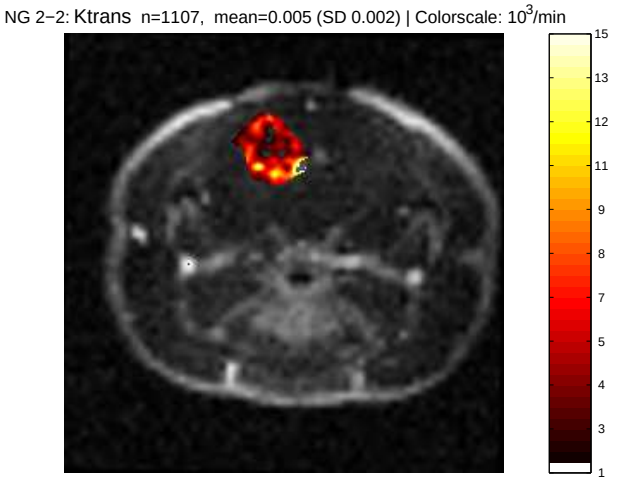

Thesis for the *Candidatus Scientiarum* degree in
Experimental and Human Physiology

Neuroinformatics and Image Analysis Group
Division of Physiology
Department of Biomedicine
University of Bergen
Bergen, Norway
2004

Contents

Acknowledgments viii

Abstract ix

Acronyms and abbreviations xi

1. Introduction 1
- 1.1. Tumor physiology and aggressiveness assessment . . . 2
- 1.2. Imaging tumor physiology with MRI . . . 3
- 1.3. Tracer kinetics and pharmacokinetic modeling . . . 4
- 1.4. The NG-2 study . . . 5
- 1.5. The objectives of this thesis . . . 6

2. Tumor Physiology 9
- 2.1. Angiogenesis . . . 10
- 2.2. Tumor microvasculature . . . 12
- 2.3. Delivery of particles to tumor tissue . . . 14
  - 2.3.1. Pathophysiology of tumor permeability . . . 15

3. Compartmental tracer kinetics 19
- 3.1. Kinetics and pharmacokinetics . . . 19
  - 3.1.1. Two-compartmental modeling . . . 20

4. MRI contrast media 23
- 4.1. Effects of MRI contrast agents . . . 23
- 4.2. Gadomer-17 . . . 24
- 4.3. Contrast agent relaxivity . . . 25

5. Dynamic contrast enhanced imaging 27
- 5.1. Introduction to DCE-MRI . . . 27
  - 5.1.1. Applications and features of DCE-MRI . . . 29
- 5.2. The quantitative approach - tracer kinetic modeling . . . 31
  - 5.2.1. Tracers in pharmacokinetic MRI . . . 33
  - 5.2.2. Assessing tissue contrast concentration . . . 34

5.2.3. The compartment model by Tofts et al. . . . 36
5.2.4. The compartment model by Su et al. . . . 40
5.3. Approach to the problems . . . 44

6. Methods and material **47**
6.1. MR scanning procedure . . . 47
6.1.1. Subjects . . . 47
6.1.2. Examinations . . . 48
6.1.3. Enhancing agents . . . 49
6.2. Experimental imaging design . . . 50
6.2.1. Details of the imaging protocol . . . 52
6.3. The dynamic scanning . . . 53
6.4. Post-processing . . . 54
6.4.1. Converting Biospec `2dseq` data to Matlab format . . . 54
6.4.2. Image alignment of multichannel acquisitions . . . 55
6.4.3. T_1 estimation . . . 56
6.5. Analyzing the dynamic data using tracer kinetic models . . . 56
6.6. ROI-wise parameter estimation . . . 58
6.6.1. Operator variability of manual ROI determination . . . 58
6.6.2. Use of different background information . . . 59
6.6.3. Heterogeneity assessment by smaller ROIs . . . 61
6.6.4. Analyzing ROIs of four different tissues ("regional differences") . . . 61
6.7. Parameter estimation at the pixel level . . . 63
6.7.1. Time development . . . 63
6.7.2. "Goodness-of-fit" analysis . . . 63

7. Results on pharmacokinetic MRI **65**
7.1. Results from ROI analysis . . . 66
7.1.1. Results from operator variability of ROI determination . . . 66
7.1.2. Results from heterogeneity assessment by smaller ROIs . . . 71
7.1.3. Results from regional difference in four tissue ROIs . . . 72
7.2. Results from *pixel-wise* analysis . . . 78
7.2.1. Results from "time-development" . . . 85
7.3. Results from "goodness-of-fit" . . . 104

8. Discussions and conclusions **111**
8.1. *ROI-wise* analysis . . . 111
8.1.1. Variability due to manual tracing of ROIs . . . 111
8.1.2. Use of different background information for ROI determination . . . 113
8.1.3. Heterogeneity assessment by smaller ROIs . . . 114
8.1.4. Regional differences in four tissue ROIs . . . 115
8.2. Pixel-Wise analysis . . . 117
8.2.1. Time development . . . 119

8.3. "Goodness-of-fit"; comparison of models 121
8.4. General methodological discussion 122
8.4.1. Theoretical differences in the two models 122
8.4.2. Conversion to CA concentration 124
8.4.3. Concluding remarks on the model assumptions 125
8.4.4. Concluding remarks on Gadomer-17 as "permeability-tracer" 126
8.5. Conclusions 127

A. The cardiovascular system **129**
A.1. Physiology of cerebral Circulation 129
A.2. Transendothelial transport 131
A.3. Features of the blood-brain barrier 133

B. MRI Contrast agents **137**
B.1. Gadolinium Chelates 137
B.2. Side effects 140

C. Functional MRI **143**

D. MR Imaging protocol **147**

E. Implemented Matlab codes **153**

List of Figures

1.1. Structural features of tumor vasculature 3

2.1. Tumor microenvironment 11
2.2. Tumor growth requires neovascularization 11
2.3. Physiological barriers in tumors 15
2.4. Pathophysiology of neoangiogenesis 16
2.5. Vesiculo-vacuolar organelles 17

3.1. General two-compartmental model 21
3.2. Concentration vs. time in two-compartmental models 22

5.1. Time course of signal intensity in selected ROI 28
5.2. Signal intensity course converted to contrast-concentration course 34
5.3. Time courses 36
5.4. Tofts compartment model 37
5.5. The Su et al. compartment model 41
5.6. $C_p(t)$ and $C_(t)$, Su model using Gd-DTPA 44

6.1. Scanner and anesthesia equipment 49
6.2. Tissue uptake of Gadomer-17 and Omniscan 50
6.3. Experimental Design 51
6.4. Time schedule for dynamic series 54
6.5. Coregistration 55
6.6. Subjects in evaluation of manual ROIs 60
6.7. Four different tissue ROIs 62

7.1. Repeated manually delineated ROIs 68
7.2. Parameter variation due to intra-operator variability of ROIs (Su model) . 69
7.3. Parameter variation due to intra-operator variability of ROIs (Tofts model) 70
7.4. Spatial heterogeneity of parameters within tumor region (NG 3-2) using multiple small ROIs 73
7.5. Concentration-time curves and estimated Su and Tofts models in tumor region (NG 3-2) using multiple small ROIs 74

7.6. Box and whisker plots of parameter distributions across different tumor subregions 76
7.7. Regional difference in four ROIs 79
7.8. Regional difference in four ROIs 80
7.9. Regional difference in four ROIs 81
7.10. Regional differences in pharmacokinetic parameters 82
7.11. Regional differences in related parameters 83
7.12. Correlations of related parameters 84
7.13. Time development of Su parameter D_0 in animal NG 1 86
7.14. Time development of Su parameter D_1 in animal NG 1 87
7.20. Time development of Su parameter D_1 in animal NG 2 88
7.15. Time development of Su parameter K_2 in animal NG 1 89
7.16. Time development of Tofts parameter K^{trans} in animal NG 1 90
7.17. Time development of Tofts parameter v_e in animal NG 1 91
7.18. Time development of Tofts parameter k_{ep} in animal NG 1 92
7.19. Time development of Su parameter D_0 in animal NG 2 93
7.21. Time development of Su parameter K_2 in animal NG 2 94
7.22. Time development of Tofts parameter K^{trans} in animal NG 2 95
7.23. Time development of Tofts parameter v_e in animal NG 2 96
7.24. Time development of Tofts parameter k_{ep} in animal NG 2 97
7.25. Time development of Su parameter D_0 in animal NG 7 98
7.26. Time development of Su parameter D_1 in animal NG 7 99
7.27. Time development of Su parameter K_2 in animal NG 7 100
7.28. Time development of Tofts parameter K^{trans} in animal NG 7 101
7.29. Time development of Tofts parameter v_e in animal NG 7 102
7.30. Time development of Tofts parameter k_{ep} in animal NG 7 103
7.31. Goodness-of-fit NG 3-2 105
7.32. Goodness-of-fit NG 7-2 106
7.33. Goodness-of-fit WT 3-2 107
7.34. Enhancement patterns 110

A.1. Willis circle 130
A.2. Transendothelial transport and fluid balance 132
A.3. Cells in microvessel walls 134
A.4. Routes across blood-brain barrier 135

D.1. TR-images for T_1 estimation 148

List of Tables

4.1. Physiochemical and pharmacological properties, Gadomer-17 24

5.1. Parameters and units in Tofts pharmacokinetic model 38
5.2. Parameters in Su's pharmacokinetic model 42

6.1. Time-frame of the MR procedure 52
6.2. MRI protocol 53

7.1. Intra-operator variability; Su model parameter variations 67
7.2. Intra-operator variability; Tofts model parameter variations 67
7.3. Resulting parameters in each of 15 tumor ROIs 75
7.4. Results; comparison of models by AIC 108

B.1. Intravenous class 2 agents 139
B.2. Intravenous class 2 agents, properties 139

D.1. Scan parameters, RARE and FLAIR 148
D.2. Scanning parameters dynamic sequence. 149
D.3. Scanning parameters post contrastT_1 sequence. 150
D.4. Doses and injected volumes, WT tumor animals, fifth-week scans. 150
D.5. Doses and injected volumes, NG-2 tumor animals, fifth-week scans. 151
D.6. Doses and injected volumes, WT tumor animals, seventh-week scans. . . . 151
D.7. Doses and injected volumes, NG-2 tumor animals seventh week scans. . . . 152
D.8. Relaxivity data: Gadomer-17 152

Acknowledgments

The work presented in this study was performed at the Neuroinformatics and Image Analysis, Division of Physiology, Department of Biomedicine, University of Bergen during the period of autumn 2002 to winter 2004.

My study has been performed on basis of MRI data acquired at the MRI-center in Trondheim as a collaborative assay between employees at the University of Bergen and SINTEF, Unimed MRI Center, Trondheim. I have denoted this co-operative venture the "NG-2 project".

I will express a special thanks to Associate Professor Arvid Lundervold who put a great deal of work into writing the Matlab code being used -and for his guidance and support throughout my thesis work. I am grateful that he gave me the possibility to combine physiology with radiography.

I give special thanks to the partners of this project who gave me access to the MRI experimental part of their study. I am very grateful to Cecilie Brekke, Christian Brekken and Tina Bugge who let participate in the MRI scanning experiments and provided me with skillful knowledge and ideas for my thesis work. Additionally, Cecilie has been a great support and teacher during frustrating times of the writing process.

I also wish to thank MR-physicist Dr. Lars Ersland, Professor Bolek Srebro and Cand. scient Åse-Marit Kristiansen for discussion and helpful comments on the manuscript, Eirik Thorsen for essential computer expertise and fellow students for causing a nice study environment.

Finally, I express my gratitude to friends and family —for their persistent encouragement and continuous support.

Bergen, February 2004

Eli Stålsett

Abstract

In management of patients with cancer, MR imaging has become increasingly important. The rapidly growing interest in continually developing MRI methods reflects a growing need, not only to evaluate the disease at the time of diagnosis, staging and treatment planning, but also to perform successive examinations during "treatment follow-up". Due to recent technical advances in MRI sequences, post-processing techniques and development of novel and improved contrast agents, new MRI methods such as *dynamic contrast enhanced MRI* (DCE-MRI) has become available. By DCE-MRI, tumors can be characterized regarding microvascular physiology and their state of angiogenesis.

This study addresses important issues using DCE-MRI as a tool for describing (microenvironmental) tumor physiology. The experimental part was performed using a selection of data sets acquired in a collaborative study denoted the "NG-2 project". In this study, nude rats having implanted subcortical glioblastoma multiforme (GBM) underwent successive multispectral MRI scans including dynamic T_1-weighted monitoring of tissue contrast enhancement. The novel "macromolecular weighted" contrast agent Gadomer-17 was used for dynamic MRI measurements.

Using the dynamic MRI measurement data, two slightly different compartment models (denoted the Su model and the Tofts model, respectively) were applied to analyze the tissue tracer concentration time curves, from which physiological model parameters, related to permeability i.e. wash-in and wash-out of tracer in tissue, were estimated.

The aim was to evaluate the models with respect to (i) their theoretical assumptions, (ii) their applicability to differentiate tumor physiology (by analyzing the same tumor at different time-points), (iii) their applicability to describe microvasculature of normal tissue regions and (iv) goodness-of-fit between observed data and the theoretical models. Moreover, the pharmacokinetic DCE-MRI procedure was evaluated concerning operator dependent variability in derived model parameters (i.e. "manual region of interest (ROI) delineations" and "ROI selection using image templates from different contrast agents").

Results showed variation due to manual ROI tracings and operator variability. Model parameter values were more difficult to reproduce when using Gd-DTPA enhancement compared to Gadomer-17 as template for the delineations, reflecting physiological differences underlying the enhancement patterns obtained with contrast agents of different molecular weights. Spatial sampling of smaller ROIs within one single tumor showed spatial heterogeneity in estimated parameter values, even in tumor areas which visually possessed homogeneous contrast enhancement. Visually, contrast enhancement in tumor regions enabled a better model-fit than in healthy tissue regions. However, healthy tissues obtained very low contrast agent concentrations during the dynamic scanning, which probably makes the models less applicable in normal tissues, using Gadomer-17 as a tracer. *Pixel-wise* analysis at two different time-points revealed increased permeability during time, and a decrease in wash-out rate. This was found in two out of three cases. Such information may have treatment implications because higher permeability leads to better drug delivery (macromolecules) to tumor tissue. Additionally, a low wash-out rate is likely to enhance therapy effects as the molecules are trapped in tumor tissue for a longer time. One tumor case in the *pixel-wise* analysis was already large and heterogenous at the first time-point, and showed a decrease in permeability during time, possibly reflecting maturation of angiogenic vessels with reduced leakage of macromolecules. By goodness-of-fit assessment, using Akaike's information criterion (AIC), I found the Su model more appropriate than the Tofts model in fitting the calculated concentration time curves, taking into consideration the handicap by Tofts model of having only two degrees of freedom, compared to three free parameters in the Su model.

In conclusion, the DCE-MRI method possesses great possibilities in assessing microvascular physiology of tumors. DCE-MRI is, however, also hampered with methodological pitfalls that are demonstrated in this thesis, being aware that my data are sparse. Such methodological problems will be less influential and easier to interpret when a standardized method (concerning scanning protocol, contrast agent type, pharmacokinetic model and presentation of data) is accepted. Also, more studies are needed, including histopathological examinations and other(micro)imaging modalities, to better understand the relationship between local physiological processes and the observed DCE-MRI time courses.

Acronyms and abbreviations

AIF Arterial input function

Axial slice In brain imaging, the plane with coordinates going from left - to - right and front - to - back

DCE-MRI Dynamic contrast enhanced imaging

B_0 External magnetic field measured in Tesla

BBB Blood-brain barrier

BOLD Blood oxygen level dependent contrast technique

CA Contrast agent

CBF Cerebral blood flow

CM Contrast media

CNR Signal-to-noise ratio

CNS Central nervous system

CO Cardiac output

CT Computer tomography

ECS Extra cellular space

Echo Induced signal in the receiver coil cased by rephasing of protons; either a gradient echo or a spin echo

EPI Echo planar imaging

EES Extravascular extracellular space

FID Free induction decay; a plot of NMR signal as a function of time

FLAIR Fluid-attenuated inversion recovery sequence to suppress signals from cerebro spinal fluid

fMRI functional MRI methods; often used in connection with the BOLD technique

FOV Field of view; area of anatomy covered in the image

GBM Glioblastoma multiforme

Gd Gadolinium

Gd-DTPA Gadolinium-diethylenetriaminepentaacetic

GE Gradient echo pulse sequence; one that uses a gradient to generate an echo

GM Grey matter

LD_{50} Dose which is lethal for 50% of the test subjects

MMCM Macromolecular-weighted contrast media

MR/MRI Magnetic resonance imaging; the process of creating an image based on differences in NMR signal from different places in a sample

MS Multiple sclerosis

MSE MSE represents mean of SSE for all pixels within ROI. SSE is the sum-of-squares errors, here used as criteria for goodness-of-fit

NG-2 Proteoglycan hypothesized to mediate tumor growth by increasing tumor angiogenesis

NMR Nuclear magnetic resonance

Pharmacokinetic MRI DCE-MRI (using pharmacokinetic models in data analysis)

PK Pharmacokinetics

PS product Product of membrane permeability (P) and surface area (S) for which the membrane is permeable.

r_1 Contrast agent relaxivity; the ability of the agent to increase T_1-relaxation rate (i.e. shorten T_1-relaxation time)

RARE Rapid acquisition with relaxation enhancement —pulse sequence

ROI Region of interest; a selected subset of pixels in an image

SE Spin echo pulse sequence; one that uses a 180°rephasing pulse to generate an echo

SI Signal intensity

TE Time from excitation pulse to echo, readout delay

TR Time to repetition, time between successive pulses

T_1 Time constant describing recovery of longitudinal magnetization after

T_2 Time constant describing disappearance of transverse magnetization

VVO Vesiculo-vacuolar organelles, interconnected vesicles related to transvascular transport in tumor microvessels and post-capillary venules

WT Wild-type tumor

1. Introduction

Development of nuclear magnetic resonance imaging

Following the discovery of x-rays in 1895, brain mapping methods and neuroimaging techniques have quickly advanced. About 50 years ago, scientists found that when certain nuclei were placed in a magnetic field, they absorbed energy in the radiofrequency range and re-emitted this energy during the transition to their original energy level [35]. This phenomena was named *nuclear magnetic resonance* (NMR[1]). NMR provides the basis for magnetic resonance imaging (MRI).

The NMR signal emitted from the excited nuclei carry encoded information about the physical and chemical environment of the nuclei. Hence, the signal provide information about the composition of the tissue in which the nuclei is situated. Signals diverted from a great number of NMR signals are spatially encoded and make the foundation for an MR image.

Discoveries concerning the NMR phenomena have been awarded the Nobel Prize in 1952 (physics), in 1991 (chemistry), in 2002 (chemistry) and in 2003 (medicine). The first clinical MRI equipment was available at the beginning of the 1980s. Over the past 20 years, MRI has become a powerful tool for evaluation of the anatomical and morphological characteristics of nearly all organs in the body. MRI of the brain and spinal cord is especially known for its excellent spatial resolution, and the progress of MRI as a clinical tool has been extraordinary [55]. Nearly all brain disorders lead to alterations in water content, which is reflected in the MR image. A difference in water content of less than one percent is enough to detect pathological changes in an MR image. In addition, a number of MRI techniques that *allow evaluation of functional or physiological parameters, while preserving anatomical specificity*, have been developed. This greatly improves the powerfulness of MRI in medical contexts. These techniques are termed functional MRI

[1] *Nuclear* because only the nucleus of the atoms react, *magnetic* due to the need of a strong external magnetic field, and *resonance* because the frequency of the RF pulse must match the precession frequency of the precessing nuclei.

(FMRI[2]).

Dynamic imaging adds the dimension of time to the anatomical detail of conventional MRI, and thereby allows evaluation of functional properties. Recently, dynamic MRI has been proposed as a valuable tool for diagnosis and prediction of response to treatment of cancer. By assuming the hypothesis that tumor growth rates correlates with vascular permeability, the degree of vascular leakage measured by MRI gives valuable information concerning a tumors ability to expand and metastasize [95]. An evaluation of pharmacokinetic models used to extract such information from dynamic MRI scanning is the main issue of this thesis.

1.1. Tumor physiology and aggressiveness assessment

Even though the struggle against cancer is continuously progressing, there is a number of battles left to fight. Cancer is still one of the most leading causes of death in many industrialized countries. The success or failure of cancer treatments depend on tumor physiology as well as sensitivity to treatment such as chemical therapy and radiotherapy [45]. Tumor physiology is further dependent on the interaction between oncogenic expression and environmental factors in the tissue in which the tumor is situated. To make matters even more complicated, transformation of oncogenic expression seems to occur as response to environmental changes and makes tumors more resistant to treatment [92]. New developments of MRI methods possess, however, good possibilities of improving cancer diagnostics and planning of therapies.

Tumors display large spatial and temporal heterogeneities in their blood supply, or perfusion. Despite apparently generally good blood supply, areas of tumors can suffer from hypoxia and necrosis due to abnormalities in the tumor capillary bed, often with consequently high interstitial pressure. Of particular functional importance, tumor vessels possess high degree of capillary leakage. Vessel leakiness seems to correlate with histological grade and malignant and metastatic potential of tumors [17, 36].

The abnormal characteristics in tumor vasculature is closely connected to angiogenesis; the process through which new blood vessels develop from already pre-existing vessels. Angiogenesis is required for a tumor to grow beyond a certain size and become aggressive [12, 29, 27]. Angiogenic vessels have certain features, such as increased permeability or capillary leakage. Attention have been paid to develop methods of visualizing these characteristics in order to display more accurate diagnosis concerning severity of cancer. In addition, treatment failure have, in some cases, been hypothesized to be related to variable anti-cancer drug penetration into tumors. Thus the question of molecular penetration into tumors remain highly important [99].

[2]FMRI techniques in general are briefly described in Appendix C

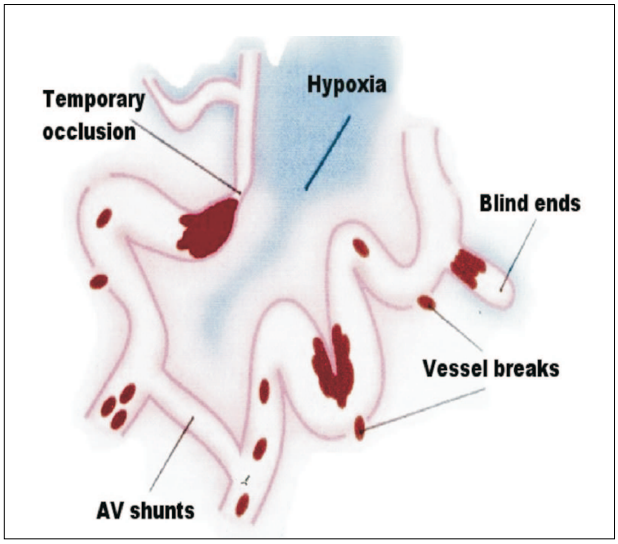

Figure 1.1.: Structural features of tumor vasculature. Tumor vessels commonly possess fragile, leaky vessels with arterio-venous shunts and blind ends. Because of its chaotic vasculature, the tumor vascular network may have transiently or chronic occluded parts, resulting in areas of hypoxia [9].

One of the difficulties concerning diagnostic evaluation of tumors is to determine their potential of progressive growth and their metastatic ability. For years, microvessel density (MVD) has been used as indicator for tumor aggressiveness and metastatic potential, as neovascularization facilitates metastasis by providing access to the circulation. However, researchers have found conflicting results when testing this hypothesis [59]. It is suggested that the different results may be caused by the pronounced heterogeneity of MVD within each individual tumor. Histological examinations have shown that capillary permeability is increased in malignant tumors. Permeability is suggested to be a better estimate of tumor aggressiveness compared to MVD [20]. Studies have shown correlation between histological tumor grade and increased capillary permeability [80]. This increased permeability is attributed to angiogenic activity [36]. As the vascular endothelial growth factor (VEGF) is known to induce neoangiogenesis in tumors, uncontrolled high VEGF expression may be used as an other indicator of tumor aggressiveness. The MRI technique *dynamic contrast enhanced MRI* (DCE-MRI) is postulated to provide a non-invasive prognostic indicator analogous to both VEGF expression and MVD count [14, 49, 68].

1.2. Imaging tumor physiology with MRI

Perfusion is central to our understanding of the tumor environment [30]. Dynamic imaging after intravenous injection of contrast agent and application of pharmacokinetic models, reveal transendothelial transport of the contrast agent in perfused tumor regions. The transport of contrast agent across the endothelium is a reflection of the integrity of the

microvessel wall [79]. By application of kinetic models, DCE-MRI display the kinetics of the distribution of contrast agent within tissues, opposed to conventional contrast MRI which shows enhancement as a result from both vascularity of tissue and accumulation of agent in the tissue interstitium. By applying a two-compartmental pharmacokinetic analysis, physiological characteristics of tumors can thus be evaluated. Parameters such as the intravascular volume of tumor, interstitial space volume of tumor, and the transport rates between plasma and extravascular extracellular space (EES) of the tumor can be derived. This technique is often referred to as *pharmacokinetic MRI*. Pharmacokinetic MRI is developed to provide local estimates of microcirculatory parameters, mainly in tissues in which there exists an increased capillary permeability. Pathological increased capillary leakage caused by dysregulated formation of new blood vessels contributes to several malignant, ischemic and inflammatory disorders (e.g. diabetic disease, MS-plaques and malignant tumors) [11].

The evaluation of tumor physiology provided by DCE-MRI may be important in a diagnostic perspective and for the purpose of treatment planning. In addition, MRI provides steady-state physiological tumor information and can be used as a tool in a "follow-up" of tumor response to treatment. Interest in DCE-MRI was stimulated by early observations that high increase in signal enhancement and fast rates of signal enhancement both appeared to correlate with well vascularized viable tumor regions. In contrast, normal tissues and benign tumor regions revealed more moderate rates and degree of signal enhancement [99]. As mentioned, the enhancement differences between benign and malignant lesions have been attributed to higher vascular volume and/or permeability associated with angiogenesis in malignant tissues [93].

The technique of DCE-MRI is now becoming increasingly widespread, not only for improving the accuracy of diagnostic imaging, but also in research into aspects of microcirculation and assessment of microvascular changes following treatment. Moreover, the method may predict the aggressiveness of the tumor [95]. In addition, development of new therapeutic agents for cancer therapy, such as those inhibiting angiogenesis and thus affect microvasculature, has increased the importance of standardizing this powerful MRI method [28].

1.3. Tracer kinetics and pharmacokinetic modeling

Earlier work in tracer kinetics has been carried out by physiologists using radioactive tracers in animals which were sacrificed to measure the tracer concentration in tissues of interest [102]. In dynamic contrast enhanced imaging, however, tracer kinetics is employed nearly non-invasively[3] by application of pharmacokinetic (PK) model to dynamically measured MRI data.

[3]DCE-MRI is considered non-invasively compared to e.g. histological assessment of angiogenesis. However, the method requires intravenously injected tracer and can thus not be considered fully non-

Pharmacokinetic modeling is *the process of developing mathematical descriptions for the rates of absorption, distribution, metabolism, and elimination of drugs and metabolites in biological systems.* Pharmacokinetic models are widely used to predict the kinetics of chemical residues in the environment, to solve pollution problems and to help understand the results of toxicological studies. Therefore, a number of different models exists, e.g. compartmental and non-compartmental models, physiologically pharmacokinetic based models and population pharmacokinetic models [110]. Both models evaluated in this thesis are two-compartmental models and will be further described later (cf. Section 5.2).

Numerous studies have been performed using dynamic contrast enhanced MR imaging as a tool in describing physiological characteristics of tumors and other conditions, such as (MS). The technique is however not yet standardized, or *routinely* included in clinical studies. Great variations exists in imaging procedure; concerning among others; choice of sequence parameters, type and dose of contrast agent, and time and speed of injection. In addition, different pharmacokinetic models to extract physiological parameters from the imaging series, have been developed.

Recently, the importance of MRI development was addressed when "The Nobel Assembly at Karolinska Institutet" awarded "The Nobel Prize in Physiology or Medicine" for 2003 to Paul C. Lauterbur and Peter Mansfield for their discoveries which have led to the development of modern Magnetic Resonance Imaging, representing a breakthrough in medical diagnostics and research. "Improved diagnostics in cancer" was given as one of the arguments for the award[4].

1.4. The NG-2 study

This thesis work is performed using MRI data from a larger study which I have denoted the "NG-2 study". I hereby briefly introduce the main topics and aims of this project.

In a research collaboration between the University of Bergen, University of Trondheim and SINTEF Unimed Trondheim, multispectral and dynamic contrast enhanced MRI was successfully performed in examination of 17 immunodeficient nude rats at five and seven weeks after sub-cortical implantation of human glioblastoma (U251N) spheroids. The tumors were of either wild type; slow growing tumors, or NG-2 positive; rapidly growing/aggressive tumors. The neural stem cell receptor NG-2 promotes angiogenesis causing acceleration of vascularization and thereby growth of tumors. An important aim of the project was to investigate tumor aggressiveness (in terms of angiogenesis, permeability, growth rate, tumor volume, edema and necrosis) and compare NG-2 positive tumors with NG-2 negative wild type (WT) glioblastomas. An additional objective embraced compar-

invasively. DCE-MRI has therefore commonly been referred to as a nearly non-invasively technique.

[4] Cite: "press release" at http://www.nobel.se/medicine/laureates/2003/press.html.

ison of pharmacokinetic models developed for assessment of neovascular characteristics in animal tumor volumes.

I was kindly given access to the MRI-data from this project in order to use the dynamic scans for evaluation of two pharmacokinetic models developed to characterize tumor microcirculation.

1.5. The objectives of this thesis

Several approaches of pharmacokinetic (PK) analysis have been proposed to achieve reliable measurements of physiological parameters from DCE-MRI. The theoretical models differ in their assumptions, mathematically implications and also in estimated parameters describing the physiology of the tissues.

In this thesis, two pharmacokinetic two-compartmental models developed for evaluation of microcirculatory parameters will be evaluated. The models have previously been described by Su et al. [94] and Tofts et al. [105], reviewed in [102, 104]. The theoretical basis of the models is presented in Section 5.2. Both models have been fitted to a selection of dynamic MRI tissue concentration data (from experiments in the "NG-2 project") using nonlinear least-square estimation.

The following work includes both theoretical and experimental parts. A theoretical overview is given in Chapters 2– 5. The aim was to address tumor microcirculation and give a fairly detailed description of methodological issues related to DCE-MRI, focusing on the two different pharmacokinetic models by Su and Tofts, respectively. Problematic issues concerning these models and pharmacokinetic MRI in general will be given in Chapter 8.

The "experimental part", where the two pharmacokinetic models have been applied to DCE-MRI scans of implanted intracranial glioblastomas is presented in Chapter 6. The purpose of this part was to investigate and demonstrate methodological aspects of estimation of physiological microcirculatory parameters based on DCE-MRI in conjunction with pharmacokinetic models (Su and Tofts).

I wished to study the variability of parameter estimates due to operator-dependent factors. Variability may be partly caused by manual outlining of ROIs. Additionally, choice of "background" image (i.e. the different enhancement pattern of the various tracers) used as "template" for ROI-tracings were evaluated with respect to variability. Also, variation in parameter-values from "smaller, enhanced" ROIs was studied and related to heterogeneity assessment. An additional aim was to address the applicability of the pharmacokinetic models to healthy tissues. Finally, it was of interest to compare the two models by a numerical "goodness of fit" criteria to see if one of the models were better aimed to fit the

actual MRI derived concentration data than the other. Results are given in Chapter 7 and discussed in Chapter 8.

Some background information and technical reports are given in appendixes. Readers are assumed to be familiar to basic principles of MRI.

2. Tumor Physiology

Capillaries of healthy tissues form anastomosis and create a three-dimensional vascular network in the tissues. The complex network of microvasculature provides a large surface area and minimizes diffusion distance to enhance the efficiency of transporting nutrients and waste products between blood and cells [25]. This intra- and extravascular exchange of fluids and solutes is exerted by the mechanisms of diffusion and convection [52, 84, 95]. The mechanisms of fluid exchange between compartments are more closely described in Appendix A.

In addition to the characteristic features of microvasculature, brain capillaries employ wall-specializations which selectively isolates the extravascular space of brain parenchyma from the blood compartment. This blood-brain barrier (BBB) tightly controls the extracellular environment in the brain in order to protect the nervous system. A common feature of malignant brain tumors however, is their ability to compromise the blood-brain barrier function, thus increasing the permeability which subsequently lead to brain edema by allowing free diffusion of large molecules and other blood components into the nervous tissue [87].

Tumors are commonly known to have a high degree of lesion heterogeneity, both within and between subjects. From a physiological perspective, the most important difference between tumors and normal tissues lies exactly in the vasculature [9]. Tumor vasculature commonly consists of two different types of vessels; 1) ingrowing vessels from host tissue and 2) newly generated (angiogenic) vessels. Tumor microcirculation often displays abnormal characteristics. In general, tumors are dramatically heterogeneous in terms of their perfusion, oxygenation and metabolism. Although overall blood supply to tumor may be good[1], abnormal characteristics of the tumor vessels may cause areas of necrosis and hypoxia. Especially is malignant brain tumors such as e.g. glioblastoma multiforme, known to be highly vascularized and to possess central areas of necrotic tissue, surrounded by patches of viable tumor tissue [107]. Although generally increased, vascular permeability in tumors is also highly variable, both within individual tumors and between tumors.

[1] A common feature of malignant tumors, is the observation of increased fractional blood volume, often associated with increased MVD counts[81]).

Vascular permeability is referred to as *the transendothelial transport of compounds across the blood vessel wall into the interstitial space of the tumor* [95]. As mentioned in Chapter 1, the degree of permeability is known to correlate with the tumors ability of progressive growth, ability to metastasize and the respondment to treatment [23, 96]. This correlation provides a basis for MRI-permeability assays, such as DCE-MRI, for staging of malignant tumors [43]. Furthermore, the hyperpermeability of tumor vessels to macromolecular plasma solutes is known to be related to VEGF (vascular endothelial growth factor)[2].

Microscopic tumors, originated as avascular aggregates of malignant cells can grow to a certain size (1–2 mm^3) by simple diffusion of nutrients and metabolic waste products. This diffusion-limited[3], prevascular stage can be maintained for a prolonged period until the process of angiogenesis is up-regulated. To grow beyond this limited size, a vascular supply has to be established. The tumor itself is, however, not capable of generating vessels and must recruit new blood vessels by vasculogenesis[4] and angiogenesis [6, 12]. Initially there are only minor pre-existing host vessels enclosed by the tumor, until the host is stimulated to generate new vessels by angiogenesis. The tumor will then enter the vascular phase; characterized by exponential growth and following clinical symptoms [20, 27]. The exact mechanisms which control angiogenesis is not fully understood, but a known connection between angiogenesis and both primary tumor growth and metastasis is established. This makes the basis for the development of techniques for non-invasive assessment of tumor biology [36].

2.1. Angiogenesis

Angiogenesis is the complex, multistep process by which new vessels grow toward and into a tissue by sprouting of capillary buds from existing microvessels [6, 72]. The process is tightly regulated by stimulators, inhibitors and interaction between different cell types. An equilibrium between proangiogenic and antiangiogenic factors causes vessel growth by angiogenesis to occur at a very small extent in healthy adults [59]. Important physiological processes such as embryogenesis, corpus luteum formation, and wound healing are controlled by acceleration of angiogenic generation of capillary vessels. Angiogenesis also plays a crucial role in pathophysiological states, such as rapid growth and metastasis of tumors. Additionally, angiogenesis is considered a pathological characteristic in conditions such as diabetic retinopathy and rheumathoid arthritis [20].

[2] VEGF is a multifunctional cytokine secreted at high levels by many malignant tumor-related cells (cf. Section 2.1).

[3] For supply of oxygen and nutrients, mammalian cells are located within 100–200 μm of blood vessels -the diffusion limit for oxygen [12].

[4] Vasculogenesis is defined as *de novo* generation of blood vessels. Vasculogenesis is an essential component of embryonic development, whereas angiogenesis accompanies organ growth and regeneration [72]

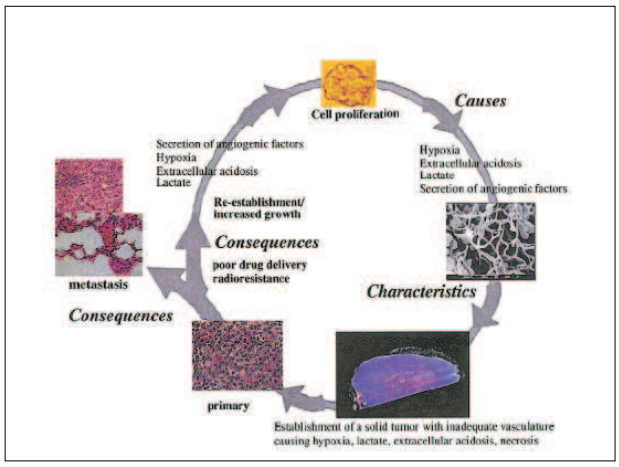

Figure 2.1.: A schematic illustration of the causes, characteristics and consequences of tumor microenvironment. Hypoxia and acidosis are products of poor perfusion and elevated metabolism, respectively. The hypoxic and acidic microenvironment in tumors significantly affect treatment and progression of cancer. The most well-studied effects of the tumor microenvironment are the physiological resistance to chemo- and radio-therapies. This resistance may be direct effect of pH and O_2, or caused by reduced perfusion in general. The illustration is from Gillies et al. [30].

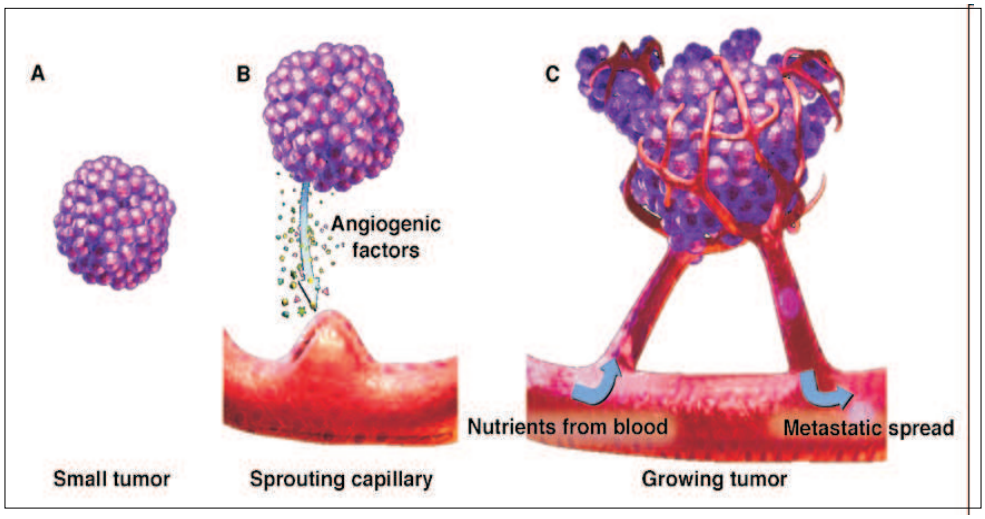

Figure 2.2.: Tumor growth requires neovascularization.. Angiogenic stimulating factors elaborated by the tumors and tumor-associated inflammatory cells induce angiogenesis by interaction with endothelial cells and pericytes in neighboring capillaries. This interaction stimulates formation of new capillary buds and prepares the local environment for their ingrowth [6]. A; Tumors less than 1–2 mm^3 receive oxygen and nutrients by diffusion from host vasculature. B; Growth beyond this size requires generation of new vessel network. Tumors secrete angiogenic factors that stimulate migration, proliferation, and neovessel formation by endothelial cells in adjacent established vessels. C; vascularization of tumors occur by angiogenesis, facilitating progressive growth (http://www.meniscus.com/horizons/3-2figs.ppt).

The onset of angiogenesis in pathology might be caused by a failure in the growth factor-feedback system [14]. Growth factors which is normally tightly controlled become unregulated and induce endothelial proliferation. Factors influencing angiogenesis are derived both from tumor cells and infiltrating cells such as macrophages and fibroblasts. The degree of angiogenesis in a tumor is thus a result of complex interactions between tumor cells, capillary endothelial cells, pericytes and recruited immune cells. Control is executed as a balance of angiogenic promotors and inhibitors [59]. A net positive balance of angiogenic factors will induce endothelial cells to rapidly proliferate and form new blood vessels.

The vascular endothelial growth factor (VEGF), originally described as vascular permeability factor (VPF), is an important angiogenic stimulator [56]. This heparin-binding angiogenic glycoprotein seems to be the angiogenic promoter which is most responsive to the abnormal physiological environments occuring in solid tumors; hypoxia, extracellular acidosis and substrate deprivation [29]. VEGF is secreted from transformed tumor cells and acts as a mitogenic factor for endothelial cells in the tumor surroundings. Activated endothelial cells release proteases, proliferate and migrate towards the tumor [56]. In addition, VEGF induces a dramatic increase in vascular permeability[5] causing leakage of macromolecular serum proteins into the interstitium. This leakage provides an ideal matrix in which new capillary buds can grow [6]. Thus VEGF seems to play a critical role in tumor angiogenesis and peritumoral edema associated with brain tumors [56]. VEGF is presumably necessary for metastasis, which in turn is closely connected to angiogenesis of new vessels [2, 95].

To summarize: as a response to a signal (e.g. hypoxia), angiogenic promotors (e.g. VEGF and acidic and basic fibroblast growth factors) induce release of cytokines from tumor cells (and endothelial cells). In turn, cytokines activate endothelial cells which proliferate and migrate along a fibrin skeleton towards the source of the angiogenic stimuli. A lumen is formed in the vascular sprout by adhesion of intracellular vacuoles initiated by contact between cells. Meanwhile, a degradation of the extracellular matrix, initiated by changes in the proteolytic balance, is performed by the pericytes. The fibrinolysis and degradation of the extracellular matrix prepares the tissue environment for ingrowth of new vessels.

2.2. Tumor microvasculature

Microvessels initiated by angiogenesis do not resemble the microvasculature of the host tissue. These newly formed vessels exhibit a series of structural and functional abnormalities. Typical features of tumor vasculature might include [29, 59]:

[5] Production of nitric oxide (NO) appears to be regulated by VEGF. NO is primarily responsible for vasodilation and the increased vascular permeability seen in tumor vessels [71].

- Spatial heterogeneity and chaotic structure without normal branching structure.
- Elongated and coiled vessels.
- Arterio-venous shunts, blind loops and alternating vascular diameter.
- Acutely collapsed vessels and transiently collapsing vessels.
- Increased endothelial proliferation rate.
- Vessel walls with lack of endothelial component, and basement membrane.
- Gaps in the endothelium.
- Poorly differentiated, fragile and leaky vessels (leading to hemorrhage and edema), lacking in smooth muscle cell lining.
- Lack of response to normal regulation of blood flow.
- Vasculature is frequently unable to match the rapid growth of cancer cells resulting in areas of hypoxia and necrosis.

Thus, vascular organization in solid tumors is chaotic with extensive branching, arteriovenous shunts and blind vascular endings. Furthermore, blood flow in tumors is not accurately regulated to meet the metabolic demand or functional status of the tissue. Typically, tumors exhibit central necrotic areas. Necrosis is most likely induced by hypoxia and nutrient deprivation due to reduced blood flow to the central region of the tumors as elevated interstitial pressure might cause collapse of angiogenic vessels[45, 108]. Interstitial hypertension can cause compression of vessels inside the tumor and limit uptake of agents [113]. In addition, the extracellular space is lager than normal due to degeneration of healthy extracellular matrix. AV shunts will cause local bypass by a fraction of the blood [59]. Additionally, adjacent to necrosis, areas of hemorrhage resulting from fragile angiogenic vessels might be present. [108]

Incomplete or missing endothelial lining (tight junctions) and basement membranes are suggested to be responsible for increased permeability. In addition, VEGF in itself increases permeability presumably by vesiculo-vacuolar organelles which have connections with both surfaces of the vessel wall (cf. Figure 2.5, Section 2.3). The hyperpermeability to macromolecules is considered essential to angiogenesis as it allows plasma proteins to seep into the tumor interstitium, forming the matrix favoring in-growth of new capillaries. In addition, leakage permits emigration of cancerous cells, allowing metastasis to occur [69].

As described above, some tumor regions receive hypoxic and nutrient depleted blood caused by the chaotic structure and the expansion of the EES, leading to a longer diffusion distance. Additionally, only 20-80% of the vascular system in tumors is functional at a given time. This may enhance the perfusion heterogeneities [29]. Jain [45] modeled that the temporal and spatial heterogeneity in tumor blood flow can be a result of;

- elevated geometric and viscous resistance in tumor vessels
- coupling between high vascular permeability and elevated interstitial fluid pressure
- vascular remodeling by intussusception[6]

He further described four different regions in tumors, based on their perfusion rates. Two regions; the *avascular necrotic region* and the *semi-necrotic region*, have low perfusion rates. The *stabilized microcirculation region* and the *advancing front region* however, have very variable perfusion rates which may even be higher than in normal tissue. The heterogeneities in blood supply within a tumor are reflected in the spatial distributions of therapautic and diagnostic agents, and can thus be exploited by temporal and spatial visualizing of contrast agent uptake, as in dynamic MRI.

Although high vascular permeability is a characteristic feature of tumors, process of maturation of vessels may lead to reduced vessel permeability in certain regions [19]. As normal neovessels grow and maturate, they acquire a more complete basement membrane and pericytic covering, both reducing endothelial permeability. VEGF is thought to regulate this vascular maturation, and hence vessel permeability [14].

2.3. Delivery of particles to tumor tissue

A blood borne molecule or particle that enters tumor vasculature reaches cancer cells via the following processes; distribution through the vascular compartment, transport across the vessel wall and transport away from the vessel wall within the interstitium. Each of these processes may involve diffusion and convection. In addition, molecules can bind or be metabolized during their journey from blood to cells [44, 45].

Transport of molecules *within the tumor vasculature* is governed by the vascular morphology and the blood flow rate, where the first includes the number, length, diameter and geometric arrangement of various blood vessels.

Transvascular transport is governed by three important parameters: the surface area for exchange, transport parameters[7] and the concentration and pressure gradients across the vessel wall. Both vascular permeability and hydraulic conductivity of tumors are significantly higher than in normal tissue. However, it is important to keep in mind that although tumor vessels may lack "permselectivness" in general, not all tumor vessels are leaky [45].

[6] In intussusception, interstitial tissue columns are inserted into the lumen of pre-existing vessels and partition the vessel lumen [12].

[7] The transport parameters; vascular permeability, hydraulic conductivity and reflection coefficient are discussed in subsection A.2 on page 131.

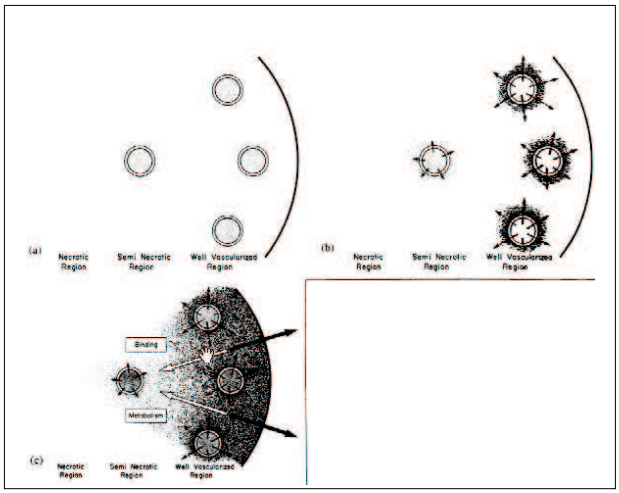

Figure 2.3.: Physiological barriers in tumors; a) Schematic illustration of a heterogenously perfused tumor with a well-vascularized periphery, a semi-necrotic intermediate patch and a non-vascularized (necrotic) center-region. Immediately after an intravenous injection, injected molecules are delivered to perfused regions only; b) Low interstitial pressure in peripheral region permits adequate extravasion of fluid and molecules; c) Macromolecules diffuse slowly towards central region of the tumor. Additionally, outflow of interstitial fluid from tumor transports molecules back to normal tissue by convection. Furthermore, interstitial movement of molecules in tumor may be hindered by binding and/or metabolism [45].

When extravasated, further transport of molecules within the tumor interstitium may be hindered by the high pressure in central regions of the tumor, which can create a small amount of outward convection. The molecules have to overcome this convection to diffuse into the tumor.

2.3.1. Pathophysiology of tumor permeability

Although the hyperpermeable nature of tumor microcirculation is well documented, it remains controversial as to which pathways are predominantly responsible for tumor hyperpermeability (and hence macromolecular transvascular transport). Increased permeability, and thereby macromolecular transport across blood vessels in brain tumors with loss of BBB-function, has been shown to occur via opening of the tight junctions between endothelial cells in the BBB [1]. Other findings suggest that the characteristic increase in permeability in tumor vessels is probably related to up-regulation of vesiculo-vacuolar organelle (VVO) function due to high levels of VEGF expression [49]. Additional routes of macromolecular leakage might include fenestrations, transendothelial cell pores and/or phagocytosis [38, 107]. Dvorak et al. [26, 22] suggest that it is possible that VVOs and endothelial pores are related structures; in response to vasoactive mediators, pores may develop from a rearrangement of VVO vesicles and vacuoles to form a larger membrane-lined vacuolar structure, and eventually, channels of sufficient size to allow passage of macro-

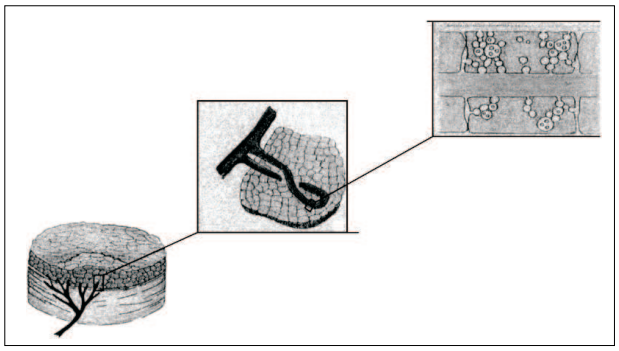

Figure 2.4.: An outline of the pathophysiologic concept of neoangiogenesis, presented by Knopp et al. [49]. Growth of tissue which has exceeded its local blood supply results in regional hypoxia and hypoglycemia, which stimulates release of e.g. the potent angiogenic stimulator VEGF. VEGF acts locally on nearby capillaries to increase endothelial permeability (which immediately leads to extravasion of macromolecules). Increased permeability not only increase the supply of nutrients, but also present an important mechanism of the metastatic process, allowing passage of tumor cells into the circulation. Increased permeability might be caused by VVOs. The number and leakage of these VVOs is regulated by VEGF. Also, Gd-chelated contrast agents use this route for extravasion. In a longer term, VEGF will stimulate mitosis in endothelial cells from local blood vessels which thus divide and develop a new vascular infrastructure to supply the tumor. The angiogenic mechanism is also responsible for breakdown of local connective tissues, preparing the local environment for ingrowth of new vessels [41, 49].

molecules. Thus, hyperpermeability in brain tumors may be determined by a combination of both the size and number of pores, and transport via VVOs [107].

VVOs are grape like clusters of interconnecting uncoated vesicles and vacuoles found in both tumor microvessels and post-capillary venules (cf. Figure 2.5). Macromolecular tracers are shown to preferently cross hyperpermeable tumor vessels through these clusters of vesicles and vacuoles which span the entire thickness of vascular endothelium cells providing a connection between the vascular lumen and the extracellular space. The VVOs might also be the most important pathway for the Gadolinium chelated agents used in MRI, especially for the preclinical MMCMs [22, 38, 49]. The individual vesicles and vacuoles comprising VVOs are bounded by membranes and interconnect with each other and with the endothelial cell plasma membranes by means of stomata that are closed with thin diaphragms. VEGF is likely to be responsible for the opening of these stomata in hyperpermeable tumor vessels, thereby accounting for the relatively free passage of macromolecular tracers (and plasma proteins) through tumor vessel VVOs.

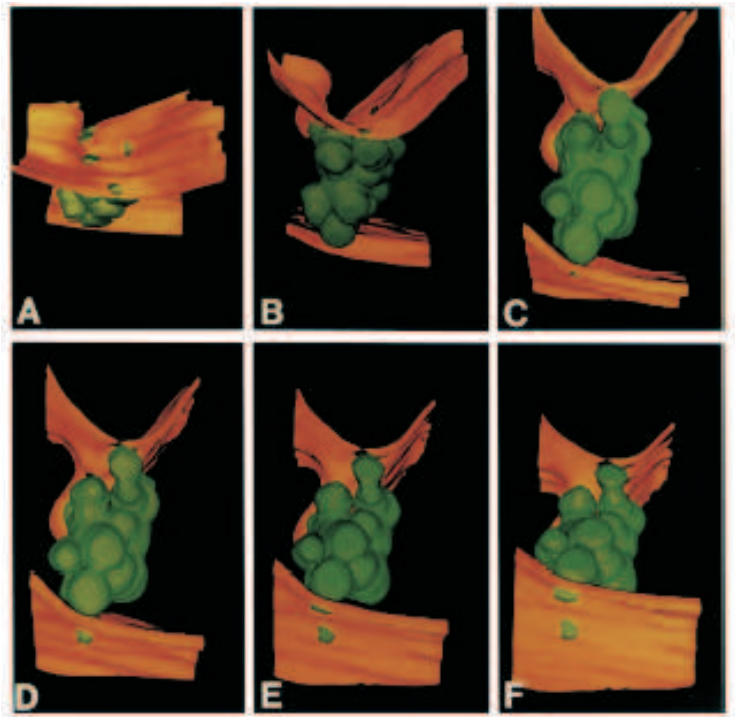

Figure 2.5.: Vesiculo-vacuolar organelles. Computer generated three-dimensional reconstruction modeling a portion of venular-VVO from mouse skin. There are two openings to the vascular lumen (E-F) and four to the abluminal surface (A) [22].

3. Modeling of tracer kinetics using compartments and rate constants

In DCE-MRI, the local microcirculation in tumors (and other tissues) is exploited by *modeling the kinetics of injected contrast agents.*

3.1. Kinetics and pharmacokinetics

The topic of kinetics address *the measure of the rates of reactions*, and *the study of the variables that affect the rates.* The rate of a process or reaction describes how fast it occurs, and is often expressed as the change in e.g. concentration per unit time, $\frac{dC}{dt}$. Kinetics is of great importance in all fields of medicine, biology and biochemistry. Bacterial growth rates and radioactive decay are both examples of processes which depend on rates of reactions [101].

Pharmacokinetics (PK) combines the topics of pharmacology and kinetics, and studies the rates of absorption, distribution, metabolism and elimination/excretion of drugs and metabolites in biological systems [45, 110].

While pharmacokinetics as a topic describes the macroscopic effects of tracer distribution and eliminations on measurable concentrations, the additional topic of physiology deals with the processes determining tracer distribution on the microscopic level, as described by parameters [100].

A pharmacokinetic model is a mathematical description of drug disposition[1] in the body. A complete model mathematically addresses all four flow rates named above. By means of their quantitative nature, pharmacokinetic models have for years been used as a tool for studying and predicting concentrations of drugs in the body as a function of time and dose. They are also used to predict the kinetics of chemical residues in the environment, to

[1]The term disposition as defined in pharmacokinetics denotes the combined action of distribution and elimination when the plasma concentration time course cannot be determined (Port et al 1999, AIF).

solve pollution problems and to provide knowledge of toxicology. As a result, a variety of different pharmacokinetic models exists; such as compartmental and non-compartmental models, physiologically based pharmacokinetic models, and population based pharmacokinetic models [110].

Compartmental modeling is based on classic kinetics which views the body as a series of compartments in which the drugs are distributed. Exchange of drugs or chemicals between the different compartments is described by *rate constants* which correspond to the flow rates of absorption, distribution, metabolism and excretion/elimination. Notice that the *compartments* in a compartmental model are not strictly physiological or anatomically based, and do not always represent real physical body volumes. In some cases, a compartment can refer to a chemical state (a metabolite of the drug).

In compartmental models, a compartment is actually considered to be a *homogeneous and well mixed* hypothetical volume or unit. Different units interact by exchanging chemicals. An animal body can be considered to contain a number of compartments, or a restricted anatomical region can be divided into compartments in which tissues are *kinetically connected*. Two-compartmental models can e.g. describe a plasma compartment in interaction with a tissue compartment.

Organisms are best described as the sum of a network of compartments [110]. A one-compartment model is best suited if the exchange between potential (sub-) compartments is so fast that they can be considered as one single unit, i.e. if the drug concentration in different compartments reach equilibrium simultaneously. Very few chemicals have these chemical properties, and multi-compartmental models would give a more realistic representation of the drug disposition in the body. In a multi-compartmental model, more than one exponential is needed to describe the decay of drug concentration with time. It can be difficult to identify and estimate more than three exponents in a multi-exponential equation. Consequently, two-compartmental and three-compartmental models are most frequently used to represent a drugs behavior in an animal body.

3.1.1. Two-compartmental modeling

When injected drugs do not distribute evenly amongst all the organs, a one-compartmental model would not provide accurate information about the drug disposition in the body (cf. Section 3.1). A two-compartmental model in which drug disposition is bi-exponential would be a better choice. In the two compartment model, the drug is assumed to distribute into a second compartment, but elimination is assumed to occur from the first compartment only. Although this is a simplification, the model can provide information of flux rates in and out of specific organs.

The theoretical models used in pharmacokinetic MR imaging are typically two-compartmental

models where the body (or region of interest, ROI) is considered as two compartments; a central compartment and a peripheral compartment. The first is usually blood or blood plasma while the latter can represent a tissue. The two compartments is connected through a leaky membrane. Intravenous injected tracer (or MRI contrast agent) will immediately

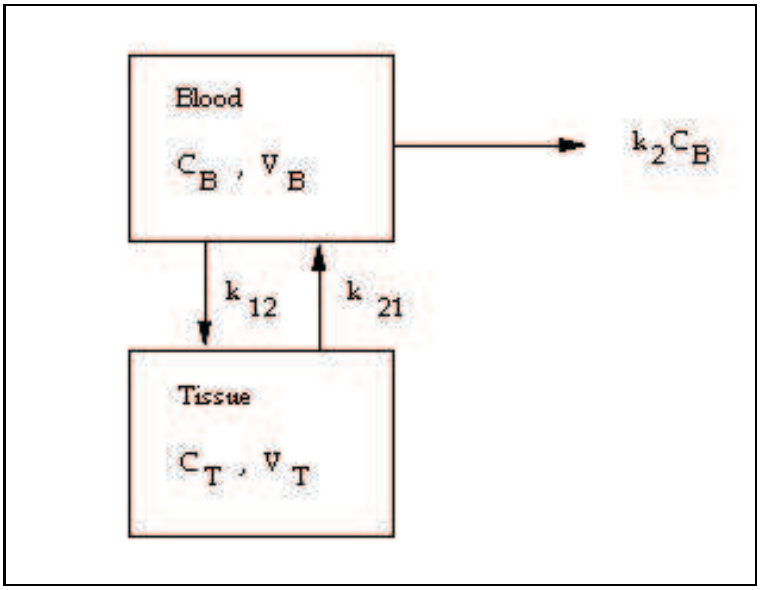

Figure 3.1.: A general two-compartmental model. Intravenous injected tracer will distribute within a central compartment blood with tracer concentration C_B and volume V_B, and a peripheral compartment tissue with tracer concentration C_T and volume V_T. Tracer is eliminated through the kidneys from the central compartment alone (k_2C_B). Tracer flux between compartment 1 (blood) and compartment 2 (tissue) is denoted k_{12}, and k_{12} for the opposite direction.

distribute in the central compartment and simultaneously in the peripheral compartment. Tracer fluxes (amount of tracer per unit time) between compartments are described by transport constants (k_{12} and k_{21} in Figure 3.1).

In pharmacokinetic MRI, tracer concentration is measured[2] indirectly by recording alteration of signal intensities. It is desirable to estimate the transport constants and possibly the volume fractions[3].

If the body is considered as two compartments where tracer is injected in the central compartment, the tracer concentration in plasma can be shown to exhibit a bi-exponential decay when all tracer is injected. The time course of plasma concentration is determined by the dose, injection time, normal distribution within the body, and elimination through kidneys [94]. Tissue-tracer time course, as measured by a time series of signal intensities in DCE-MRI, is dependent on several factors [78]:

[2]By knowledge of the contrast agents effect on the signal intensity, contrast concentration can be decided.
[3]Volume of compartments per unit volume of tissue.

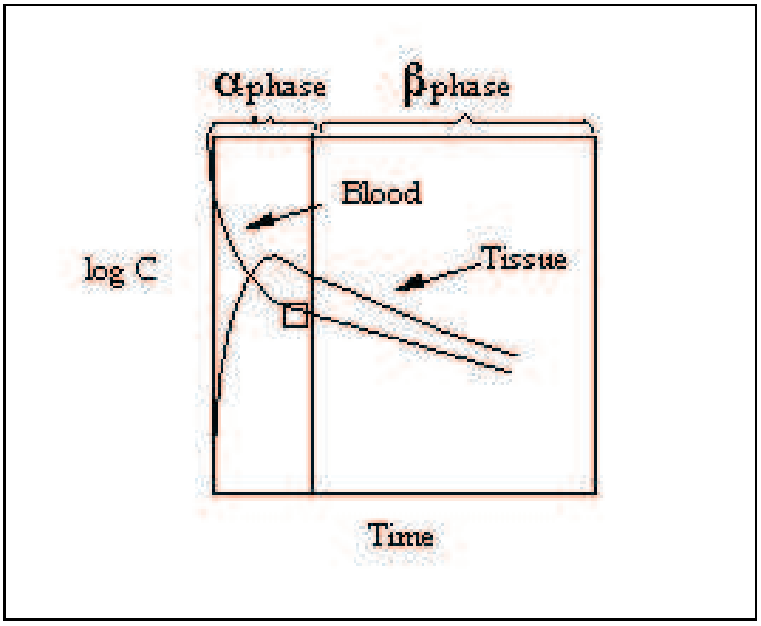

Figure 3.2.: Time course of tracer in two-compartmental models. A bi-exponential decay in tracer plasma concentration follows an intravenous injection. Immediately after the end of an injection, plasma concentration will decay rapidly caused by both distribution to peripheral compartment and elimination from kidneys (α-phase). After equilibrium, the decay is slower, caused by elimination alone (β-phase).

- Histology/physiology of the tissue (especially the microvasculature and the blood-brain barrier).
- Distribution volume of the contrast agent.
- Given concentration and dose of contrast agent.
- Original T_1-relaxation of the tissue.
- The agents relaxivity in the actual tissue for a given temperature and field strength.
- The MRI scanning method (equipment and sequence parameters).

Tracer concentration during time in each compartment is illustrated in Figure 3.2. Initially the plasma drug concentration will decay rapidly due to distribution into the second compartment and the (e.g. renal) elimination from plasma. After reaching equilibrium, the plasma drug concentration declines more slowly caused by elimination alone. Simultaneously, tissue concentration will build up to a maximum concentration at equilibrium and subsequently decay due to elimination of tracer from the compartments.

4. MRI contrast media

Tumor vasculature can be investigated by time-dependent tissue delivery of injected contrast agent [30].

4.1. Effects of MRI contrast agents

In MRI, the signal intensity at a given location in the image depends on a combination of different factors such as proton density, relaxation times and intrinsic variations in the magnetic susceptibility (cf. Section B.1, Appendix B). When these properties vary between regions, good image contrast is achieved.

Exogenous contrast agents (CA) affect the relaxation times of the tissues, thus enhancing signal intensity-differences between them, They are valuable in detecting pathologies such as tumors, infection, infarction, inflammation and post-traumatic lesions. Moreover, use of contrast agents has made development of several new functional MRI techniques possible[1]. An introduction to commercial (and future) MRI contrast agents and their pharmacokinetics is given in Appendix B.

The predominant effect of paramagnetic agents (Gadolinium chelates) at low doses (e.g. 0.1–0.2 mmol/kg) is shortening of T_1-relaxation time. This effect is displayed as enhancement of signal intensity in T_1-weighted imaging [6]. Clinically approved contrast media for intravenous injections are low molecular agents such as Gadolinium-diethylenetriaminepentaacetic (Gd-DTPA). Gd-DTPA is considered a low molecular agent, possessing a molecular weight of 0.58 kDa. However, transvascular transport (i.e. the product of permeability-surface area (PS-product)) is more accurately reflected using a contrast agent which is transported across the vessel wall at a rate slower than its perfusion [45, 96, 109]. Macromolecular contrast agents, whose advantages have been demonstrated in preclinical studies, most likely possess such permeability-limited extravasation [7]. In this study, dynamic MRI measurements were performed using the novel contrast agent Gadomer-17 as enhancement media.

[1] Some of the FMRI techniques applicable in cancer diagnostics are briefly presented in appendix C.

4.2. Gadomer-17

Gadomer-17 is a new synthetic dendritic gadolinium complex chelating 24 Gd ions, which causes high density of gadolinium per molecule of contrast agent. Gadomer-17 has a molecular weight of 17 kDa. However, due to its molecular shape, the CA possess an apparent molecular weight of 30–35 kDa [37] . A slower molecular tumbling rate causes Gadomer-17 to have a high T_1-relaxivity compared to low-molecular-weight agents (<1 kDa) such as Gd-DTPA [60].

Trimesoyl triamide represents the central core of the Gadomer-17 molecule. The molecule employs 18 lysine amino acid residues, binding 24 Gd(dota)-monoamide complexes, attached to the central core. The gadolinium complexes are thus situated on the surface of the dendrimer [66]. The complete Gadomer-17 complex has a low osmolality (about 380 mOsm/kg) and low viscosity (approximately 7 mPas) [60].

Gadomer-17 has been described as a medium-molecular/macro-molecular blood-pool agent. After an intravenously injection Gadomer-17 distributes almost exclusively within the intravascular space with minimal extravasion. This agent thus have a smaller volume of distribution space compared to the monomer agents which distribute in both the intravascular and the extravascular compartment. Additionally, Gadomer-17 have a longer lasting vascular enhancement compared to clinically available agents. Even though Gadomer-17 possess sufficient intravascular retention, the molecule is small enough to undergo fast and quantitative elimination from the body via glomerular filtration [60].

Gadomer-17	
Molecular Weight (nominal)	17,454 kDa
Molecular Weight (apparent)	30-35 kDa
Gd-concentration	500 mmol/l
Plasma Protein binding	n.d %
Partition coefficient (at pH 7,6; butanol (water))	0,0002
Blood/plasma elimination	tα: 2,4 min
Half life (Rat)	tβ: 37,5 min
Clearance (CL total), plasma	9,5 ml min^{-1} kg^{-1}
Distribution volume (Vss), plasma (rat)	0,14 L/kg

Table 4.1.: Physiochemical and pharmacological properties of Gadomer-17. These data was kindly provided by Dr. B. Misselwitz (Schering) by personal mail correspondence. Relaxivity data were also received. These are presented in Table D.8, Appendix D.

Misselwitz et al. [60] tested elimination of Gadomer-17 after a single i.v. injection in rats. The dendritic chelate was rapidly and completely eliminated from the body, mainly via glomerular filtration. No long-term accumulation or retention of the agent was detectable in organs or tissues. 75% of the injected dose was present one minute after injection. At five minutes post-injection, 21% was present in blood, and only 1% was still present

at 30 minutes post-injection. It was observed an early, rapid decline (half-life of about two minutes), characterized by distribution in vascular space and partly renal elimination. Distribution volume in this initial (α) phase was assessed to be about 0.044 L/kg in rats. The distribution volume thus reflects the plasma-volume, which is about 0.03 L/kg. Due to their larger size, macromolecular weighted contrast media have in general smaller distribution volume than do small-molecular weighted agents.

As described, tumor tissues have large extracellular volumes and will thus show strong enhancement of contrast agents. Agents of low molecular weight will, however, pass unselectively across a leaky tumor vessel. Contrast agents of larger molecular size, which mainly acts as blood-pool agents remaining in the vasculature, can thus provide a better information on the leakage status of a vessel [97].

Su et al. [96], estimated vascular pharmacokinetic parameters using three different contrast agents; Gd-DTPA (<1 kDa), Gadomer-17 (35 kDa) and Albumin-Gd-DTPA (70–90 kDa). It was found that by using Gd-DTPA, one could differentiate between benign and malignant tumors, but not between tumors of different grades. However, Gadomer-17 could distinguish high from low grade tumors, but could not detect differences between low grade tumors and benignant tumors (which despite differences in origin showed surprisingly similar enhancement patterns). The largest agent could differentiate both, but achieved low contrast to noise ratio and thus high variability. Additionally, biological concerns such as long retention in the body limits this agent for human use.

4.3. Contrast agent relaxivity

Relaxivity characterizes the efficiency with which an agent enhances water relaxation and thus signal intensity, and can be defined as follows:

> *The proton relaxivity, r_1 of an agent represents the enhancement of the relaxation rate of water protons in the presence of the paramagnetic compound compared with that in pure water, referred to a 1 mM concentration of Gd [67].*

In pharmacokinetic MR imaging, information about the agents' relaxivity is required in order to determine CA tissue concentration from measured signal intensity (cf. Section 5.2).

The relaxivity effect on the contrast agent concentration [Gd] on the T_1-relaxation of the water protons can be expressed as:

$$\Delta R_1 = \frac{1}{T_1} - \frac{1}{T_{10}} = r_1[Gd] \tag{4.1}$$

where ΔR_1 denotes the change in relaxation rate. $1/T_1$ is the T_1 relaxation rate in presence of contrast agent (R_1) and $1/T_{10}$ is the precontrast relaxation rate (R_{10}). The relaxivity (r_1) is the increase in relaxation rate per unit concentration of tracer, given in $mM^{-1}sec^{-1}$ [21, 37, 91, 104]. Thus, the higher the concentration and/or the relaxivity of Gd, the shorter the blood T_1 and the higher the blood signal intensity in T_1-weighted images, assuming that Equation 4.1 holds for a wide ranges of Gadolinium concentrations [115].

Compared to monomers, macromolecular contrast agents gain increased relaxivity from their increased molecular weights [67]. In general, Gadomer-17 relaxivity is about 3.5–4.5 times the Gd-DTPA relaxivity [97]. Specifically, the novel agent possesses a relaxivity of 14.7 $mM^{-1}s^{-1}$ at 2 T and 40 ^{0}C in bovine plasma (Misselwitz, Schering).

5. Dynamic contrast enhanced imaging

The method of dynamic contrast enhanced MRI (DCE-MRI) will here be described, both in general and in conjunction with the two pharmacokinetic models which were applied to extract physiological parameters from the recorded MRI data sets. When used in combination with pharmacokinetic modeling, DCE-MRI is often referred to as **pharmacokinetic MRI**.

5.1. Introduction to DCE-MRI

Conventional MRI is a relatively slow imaging technique. In the late 1980s, when rapid imaging sequences became available, MRI thus possessed new possibilities. Rapid serial imaging made it possible to follow the dynamic signal intensity changes after contrast injection. The basis of such *contrast enhanced dynamic imaging*[1] is to;

> inject a bolus of a contrast agent into the vasculature (typically a vein) while rapidly acquiring images (repeatedly) from the anatomical region of interest being perfused. The recorded contrast agent behavior, in terms of changes in signal intensities, is then visualized and described mathematically. In some applications, the time course data are fitted to pharmakocinetic models such that physiological model parameters can be estimated, and parametric images be generated.

As opposed to conventional X-ray CT imaging, signals forming the basis of MR images, are generated from the body itself. Image contrast is derived from differences in signal intensity emitted from proton-spin populations located in various physico-chemical environments in the body tissues. By being sensitive to different types of information from the induced NMR signal, distinctive image contrast mechanisms can be expoited by selecting appropriate

[1] DCE-MRI as opposed to T_2*-weighted dynamic susceptibility contrast MRI (DSC-MRI) is briefly elucidated in Appendix C.

pulse sequences. In its simplest form, this is referred to as image-weighting, producing e.g. T_1-weighted, T_2-weighted, or proton density (PD) weighted images [16, 35, 76, 77, 111, 112].

In this study, a T_1-weighted DCE-MRI technique was used, in which image contrast is based on differences in T_1-relaxation times between tissue voxels. While tissues with long T_1-relaxation times (e.g. CSF and edema with high fraction of mobile water) generates low signals and thereby dark pixels, tissues with short T_1-relaxation times (e.g. adipose tissues with less proton mobility) generate higher signal intensities, shown as brighter pixels. If we inject a contrast agent, such as Gd-DTPA, with a T_1-shortening effect on water protons in its vicinity, we will observe enhanced signal intensity in regions where the contrast agent is transported (vessels) and accumulated (tissue).

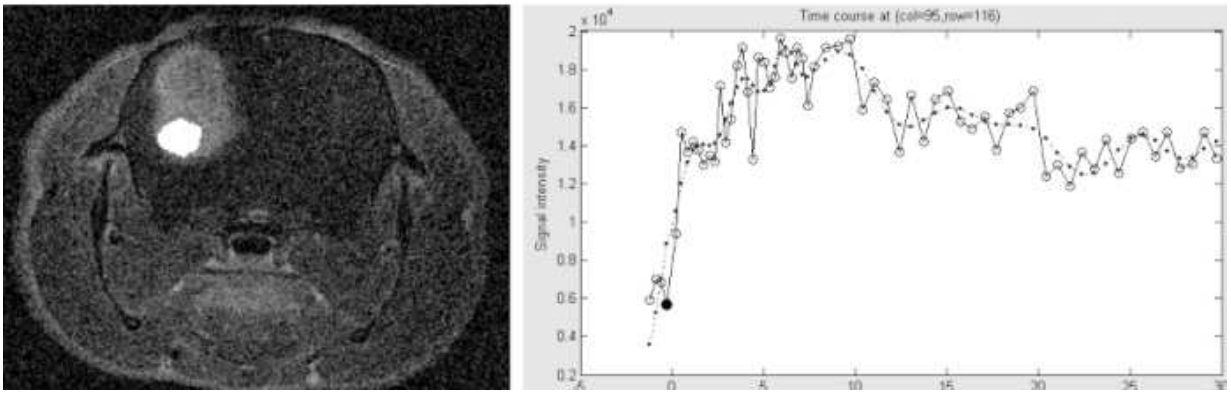

Figure 5.1.: Time course of signal intensity from one single pixel (right panel) within selected region of interest (left panel) covering a part of the tumor region (implanted glioblastoma multiforme). The dotted line is the result of smoothing the pixel-based curve in the time domain. Maximum signal intensity in the pixel was achieved 5–7 minutes after bolus injection of a MRI contrast agent (Gadomer-17).

If an anatomical region is sequentially imaged over time after a bolus of contrast agents has been intravenously injected, a signal-intensity curve can be generated for each resolution cell (pixel or voxel) in the image. In the first phase (minutes) following injection, the contrast agent may gain access to the extravascular space[2] and cause signal increase due to shortening of tissue T_1-relaxation times. During time, signal increase thus arise from both the vascular and the interstitial compartments. The injected contrast agent can also diffuse into tissue compartments further away from the vasculature, including areas of necrosis or fibrosis. Over a period, typically lasting several minutes to half an hour, the agent diffuses back into the vasculature (descibed with the rate constant k_{ep}) from which it is excreted from the body (mainly by the kidneys) [69].

After acquiring such DCE-MRI time series, the data can be assessed in two ways: (i) by explorative or descriptive analysis of signal intensity changes ($S(t)$), denoted *semi-quantitative analysis*, or (ii) by model-based quantification of contrast agent concentration

[2] Contrast agents (CA) approved for bolus injection in humans, distribute in the vascular- and extravascular (extracellular) space (cf. Appendix 4).

change ($C(t)$) and estimation of microvasculatory parameters typically using multicompartment, pharmacokinetic modeling techniques. This methods is entitled (*quantitative analysis* or *pharmacokinetic MRI*). The latter approach is employed in this thesis.

5.1.1. Applications and features of DCE-MRI

DCE-MRI provides important applications to biomedical research by *adding the dimension of time to anatomical imaging*. Morphological changes are often more unspecific than are physiological changes. By using DCE-MRI, pathologies and effects of therapy can be detected before changes in volume or (static) signal intensity can be measured by conventional diagnostic tools. By demonstrating changes in enhancement curves such as slower initial enhancement, decreased amplitude and slower wash-out, DCE-MRI provides a direct and early evidence of therapeutic effects [14].

Compared to other imaging modalities such as PET, X-ray CT, ultrasound or SPECT, DCE-MRI has a number of advantages: (i) the signal to noise ratio and contrast to noise ratio of MR images are high, (ii) temporal resolution is usually adequate regarding the underlying dynamics being studied, (iii) spatial resolution is often comparable to that of corresponding anatomical images, which can be acquired in the same imaging session, and (iv) the scanning procedure can be repeated several times (follow-up) without harm to the subject. Moreover, conventional histopathological techniques for characterization of microvascualature (such as tumor invasion or spread) are, contrary to MRI, invasive. Such methods can thus not be repeated frequently. Moreover, using histopathological approaches, the animals may have to be sacrified to perform the tissue investigations. Furthermore, isolated regional biopsies hardly reflect the spatial heterogeneity which typically occurs in tumor vasculature [41]. With DCE-MRI, the entire tumor or tissue region can be sampled with high spatial resolution, demonstrating both anatomical (i.e. vascular volume) and physiological (i.e. permeability) features [8].

Interest in DCE-MRI has grown largely with the development of antiangiogenic and neoadjuvant strategies for tumor therapy. Although angiogenic inhibitors represent a novel strategy for tumor therapy, DCE-MRI can monitor conventional therapy as well, because vessel loss is the final common pathway for many therapies such as cytotoxic therapies, radiation treatment and local therapies (e.g. cryotherapy[3]) [14]. While cytotoxic therapy effects can be measured by changes in enhancement kinetics in the tumor, success of radiation therapy can be detected as a decrease in vascularity [14]. Even though MRI-based assessment of therapy response can be sensitive, it lacks specifity, reflecting the fact that killing tumor cells, in all cases ultimately results in vascular compromise[68]. So, although DCE-MRI can serve as an early marker of therapy response, underlying nonvasular changes can not be assessed.

[3] Cryotherapy denotes use of low temperatures in medical therapy.

For the purpose of therapy planning, it is established that tumors with higher initial permeability often respond better to chemotherapy because more cytotoxic drugs are delivered to the target areas [14, 48]. Thus, in conventional cytotoxic cancer treatment, DCE-MRI can be of value by predicting the grade of drug delivery to all regions of tumor [45]. In addition, more permeable tissues can receive more oxygen, and are therefore initially more radiosensitive.

Parameters derived from DCE-MRI in conjunction with pharmacokinetic modeling techniques have in some cancers been able to predict prognosis. The method have also been shown to discriminate between scar tissues and recurrent tumor in breast [68].

Methodological problems and challenges with DCE-MRI

Although several promising areas for clinical utilization continually arise, also drawbacks of the method are emerging as the DCE-MRI is further used, both in preclinical and clinical studies. Application of DCE-MRI do not substitute for histopathological investigations. Microscopic disease may still be present even if DCE-MRI studies show no evidence of tumor. Some malignant processes can also mimic benign contrast kinetics - and some benign processes (e.g. inflammation) can mimic malignant contrast kinetics. Furthermore, changes on DCE-MRI after therapy may be non-predictive, and physiological changes in tumor caused by therapy does not necessarily affect overall patient survival [14].

The method is less applicable in body regions which are heavily affected by respiratory motions (such as lungs and liver). In other body regions, such as the brain, in which invasive procedures can be prohibited, DCE-MRI is of great value. Although DCE-MRI is a relatively easily performed scanning procedure, great care must be exercised in pre-contrast acquisitions (baseline [14]), injection rate and dose of contrast agent.

As will described later, pixel-by-pixel estimation and corresponding histograms of the parameters from pharmacokinetic models can provide information about tumor heterogeneity in a selected region. Although pixel-mapped analyses provide good visualization of tumor heterogeneity, pixel-based estimations can be difficult, or not even feasible [68]. On the other hand, ROI-based measurements are limitated by the fact that they must be obtained from comparable regions to be valid in serial studies. This is because tumor heterogeneity alone could account for an apparent change in measurements [14].

As already mentioned, many cancers display characteristic enhancement patterns: rapid and high amplitude wash-in, followed by a relatively rapid wash-out. Benign lesions and healthy tissues are shown to enhance and wash-out more slowly. It is however important to keep in mind that microscopic disease can be present even though DCE-MRI assys do not reveal any signs of tumor. Although extensive neoangiogenesis is a distinctive feature of larger tumors, small clusters of malignant cells, do not exhibit detectable neoangiogenic

properties. DCE-MRI can thus only detect tumors in which "the angiogenic switch" has been turned on [47].

DCE-MRI exhibit great sensitivity to sites of in-angiogenic activity, but a number of benign processes and high-risk lesions also enhance, reducing the specificity of the method [68]. Enhancement of non-malignant tissues can be caused by fibroadenomas, inflammatory conditions, scar tissue, dysplastic changes, sklerosing adenosis, radial scar, atypical ductal hyperplasia, of lobular carcinoma in situ [63].

Another factor contributing to the uncertainty of quantitative data acquired with dynamic imaging is the wide scatter of blood volumes, transit times etc. in different organs, or even within similar organ structures. These differences may be substantial and can overlap the values of pathologies [77]. Liney et al. [53] go far in claiming that quantifications of DCE-MRI (breast lesions) have not yet shown a conclusive benefit over empirical approaches which are widely used in clinical settings, taken into account that signal intensity not directly reflect contrast agent concentration and analysis thus is complicated.

Although DCE-MRI has an enormous potential and have also entered the clinical stage, further research is needed to better understand the biological basis of the enhancement curves, the estimated parameters - and their changes. More efforts are needed to develop (standardized) DCE-MRI methods that in the best way fulfill the assumptions of the applied pharmacokinetic models. Alternatively, new physiological models are needed to explain the DCE-MRI contrast mechanisms coming into play. Thus, preclinical studies are still very important, particularly when using contrast agents that are not yet approved for humans, or when the host or the tumor itself is under (genetically) experimental control. Such animal studies will enable MRI monitoring of novel therapies in conjunction with other in vivo assays. Moreover, they provide the ability to precisely cross correlate DCE-MRI with other imaging techniques [14].

5.2. The quantitative approach - tracer kinetic modeling

As menationed, using dynamic MRI with bolus injection of a contrast agent (hereafter denoted *tracer*), quantitative information about regional tissue-enhancment from the signal intensity time courses can be obtained. A simplistic and frequently applied quantification-method is based on parameter extraction directly from the observed signal intensity time courses ,S(t), either pixel-by-pixel (*pixel-wise*), or region-by-region (*ROI-wise*, i.e. by spatial averaging).

One example of such *semi-quantitative* approach is calculation of $T90$ from the intensity curves. The $T90$ parameter represents the time taken to achieve 90% of the maximal

enhancement, defined as the increase in signal intensity in a pre-determined time period (i.e. baseline). The measure is simple to compute. According to Jackson & Jayson [42], it is found to be relatively free from variations due to changes in dose of contrast agent, DCE-MRI imaging sequence parameters, or scanner settings. This favors reproducibility of the "$T90$-method". A drawback concerning the $T90$ measure is its failure to distinguish between contrast changes resulting from intravascular changes and those resulting from actual leakage. The value of $T90$ will be highly affected if large vessels are present in a voxel, and may thus provide a problem when analyzing large regions of interest since separation of signal change effects due to blood flow and contrast leakage is impossible. Contrary to the study by Jackson & Jayson [42], Jackson [41] claimed that metrics such as $T90$ has the disadvantage of being unpredictably affected by variations in scanning protocol. Padhani et al. [68] also claim semi-quantitative measures to be limited by the fact that they do not accurately reflect CA concentration in the tissue and can be influenced by scanner settings. Additionally, it can be difficult to understand what semi-quantitative metrics mean physiologically and whether they are robust to variations in cardiac output.

One way out of these problem with extracting metrics directly from the "raw" signal intensity time curves, is attempting to estimate inherent physiological parameters through application of an appropriate mathematical (PK) model[4]. The purpose of such mathematical modeling is

> to define the relationship between observed data (i.e. a time series of signal intensites) and the physiological (microvascular) parameters that affect the time course of the injected tracer.

In DCE-MRI, various pharamacokinetic models has been used for this purpose, based on (i) converting signal intensity (S) to tracer concentration (C), and (ii) by introducing compartments and intercompartment fluxes of tracer to formally describe underlying physiological transendothelial transport and tracer accumulation in the tissues (i.e. pharmacokinetic modeling).

In favor of such pharmacokinetic (PK) quantification, the calculated dynamic concentration curve $C(t)$ is much more independent of methods and conditions used to acquire the dynamic MRI measurements than $S(t)$ is [77, 99]. Moreover, with the use of tracer kinetic modeling, there is the potential for extraction of important biological information that is not obtained by simple analysis of the signal intensity time courses.

[4] This approach is analogous to estimating the apparent T1- or T2-relaxation times in tissue from observed data using appropriate solutions (for the applied pulse sequence) of the Bloch equations.

5.2.1. Tracers in pharmacokinetic MRI

In general, tumor vessels are shown to have wide endothelial junctions, a large number of fenestrae and transendothelial channels which may have been formed by vesicles, and a disrupted or absent basement membrane (cf. Chapter 2. These properties allow leakage of large molecules into the interstitium in which they are further distributed by molecular diffusion and convection due to pressure gradients within the interstitial space. The size of the molecules is therefore a major factor determining extravascular transport and distribution [95].

Most contrast enhanced MRI studies of tumors have been performed with low molecular weighted contrast agents such as Gd-DTPA. The molecular size of these chelates may, however, be too small to detect small differences in permeability and hence distinguish between benign and malignant tumors (i.e. tumor vessels are non-selective for passage of small molecules) [37]. The rapid distribution of Gd-DTPA is thus not dependent on transvascular transport. Hence, Gd-DTPA is not the most favorable agent to assess vascular permeability. Conversely, the distribution of a macromolecular agent is determined by transvascular transport. After intravenous injection, macromolecular agents (>30 kDa) would remain mainly in the vasculature, and leak into tissue depending on the degree of vessel permeability. In addition, they more closely match the size of the pores in capillary vessels [37, 54, 95].

Furthermore, the vascular volume can be more accurately assessed using agents which remain in the vasculature for a prolonged period of time [96]. Use of macromolecular agents in DCE-MRI is still at the preclinical stage, but very promising [14, 68].

Contrast agent dose and injection procedure

Rinck and Muller [78] recommended a dose of 0.1 mmol/kg of body weight for gadolinium-based (extracellular) agents as a lower limit of diagnostically sufficient contrast enhancement for clinical imaging at all field strengths (0.0002–4.7 T). It was further implied that increasing the dose would influence positive contrast enhancement more at high than at low fields. However, high doses (above 0.2 mmol/kg) can cause reversed enhancement due to competitive T_2 effects.

Choyke et al. [14] propose a slow bolus injection duration (40–60 seconds). Several imaging time points can then be obtained during the injection period. These time samples are important for establishment of the wash-in phase of the curve. If injection speed is fast compared to imaging speed, only one, or few, time points determine the wash-in phase. If very few data points from this initial phase of tracer uptake are present (i.e. if bolus injection is very fast), proper estimation of vascular volume fraction can be difficult [109].

On the other hand, a rapid bolus achieves a given tissue concentration of agent in a shorter time and may require a lower dose than a more slowly injected bolus [103]. Additionally, errors in estimated exchange rates caused by renal failure is reduced using a short bolus injection [41, 48, 47, 103].

Tofts and Berkowitz [103] compared constant infusion rate injections with bolus injections, and found that in case of reduced renal function, the error in calculating permeability from a certain value of enhancement is lower for the bolus than for infusion. Alteration in kidney function, will affect the clearance of contrast from plasma and thus the blood concentration curve, and the error will increase with time. As a particular tissue concentration (and hence enhancement) is reached earlier with a bolus than with an infusion of same dose, a bolus permits permeability to be measured earlier than does an infusion (i.e. total imaging time can be shorter).

At last, a bolus injection is not only much easier performed (no special equipment except from a timer is needed), but it has a significantly higher reproducibility compared to infusion method which often fail to produce steady plasma concentrations. Bolus injections produce more efficient and effective procedures which require less total tracer and less imaging time [42].

5.2.2. Assessing tissue contrast concentration

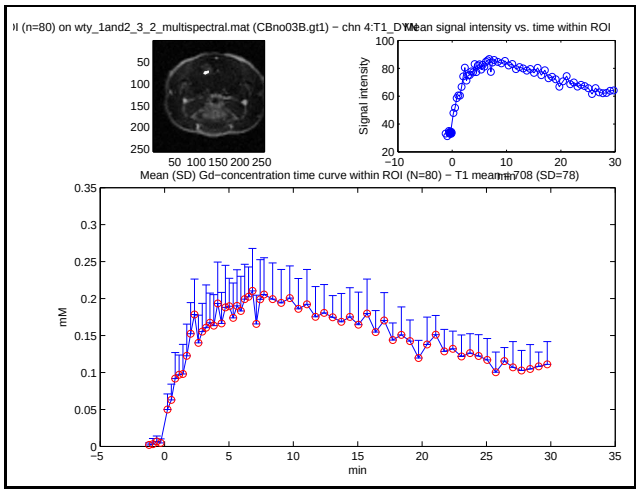

Figure 5.2.: Signal intensity course converted to contrast-concentration curve. In DCE-MRI, signal intensity with time (S(t), upper right curve) for selected ROI within tumor must be converted to Gd-concentration with time (C(t), lower curve) in order to extract physiological parameters by PK modeling. Open circles represent time points for acquired images. These curves are generated for a selected tumor region demonstrated in upper left image as a bright spot.

As there is no standard units for signal intensity (SI) in MR imaging, the signal intensity curves ($S(t)$) derived from dynamic measurements, provide only qualitative characteristics

of bolus passage through tissues. However, application of pharmacokinetic models requires physical quantities such as concentrations. Therefore the intensity time curve must be converted to a concentration time curve ($C(t)$) which is fitted to a theoretical model of pharmacokinetics to acquire quantitative information of physiological parameters.

Signal intensity in any pixel in the image depends on both the local tissue parameters; proton density, T_1-relaxation time and T_2-relaxation time, and on the sequence parameters; echo time (TE) and repetition time (TR). For spin echo sequences (SE), as used in this study, signal intensity (SI) in a pixel at a given time will be given by (assuming $TR >> TE$):

$$SI = \rho \cdot e^{(TE/T_2)} \cdot [1 - e^{(-TR/T1)}] \text{ [94]} \tag{5.1}$$

where TE is the echo time (i.e the time from excitation pulse to collection of signal from echo), and TR is the repetition time of the sequence (i.e. the time between two 90° excitation pulses). ρ is the proton density, whereas T_1 and T_2 is the tissue T_1-relaxation time and tissue T_2-relaxation time, respectively.

Assuming *negligible CA effects*[5] *on* ρ *and* T_2, the relative change in signal intensity is given by:

$$\Delta SI = \frac{SI(CA)}{SI} = \frac{[1 - e^{(-TR/T_1)}]}{[1 - e^{(-TR/T_{10})}]} \tag{5.2}$$

where *SI(CA)* is the signal intensity in presence of contrast agent and *SI* represents the signal intensity in absent of contrast agent, given from baseline (pre-contrast) images acquired prior to injection. $\underline{T_1}$ (unknown) represents the T_1-relaxation time in presence of contrast agent, and $\underline{T_{10}}$ is the inherent tissue T_1-relaxation time without contrast agent influence. T_{10} is calculated from a series of SE images with different TR times, to obtain co-registered T_1-maps.

As described in Chapter 4 (cf. also Appendix B), Gd-based MRI contrast agents affect signal intensity by shortening T_1-relaxation times of the protons in tissues in which injected contrast agents accumulate. Generally, shortening of T_1 will increase relaxation rate ($R_1 = 1/T_1$). Assuming that the *increase in relaxation rate* (R_1) *is directly proportional to the concentration of Gd-based tracer*[6] we have:

$$[CA] = \left(\frac{1}{T_1} - \frac{1}{T_{10}}\right) \times \frac{1}{r_1} \tag{5.3}$$

where CA is the total tissue concentration of tracer, T_1 is the relaxation time at a given tracer concentration (i.e. the shortened value), T_{10} is the relaxation time in absence of tracer (i.e. intrinsic T_1 of the tissue) and r_1 is the relaxivity of the actual contrast agent at

[5] T_2 « T_1 in most tissues. So, if CA have equal effects on T_2 and T_1, the relative drop in T_1 will be relatively larger than the relative increase in T_2.

[6] i.e. $\Delta R_1 = (\frac{1}{T_1} - \frac{1}{T_{10}}) = k \cdot [CA]$, where k is a contrast agent dependent constant denoted T_1-relaxivity (=r_1)

a given field strength and temperature [37, 77]. A *"fast water exchange regime"* assumption, implying "equal" T_1 relaxation in extra- and intracellular spaces, has been generally accepted [21].

Thus, the concentration time curve, $C(t)$ can be solved from Equations 5.2 and 5.3 using plug in values for TR, $r_1^{Gadomer-17}$, T_{10} from T_1-maps, and ΔSI from the observed signal intensity time curve, $S(t)$.

Notice that inherent tissue T_1-relaxation times must be estimated in order to generate the concentration time course (Figure 5.3). By fitting the resulting concentration-time curve curve to pharmacokinetic models, values of physiological parameters such as e.g. permeability, vascular volume fraction and volume of leakage space can be derived.

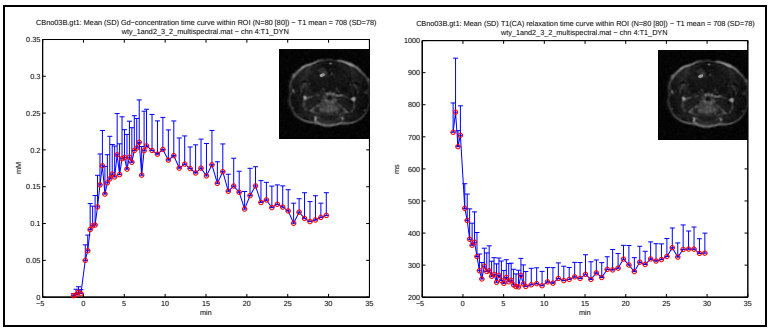

Figure 5.3.: Time course of tissue contrast is a result of change in T_1-relaxation. Time course of tissue concentration (in mM, left panel), and corresponding T_1-relaxation (in ms, right panel) after bolus injection of Gadomer-17. Due to the injection of contrast agent, T_1-relaxation time is shortened, causing signal intensity to increase (by-passing effect). It can be seen from this figure that maximum effect is reached about 7 minutes post-injection.

5.2.3. The compartment model by Tofts et al.

Dynamic MRI data were in this thesis analyzed using two differnt pharmacokinetic models, the Tofts model and the Su model, respectively. To give a general description of the "Tofts model" used in this thesis, the concepts and model assumptions, presented in three previous reports by Tofts and coworkers [105, 102, 104], is presented in the following.

A pioner in pharmacokinetic modeling applied to dynamic contrast enhanced MR imaging of pathologies is Paul Tofts at University College in London. The Tofts model is, in the Matlab-implementation being used, reduced to solving Equations (6a) and (6b) in [105], using nonlinear least-squares data fitting to estimate the model parameters k ("transfer coefficient") and v_l ("fraction of lesion tissue that the leakage space occupies").

Tofts compartment model is graphically introduced in Figure 5.4. The notations and

symbols being used are presented in Table 5.1. Two compartments are considered in case of brain lesions: a central plasma compartment and a peripheral lesion compartment. The two compartments are connected through a leaky membrane. The tracer is injected into the vascular compartment. Only the central compartment is in "direct" connection with the kidneys, by which injected tracer finally is excreted from the body.

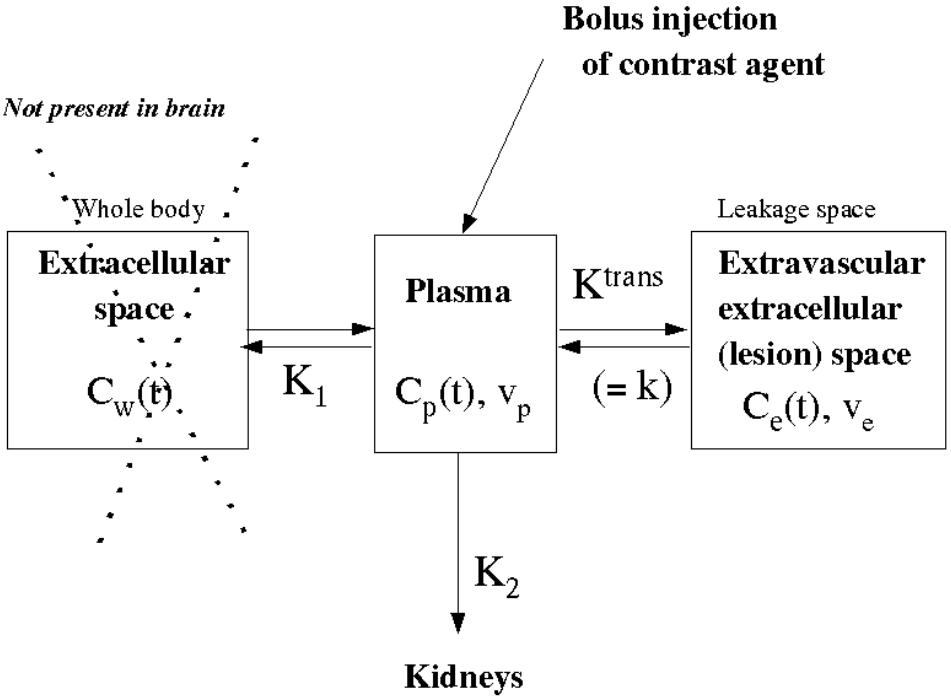

Figure 5.4.: The compartment model of Tofts & Kermode (1991) [105]. The parameters estimated by Tofts model in this thesis are the transfer constant, $\underline{K^{\text{trans}}}$ between the blood plasma and the extravascular extracellular leakage space (EES), and the fraction, $\underline{v_e}$ of EES per unit volume of tissue. From these two parameters we also obtain $\underline{k_{ep} = K^{\text{trans}}/v_e}$, the rate constant between EES and blood plasma. The lesion leakage space (EES) is conceptually the abnormal space in pathological tissue to which the tracer has access, and which is distinct from normal extracellular space. Other parameters used in the calculations are; the time-dependent plasma concentration, $C_p(t)$, and blood plasma volume per unit volume of tissue, v_p. The "whole body" extracellular compartment is used to derive the equation for the plasma concentration curve, $C_p(t)$, as a bi-exponetial decay curve. This derivation incorporates the rate constant K_1, describing the flux rate of tracer per unit concentration difference between plasma and extracellular whole body space, and excretion rate, K_2 of tracer from plasma in the kidneys. The two amplitudes and the two decay rates of the bi-exponential plasma curve could be estimated from experimental plasma concentration data provided by Dr. Misselwitz, Schering for the "NG2 project".

The Tofts equation being fitted to the data (cf. e Equations (6a) and (6b) in [105]) is:

$$C_t(t) = D\{b_1 e^{-m_1 t} + b_2 e^{-m_2 t} + b_3 e^{-m_3 t}\} \tag{5.4}$$

where D is the injected dose of contrast agent, $m_3 = K^{\text{trans}}/v_e$ is the ratio ($= k_{ep}$) between the *two free parameters* in the model; $b_1 = K^{\text{trans}} a_1/(m_3 - m_1)$, $b_2 = K^{\text{trans}} a_1/(m_3 - m_1)$, $b_3 = -(b_1 + b_2)$. The pairs

Symbol	Definition	Unit
K^{trans}	Volume transfer constant between blood plasma and EES ($K^{in} = K^{out} = K^{trans}$); same as k [105], and $k^{PS\rho}$ [102]	min^{-1}
v_e	Volume of extravascular extracellular space per unit volume of tissue (interstitial space, leakage space) $0 \leq v_e \leq 1$	-
k_{ep}	Rate constant between EES and blood plasma ($k_{ep} \equiv K^{trans}/v_e$)	min^{-1}
D	Injected dose of contrast agent	mM kg^{-1}
v_p	Volume of blood plasma per unit volume of tissue, $0 \leq v_p \leq 1$	-
V_t	Total tissue volume	ml
V_p	Total blood plasma volume. $V_p = v_p V_t = (1 - Hct)V_b$	ml
V_e	Total extravascular extracellular (EES) volume	ml
C_a	Tracer concentration in arterial whole blood	mM
C_v	Tracer concentration in veneous whole blood	mM
E	Initial extraction ratio (fraction), when there is no backflux from ESS to plasma; $E = (C_a - C_v)/C_a \overset{[104]\ \text{eq.}(21)}{=} 1 - e^{-PS/F(1-Hct)}$	-
C_p	Tracer concentration in (arterial) blood plasma $C_p = C_a/(1 - Hct)$	mM
C_e	Tracer concentration in EES (leakage space)	mM
C_t	Tracer concentration in tissue. $C_t = C_p v_p + C_e v_e = C_e v_e$ (assuming contribution from plasma compartment is negligible)	mM
ρ	Tissue density; assuming $\rho = 1$	g ml^{-1}
F	Capillary flow of whole blood per unit mass of tissue	ml g^{-1} min^{-1}
P	Total permeability of capillary wall	cm min^{-1}
S	Surface area of capillaries per unit mass of tissue	cm^2 g^{-1}
PS	The permeability surface area product per unit mass of tissue,	ml min^{-1} g^{-1}

Table 5.1.: Parameters and units in Tofts pharmacokinetic model. The parameters K^{trans} and v_e, listed above the double horizontal line, are the two parameters in the Tofts model being estimated from the calculated concentration-time curves (using nonlinear least-squares fitting). I have also reported *ROI-wise* and *pixel-wise* results for the calculated the k_{ep} parameter - which corresponds to the K_2 ($\equiv k_2/v_e$) parameter in the Su model. EES = extravascular extracellular space; Hct = hematocrit (volume fraction of whole blood taken up by cells). Table has been modified from Tofts [102] and Tofts et al. [104].

of constants a_1 and a_2, and m_1 and m_2 are the concentration amplitudes and decay constants, respectively. These were specified from the bi-exponential plasma concentration curve data provided by Dr. Misselwitz, Schering.

The tri-exponential Equation (5.4) is a solution of an initial value problem related to a coupled linear system of first-order differential equations. This coupled linear system can be formulated directly from the compartment model using simple "conservation of mass" principles, the above solution and its assumptions. Following assumptions were included in the compartment model by Tofts et al. [105]:

- After bolus injection, tracer is distributed instantaneously in central compartment and simultaneously to the peripheral compartment. At time zero, the plasma concentration (C_p) equals the dose injected divided by the volume, V_p ($C_p(0_+) = D/V_p$, $C_e(0_+) = 0$). Immediately after all tracer is injected, the plasma concentration will start to decline.

- The plasma compartment has a tracer concentration C_p and a volume fraction v_p[7]. The lesion compartment, or EES, has a tracer concentration C_e and a volume v_e per unit volume of tissue ($0 v_e 1$).

- All tracer injected and distributed within the EES compartment will in time return to plasma and eventually be eliminated through the kidneys ($K_1 \gg K_2$).

- Signal from intravascular tracer was ignored by assuming a very small vascular compartment compared to the EES ($v_p \ll v_e$). Thus tissue tracer concentration was defined to $C_t = C_e v_e$.

- Tracer was assumed to be well mixed within compartment.

- Flow is assumed high enough ($PS \ll F$) to replace tracer leaking out of plasma, thus preventing that C_p is locally depleted due to leakage of tracer. The venous tracer concentration (C_v) thus equal the arterial tracer concentration (C_a).

- The flux of tracer from plasma to EES was assumed proportional to the transcapillary difference in tracer concentration. The transport of tracer is isodirectional; i.e. the transport rate out of plasma equals the rate of transport back into plasma. At time of equilibration, tracer concentration in plasma equals tracer concentration in EES ($C_p = C_e$).

- Basically, Tofts model imply that when intravascular signal contribution is ignored, contrast agent in tissue depend upon three important factors; the time course of plasma concentration, the influx volume transfer constant (K^{trans}) and the fractional EES volume (v_e). Mathematically, tracer flux is expressed by: $\frac{dC_t}{dt} = K^{trans}(C_p - C_t/v_e)$.

[7] ($v_p = V_p/V_t$) and $V_p = V_b$(1-Hct).

The estimated transfer constant K^{trans} reflects a combination of flow (F), permeability of capillary wall (P), and capillary surface area (S). In case of sufficient flow where tracer flux between plasma and leakage space is *permeability limited* (i.e. $PS \ll F$), we will have $K^{trans} \approx PS\rho$ (as assumed above). In cases where flux of tracer across the endothelium are *flow-limited* (i.e. $F \ll PS$) we will have $K^{trans} \approx F\rho(1 - Hct)$.

5.2.4. The compartment model by Su et al.

The second compartmental pharmacokinetic model employed in this thesis is referred to as the Su model [94]. The Su model is also a two-compartment model (which includes blood plasma and extravascular extracellular space, respectively), but in contrast to the Tofts model a *vascular volume fraction (v_p)* is also included, whereas the Tofts model ignores the contribution of intravascular tracer to the total tissue concentration.

The Su model also includes *two different transport constants*, k_1 from plasma to interstitial space and k_2 from interstitial space back into plasma, as opposed to the Tofts model which assumes only simple diffusive transport with isodirectional tracer-flux between the two compartments. In contrast to the Tofts model, the Su model thus allows *convection* as an additional tracer-transport mechanism between plasma and extravascular leakage space (and back-flux from interstitium to plasma). Taking *Starling forces* into consideration, the transport constants k_1 and k_2 need no longer to be equal.

Beside concentration gradients, driving forces for transvascular flow[8] will be proportional to the capillary permeability surface area product (PS), and the difference between the capillary hydrostatic pressure (P_c) and the interstitial hydrostatic pressure (P_i) minus the difference between capillary osmotic pressure (COP_c) and the interstitial osmotic pressure (COP_i). Starling forces also explain "permeability edema" which can occur in tumor regions with leaky capillaries (peritumoral edema). Aspects of transendothelial transport and fluid balance (included Starling forces) have been introduced in Appendix A.

A graphical representation of the Su model is given Figure 5.5. Symbols and their definitions are given in Table 5.2. Further description of implications important for the Matlab-implementation of Su (and Tofts) model have also been added here. These have been written in footnote-size as they represent "methodological issues".

In contrast to Tofts model, which assumes a single bi-exponential plasma concentration decay curve, the Su model introduces a *two-step plasma curve* (cf. Figure 5.6):

$$C_p(t) = \begin{cases} \{(a_1 + a_2)/t_0\}\, t \equiv (a_0/t_0)t & \text{if} \quad t \le t_0 \\ a_1 e^{-m_1(t-t_0)} + a_2 e^{-m_2(t-t_0)} & \text{if} \quad t > t_0 \end{cases} \tag{5.5}$$

[8] Su et al. describe diffusion as proportional to S(C_p-C_e) and convection as proportional to the vessels leakage rate, which itself is proportional to [S(P_p-P_i) - (COP_p-COP_i)] (cf. Appendix A).

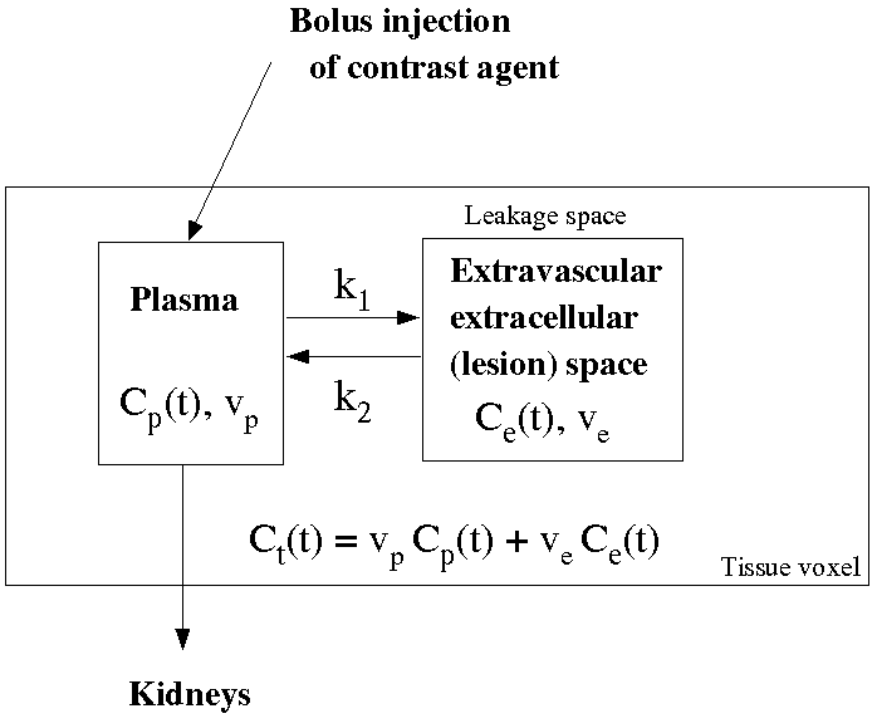

Figure 5.5.: The compartment model of Su, Jao & Nalcioglu (1994) [94]. The Su model assumes total concentration of tracer in tissue ($C_t(t)$) to be defined by contributions from both the plasma compartment ($C_p(t), v_p$) and the leakage space ($C_e(t), v_e$). The model allow concentration of tracer in blood and EES to be expressed explicitly, and derives a parameter-estimate representing vascular volume fraction (blood volume). The Su model allows different transport constants in and out of tissue; k_1 and k_2, respectively. This implies that mechanisms for transvascular transport of tracer may include convection (i.e. transport is not exerted by diffusion exclusively). The three free parameters derived by the Su model are D_0, D_1 and K_2 (cf. Table 5.2). These are related to vascular volume fraction, tracer accumulation in tissue (i.e. permeability) and rate of wash-out from tissue, respectively. Tracer accumulation in tissue (D_1) is theoretically related to Tofts "permeability-parameter" K^{trans}, and wash-out rate (K_2) is by definition comparable to Tofts efflux rate constant k_{ep}.

Symbol	Definition	Unit
D_0	Derived parameter related to the initial rising slope of the concentration time curve and vascular volume fraction; i.e. $D_0 \equiv v_p a_0$	mM
D_1	Derived parameter related to the rate of tracer accumulation in the interstitial space (EES); i.e. $D_1 \equiv v_e a_0 K_1$	mM min^{-1}
K_2	Transport constant for tracer from interstitial space (EES) back back to the plasma compartment, $K_2 \equiv k_2/v_e$	min^{-1}
k_1	Transport constant from plasma compartment to interstitial space (EES)	min^{-1}
k_2	Transport constant from interstitial space (EES) back into plasma	min^{-1}
v_p	Plasma volume fraction in selected ROI e.g. plasma volume per voxel volume	-
v_b	Vascular fraction of whole blood in selected ROI $v_p = v_b(1 - Hct)$	-
v_e	Leakage space volume fraction in selected ROI e.g. EES volume per voxel volume	-
C_p	Plasma tracer concentration (amount of tracer in plasma per unit volume)	mM
C_e	Leakage space tracer concentration, i.e. the amount of tracer accumulating in EES per unit volume	mM
C_t	Total tissue concentration, i.e. $C_t(t) = v_p C_p(t) + v_e C_e(t)$	mM
K_1	Transport constant from plasma to EES, related to leakage space i.e. $K_1 \equiv k_1/v_e$	min^{-1}
a_0	Maximum tracer concentration in plasma ($a_0 = \sum_{i=1}^{n} a_i$), occuring at time $t = t_0$	mM
t_0	Time from start of injection ($t = 0$) to time of peak plasma concentration, i.e. $C_p(t_0) = a_0$	min
Δt	Delay time from start of injection ($t = 0$) to tissue delivery i.e. $C_p(t) = 0$ for $0 \leq t < \Delta t$	min
m_i	Decay rate of the i-th term in the multi-exponential plasma concentration decay model, $i = 1, \ldots, n$	min^{-1}
a_i	Amplitude (weight factor) of the i-th term in the multi-exponential plasma concentration decay model, $i = 1, \ldots, n$	
n	Number of terms in the multi-exponential plasma concentration decay model (the Su model assumes $n = 2$, i.e. bi-exponential decay)	-
x	The ratio of amplitudes, a_1/a_2 defined in the plasma concentration model	-

Table 5.2.: Parameters and units in the Su pharmacokinetic model. The parameters D_0, D_1 and K_2, listed above the horizontal double line, are the three parameters in the Su model that are estimated from the calculated concentration time curves (using nonlinear least-squares fitting). Note that the present notation is slightly different from that used in the original report by Su et al. [94], in order to be consistent with the previous formalism of the Tofts model (Table 5.1). EES = extravascular extracellular space. Hct = hematocrit .

where a_0 is the maximum tracer concentration in plasma (occurring at $t = t_0$), m_1 and m_2 are the decay rates of each of the terms in the bi-exponential decay, and a_1 and a_2 are the corresponding concentration amplitudes. The plasma concentration model is motivated from the following reasoning. Just after bolus injection, the plasma concentration increases steadily following linear increase from $t = 0$ to the time point $t = t_0$ when maximum plasma concentration is attained. The most important factor determining t_0, is injection time (which is kept fixed in all experiments). t_0 is assumed equal between animals or between different ROIs in the animal (justified experimentally by Su et al. (1994), who found very little variation, so that the parameter t_0 could be specified rather than estimated)[9].

The second branch of the the plasma concentration function defined in Equation 5.5 incorporates a weighted sum of two exponential decay terms. The first term relates to the fast distribution of tracer throughout the body, with amplitude (weight factor) a_1 and decay rate m_1. The second term relates to a slower phase of renal elimination/clearance, characterized by weight factor a_2 and decay rate m_2.

Methodologically, for calculating the plasma curve in the Su model, the decay rates m_1 and m_2 were fixed, and so were the concentration amplitudes a_1 and a_2 (and the ratio $x = a_1/a_2$). Since we wanted to compare the pharmacokinetic models of Tofts et al. and of Su et al. for a given experiment, and even for a given pixel, these parameters were all set the same in the two models[10]. Viewed from a faster time scale, the plasma concentration $C_p(t)$ might be characterized by a small delay Δt such that $C_p(t) \equiv 0$ when $0 \leq t \leq \Delta t$ and $C_p(t) = (a_0/t_0)t$ for $\Delta t \leq t \leq t_0$. This delay Δt will thus describe tracer delivery time to tissue. In our implementation we have neglected this delay time since it occurs very early along the observed time courses and also at a finer time scale ($\Delta t \leq 9$ s in [94]).

Combining the plasma concentration time curve, $C_p(t)$ described in Equation(5.5) with the following two equations (derived from the model in Figure 5.5)

$$v_e \frac{dC_e}{dt} = k_1 C_p - k_2 C_e \tag{5.6}$$

or equivalently, $\frac{dC_e}{dt} = K_1 C_p - K_2 C_e$ (using the definitions of K_1 and K_2), and

$$C_t(t) = v_p C_p(t) + v_e C_e(t) \tag{5.7}$$

we arrive at the solution for the total tissue concentration curve (cf. Equation (9) in [94]):

$$C_t(t) = \begin{cases} D_0\left(\frac{t}{t_0}\right) + \frac{D_1}{{K_2}^2 t_0}\left(e^{-K_2 t} - 1\right) + \frac{D_1}{K_2}\left(\frac{t}{t_0}\right) & \text{if} \quad t \leq t_0 \\ \left(D_0 + \frac{D_1}{K_2 - m_1}\right)\left(\frac{x}{1+x}\right)e^{-m_1(t-t_0)} & \\ + \left(D_0 + \frac{D_1}{K_2 - m_2}\right)\left(\frac{1}{1+x}\right)e^{-m_2(t-t_0)} & \\ + \left[\frac{D_1}{{K_2}^2 t_0}(e^{-K_2 t_0} - 1) + \frac{D_1}{K_2} - \frac{D_1}{K_2 - m_1}\left(\frac{x}{1+x}\right)\right. & \\ \left. - \frac{D_1}{K_2 - m_2}\left(\frac{1}{1+x}\right)\right] e^{-K_2(t-t_0)} & \text{if} \quad t > t_0 \end{cases} \tag{5.8}$$

The three model parameters being estimated by an iterative nonlinear least-squares fit (i.e. `nlinfit` in Matlab) to calculated tracer concentration time curves, were D_0, D_1 and K_2 (cf. Figure 5.5 and Table 5.2). Initial parameter guesses in the fitting procedure were taken from values in Table 2 of [94]).

[9] t_0 is regarded as a universal constant for the experimental protocol used in this thesis.

[10] Their values ($a_1 = 38.8$, $a_2 = 0.79$ [kg l^{-l}] ($x = a_1/a_2 = 49.2$) and $m_1 = 0.417$, $m_2 = 0.027$) were

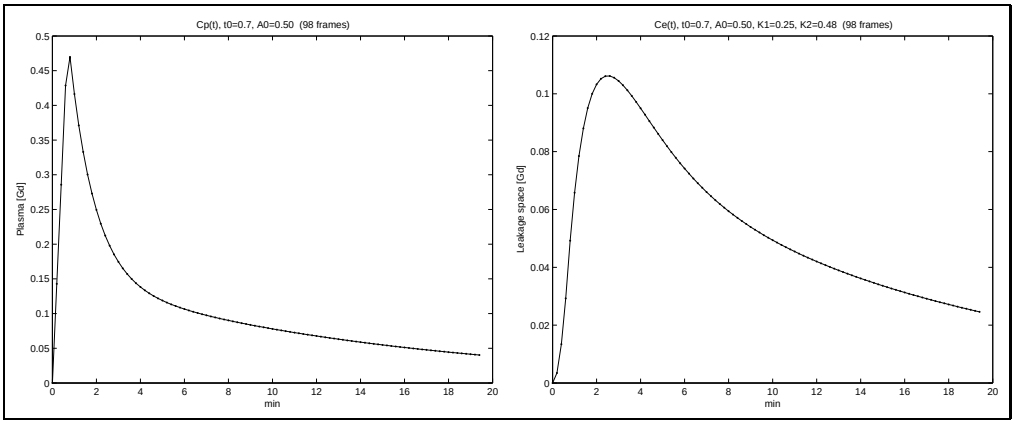

Figure 5.6.: Plasma-time course and tissue-time course of intravenously injected Gd-DTPA (Su's model). The time course of gadolinium plasma concentration (left) is determined by injection dose, injection time, normal distribution within the body and clearance via the kidneys. In Su's model, plasma tracer concentration is assumed two-parted (i.e. a linear increase followed by a decay). The right panel demonstrates $C_T(t)$; the time course of contrast agent concentration in tissue, which is fitted by non linear-least squares to estimate parametric values related to physiological processes. In other words, each tissue concentration curve has its own characteristics which can be described by D_0, D_1 and K_2; peak enhancement is determined by D_1, the decay rate is determined by K_2 and initial rising slope corresponds to D_0.

5.3. Approach to the problems

DCE-MRI as a method have previously been tested extensively, both experimentally and clinically, as a method to characterize tumors regarding the state of angiogenesis and other characteristics of microcirculation. However, an established technique is not yet generally accepted (neither for scanning nor post-processing of dynamic data) and quantitative outcomes of DCE-MRI are thus not easily compared —which in turn makes physiological interpretation of the estimated parameters difficult. Additionally, the type of contrast agent best suited for DCE-MRI is yet not decided. Therefore, a main goal of this thesis was to demonstrate feasibility and pitfalls related to DCE-MRI estimations using two different theoretical PK models (denoted Su's model and Tofts' model). The MRI data being analyzed were obtained using the novel contrast agent Gadomer-17 which is considered macromolecular compared to the commercial Gd-DTPA.

Thus, for a selection of multispectral data sets (acquired in the "NG-2 study"), parameter estimation were performed using both Su's model and Tofts' model. The pharmacokinetic models were intentionally evaluated with respect to their theoretical assumptions, their applicability to describe and differentiate tumor physiology (evaluated by analyzing tumors development during time), their applicability to describe microvasculature of normal tissue regions and their numerical fit to the recorded dynamic data. Moreover, opera-

obtained from plasma concentration curve data provided to the "NG2 project" by Dr. Misselwitz. Time from injection to peak plasma concentration, t_0, was set fixed to 0.5 min (as in Su et al., 1994).

tor dependent variability was evaluated, due to (i) manual delineation of ROIs and (ii) ROI selection on basis of different CA enhancement-templates. Additionally, a comparison analysis (Akaike's information criterion) was performed to see which of the PK models was more likely to be correct (i.e. provided the best fit). Both *ROI-wise* and *pixel-wise* analysis were performed. Their respective advantages and disadvantages have consequently been discussed.

By addressing these issues, I wished to contribute to a closer general understanding of DCE-MRI as a tool in assessing physiology of microvasculature. More specifically, the "problem areas" which have been studied are:

- **Operator variability due to manual ROI depiction**
- **Variability of ROI tracing-outcomes using Gd-DTPA as enhancement template compared to those using Gadomer-17 as enhancement template**
- **Addressing spatial heterogeneity within the tumor region by depicting several smaller ROIs.**
- **Differences in parameter estimates (and variance in fit) between four different tissue regions**.
- **Differences between week-five and week-seven NG-2 tumors (i.e. time development).**
- **The goodness of model-fit to observed data**

The "problem areas" are further described in Section 6.5.

6. Methods and material

The present work is based on the multidisciplinary "NG-2 Project". The MRI examination protocol was developed by Cecilie Brekke in collaboration with Christian Brekken (SINTEF Unimed MRI Center, Trondheim). I took part in the animal scanning at the MRI center in Trondheim during the "fifth-week post-implantation scanning". My supervisor converted and imported scanning data into Matlab and wrote the Matlab-code being used.

Using these tools and a carefully selected set of multispectral data from the imaging experiment, I have performed subsequent image analysis, statistical evaluation and interpretation, as reported in Section 6.4 in order to provide an evaluation of DCE-MRI as a method for assessment of physiological parameters.

6.1. MR scanning procedure

6.1.1. Subjects

Repetitive cerebral MRI scans were successfully performed on 17 immunodeficient Nude rats (Han: *rnu/rnu* Rowett), at *five* and *seven* weeks after implantation of brain tumors (human glioblastomas) as a part of the "NG-2 project".

Suspensions of spheroids containing about 4000 human glioblastoma (GBM) U251[1] spheroid cells had been stereotactically injected into the right subcortex of the rats. The injection site was localized 1.5 mm right of the sagittal suture, 0.5 mm posterior to bregma and at a depth of 1.5 mm from the brain surface. The rats had been anesthetized with subcutaneous injection (fentanyl/fluamisone/midazolam) prior to surgery. For aggressive tumors, human glioblastoma[2] cell lines was transfected with the rat NG-2 gene[3] prior to injection. The

[1] American Type Culture Collection, Rockville, Maryland.

[2] Glioblastoma multiforme (GBM, grade IV astrocytoma) is the most common and most aggressive of the primary brain tumors.

[3] Over expression of NG-2 have been correlated with aggressive tumor development in terms of increased growth rates, cellular proliferation and angiogenesis [13].

implantation procedure will not be further exploited as it was part of an other project.

The rats were of both sexes. Nine rats had parental **wild type tumor** (slow-growing), while the remaining eight had a **NG-2 positive tumor** (fast-growing/aggressive). After surgery, the animals had been given a recovery time of one week before they were transported to Trondheim, where they got additional two weeks of recovery prior to MRI scanning.

Prior to the experiment, a few animals went through pilot tests to optimize the imaging sequences and procedure. It was decided to perform the study using Gadomer-17 for dynamic enhancement imaging. Because of its stronger ability to shorten T_1-relaxation time (i.e. higher R1 effect, cf. Section B.1, Appendix B), pilot tests revealed higher signal enhancement in dynamic scan using this novel contrast agent compared to the commercial Gd-DTPA.

Before and after examination, the rats were kept in the animal facilities at St. Olavs Hospital in Trondheim. Effort was made to keep the environment as pathogen-free as possible to avoid infections. In case of illness such as infections —or behavioral symptoms due to the brain tumor, animals were to be sacrificed.

6.1.2. Examinations

MR examinations were performed by Cecilie Brekke (University of Bergen), Christian Brekken and Tina Bugge (both SINTEF Unimed MRI Center, Trondheim).

The rats underwent successive MRI scans on a 2.35 T Bruker Biospec Avance DBX - 100 horizontal bore magnet (Bruker, Germany). The animals were placed in a rat-head radiofrequency (RF) coil with inner diameter of 4 cm during scans. To ensure stable temperature while anesthetized, the rats were placed supine on a cradle filled with circulating fluorocarbons at 37–38 ^{0}C. Total time of imaging experiment was about 130 minutes with a total scan time of approximately 80 minutes.

Prior to MR examination each animal was first anesthetized with 3.5% Isofluran in a mixture of 70%/30% N_2/O_2 and further continuously kept anesthetized during scanning with 2.0% Isofluran in a mixture of 70%/30% N_2/O_2. The anesthetic gas was provided by a face mask. Total time of anesthesia was in a range of 2 hours—to 2 hours, 45 minutes.

When anesthetized, a polyethylene catheter was placed in right femoral vein for intravenous injection of contrast agent. The wound was anesthetized with Xylocain spray and sutured.

After the MR scanning procedure, the catheter was removed. The rat was kept in a cage by itself to make sure the bleeding had stopped before being re-united with its cage-mates.

Figure 6.1.: The scanner and anesthesia equipment. The MRI scanner (left panel) being used was a 2.35 T Bruker Biospec Avance DBX-100 with 40 cm bore size. Right panel shows equipment by which animals were anesthetized.

All animal procedures were performed using protocols approved by The National Animal Research Authority (Oslo, Norway).

6.1.3. Enhancing agents

In the "NG-2 project", two contrast agents of different molecular weights were used to enhance tumors. The new dendritic contrast agent Gadomer-17 were used for dynamic scanning (cf. Section 4.2). The molecular shape of this agent causes a relatively large apparent molecular weight of 30–35 kDa. It is therefore to be considered as a macromolecular (or mediomolecular) weight agent compared to the commercial Gd-DTPA (Omniscan, Amersham Health), which were used post-dynamic to provide accurate delineation of tumor. Gd-DTPA possess a molecular weight of 0.58 kDa. Properties of this agent have been elucidated in Appendix B.

Most DCE-MRI studies are performed with low molecular weight Gd-chelates leaking through the smallest capillary pores in tumor. However, larger molecular weight agents will leak from the microvessels at a rate related to the number and size of the pores, and other active transport mechanisms such as vesiculo vacuolar organelle [14, 24]. Hence, in case of tumor heterogeneity with patches of abnormal and leaky microvasculature, Gadomer-17 has the potential to more accurately describe this heterogeneity compared to conventional low molecular weight MRI contrast agents like the Gd-DTPA family [60, 109].

Both types of agents have neutral pH and low osmolarity. They are also both completely eliminated from the body, mainly via renal excretion [64, 60, 85]. Pharmacokinetic properties of both agents have been described in Chapter 4 (Gadomer-17) and in Appendix B (Gd-DTPA).

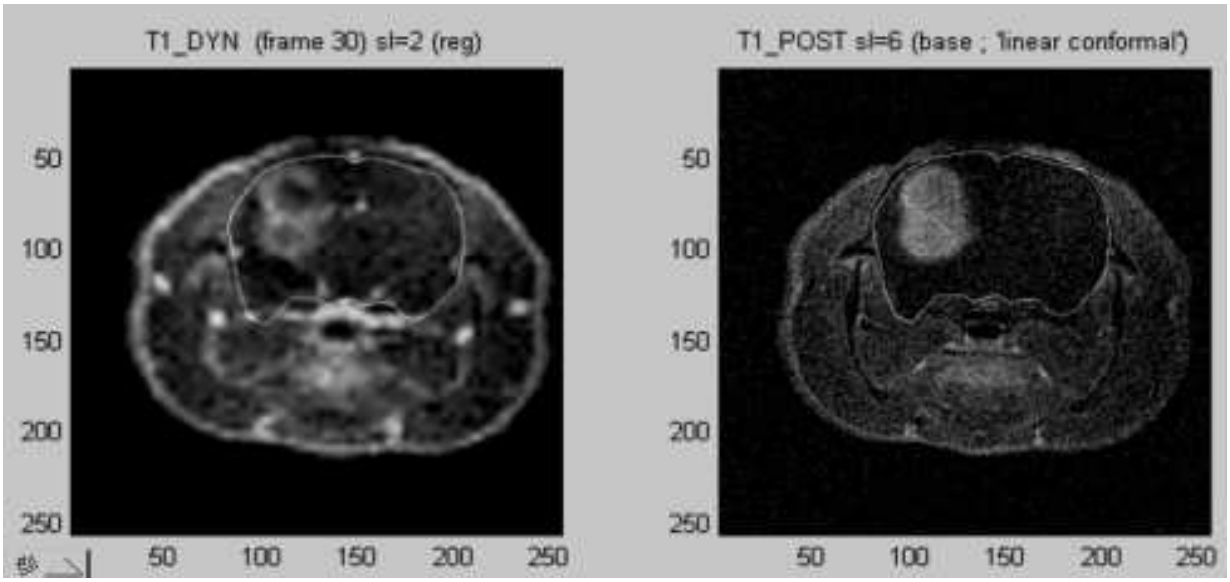

Figure 6.2.: Tissue uptake of Gadomer-17 and Omniscan. Leakage of Gadomer-17 is permeability limited due to its large effective molecular size and thus provide a better visualization of tumor heterogeneity than does Gd-DTPA (Omniscan^{TM}). **Left panel**: Image from the dynamic series of an aggressive (NG-2) tumor. Tumor is enhanced by Gadomer-17 and reveals a clearly heterogeneous appearance with high peripheral contrast leakage surrounding dark hypodense necrotic regions. **Right panel**: Image of the same tumor from the post-contrast image. Tumor is enhanced by Gd-DTPA and shows higher and more homogeneous contrast agent leakage, not differentiating the intra-tumor regions as well as Gadomer-17.

After performing the dynamic MRI measurements, Gd-DTPA was given as a bolus injection prior to a T_1-weighted scanning in order to provide a good delineation of solid tumor tissue.

6.2. Experimental imaging design

Figure 6.3 illustrates the five sequences which were acquired from each animal at both five and seven weeks after implantation. The order in which scans were measured , and the duration of each series is given in table 6.1.

A gradient echo scout scan, performed in sagittal direction, was used to localize tumor in order to plan slice geometry of the following sequences and to ensure coverage of the entire lesion. It was important that slice positions in all sequences were the same (i.e. in register) so that the following multispectral analysis would be valid.

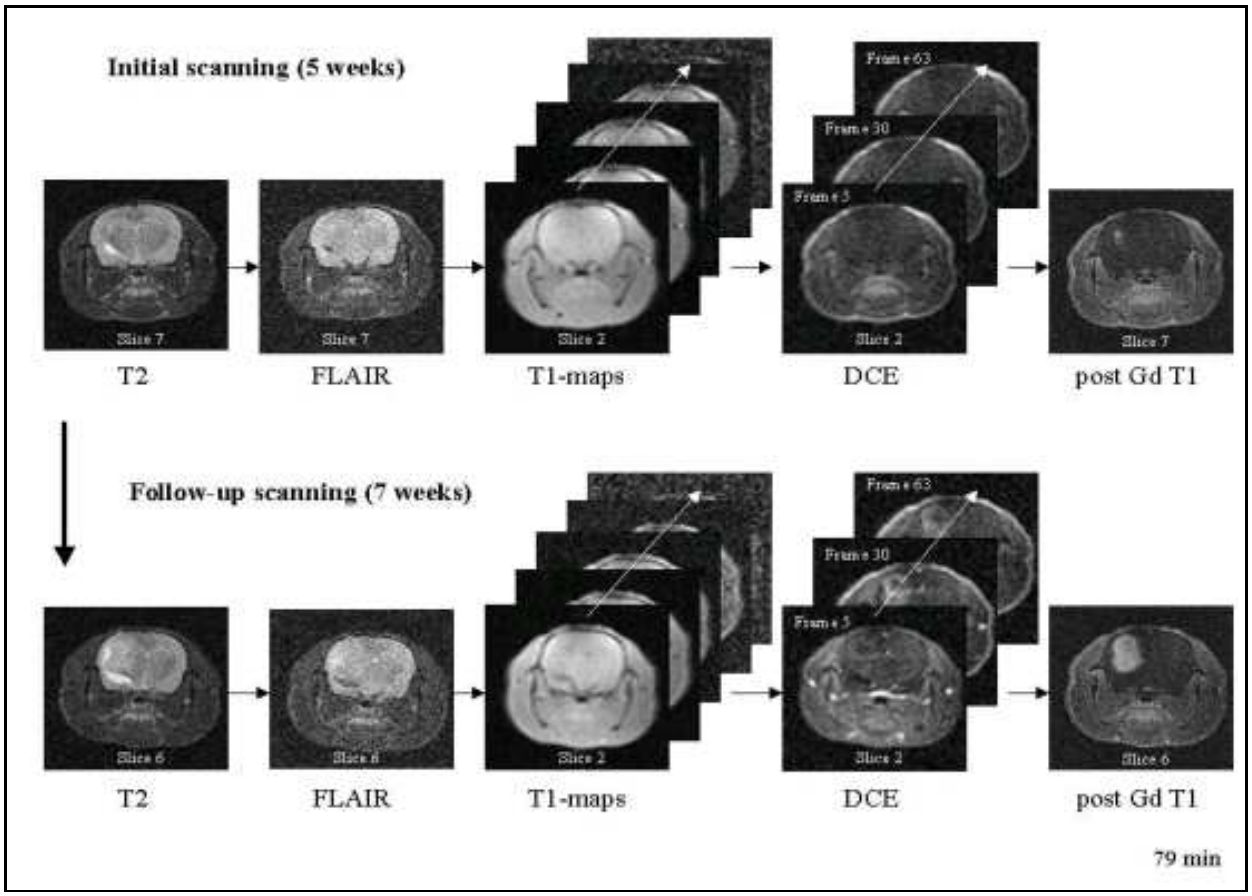

Figure 6.3.: The experimental design. For each animal, five measuring sequences were applied, here denoted T2, FLAIR, T1-maps, DCE, and post-Gd T1 (for details see table 6.1). The entire imaging protocol was repeated two weeks later (Courtesy: Cecilie Brekke).

Series #	Type of measurement	Duration
1	GEPI-rat-scout	3 min
2	RARE-8-T_2-128-60	8 min
3	FLAIR-8-128-60-2500	21 min
4	M SME-T_1-5 (2000)	-
5	M SME-T_1-5 (1500)	-
6	M SME-T_1-5 (500)	-
7	M SME-T_1-5 (300)	-
8	M SME-T_1-5 (100)	7 min
9	DYNA-T_1-ROTTE-20	30 min
10	SME-T_1-256	10 min
Total scan time:		∼80 min

Table 6.1.: Time-frame of the MR procedure The order and the duration of the different measuring sequences used in each rat examination GEPI = gradient-echo planar imaging, RARE = rapid acquisition with relaxation enhancement , FLAIR = fluid-attenuated inversion recovery , SME-T_1-5 = spin echo sequence with five different TR times and total scan time of 7 min, DYNA-T_1 = dynamic contrast enhanced scanning with injection of Gadomer-17, SME-T_1-256 = high resolution (256×256) spin-echo sequence, post-Gd-DTPA contrast injection.

The successive five measuring sequences were performed using variations of the fast spin-echo technique. Together, the T_2 sequence and the FLAIR sequence enables separation between edematous tissue and free liquid such as cerebro spinal fluid (CSF). A series of five spin-echo images with different TRs (2000 ms–500 ms) were acquired to estimate the T_1-relaxation times of tissues in absence of contrast agent. As explained earlier (cf. Section 5.1), T_1-relaxation is needed for conversion from observed signal intensities to contrast agent concentration in the dynamic data. As the last sequence in the procedure, a single multislice contrast enhanced T_1-weighted series was acquired after injection of Omniscan (0.1 mmol/kg) to provide accurate delineation of tumor and for assessment of tumor volume.

6.2.1. Details of the imaging protocol

Scan parameters for all measurements applied for at each examination in the "NG-2 study" are presented in Table 6.2. T_1 maps and dynamic scanning were acquired with three slices, positioned on basis of the RARE image slices, to cover central parts of the tumor. In addition, FLAIR and post-contrast slices were scanned with geometrically placement equal to the RARE slices.

	Scout	RARE	FLAIR	SE TR-5	Dynamic	T1 post
Main purpose	ROI/ slice pos.	Lesion- vol.	CSF- vol.	T1- estim.	Microvas. status	Tumor- vol.
FOV [mm]	60	30	30	30	30	30
Matrix	256	128	128	64	64	256
No. slices	3	11	11	3	3	10
Slice thk [mm]	3	1	1	3	3	1
NEX	2	4	2	1	2	4
Interslice [mm]	3.3	1.2	1.2	3.5	3.5	1.2
Pack ext [mm]	9.6	13	13	10	10	11.8
Slice orient	SAG	AXI	AXI	AXI	AXI	AXI
TE [ms]	5.3	60	60	8.8	5	13
TR [ms]	50	6000	6000	X	122.5	407
TI [ms]	-	-	(2500)	-	-	-
Scan time [min]	1	8	21	7	32	10
No. images	3	11	11	3	189	10

Table 6.2.: The MRI protocol. Scan parameters of the scout series and the five successive pulse sequences included in the multispectral imaging protocol (cf. Figure 6.3).

6.3. The dynamic scanning

For dynamic MRI measurements, a three-slice dynamic T_1 weighted series (TR/TE = 122.5 ms/5 ms) was acquired. Contrast agent (0.2 mmol/kg Gadomer-17) was given as a short bolus (duration about 12 seconds) after four baseline pre-contrast images were measured. The following enhanced images were acquired at 59 time frames, with a temporal resolution of 16.7 seconds for the first 30 frames, and a temporal resolution of 43 seconds for the remaining frames (cf. Figure 6.4). Thus, the total number of repetitions (or time frames), including the four pre-contrast acquisitions, was 63. Aquisition time for each frame was 15.7 seconds[4] and total sequence time was 32 minutes.

Based on information in the T_2-weighted images, the middle slice of the dynamic T_1-weighted was positioned such that it transected the center of the tumor. Thus, the dynamic image series from the slice where tumor area was maximum in the T_2-weighted sequence was used, together with the corresponding images from the other sequences, in the multispectral analysis.

This thesis is focused on data from the dynamic scanning acquired in the "NG-2 Project". The other sequences have therefore only been briefly mentioned. However, some further information about these sequences are given in Appendix D.

[4]Total acquisition time = TR x matrix x NEX = 122.5 ms x 64 x 2 = 15.68 s.

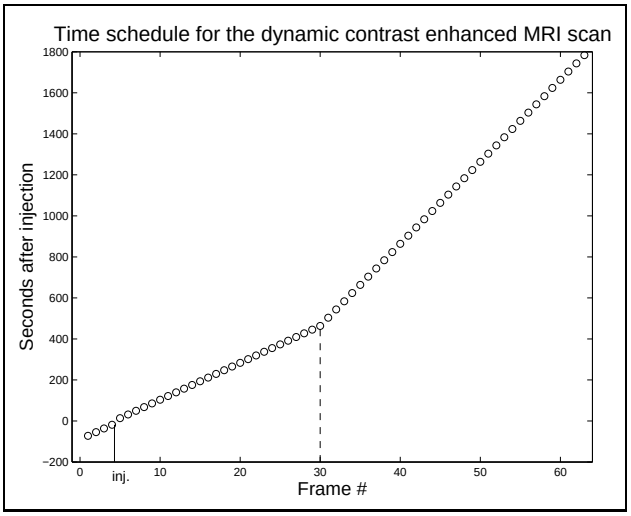

Figure 6.4.: Time schedule for the Gadomer-17 contrast enhanced dynamic imaging. Vertical solid line indicate i.v. bolus injection of Gadomer-17. The bolus injection, lasting about 12 seconds, was started 5 seconds prior to start of scan #5 (t_0). The first 30 frames had a frame-to-frame time interval of 16.7 s in order to better sample the fast initial dynamics of the contrast enhancement. After a short delay (vertical broken line), the remaining 33 acquisitions had a longer time interval (43 s) since the late phase of contrast enhancement exhibits a slower dynamics.

6.4. Post-processing: multispectral analysis and model-based parameter estimation

In this section all processing steps are reported, from data conversion to visualization of parameter estimates and final statistical analysis. All processing and image analysis were performed using inhouse Matlab[5] codes (Matlab v.6.5).

6.4.1. Converting Biospec `2dseq` data to Matlab format

Image data from the MRI-examinations used in the present work were all burnt on CD and transferred to UiB for further analysis. The first preparation step was to convert the "Bruker proprietary binary `2dseq` image files" (`uint16`) to Matlab format for each of the five pulse sequences in the protocol and for each animal examination. During this conversion proper naming conventions for all multichannel studies were introduced, such as `wty_1and2_8_1_9.mat`, denoting measuring series #9 (dynamic Gadomer-17 contrast enhanced T1-weighted series) from session #1 (five weeks after implantation) in wild type animal #8 of those in this group being scanned twice; and `ng2_1and2_3_2_4_8.mat`, denoting measuring series 4–8 (spin echo sequence with five different TRs for T1-estimation)

[5]Matlab (MathWorks, Inc., Natick, MA; `www.mathworks.com`) is a commercial software-tool with a powerful scripting language for technical computing and visualization of data.

from session #2 (follow-up, seven weeks after implantation) in animal #3 (expressing NG-2 tumor type among those in this group being scanned twice).

6.4.2. Image alignment of multichannel acquisitions

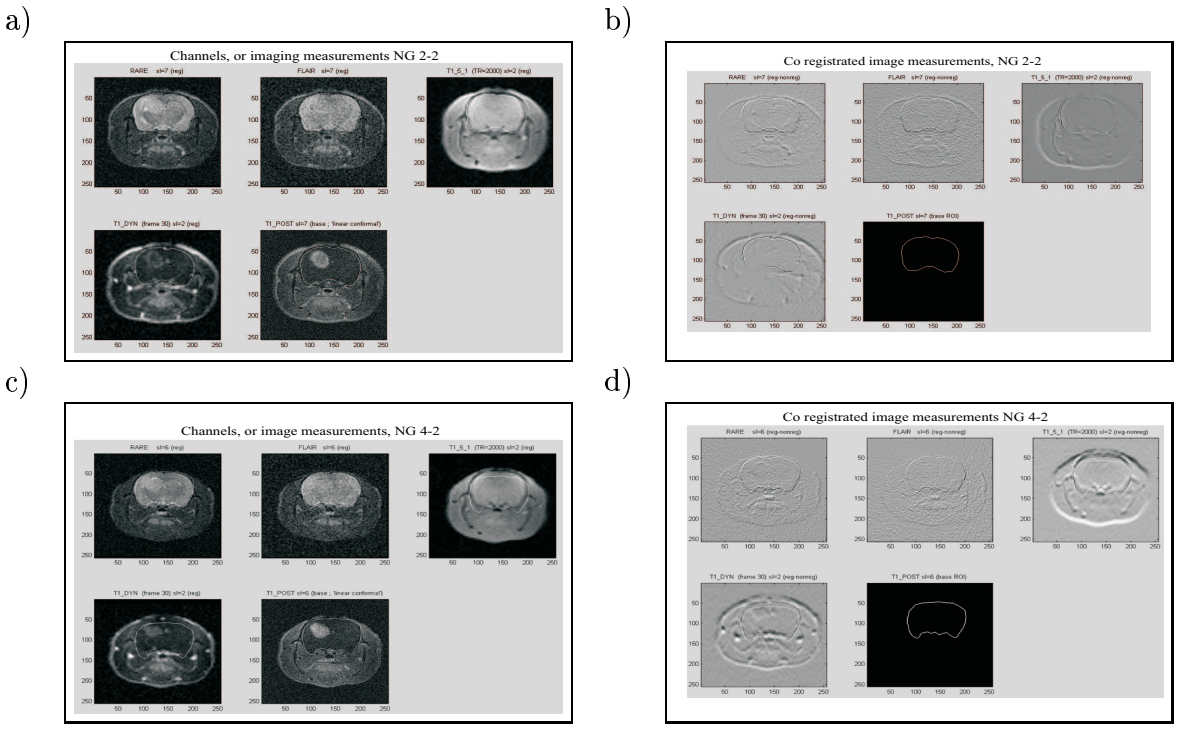

Figure 6.5.: Coregistration of imaging channels for generation of multispectral data. Data from the five imaging channels (a) and c)) were coregistrated to generate multispectral data which could be analyzed by pharmacokinetic models. In b) we see coregistration which were successful and hence included in the study. While d) shows coregistration of an experiment excluded for further analysis due to misalignments.

With the midslice image (or the one transectioning the largest part of the tumor) from the T_1 post-contrast series as base, the corresponding slices from the other sequences were decided for each examination. Given the multichannel images from this slice, the first processing step in the data analysis chain was resampling to a common 256×256 matrix (using bicubic interpolation) and spatial co-registration of all five channels (RARE, FLAIR, SE with five TRs, dynamic T1-weighted sequence with Gadomer-17, T1-weighted post-Gd-DTPA).

To improve the validity of the multispectral analysis, the resampled channel-images were aligned using a graphical user-interface for careful selection of corresponding control points with a normalized cross-correlation technique to further adjustment of each pair of control

points. A linear conformal transformation from control point pairs was then computed and applied to all channel images, including all frames within the DCE-series and the sequence of images used to compute the T_1-maps. The resulting realignment was visually checked (cf. Figure 6.5) by simple images subtraction in order to confirm accurate correlation between the different image channels prior to further analysis.

Thus, a multispectral image of the selected slice consisted of a feature vector:

$$[\text{RARE, FLAIR, [SE TR}_{2000}, \text{TR}_{1500}, \text{TR}_{500}, \text{TR}_{300}, \text{TR}_{100}], [\text{DYN}_1,...,\text{DYN}_{63}], \text{T}_1 \text{ POST Gd}],$$

having 71 components (cf. Figure 6.3). This collection of 71-dimensional multispectral images from all animal examinations were saved in Matlab format, and a subset of these images were used in the further analysis.

6.4.3. T_1 estimation

In order to apply tracer kinetic models, contrast concentration had to be derived from the signal intensity data. As described in Section 5.2, contrast concentration can be determined from signal intensity when contrast agent relaxivity and inherent tissue T_1 are known. From the five TR measurement acquired in the scanning procedure of the "NG-2 project", T_1-relaxation times were estimated by standard nonlinear least-squares method.

6.5. Analyzing the dynamic data using tracer kinetic models

Having established the concentration-time curves, the main focus of this thesis was to demonstrate parameter estimation by pharmacokinetic models introduced by Su et al. [94] and Tofts et al. [102], respectively. The pharmacokinetic parameters were fitted to the concentration time curves using non linear least-squares data fitting by the Gauss-Newton method where in general, N data points (t_i, y_1), $i = 1, ..., N$ are fitted to a non-linear continuous model having M adjustable parameters p_j, $j = 1, ..., M$. The model can be written as $y(t) = y(t; p_1, ..., p_M)$. For each model, in each of the selected examinations, for each ROI and each pixel within the ROI, and for each model parameter p_j, the fitted value $\hat{p}_j$ was estimated.

Regions of interest (ROIs), in which parameters were estimated, were drawn using a manual cursor. Parameter estimation were done either *ROI-wise* (i.e. the mean of the image data within each ROI was calculated for the dynamic images, resulting in one single time-intensity data set) or *pixel-wise* (time-intensity data were obtained for each pixel within the chosen ROI).

The implemented Matlab-codes being used to estimate microcirculatory parameters from the two models, are given in Appendix E.

Experiments were performed using the two pharmacokinetic models which were elucidated with respect to their:

- *Theoretical assumptions, including contrast agent requirements*
- *Their applicability to differentiate tumor physiology (i.e. NG-2 tumors at post-implantation week five versus post-implantation week seven), including operator dependent interaction (e.g. "manual delineation" and "different CA enhancement used as basis for ROI selection")*
- *Their applicability to describe microvasculature of normal tissue regions*
- *Their fit to the obtained dynamic data*

For selection of rat examinations, following criteria were used:

1. Inclusion of multispectral examinations showing large and clearly delineated tumor regions in the T_1-weighted post-Gd-DTPA component (channel five).
2. Exclusion of multispectral images where co-registration was unsuccessful, evaluated by visual inspection of difference images between channels, or cine loops of channels representing serial imaging (channel three and channel four, Figure. 6.5).
3. Inclusion of examinations from both the wild type (WT) tumor group and the aggressive (NG-2) tumor group.
4. Inclusion of examinations of animals having both fifth-weeks post-implantation scans and seventh-weeks post-implantation scans, to assess tumor growth and changes in pharmacokinetic parameters.

From these criteria, ten (out of 17 successful) examinations were selected for further analysis. Of these ten examinations, four were from week five and six were from week seven-scans. Only two examinations of wild type tumors were included (whereas one were from week five and the other from week seven-scans).

In the experimental part, the following methodological issues and problems have been addressed:

1. *Variability in estimated microvasculatory parameters related to the* **operator variability of manual ROI determination** *(i.e. tracing of ROIs).*

2. *Variability in parameters estimated from ROIs drawn from Gd-DTPA enhanced template compared to those depicted from Gadomer-17 enhanced template, i.e.* **different contrast agents in the "background image" which is used for ROI determination.**

3. *Variability in parameters derived from* **smaller ROIs** *of both enhanced and non-enhanced tumor regions, i.e. assessment of* **spatial heterogeneity** *within the tumor region.*

4. *ROI-wise analysis of four different tissues; to elucidate model fit and differences in estimated parameters between tissues (i.e.* **"regional differences"***).*

5. **Parameter estimation at the pixel-level** *to reveal and depict differences between week-five and week-seven NG-2 tumors (i.e.* **time development***).*

6. *The* **goodness of model-fit***, of the Su model and the Tofts model, to the observed data (i.e. contrast agent concentration time curves) in both the tumor regions and in healthy tissues.*

These issues are further described in the following sections.

6.6. ROI-wise parameter estimation

6.6.1. Operator variability of manual ROI determination

When analyzing DCE-MRI measurements with application of a pharmacokinetic model, the region of interest (ROI), in which one want to estimate model parameters, has to be determined. This is usually done by the researcher (operator) by manually tracing the boundary of the cancerous lesion. Such a procedure has a clear methodological weakness since it is not precisely reproducible and is also subject to the operator's judgment in each case. It therefore affects the degree of "validity" or reproducibility of pharmacokinetic DCE-MRI studies in a way that is hard to predict or account for statistically. Thus, in this part of the investigation, I wished to address variability and sensitivity of ROI-based parameter estimates due to manual delineation of tumor-ROIs.

Three (NG 3-2, NG 7-2 and WT 3-2) out of the ten examinations (cf. Section 6.5) was chosen for this analysis. The choice was made on the basis of apparent clearly delineated tumor edges in both the dynamic scan and the post-Gd-DTPA scan (cf. Figure 6.6). For each of the threee examinations, ROI tracing and parameter estimation was employed five times. The dynamic measurement image frame number[6] 30 provided basis for the

[6]Frame #30 represents a time of six–seven minutes post-Gadomer-17.

manual tracings. ROI was carefully delineated to include the enire tumor region each time. Tracings did not exclude central necrotic tissue, however surrounding fat and parenchymal tissue were tentatively avoided.

To evaluate variation in parameter estimates between the five consecutive tracing experiments, the mean and the standard deviation was computed for each pharmacokinetic parameter. Additionally, for comparison of variability in different distributions (i.e. parameters), the coefficient of variation (CV) was computed for each parameter from both models. The coefficient of variation (i.e. variability) is given as:

$$CV = SD/M \times 100 \tag{6.1}$$

where SD denotes standard deviation and M represents the mean. CV represents the relative variation and can thus be used to compare variation in different sets of data based on different measure scales.

The physiological properties extracted from the time-course of tracer distribution (in each of the two pharmacokinetic models) from the five repeated ROIs in three different examinations, were thus tabulated to give the mean, standard deviation, and the coefficient of variation (CV). The results are given in Table 7.1 for the Su parameters, and Table 7.2 for the Tofts parameters.

6.6.2. Use of different background information that guides ROI determination

I was also interested to see if ROI-tracing based on different images with distinct depictions of the tumor regions (i.e. enhancement distribution) affected the parameter estimates. More specifically, I was interested in the parameter-variability when the ROIs were manually delineated from the post-Gd-DTPA image compared to using one of the frames in the Gadomer-17 dynamic scan.

As demonstrated in Figure 6.6, contrast agent enhancement reveal differences (especially in tumor periphery and central areas) using eighter Gadomer-17 or Gd-DTPA. Testing variability in ROI tracings from both may imply if the enhancement distribution using one of the agents is more representative for tumor regions in which models are applicable (compared to the enhancement pattern of the other agent).

This part of the study was based on the fact that tumor edges are generally more clearly presented (tumor is more enhanced) in the post-contrast (Gd-DTPA enhanced) image than in dynamic (Gadomer-17 enhanced) images. In some of the early (fifth week post-implantation) scans of NG-2 tumors, and in many of the wild-type (WT) tumors, the tumor edges could be difficult to define visually from information in the dynamic scans.

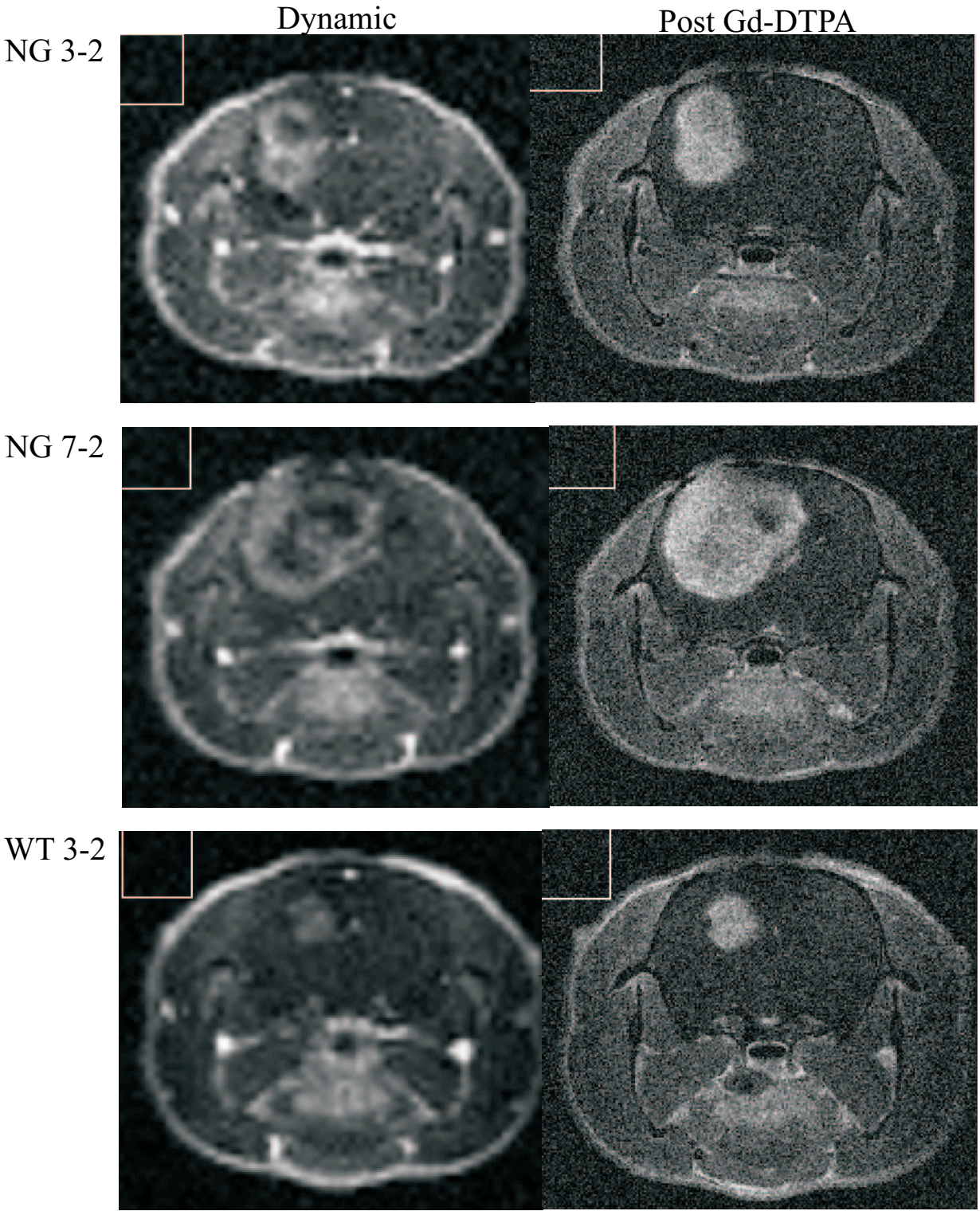

Figure 6.6.: Subjects in evaluation of manual ROI. The figure shows Gd-DTPA enhanced (right) —and Gadomer-17 enhanced (left) measurement of the three tumors which were used to manually draw ROIs in order to evaluate **operator variability** in pharmacokinetic parameter estimates. These subjects were also used for investigation of "template-related" variability. The squares in upper left corner of each image represent reference-areas to account for image noise.

This observation supports criticism regarding difficulties and subjectiveness with manual ROI determination. Initially, it seemed that drawings were more easily repeated in Gd-DTPA enhanced tumor-images. However, theoretically PK modeling better apply when using contrast agent of higher molecular weight. Gadomer-17 is such an agent, whose leakage depends upon hyperpermeable vessels. Both the Su- and the Tofts model, as used in this thesis, were implemented with Gadomer-17 based kinetics (decay rates and concentration amplitudes). Thus theoretically, Gadomer-17 enhanced areas might provide the best background for ROI-tracings. It was therefore of interest to see *if parameter variability was affected by the image channel used for tumor delineation*, considering the fact that the pharmacokinetic models are applied to Gadomer-17 kinetics (dynamic measurements) and not to the post-Gd-DTPA.

Thus, five new ROI-tracing experiments (in the examinations shown in Figure 6.6), delineating the entire tumor region, were done. This time using information from the post-Gd-DTPA image to guide the tracing. Complete tracing results are reported in Figure 7.1.

6.6.3. Heterogeneity assessment by smaller ROIs

In one examination (NG 3-2), *ROI-wise* analysis were performed in 13 different smaller ROIs. Of these ROIs, some were in enhancing areas, or hotspots (n = 7), while some were in non-enhanced tumor parts (possibly necrotic areas), dark spots (n = 6). The purpose of this part of the study was to assess tumor heterogeneity in terms of parameter variations between multiple small ROIs within a tumor (i.e. *assess parameter variability between tumor regions exhibiting the same visual degree of enhancement*). ROIs drawn for this part of the analysis is shown in Figure 7.4, page 73.

6.6.4. Analyzing ROIs of four different tissues ("regional differences")

As pharmacokinetic models are theoretical models and not models developed for our data exclusively, it was of interest to see if one of the models applied (*visually*) seemed better fitted to the concentration data than the other. Furthermore, I wanted to evaluate the fit to the concentration-time courses from ROIs covering entire tumor compared to the fit to concentration curves from smaller ROIs in tumor. These smaller ROIs represented highly enhanced homogeneous regions. In addition, model curves from ROIs of healthy tissues (grey matter and muscle tissue) were evaluated and compared to the "tumor tissue fit"

Additionally, parameter estimates were evaluated to elucidate eventual regional differences and/or relation between parameters. More specifically, I wanted to demonstrate relation across regions in the theoretically related parameters from both models: *blood-tissue per-*

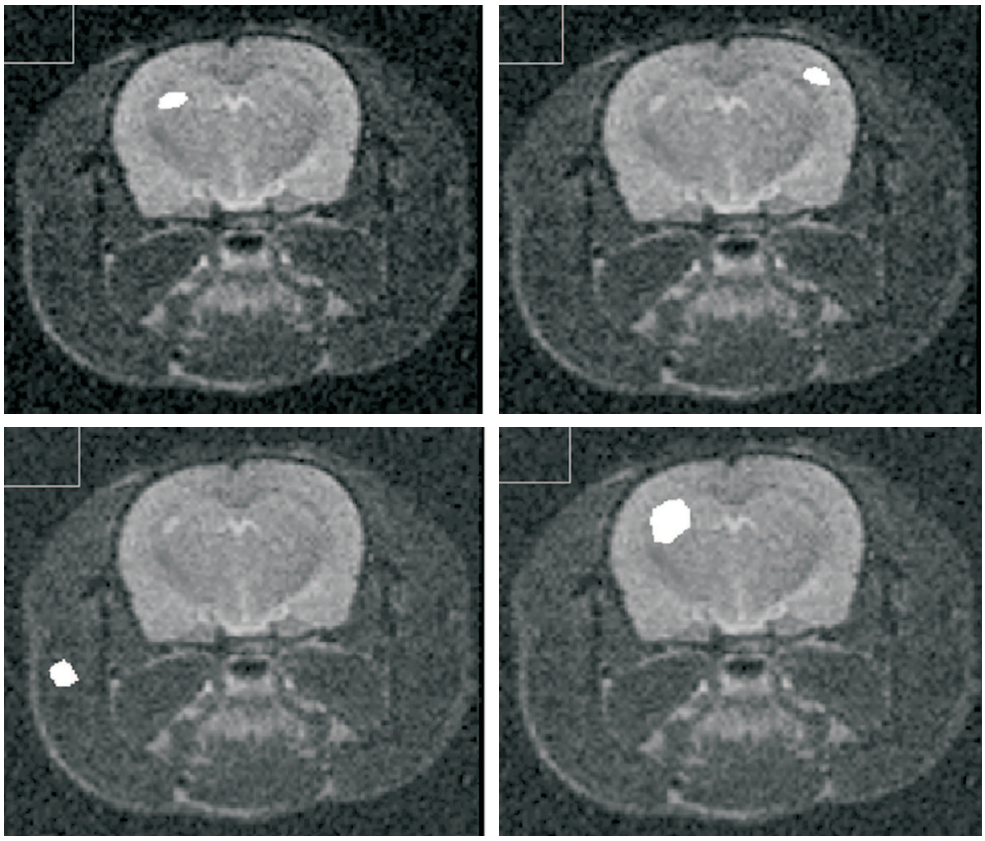

Figure 6.7.: Four different tissue ROIs for elucidation of regional differences. Parameters from both models were estimated for these four different ROIs in nine examinations. Additionally, model fit were elucidated by visual evaluation of fitted model curves for each ROI (in each of the nine trials). The four different ROIs were "Uniformly enhancing subregion of tumor" (upper left), "brain tissue (grey matter) region" (upper right), "muscle tissue region" (lower left) and "whole tumor region" (lower right).

meability (D_1 and K^{trans}) and *wash-out of tracer from tissue (K_2 and k_{ep}).* Further, I wished to assess the relation between D_1 (Su) and K^{trans} (Tofts) and the relation between K_2 (Su) and k_{ep} (Tofts) running least-squares linear regression analysis.

In nine examinations, four *ROI-wise* parameter estimations were thus executed in each:

- Uniformly enhancing subregion of tumor
- Brain tissue (grey matter) region
- Muscle tissue region
- Whole tumor region

Tumor ROIs ("whole tumor" and "enhanced tumor" area) were traced from dynamic frame number 30 in all cases, and "normal tissue" ROIs were traced from T_2-weighted (RARE) sequence. Evaluation of fit was done by visually inspection of enhancement curves.

6.7. Parameter estimation at the pixel level

6.7.1. Time development

Data were also analyzed using a more demanding procedure with *pixelwise* estimation of the pharmacokinetic parameters to see if parametric maps and their corresponding histograms generated by estimations from individual pixels in tumor ROIs revealed a more heterogeneous pattern in seventh week tumors than in fifth week tumors. Also, I wanted to demonstrate parameter chances which may be related to time related development of tumors.

ROI covering entire tumor was manually drawn from dynamic measurement image in each examination. Estimated parameters were presented as parametric maps with calculated mean of pixel-values, and in histograms showing the parameter distribution.

6.7.2. "Goodness-of-fit" analysis

For a more conclusive comparison of the fit for both models, a statistical measure of "goodness-of-fit" (Akaike's information criterion, AIC) was derived from *pixel-wise* analysis of four different tissue-ROIs in three examinations (NG 3-2, NG 7-2 and WT 3-2). The regions of interest were manually traced to include 30–50 pixels and represented following

tissues; "viable tumor", "tumor necrosis", "healthy grey matter" and "healthy skeletal muscle". Areas of high Gadomer-17 enhancement were defined as viable tumor tissue while areas of no enhancement were defined to be necrotic tissues. Grey matter areas and muscle tissue were determined from the anatomical T_2-weighted (RARE) sequence.

For each pixel time course in each of these regions (for each examination) the parameters defined in the models by Su et al. and Tofts et al. were fitted using non-linear least-squares data fitting (cf. Section 6.5, page 56).

Akaike developed an information theoretical-based method for comparing two models to one data set. The Akaike approach does not rely on P values or the concept of statistical significance, and is applicable even when one of the models to be compared is a simpler case of the other (nested model). The AIC method provides determination of which model is likely to be correct, and quantify how much more likely [61]. The AIC is defined by:

$$AIC = N \cdot ln\left(\frac{SSE}{N}\right) + 2K \tag{6.2}$$

where N is the number of time points, SSE is sum-of-squares errors and K equals M + 1, where M denotes the number of model parameters. Thus the AIC takes both SSE[7] and the number of model-parameters into account. In Su's model three parameters were fitted (D_0, D_1 and K_2) while Tofts model determined two parameters by nonlinear least-squares fit (K^{trans} and v_e).

The sum of squares errors, SSE (for each examination, each pixel at each time-point) were calculated as:

$$SSE_i = \sum_{k=1}^{N} e_k^{i^2} \tag{6.3}$$

where $e_k^i = y_k^i - y(t_{k;\hat{p}_1^i,.....,\hat{p}_M^i})$ is the residual in the time course for pixel i. $k = 1, ..., N$ is the number of the actual time-frame (N = 63) for the DCE-MRI series. Corrected AIC were calculated by:

$$AIC_c = AIC + \frac{2K(K+1)}{N-K-1} \tag{6.4}$$

The model with the lower AIC_c is more likely to be correct. The difference in AIC between the Su and the Tofts model is denoted ΔAIC_c. The probability that the correct model (of the two) has been chosen, is computed as:

$$Probability = \frac{e^{0.5\Delta AIC_c}}{1 + e^{0.5\Delta AIC_c}} \tag{6.5}$$

For comparing the Su and the Tofts model, the probability that one model is correct (i.e. Tofts) was thus divided by the probability that the other model (i.e. Su) is correct. This *evidence ratio* or *relative likehood* is defined as [61]:

$$Evidence\ ratio = \frac{Prob.\ Tofts\ model\ is\ correct}{Prob.\ Su's\ model\ is\ correct} = \frac{1}{e^{0.5\Delta AIC_c}} \tag{6.6}$$

The Matlab-code used for comparison of "goodness-of-fit" for the two models by the Akaike's method is given in Appendix E.

[7] The sum of square errors represents the sum of the estimate's deviations from target (i.e. the "measured" concentration). The mean of square errors may be denoted MSE.

7. Results on pharmacokinetic MRI

The two different pharmacokinetic models (cf. Section 5.2) evolved by Su et al. [94] and Tofts et al. [105], respectively, were applied on a subset of examinations as described in Section 6.5. The estimated Tofts' parameters were:

$\mathbf{K}^{trans}$ [min^{-1}] , $\mathbf{v}_e$ ($0 < v_e < 1$) and $\mathbf{k}_{ep}$ [min^{-1}].

K^{trans} is the influx volume transfer constant, representing the product $P \cdot S$ of the permeability (P) and surface-area (S). PS is usually denoted "permeability" for short. v_e denotes the fractional leakage volume accessible to the actual tracer, and k_{ep} is the efflux rate constant which represents wash-out of tracer from tissue. The parameters derived by the model by Su et al. were:

$\mathbf{D}_0$ [mM], $\mathbf{D}_1$ [mM/min] and $\mathbf{K}_2$ [min^{-1}].

These are related to vascular volume fraction, tracer accumulation in tissue (i.e. permeability), and rate of tracer wash-out from tissue, respectively.

Thus, both D_1 (Su) and K^{trans} (Tofts) are parameters related to permeability, or tracer leakage into tissue. Correspondingly do K_2 (Su) and and k_{ep} (Tofts) both reflect tracer wash-out from tissue.

Here, results are given for estimated parameters when the calculations were done from all pixels within carefully traced ROIs (i.e. *ROI-wise* analysis), and when data were analyzed pixel-by-pixel (i.e. *pixel-wise* analysis), without user interaction[1]

[1]However, in case of automated pixel-by-pixel analysis, I also made (rough) ROI tracings to reduce computation time (exclude parameter estimation in non-interesting tissue or in background air).

7.1. Results from ROI analysis

7.1.1. Results from operator variability of ROI determination

In this section, results are given from both the *"operator variability of manual ROI determination"* experiment, and the *"use of different contrast agent enhancement for guidance ROI determination"* experiment. Parameter-variability was assessed by standard deviations and by computing the coefficient of variation (cf. Section 6.6.1). Coefficient of variation quantifies measurement-error relative to the size of the parameters [70].

The manual tracings from three tumor cases (NG 3-2, NG 7-2, WT 3-2) were analyzed. From Figure 7.1, demonstrating ROI tracings from five independent trials on these three different animal examinations, we see that manually delineated ROIs representing the whole tumor region are hard to reproduce precisely. To demonstrate the effect of this intra-operator variability on the parameter estimates in the delineated tumor region, each trial result is depicted in Figure 7.2 for the Su model parameters, and in Figure 7.3 for the Tofts model parameters. The corresponding means, standard deviations, and coefficients of variation are given in Table 7.1 (Su-model) and Table 7.2 (Tofts-model).

Intra-operator variability of parameters in the Su model is tabulated in Table 7.1. Variation in D_0 was slightly higher when the post-contrast Gd-DTPA images were used as template compared to using visual guidance from the Gadomer-17 image. However, D_0 estimates in case NG 7-2 showed very small variability. The same tendency of larger variability using the post-contrast Gd-DTPA image as template was also found for the D_1 and K_2 parameters. Again, this effect was smallest in case of the NG 7-2 examination. The parameter K_2 in the WT 3-2 case was the only parameter showing largest variability using Gadomer-17 as enhancement template. However, this parameter case revealed low variability using both "tracer-templates". From Figure. 7.2 we see that parameter estimates for the individual trials were all within $\pm$ 1.96 standard deviations from the sample mean across all five trials, *indicating repeatability of parameters estimates within a reasonable interval* ($\sim$ 95% confidence interval around mean).

Parameter variations in the Tofts model are summarized in Table 7.2. Tracings using the post-contrast Gd-DTPA image as template gave generally larger variability in K^{trans}, v_e and k_{ep} estimates compared to tumor delineations using the Gadomer-17 information. One exception to this finding was slightly lower CV in k_{ep} (related to Su's K_2) for case WT 3-2 when using Gd-DTPA information compared to Gadomer-17 information for tumor delineation. Moreover, Tofts' parameter estimates were all within $\pm$1.96 SD from the sample mean (cf. Figure 7.3).

Notice that one case (NG 3-2) exhibited twice as high CV (i.e. variability) for all parameters (both models) using the Gd-DTPA template compared to the Gadomer-17 template.

Summary of results from operator variability of ROI determination

For all six pharmacokinetic parameters estimated in this experiment, *the operator variability had largest influence when tumor delineation was based on the post-contrast Gd-DTPA image information.* Moreover, the variability, in terms of CV, across the different parameters and template information being used, was substantial (CV range: 0.77–13.90). As seen from these experiments, one should be careful in interpretation of changes in pharmacokinetic parameters, and include the inherent methodological variability ("noise") that are due to manual ROI delineation.

		D_0			D_1			K_2		
Case	Templ.	Mean	SD	CV	Mean	SD	CV	Mean	SD	CV
NG 3-2	P	0.027	0.002	7.06	0.048	0.004	8.91	0.044	0.003	6.01
NG 7-2	P	0.026	0.000	1.38	0.040	0.001	1.67	0.058	0.002	2.62
WT 3-2	P	0.036	0.001	3.96	0.066	0.004	5.59	0.036	0.000	0.77
NG 3-2	D	0.028	0.001	3.31	0.051	0.002	4.65	0.045	0.001	3.31
NG 7-2	D	0.027	0.000	0.78	0.042	0.000	1.07	0.059	0.001	2.09
WT 3-2	D	0.038	0.000	1.21	0.070	0.001	2.12	0.036	0.000	1.25

Table 7.1.: The effect of intra-operator variability on parameter estimates (Su model). The column "Templ." denotes type of template image for ROI tracings: P = post-contrast Gd-DTPA image, D = Gadomer-17 dynamic image. Sample mean, standard deviation (SD) and coefficient of variation (CV) are computed over all five trials, each aiming to delineate the whole tumor region.

		K^{trans}			v_e			k_{ep}		
Case	Templ.	Mean	SD	CV	Mean	SD	CV	Mean	SD	CV
NG 3-2	P	0.007	0.001	8.90	0.163	0.023	13.90	0.041	0.002	5.97
NG 7-2	P	0.006	0.000	1.66	0.102	0.004	3.48	0.054	0.001	2.51
WT 3-2	P	0.009	0.000	5.51	0.266	0.017	6.28	0.034	0.000	0.90
NG 3-2	D	0.007	0.000	4.64	0.170	0.013	7.84	0.042	0.001	3.35
NG 7-2	D	0.006	0.000	1.10	0.104	0.003	2.88	0.055	0.001	1.98
WT 3-2	D	0.010	0.000	2.10	0.288	0.008	2.61	0.033	0.000	1.29

Table 7.2.: The effect of intra-operator variability on parameter estimations (Tofts model). The column named "Templ." denotes template image for ROI tracings: P = post-contrast Gd-DTPA image, D = Gadomer-17 dynamic image. Sample mean, standard deviation (SD) and coefficient of variation (CV) is computed over all five trials, each aiming to delineate the whole tumor region.

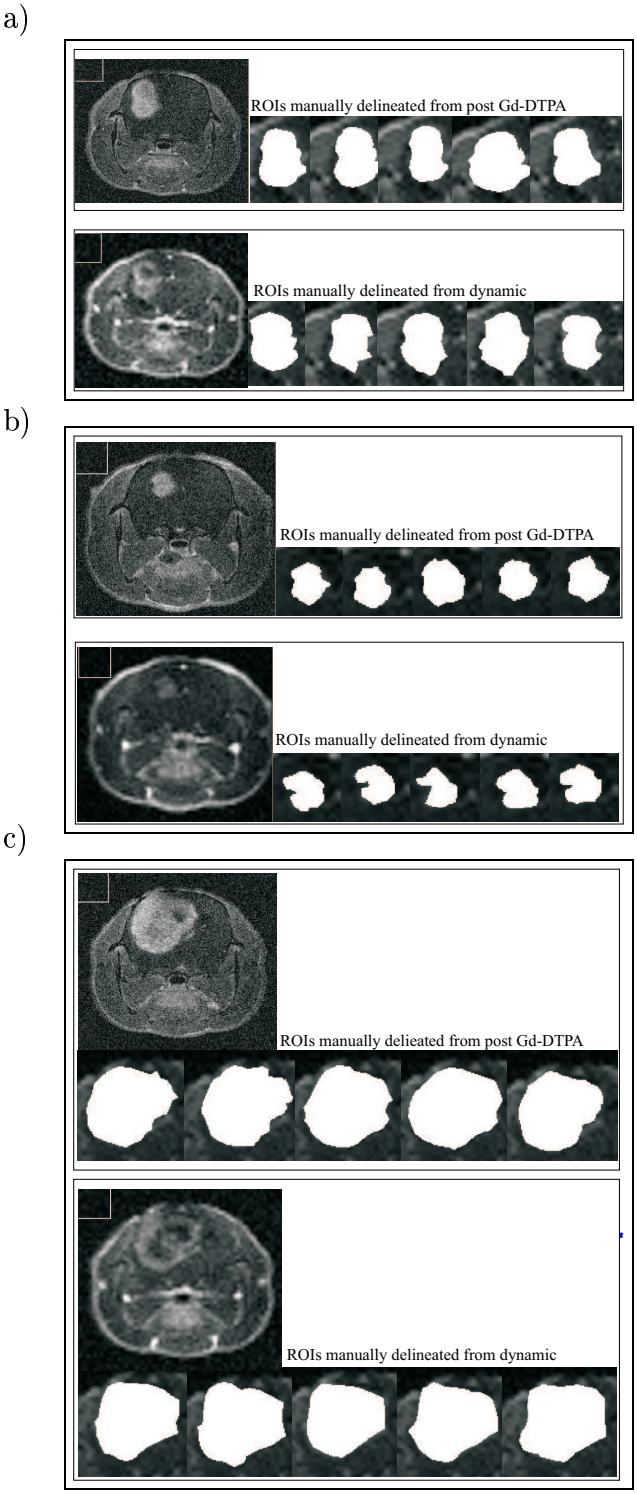

Figure 7.1.: Repeated manual delineation of the whole tumor region; The variation in pharmacokinetic parameters may be partly caused by variability in user defined ROI selection (i.e. intra-operator variability). Manually ROIs, aiming to cover the whole tumor region, were traced for three examinations: a) NG 3-2, b) WT 3-2, and c) NG 7-2. Results from using the post-contrast (Gd-DTPA) image as template ("background") are depicted in upper panels. Results from using a time frame from the dynamic Gadomer-17 series as template are shown in lower panels.

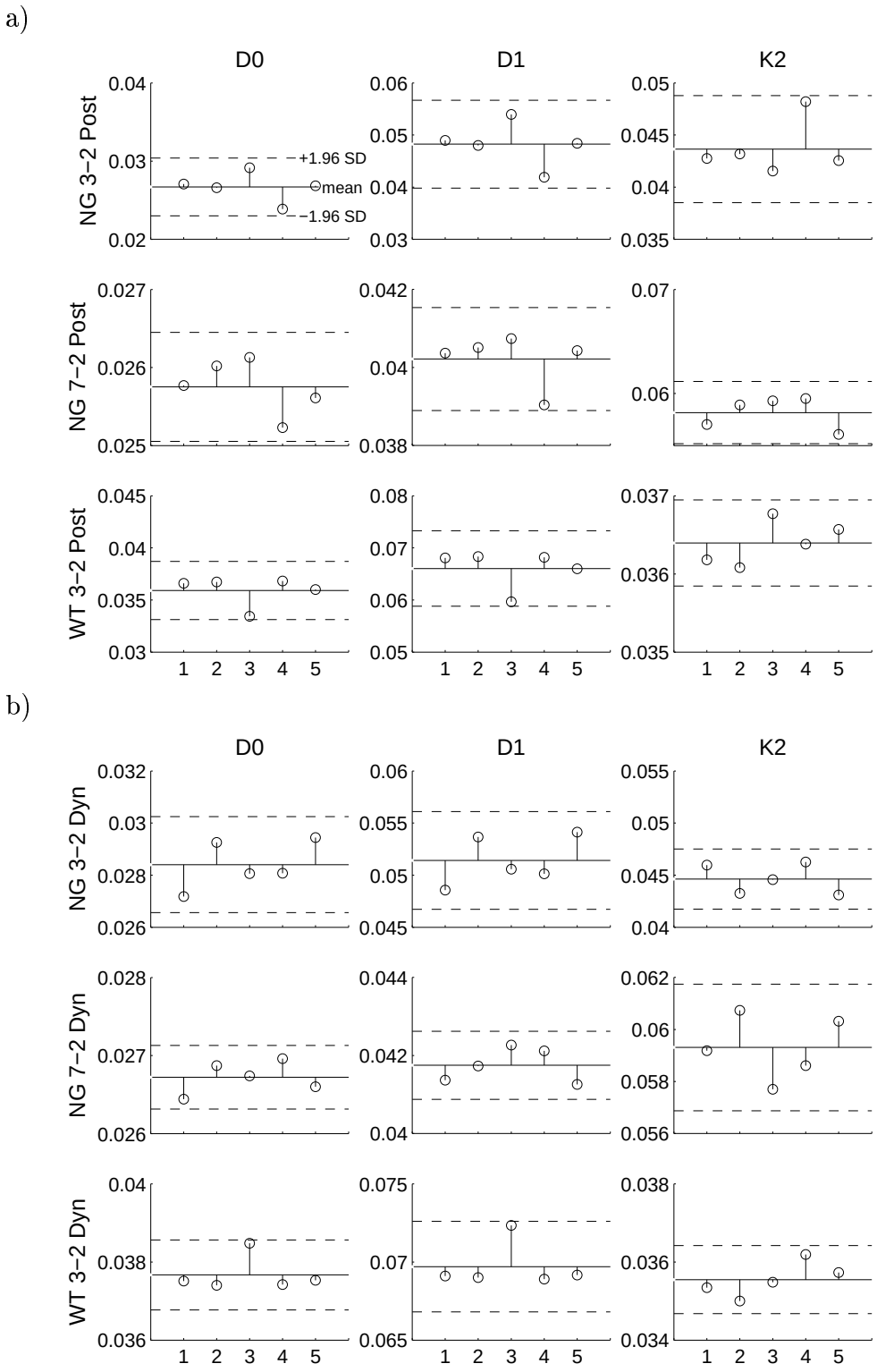

Figure 7.2.: Parameter variation (Su model) due to intra-operator variability of ROI tracings. ROI trial numbers (1, 2, 3, 4, 5), each aiming to delineate the whole tumor region, correspond to the order of ROI masks depicted in Figure 7.1. a) Variation (deviation from sample mean) in the Su model parameters using post-contrast (Gd-DTPA) image as template. b) Variation (deviation from sample mean) in the Su model parameters using a time frame from the dynamic Gadomer-17 series as template. The horizontal, unbroken line is the sample mean, and the two dashed lines denote ±1.96 SD, respectively, from sample mean across the 5 trials.

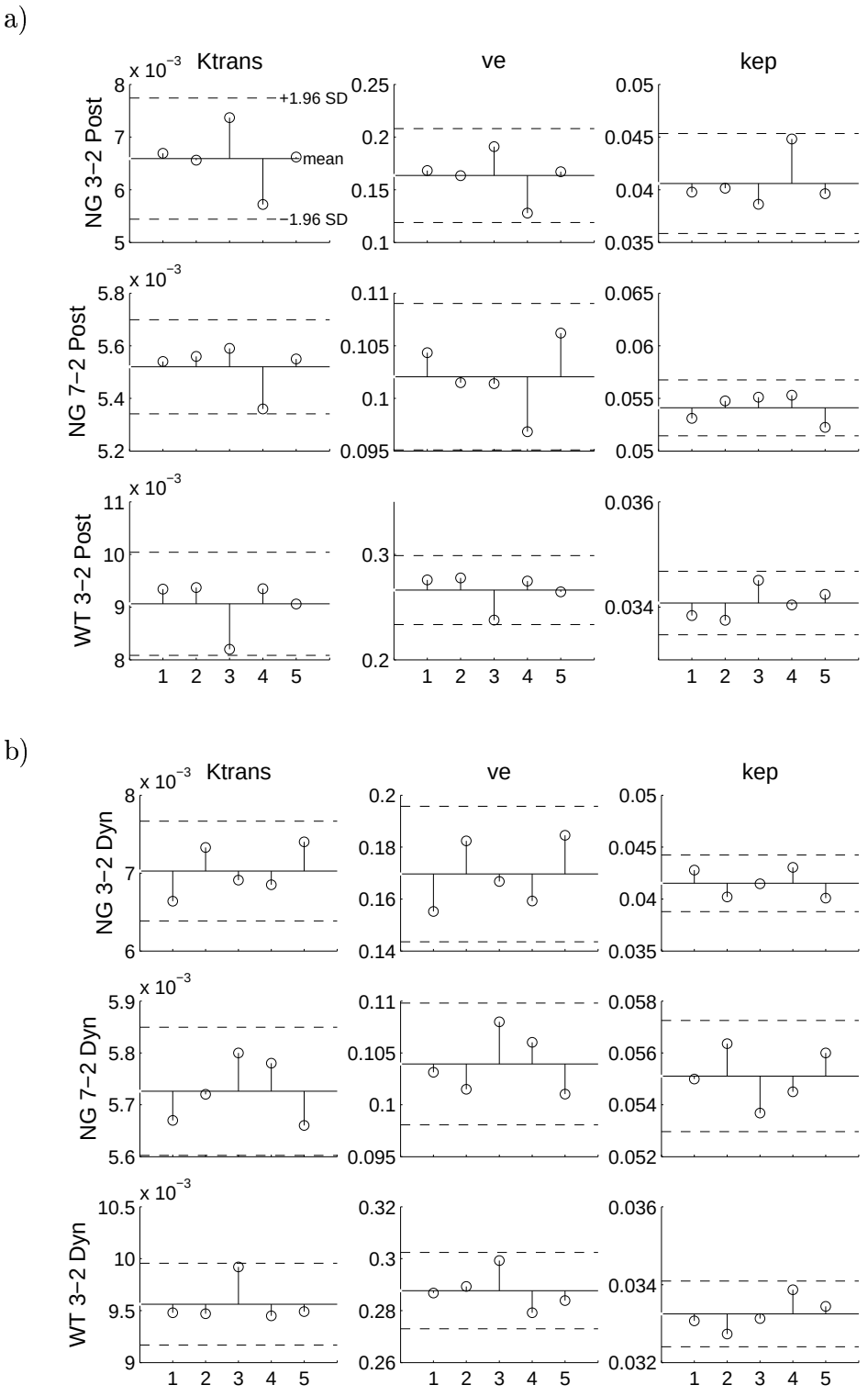

Figure 7.3.: Parameter variation (Tofts model) due to intra-operator variability of ROI tracings. ROI trial numbers (1, 2, 3, 4, 5), each aiming to delineate the whole tumor region, correspond to the order of ROI masks depicted in Figure. 7.1. a) Variation (deviation from sample mean) in the Tofts model parameters using post-contrast (Gd-DTPA) image as template. b) Variation (deviation from sample mean) in the Tofts model parameters using a time frame from the dynamic Gadomer-17 series as template. The horizontal, unbroken line is the sample mean, and the two dashed lines denote ±1.96 SD, respectively, from sample mean across the 5 trials.

7.1.2. Results from heterogeneity assessment by smaller ROIs

After having investigated the effect of operator-variability of "whole-tumor" delineation on the parameter estimates, and variability using two types of contrast agent information (Gd-DTPA and Gadomer-17), *tumor heterogeneity in terms of parameter variations between multiple small ROIs in the tumor region* was assessed. Results from this part of the study are reported below.

Figure 7.4 depicts the spatial sampling of small (and large) ROIs within the tumor region of a single examination (NG 3-2). The corresponding Su and Tofts models (concentration-time courses) are shown in Figure 7.5, and the corresponding numeric parameter values are given in Table 7.3. To make proper distinction between the different ROIs being traced, the following terminology was used:

- delineations of small intra-tumoral regions expressing high signal intensity were denoted *"enhanced"*[2] ROIs,
- small intra-tumoral regions with low signal intensity were denoted *"non-enhanced"*[3] ROIs,
- large ROIs, covering the whole tumor, were denoted *"whole tumor"* ROIs.

Box and whisker plots for the Su model parameter and the Tofts model parameter, grouped according to region type ("enhanced", "non-enhanced", "whole tumor"), are shown in Figure 7.6. Using this graphical representation of data distributions, I could more clearly inspect the spatial heterogeneity of the pharmacokinetic parameters within the NG 3-2 tumor. Notice the variability in parameter estimates even within types of tumor regions that looks visually the same (i.e. "enhanced", or "non-enhanced"). It can also be seen that the pharmacokinetic parameters have generally larger values in "enhanced" tumor regions, compared to "non-enhanced" regions, with little overlap of the inter-quartile ranges between the corresponding distributions. One exception to this finding was the overlapping distributions of v_e estimates in "enhanced" and "non-enhanced" regions. Correspondingly, inspection of tabulated values in Table 7.3 show that for all parameters, mean values were higher in "enhanced" regions compared to "non-enhanced" regions (again except for v_e). As would be expected, "whole-tumor" ROIs possessed values in between those for viable and non-viable areas (n = 2). Variability (CV) of estimated parameters were larger in "non-enhanced" regions (except for K_2 and k_{ep}) compared to "enhanced" regions. Within "enhanced" ROIs, the parameter variations (CV) were highest for K_2 and k_{ep}.

[2] Regions displaying high signal intensity presumably represent "viable" areas which express high degree of cell proliferation and angiogenic activity.

[3] Central areas displaying low signal intensity are likely to represent non-viable regions of necrotic/fibrotic tissue.

Figure 7.5 show MRI-measured concentration-time curves and the fitted Su- and Tofts model (for the 15 ROIs) revealing spatial heterogeneity within the NG 3-2 tumor. From these fifteen fitted tissue-time courses it seem like "enhanced" ROIs generally acquire a *steeper up-slope* (i.e. "wash-in"), a *higher total concentration* and a *faster decay* compared to "non-enhanced" ROIs.

Summary of results; spatial heterogeneity

I have shown that the estimated pharmacokinetic parameters display different values in different parts of the tumor , and that such differences exist even between regions where signal intensity visually was very similar. This might reflect spatial heterogeneity in tumor physiology. Moreover, the parameter values in the Su model and in the Tofts model were generally higher in "enhanced" tumor regions compared to "non-enhanced" regions. I also found that in "enhanced" tumor regions, probably corresponding to areas with viable tumor cells and proliferation, variation/heterogeneity was more pronounced for parameters reflecting wash-out rates (i.e. K_2 and k_{ep}) than for parameters describing blood-tissue permeability (i.e. D_0 and K^{trans}).

7.1.3. Results from regional difference in four tissue ROIs

As described in Section 6.6.4, four different ROIs were analyzed (*ROI-wise*) in nine examinations. The intention of this experiment was to elucidate model-fit and parameter estimation from different tissue-ROIs using both models. Results are graphically presented in Figures 7.7– 7.9.

Visual inspection of the curve-fit to "observed" concentration data in this experiment revealed no clear tendencies concerning the "goodness-of-fit" of one model compared to the other (Figures 7.7– 7.9). However, Su's model seemed to better account for the early maximum concentrations than Tofts's model did. Su's model gave thus impression of a higher maximum tissue-tracer concentration and a more rapid wash-out than Tofts model. Moreover, this property of Su's model (*better fitting early peak concentrations*) was more pronounced in case of healthy tissues compared to tumorous tissue.

The observed concentration data obtained in healthy tissue ROIs were scattered compared those in tumor ROIs. Thus, for both models, fit seemed poorer in healthy tissues (grey matter and muscle tissue) than in tumor ROIs. However, tracer concentrations were generally much lower in healthy tissue (especially in grey matter) compared to tumor tissue, and the signal increases and fluctuations during the time course were close to the noise level in healthy tissues. Hence, the model fit in healthy tissue ROIs, showing very little Gadomer-17 enhancement, was probably more towards fitting the noise in the dynamic

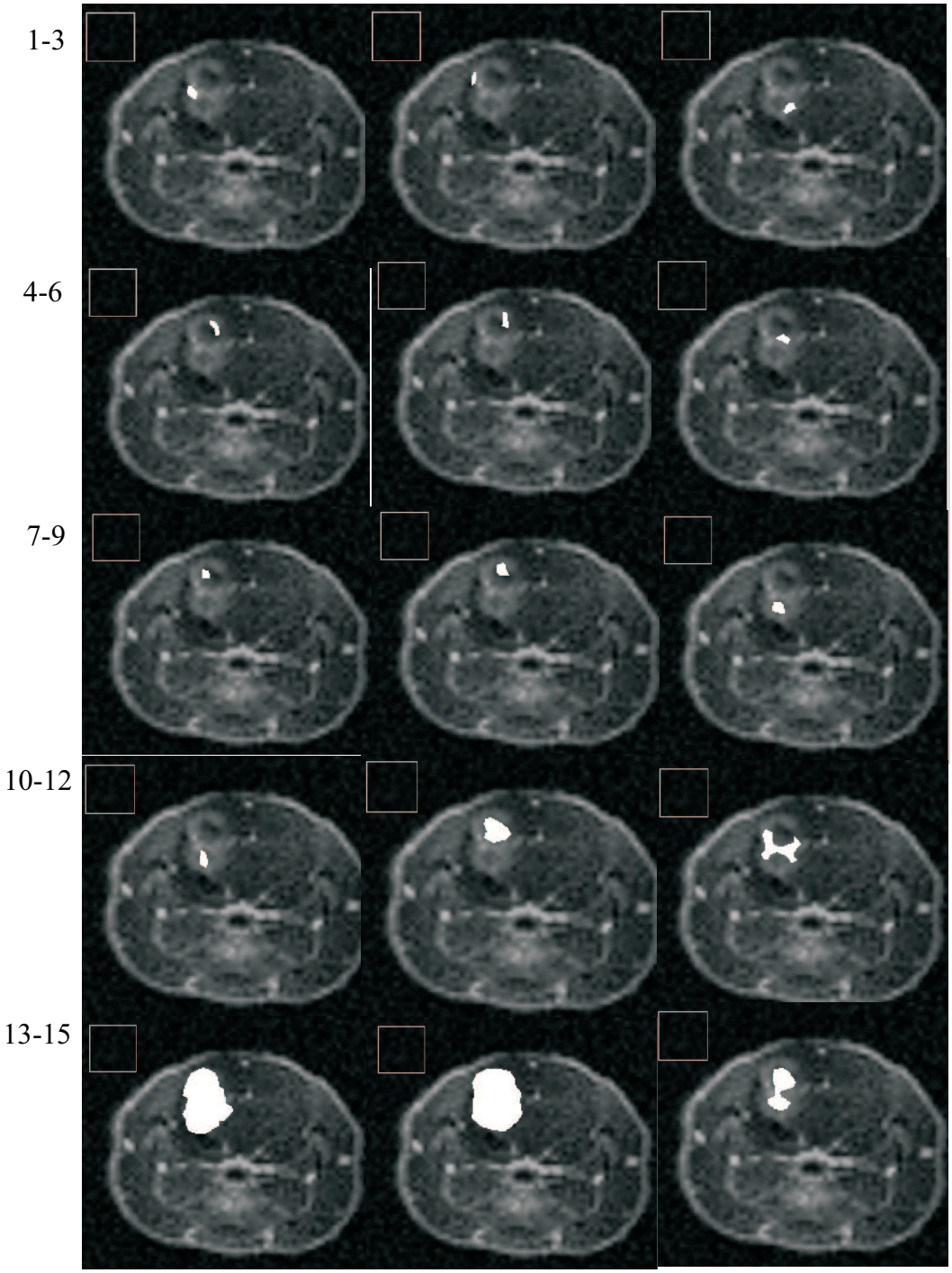

Figure 7.4.: Assessment of spatial heterogeneity of parameters within tumor region (NG 3-2) using multiple small ROIs. Pharmacokinetic parameters in both the Su and the Tofts model were estimated from 15 different intra-tumoral regions in examination NG 3-2, using *ROI-wise* analysis. ROIs numbered 1–6 and 12 represent "enhanced" parts of tumor. ROIs numbered 7–11 were delineations of "non-enhanced" tumor regions, while ROI number 15 was taken to represent total "non-enhanced" area of tumor. Two approximations of "whole tumor" ROIs are numbered 13 and 14, respectively.

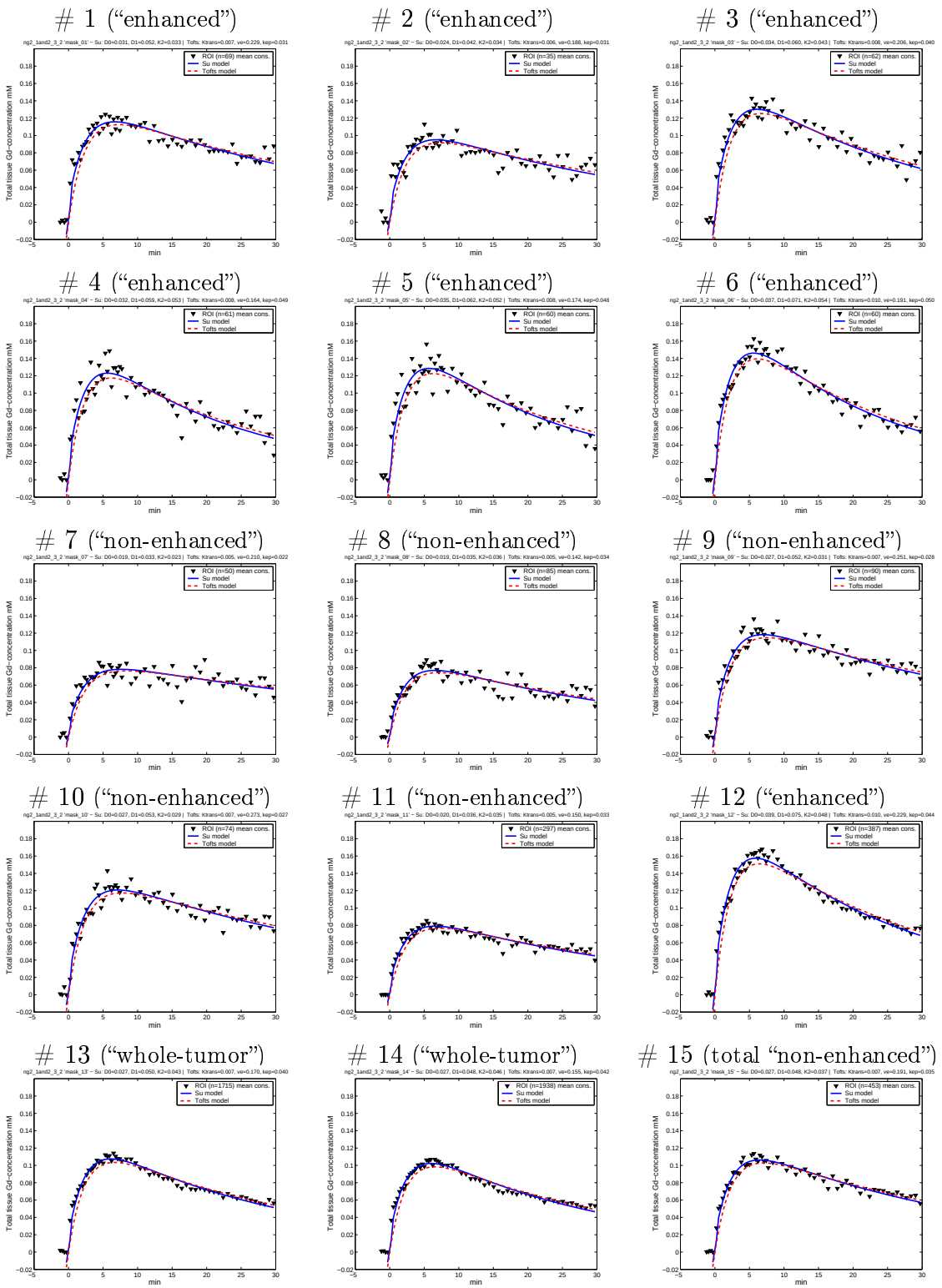

Figure 7.5.: Concentration-time curves and estimated Su and Tofts models showing spatial heterogeneity within tumor region (NG 3-2). Pharmacokinetic parameters in both the Su and the Tofts model were estimated *ROI-wise* in each of the 15 different intra-tumoral regions (labeled # 1 – # 15) according to the numbering in Figure 7.4. Notice the use of a fixed y-axis in all panels to better depict the spatial heterogeneity in tracer concentrations and the corresponding “wash-in” and “wash-out” time courses.

ROI	No. pixels	D_0	D_1	K_2	K^{trans}	v_e	k_{ep}
	" Enhanced"						
# 01	69	0.031	0.052	0.033	0.007	0.229	0.031
# 02	35	0.024	0.043	0.034	0.006	0.188	0.031
# 03	62	0.034	0.060	0.043	0.008	0.206	0.040
# 04	61	0.032	0.059	0.053	0.008	0.164	0.049
# 05	60	0.035	0.062	0.052	0.008	0.174	0.048
# 06	60	0.037	0.071	0.054	0.010	0.191	0.050
# 12	387	0.039	0.075	0.048	0.010	0.229	0.044
	Mean	0.033	0.060	0.045	0.008	0.197	0.042
	CV	14.63	18.07	19.95	17.89	12.78	19.73
	"Non-enhanced"						
# 07	50	0.019	0.033	0.023	0.005	0.210	0.022
# 08	85	0.019	0.035	0.036	0.005	0.142	0.034
# 09	90	0.027	0.052	0.031	0.007	0.251	0.028
# 10	74	0.027	0.053	0.029	0.007	0.273	0.027
# 11	297	0.020	0.036	0.035	0.005	0.150	0.033
# 15	453	0.027	0.048	0.037	0.007	0.191	0.035
	Mean	0.023	0.043	0.032	0.006	0.203	0.030
	CV	18.14	21.61	16.30	21.43	26.01	16.61
	"Whole-tumor"						
# 13	1715	0.027	0.050	0.043	0.007	0.170	0.040
# 14	1938	0.027	0.048	0.046	0.007	0.154	0.042
	Mean	0.027	0.049	0.044	0.007	0.162	0.041
	CV	1.67	2.89	3.86	2.86	6.79	3.96

Table 7.3.: Resulting parameters in each of 15 tumor ROIs; Parameter estimated from fitting the pharmacokinetic models of Su and Tofts in each of the 15 tumor regions depicted in Figure 7.4 (NG 3-2). CV = coefficient of variation. Notice that K_2 and k_{ep} are both higher in "enhanced" tumor regions compared to "non-enhanced" regions; and that the same holds for D_0 and K^{trans}. Also, D_1 mean is higher for "enhanced" areas, however, the opposite is true for v_e. Notice also that in "enhanced" tumor regions the parameter variation *(CV) is slightly larger for K_2 and k_{ep}, compared to D_0 and K^{trans}* .

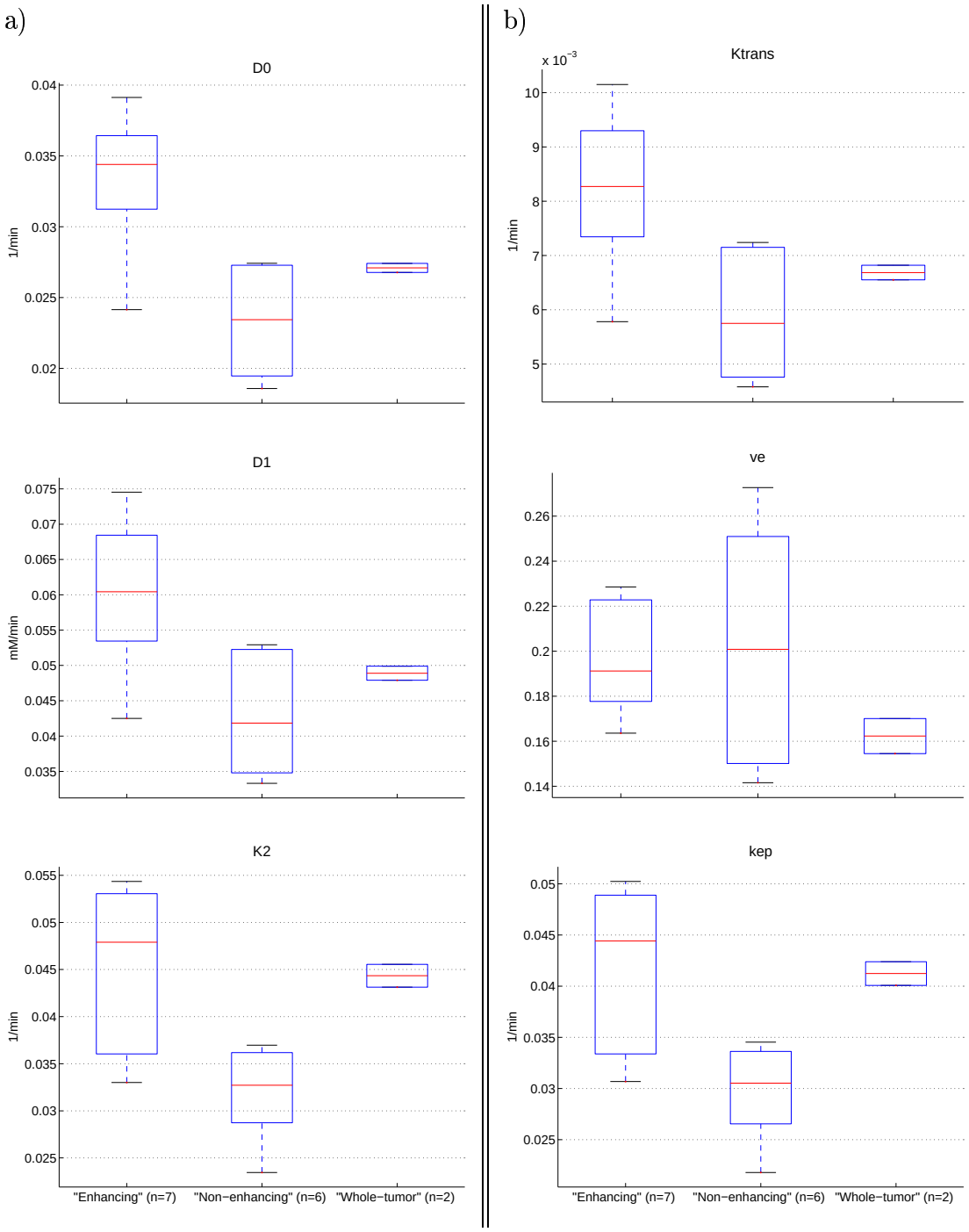

Figure 7.6.: Parameter dispersion across tumor subregions. Box and whisker plots depicting the Su model (a) and Tofts model (b) parameter distributions across "enhanced" and "non-enhanced" subregions, as well as "whole-tumor" region (cf. tabulations in Table 7.3). Boxes have lines at the lower quartile, median (middle red line) and upper quartile values. Whisker lines are drawn vertically up to largest parameter value and down to smallest value.

time series than fitting the signals, except for a small initial increase. In one of the nine examinations (NG 1-1) No Gadomer-17 uptake in grey matter tissue was found, and no reasonable model-fit could be obtained. In all other cases, both the Su model and the Tofts model could be fitted to the data with visually acceptable results.

Inspecting Gadomer-17 peak concentrations across all tissue regions in all nine examinations, total tissue tracer concentration was found to be in the range of 0.01–0.04 mM for grey matter and 0.05–0.11 mM for muscle tissue. In tumor ROIs (both "whole-tumor" ROIs and "enhanced" ROIs included) these peak values varied in the range of 0.05–0.20 mM. Both WT tumors at week-five showed tissue concentrations below 0.1 mM, while the WT tumors at week-seven, and all NG-2 positive tumors (at both times) showed contrast concentrations above 0.1 mM. Notice that different concentration scales has been used in figures 7.7- 7.9 to better depict the curve fittings.

Whether ROIs covering entire tumor, or smaller ROIs covering only viable (i.e. enhanced) tumor regions gave the best fit between pharmacologically modeled curves and the observed concentration data, was not possible to determine by visual inspection. However, in one case (NG 7-2) the pharmacokinetic model fit seemed better when using time-course data from only the enhancing part of the tumor compared to the whole (heterogeneous) tumor region.

Wash-out rates (decay) seemed to be higher in healthy tissues than in tumor tissues. This is not consistent with literature findings and might be explained by the low tracer uptake (i.e. low signal response) in these tissues. *Theoretically, no uptake should be seen in healthy tissues, especially not in brain tissues where the blood-brain barrier is intact. The observed signal intensity changes in healthy tissue areas might thus be due to presence of tracer within the microvasculature during bolus passage.*

Figure 7.10 displays regional difference between the four regions for mean value of all six estimated parameters. The figure indicates that parameters are related across regions. Between regions, we see that permeability (D_0 and K^{trans}), plasma volume fraction (D_1) and fractional EES volume (v_e) are ordered as: [*"enhanced"* > *"whole-tumor"* > *"muscle"* > *"GM"*]. Conversely, tissue tracer wash-out rates (K_2 and k_{ep}) revealed regional parameter values in exact opposite order: [*"GM"* > *"muscle"* > *"whole-tumor"* > *"enhanced"*].

Additionally, it was desired to see whether the estimated parameters from the different models were (linearly) related to each other, and if they were related across regions of different tissues (cf. Figure 7.11). As mentioned, the theoretical kinetic models, D_1 and K^{trans} should be highly correlated in that both parameters expresses the transfer rate of tracer from the blood compartment to leakage space (i.e. permeability or PS-product). Also, K_2 and k_{ep} should be positively correlated since both parameters represents rate of tracer back-flux.

Histograms in Figure 7.11 demonstrate that both the permeability measure and the back-

flux rates from the two models were proportionally related between the four regions. Scatter diagrams (Figure 7.12) revealed a tight linear relation between D_1 and K^{trans}, whereas relation between K_2 and k_{ep}, was piecewise linear (cf. figure legend).

While permeability (D_1 and K^{trans}) was estimated higher in tumor tissues than in healthy tissue ROIs, back-flux rates (K_2 and k_{ep}) showed higher mean values in healthy tissues. *Regarding healthy tissues, the fast but very small concentration increase and the fast wash-out rates might reflect bolus passage in the microvasculature and not (slow) leakage to the tissue compartment as accounted for by the pharmacokinetic models.*

Summary of results; regional differences in four tissue ROIs

I have demonstrated that the peak Gadomer-17 tissue concentration range in different tissues is ordered as: *tumor* (0.05-020 mM) > *muscle* (0.05-0.11 mM) > *grey matter* (0.01-0.04 mM). Both the Su model and the Tofts model can be used to fit the time course data from ROIs covering tumor tissues and also some normal tissues. However, the Su model seems to better adapt the initial peak concentration, compared to the Tofts model. Tissues with low tracer uptake (e..g. grey matter) show scattered concentration measurements and may possess poorer model-fit. A poorer fit may possibly be due to poorer signal to noise ratio. Furthermore, a highly linear correlation between D_1 and K^{trans} was demonstrated. "Regional difference" in these parameters showed highest permeability in enhanced (i.e. viable) tumor tissue. In contrast to literature findings, wash-out was estimated higher in healthy tissues. *However, the rapid wash-out in healthy tissues may reflect simple bolus passage of the macromolecular contrast agent in the highly vascularized tissue - and not transvascular leakage.*

7.2. Results from *pixel-wise* analysis

pixel-wise parameter estimation of tumor tissues were performed in a subset of experiments as described in Section 6.7. Region of interest was traced to cover entire tumor (central tumor areas of necrotic/fibrotic tissues were not excluded). For each pixel in region of interest, K^{trans}(representing the influx volume transfer constant), v_e (representing the EES volume fraction) and k_{ep} (representing the efflux rate constant), were estimated in accordance with Tofts et al. [102]. Furthermore, D_0 (related to fractional blood volume), D_1 (related to leakage of tracer to tissue) and K_2 (related to wash-out from tissue) were estimated with reference to Su et al. [94].

Parametric maps and corresponding histograms for each parameter were made to elucidate heterogeneity and spatial distribution of the different parameters. The parameter values were coded according to the color scales shown to the right of each parametric map.

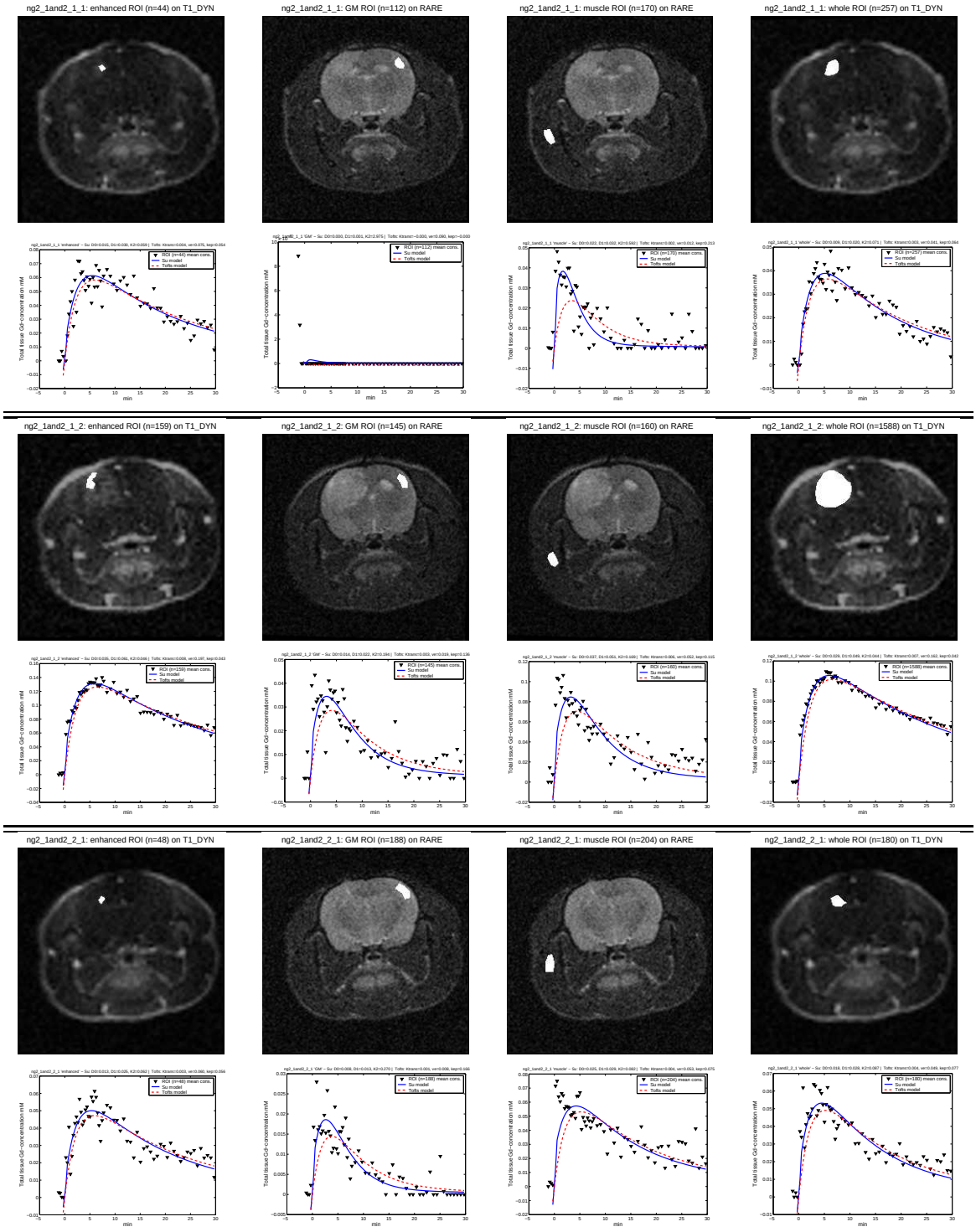

Figure 7.7.: Elucidation of differences in model fit between four selected ROIs, and between the two theoretical models used (Examinations 1-3) Solid line: *Su model*; Dashed line: *Tofts model*; 1st column: *Enhancing part* of tumor; 2nd column: *Grey matter* region; 3rd column: *Muscle* region; 4th column: *Whole tumor* region. (Notice different concentration scales on y-axis).

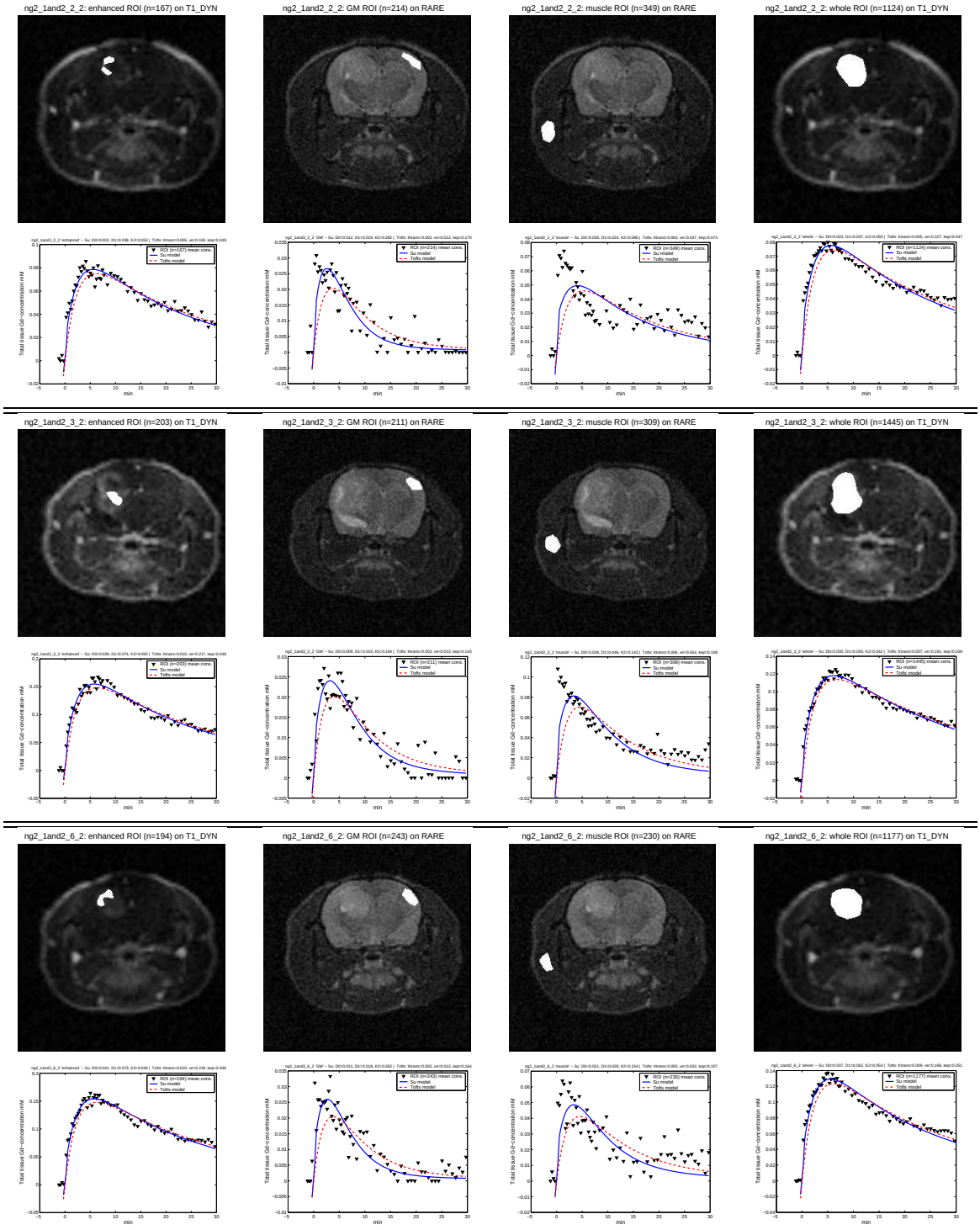

Figure 7.8.: Elucidation of differences in model fit between four selected ROIs, and between the two theoretical models used (Examinations 4-6) Solid line: *Su model*; Dashed line: *Tofts model*; 1st column: *Enhancing part* of tumor; 2nd column: *Grey matter* region; 3rd column: *Muscle* region; 4th column: *Whole tumor* region. (Notice different concentration scales on y-axis).

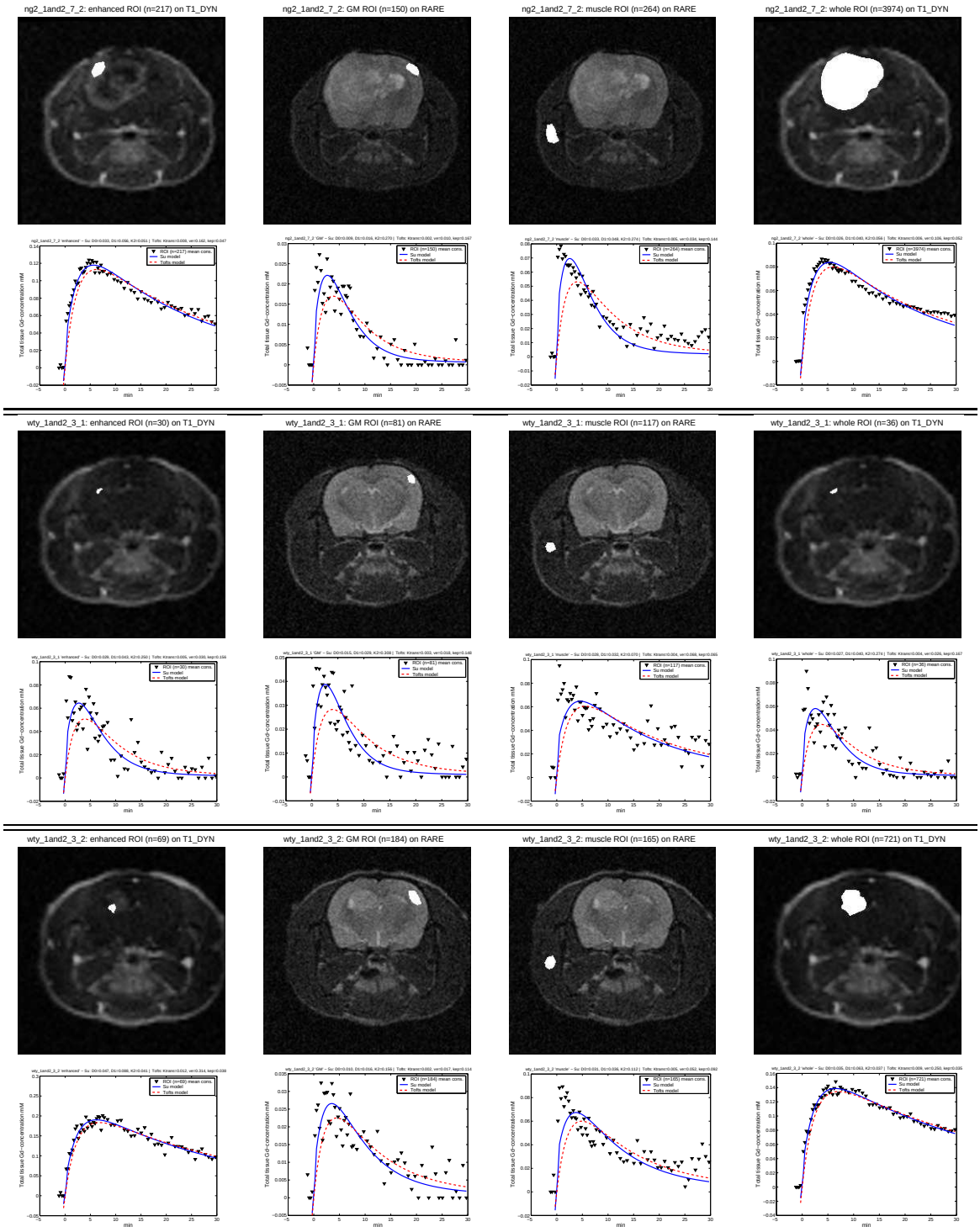

Figure 7.9.: Elucidation of differences in model fit between four selected ROIs, and between the two theoretical models used (Examinations 7-9) Solid line: *Su model*; Dashed line: *Tofts model*; 1st column: *Enhancing part* of tumor; 2nd column: *Grey matter* region; 3rd column: *Muscle* region; 4th column: *Whole tumor* region. (Notice different concentration scales on y-axis).

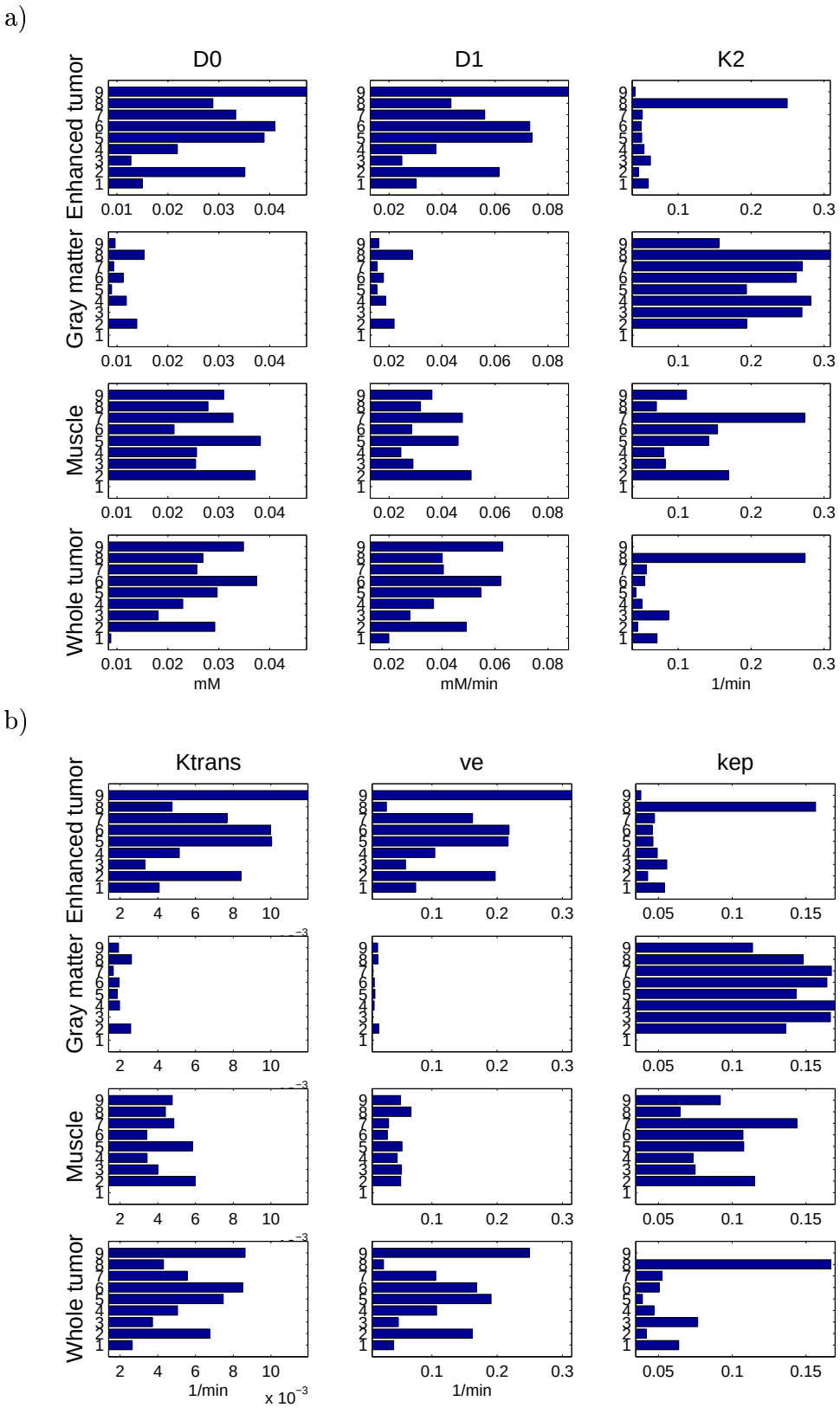

Figure 7.10.: Regional differences in pharmacokinetic parameters (examinations 1,...,9 and 4 ROIs. a) Estimated parameters in the *Su model*. b) Estimated parameters in the *Tofts model*. The order of examinations 1,...,9 (i.e. y-axis) is the same as that in Figs. 7.7-7.9.

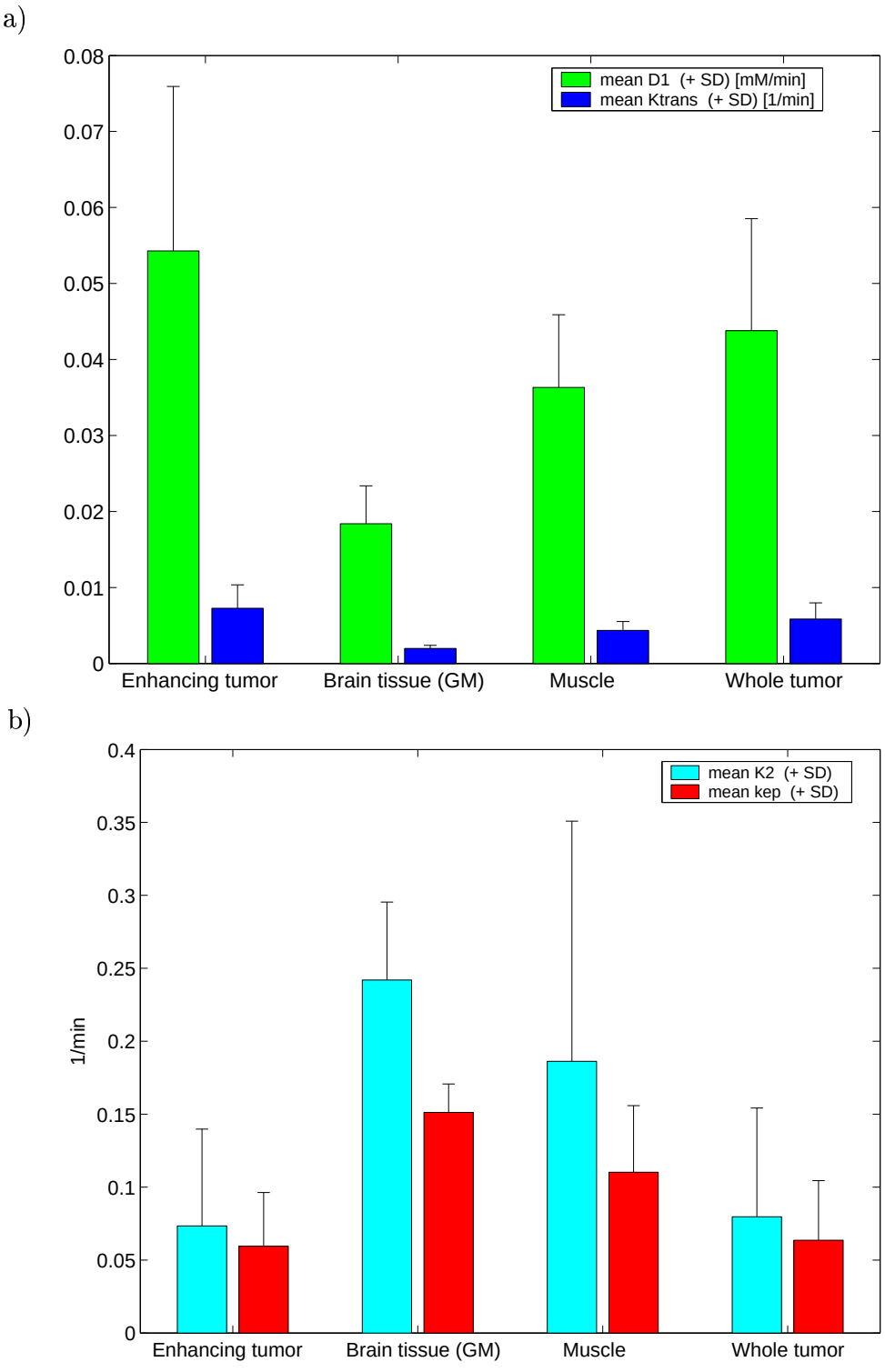

Figure 7.11.: Related parameters in the Su- and the Tofts model show regional (ROI) dependencies. Here is shown the related parameters: a) *Permeability*; D_1 and K^{trans}, and; b) *Wash-out rates*; K_2 and k_{ep} in four different ROIs denoted "whole tumor", "brain tissue" (grey matter), "muscle" (striate muscle tissue) and "enhancing tumor" (uniformly enhanced tumor part). Parameters were obtained from nine animal examinations (cf. figs. 7.7-7.9). Sample mean value of parameters, pooling the 9 examinations, were used for histograms. The "GM" parameters in examination ng2_1and2_1_1 (NG 1-1) were excluded from calculations (since no Gadomer-17 effect was observed in grey matter for this case). Notice that parameters in a) are given in different units using a common scale.

a)

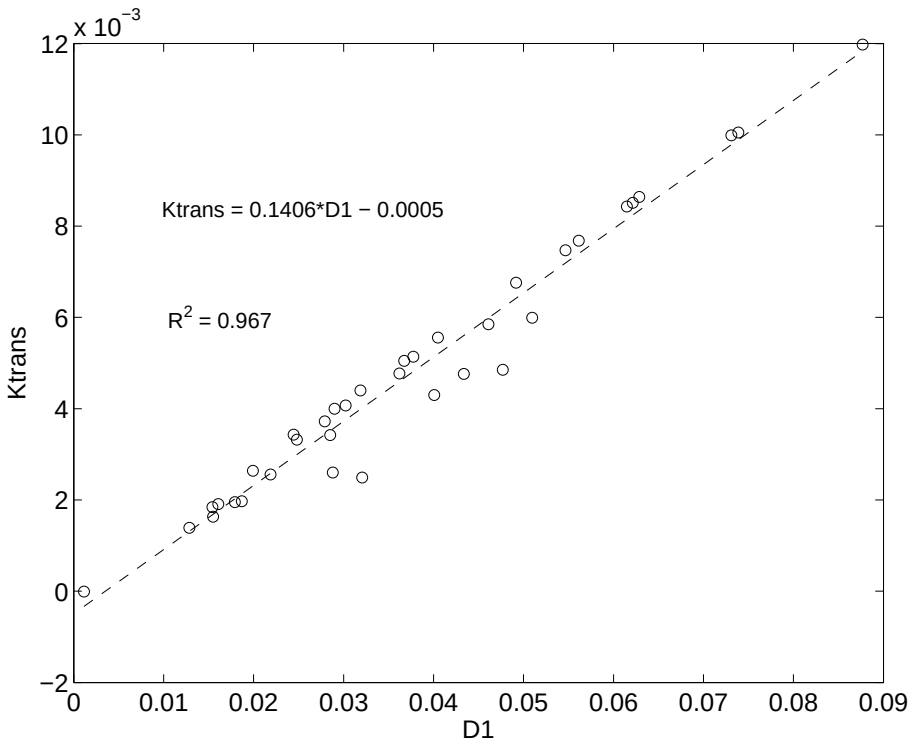

b)

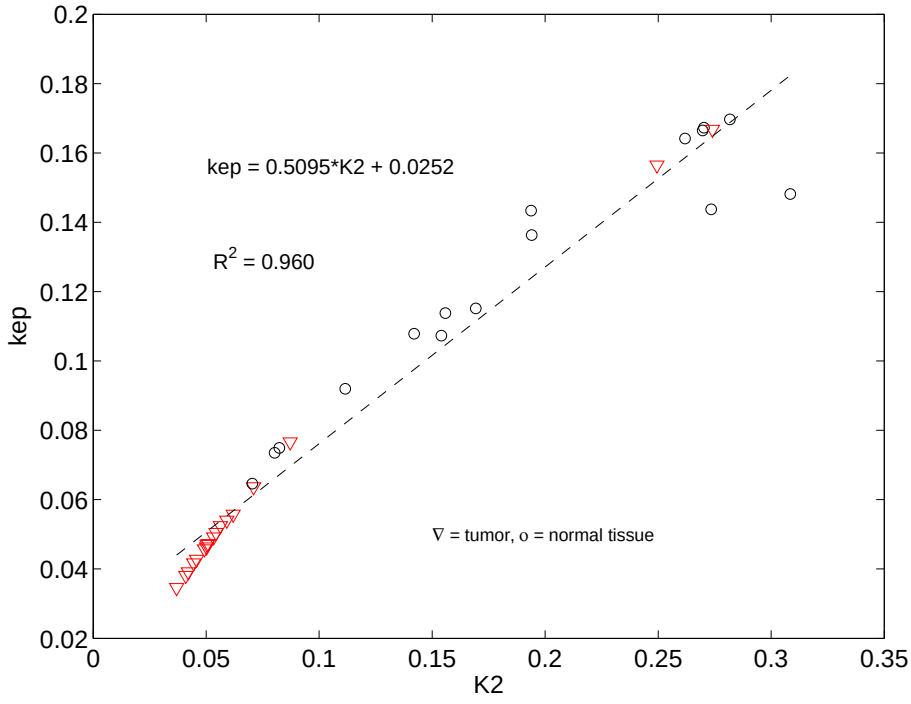

Figure 7.12.: Estimated parameters from the two models are linearly related to each other. Least squares linear regression analysis, pooling all 9 examinations, was performed to assess; a) the relation between K^{trans} and D_1 (*permeability*), and; b) the relation between k_{ep} and K_2 (*wash-out*). The latter indicate a piecewise linear relation between small (K_2, k_{ep})-values (tumor = ∇), and between higher values (probably representing microvascular bolus passage in normal tissues = o), with slightly different slopes. For simplicity we have estimated a single regression line for the whole range of parameter values.

7.2.1. Results from "time-development"

To illustrate tumor development during time (denoted "time development"), parametric maps and corresponding histograms for three tumors are presented at both five- ("first scanning") and seven weeks ("second scanning") post-implantation (Figures 7.13– 7.30).

In two of the three tumors (NG 1 and NG 2), mean **permeability** (D_1 and K^{trans}), mean plasma volume fraction (D_0), and mean leakage volume fraction (v_e) **increased** during the time between scans. Moreover, histograms displaying dispersion of these parameters illustrated increased heterogeneity at the second scan. Conversely, mean **wash-out rates** (K_2 and k_{ep}), and their spread, **decreased** with time. In contrast, the third tumor (NG 7) exhibited opposite time-development, displaying reduced plasma volume fraction and permeability at second scan. This tumor also displayed a large increase in tumor volume, with development of central necrosis. Notice that permeability values in NG 7 were higher in first scan than permeability values in the two other tumors at second scan.

Summary of results; change in parameters with time

Pixel estimation of microvascular parameters in region of interests covering entire tumor (including central areas of necrosis/fibrosis) showed that in two of three cases, the permeability-surface area product and the fractional blood volume increased with time. The same two cases revealed a decrease in flux rate back to blood, and an increase in leakage volume to Gadomer-17. Increase in parameter dispersion with time was also observed, except for K_2 and k_{ep}.

Figure 7.13– 7.15 (NG 1), Figure 7.19– 7.21 (NG 2) and Figure 7.25– 7.27 (NG 7) demonstrate "time-dependent" parameter changes for three different tumors, estimated in accordance with Su's pharmacokinetic model. The same phenomenon (i.e. tumor development with time), estimated by Tofts model, is presented in Figure 7.16– 7.18 (NG 1), Figure 7.22– 7.24 (NG 2) and Figure 7.28– 7.30 (NG 7).

D_0 - first scanning:

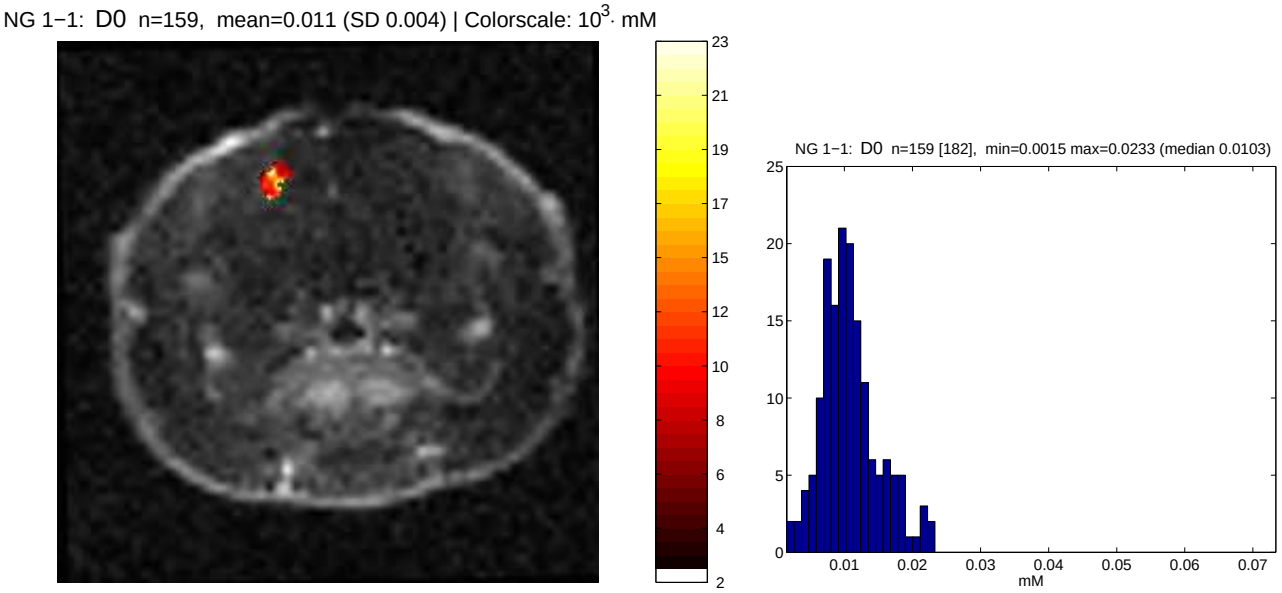

D_0 - second scanning:

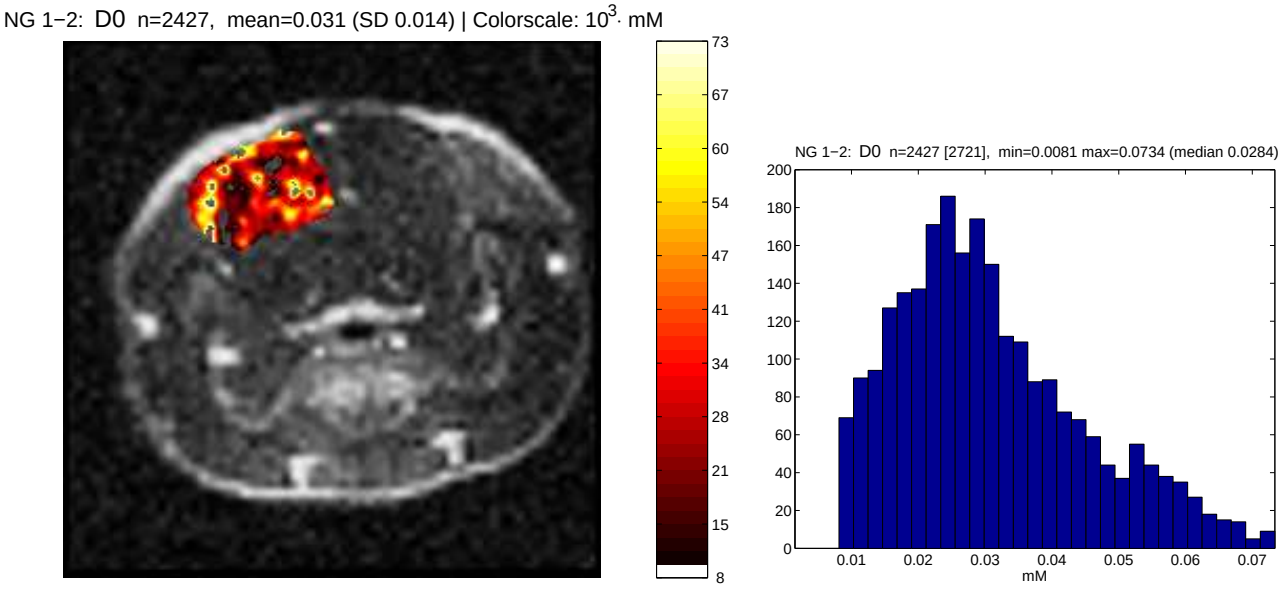

Figure 7.13.: Time development of Su parameter D_0 in animal NG 1; illustrating increased plasma volume at the second scan (represented by increased mean value and increased fraction of yellow patches). Histograms show higher dispersion (i.e. a more heterogenous distribution of D_0) with time.

D_1 - first scanning:

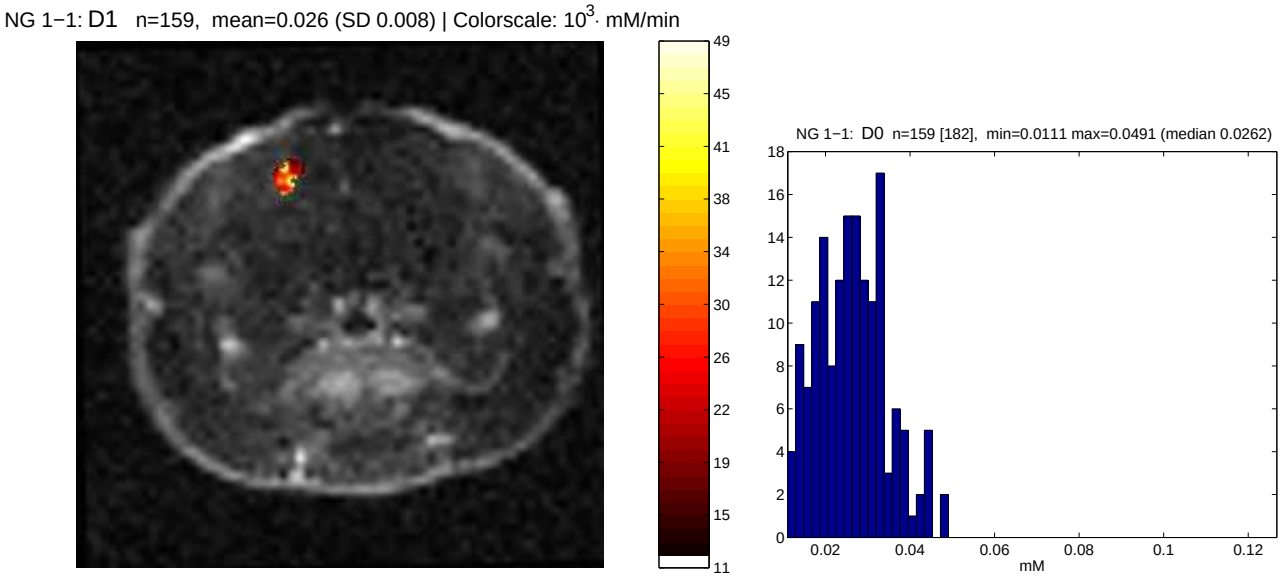

D_1 - second scanning:

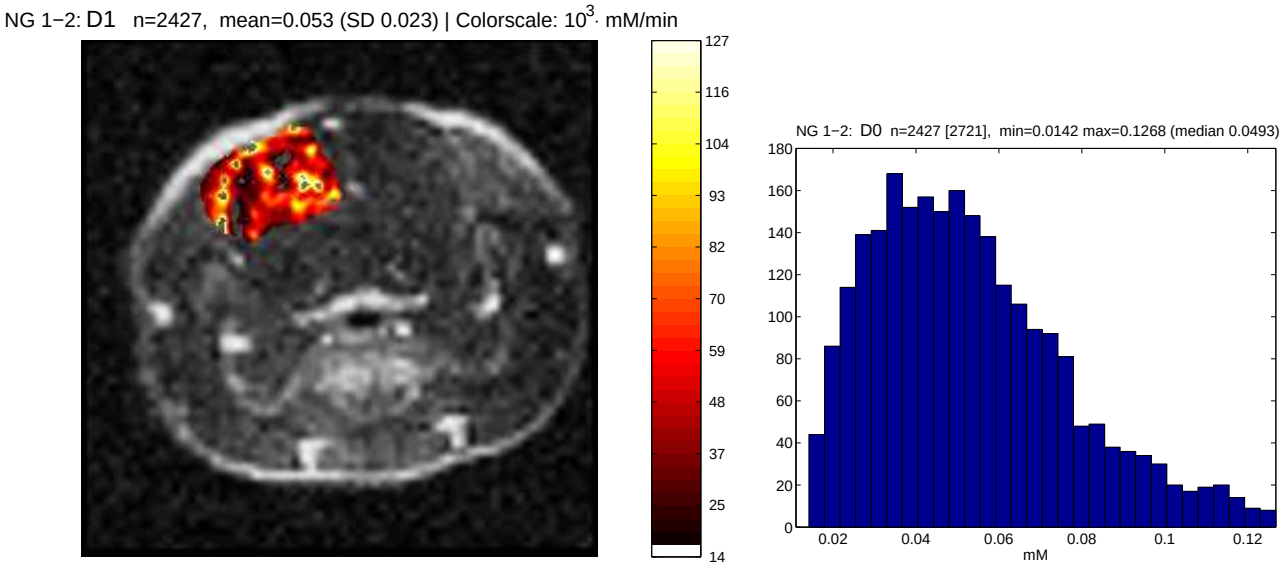

Figure 7.14.: Time development of Su parameter D_1 in animal NG 1; illustrating increased permeability at the second scan (represented by increased mean value and increased fraction of yellow patches). Histograms show higher dispersion (i.e. a more heterogenous distribution of D_1) with time. Notice that high-permeability spots in first scan is only present in peripheral parts of the tumor.

D_1 - first scanning:

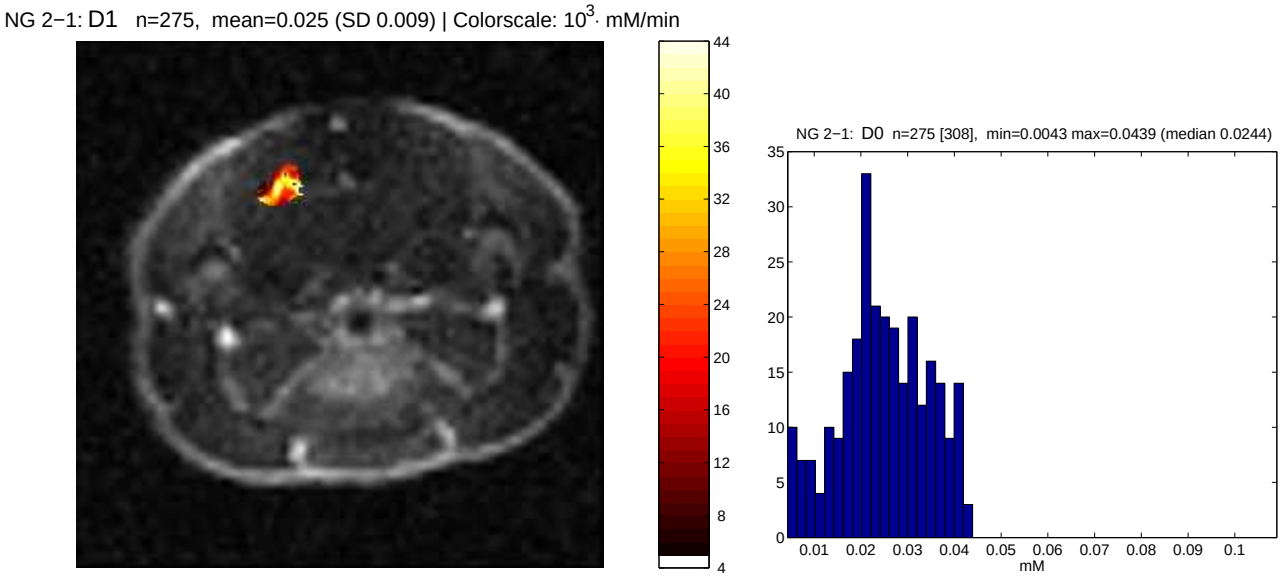

D_1 - second scanning:

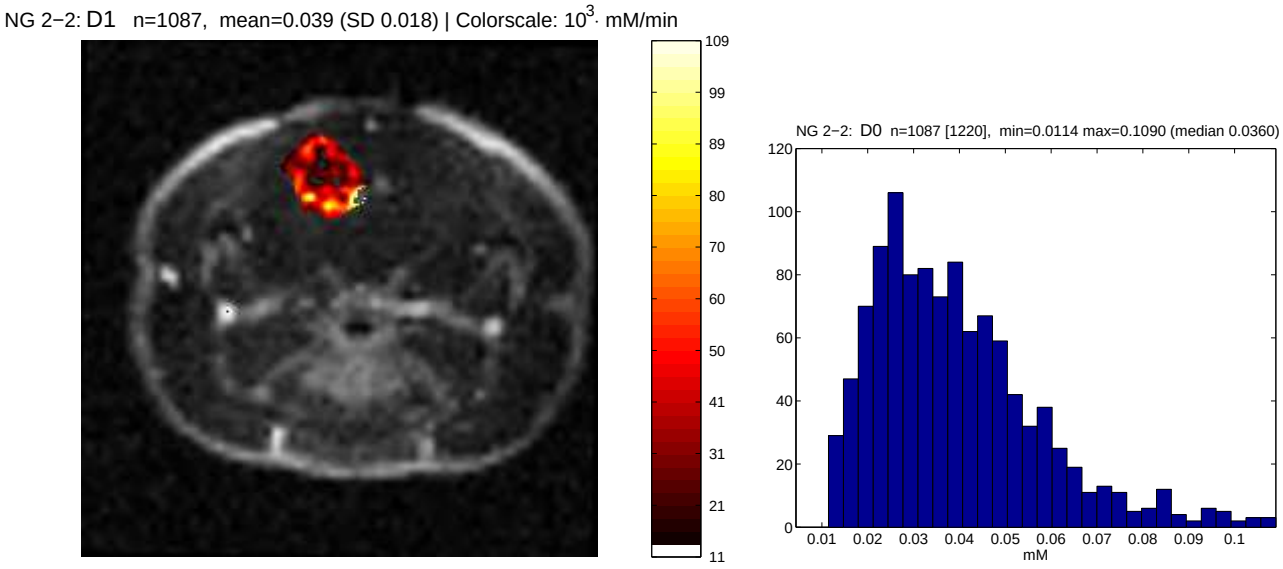

Figure 7.20.: Time development of Su parameter D_1 in animal NG 2; illustrating increased permeability at the second scan (represented by increased mean parameter value). Histograms show higher dispersion (i.e. a more heterogenous distribution of D_1) with time. Notice that high-permeability spots in first scan is only present in peripheral parts of the tumor.

K_2 - first scanning:

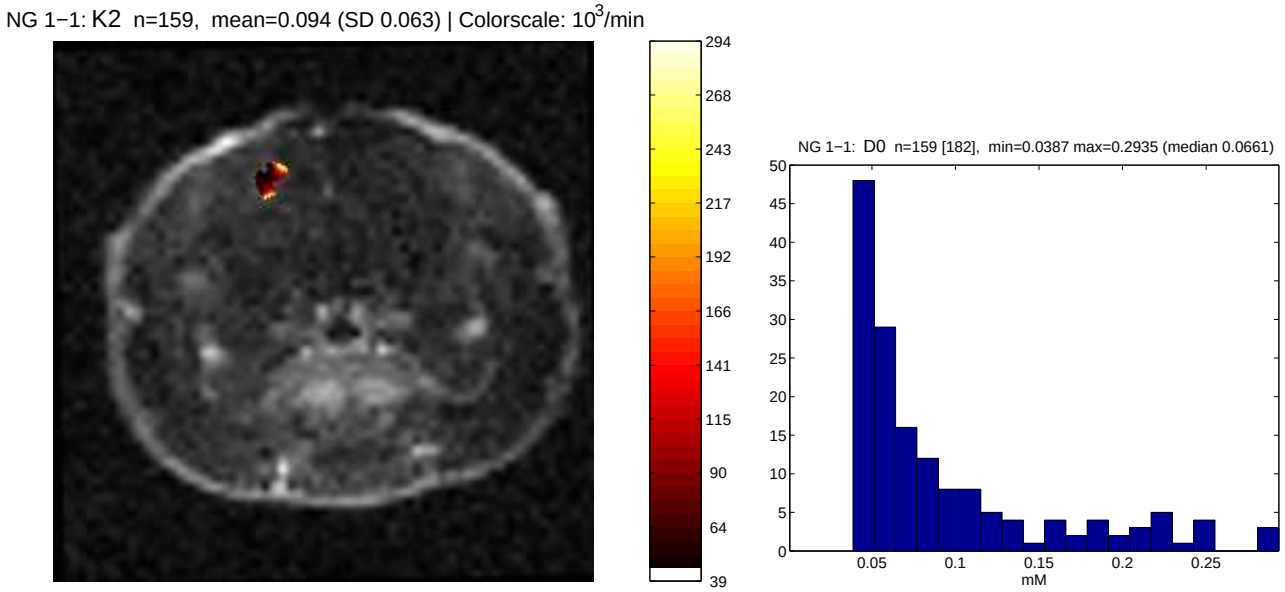

K_2 - second scanning:

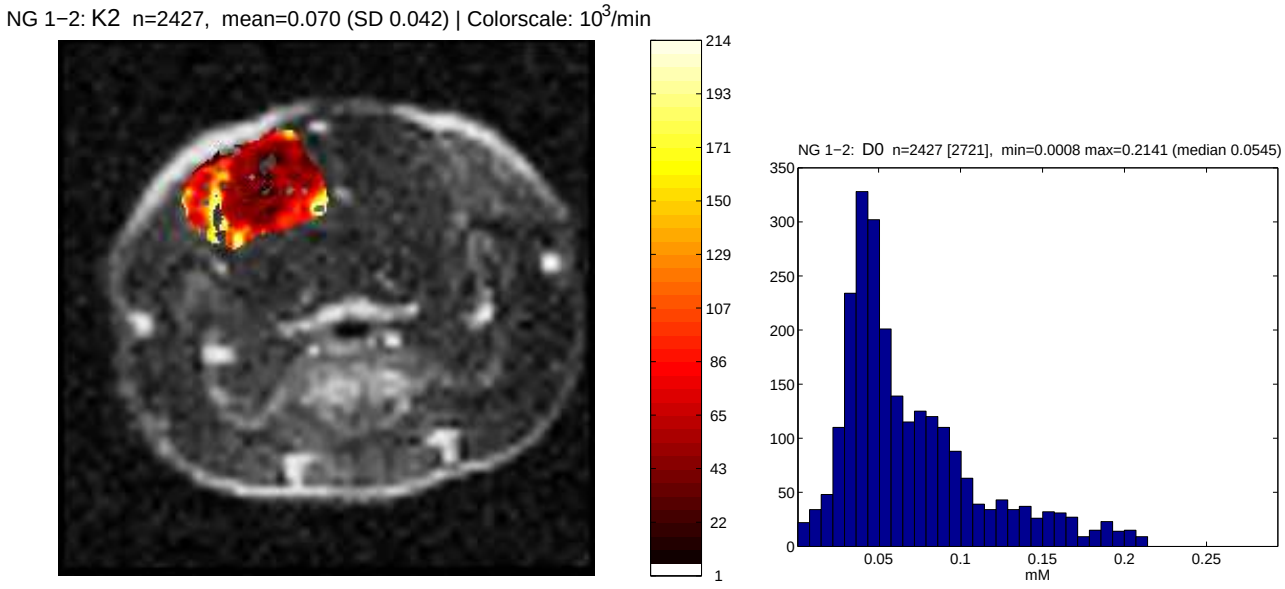

Figure 7.15.: Time development of Su parameter K_2 in animal NG 1; illustrating decreased wash-out rate at the second scan (represented by decrease in mean value). Histograms show slightly less dispersion with time.

K^{trans} - first scanning:

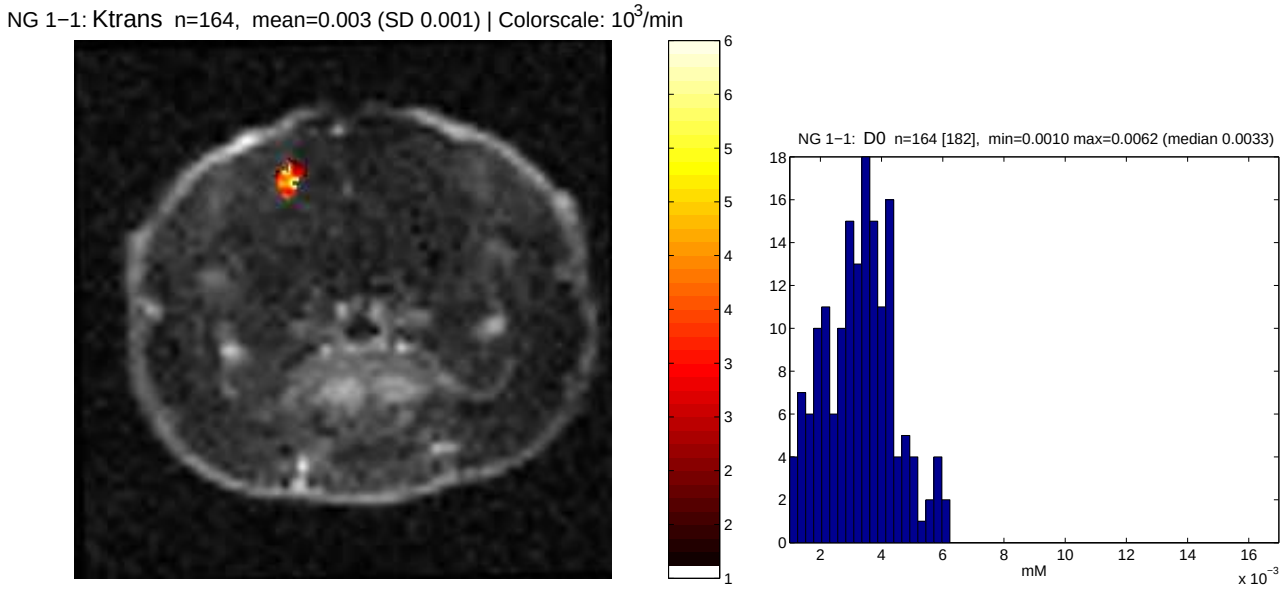

K^{trans} - second scanning:

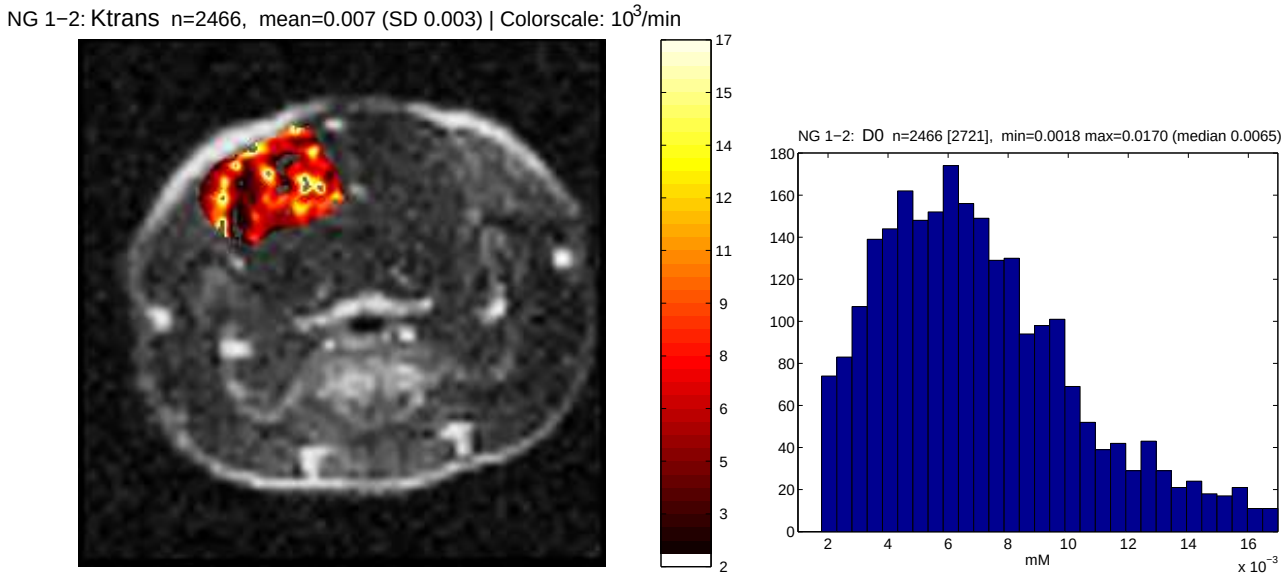

Figure 7.16.: Time development of Tofts parameter K^{trans} in animal NG 1; illustrating increased permeability at the second scan (represented by increased mean value and increased fraction of yellow patches). Histograms show higher dispersion (i.e. a more heterogenous distribution of D_1) with time. Notice that high-permeability spots in first scan is only present in peripheral parts of the tumor.

v_e - first scanning:

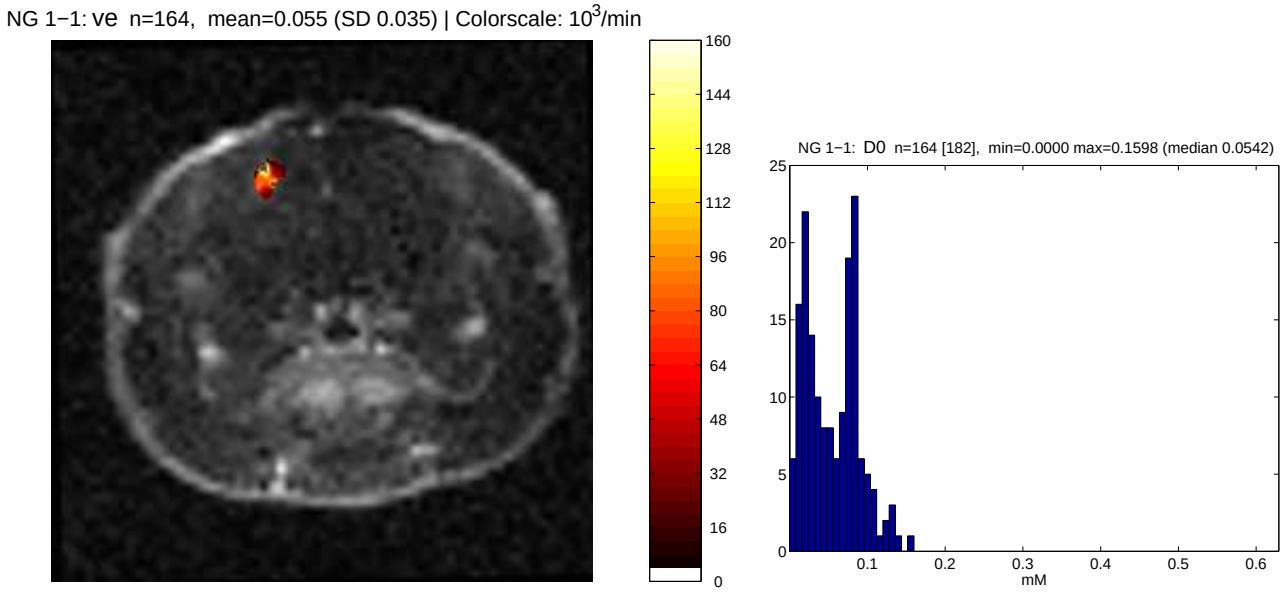

v_e - second scanning:

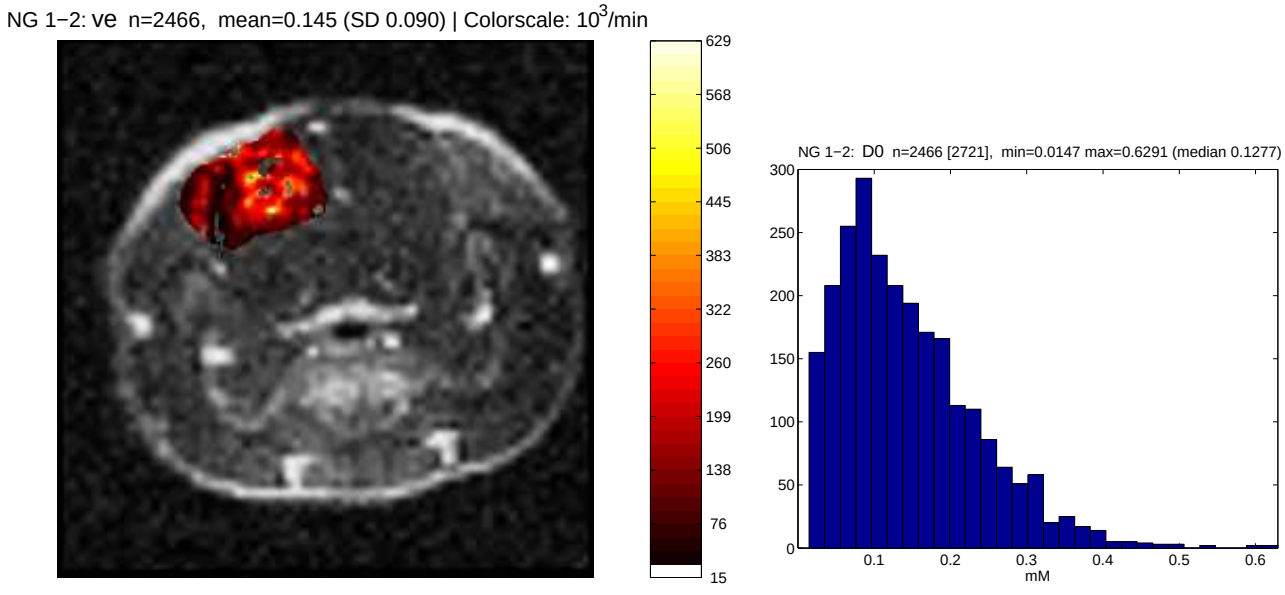

Figure 7.17.: Time development of Tofts parameter v_e in animal NG 1; illustrating increased fractional leakage volume at the second scan (represented by highly increased mean value). Histograms show higher dispersion (i.e. a more heterogenous distribution of v_e) with time.

k_{ep} - first scanning:

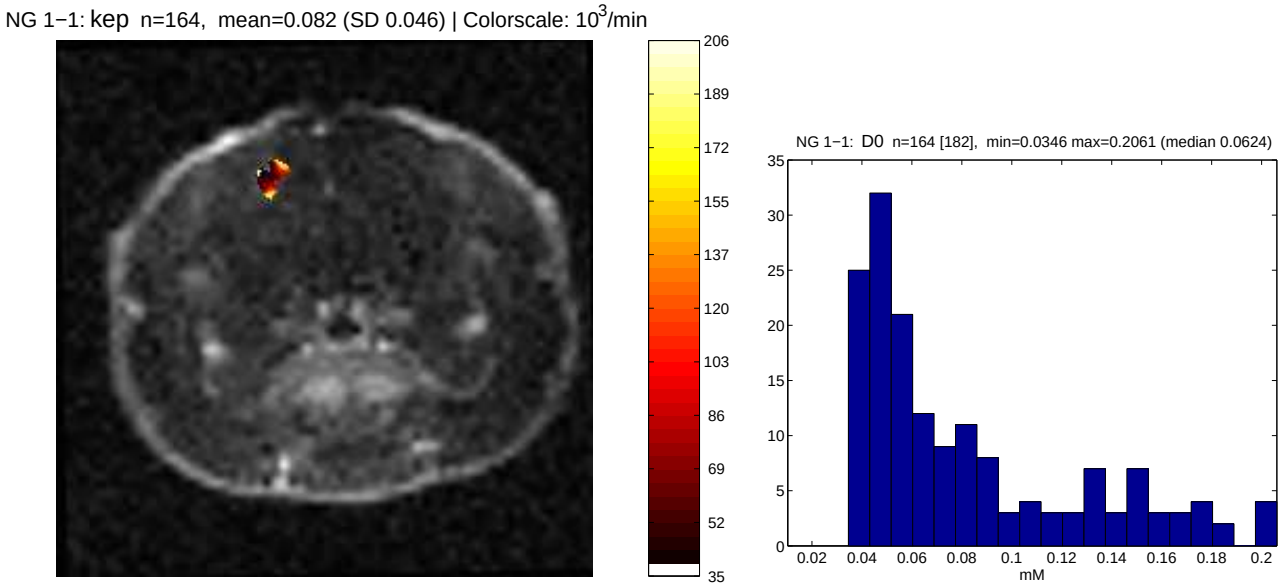

k_{ep} - second scanning:

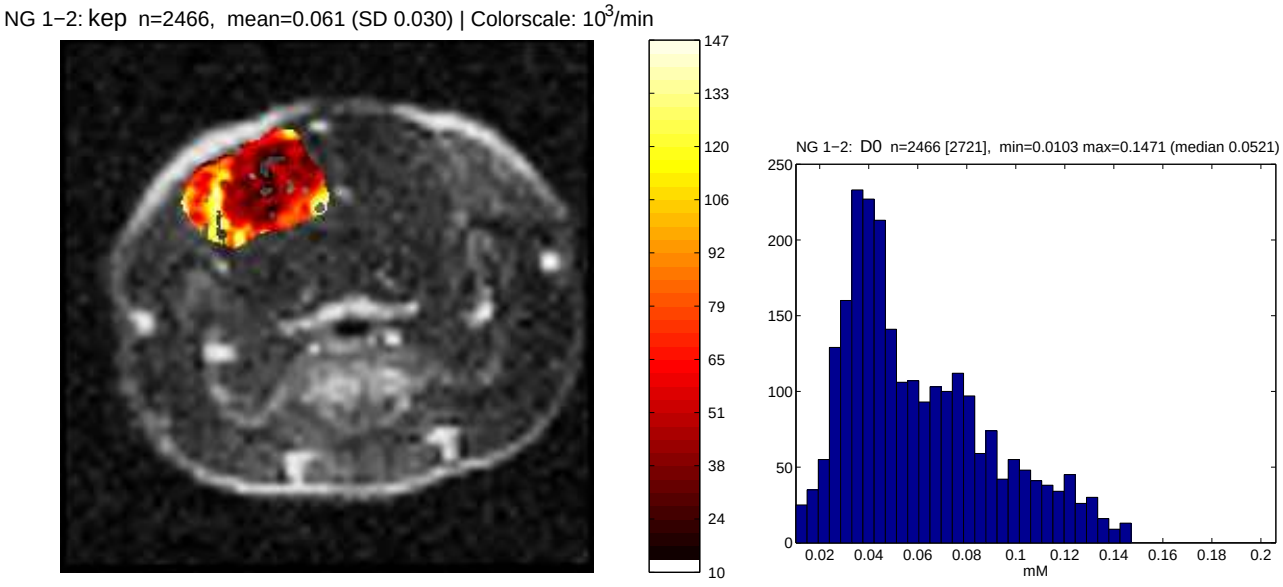

Figure 7.18.: Time development of Tofts parameter k_{ep} in animal NG 1; illustrating decreased wash-out rate at the second scan (represented by decrease in mean value). Histograms show less dispersion with time.

D_0 - first scanning:

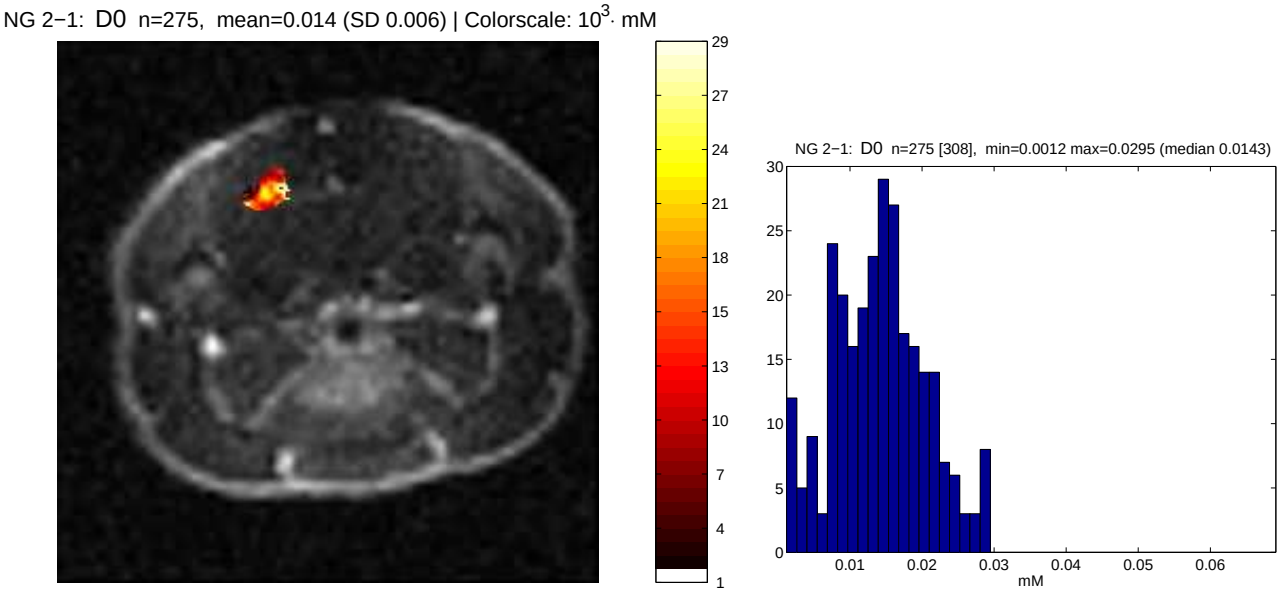

D_0 - second scanning:

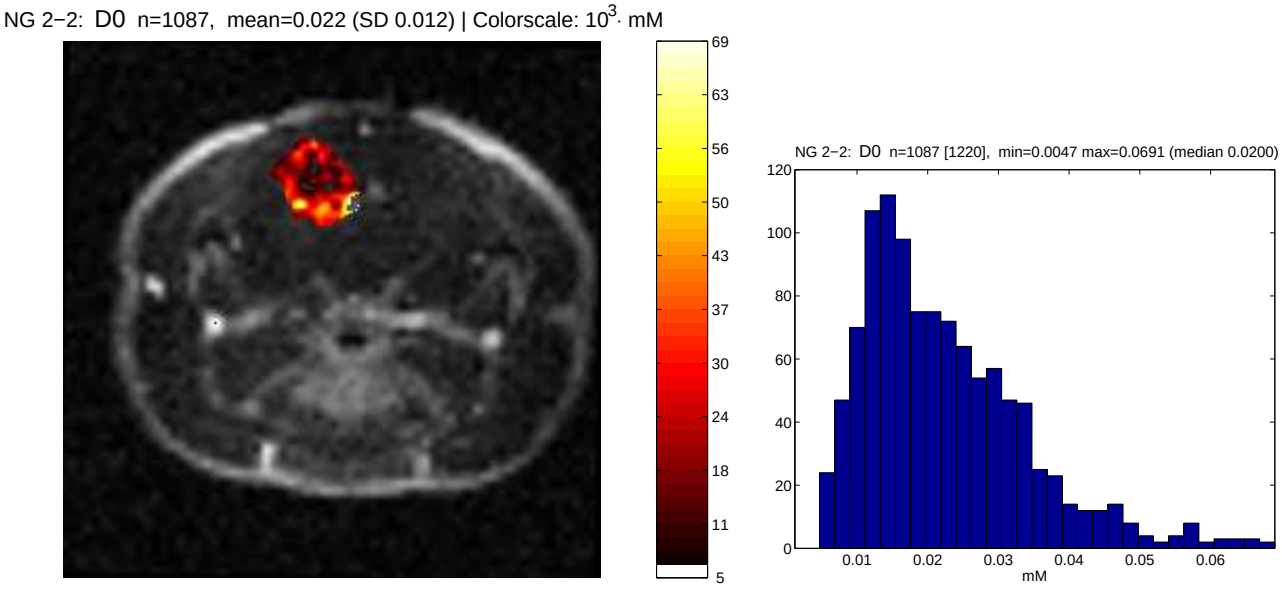

Figure 7.19.: Time development of Su parameter D_0 in animal NG 2; illustrating increased plasma volume fraction at the second scan (represented by increased mean value). Histograms show higher dispersion (i.e. a more heterogenous distribution of D_0) with time.

K_2 - first scanning:

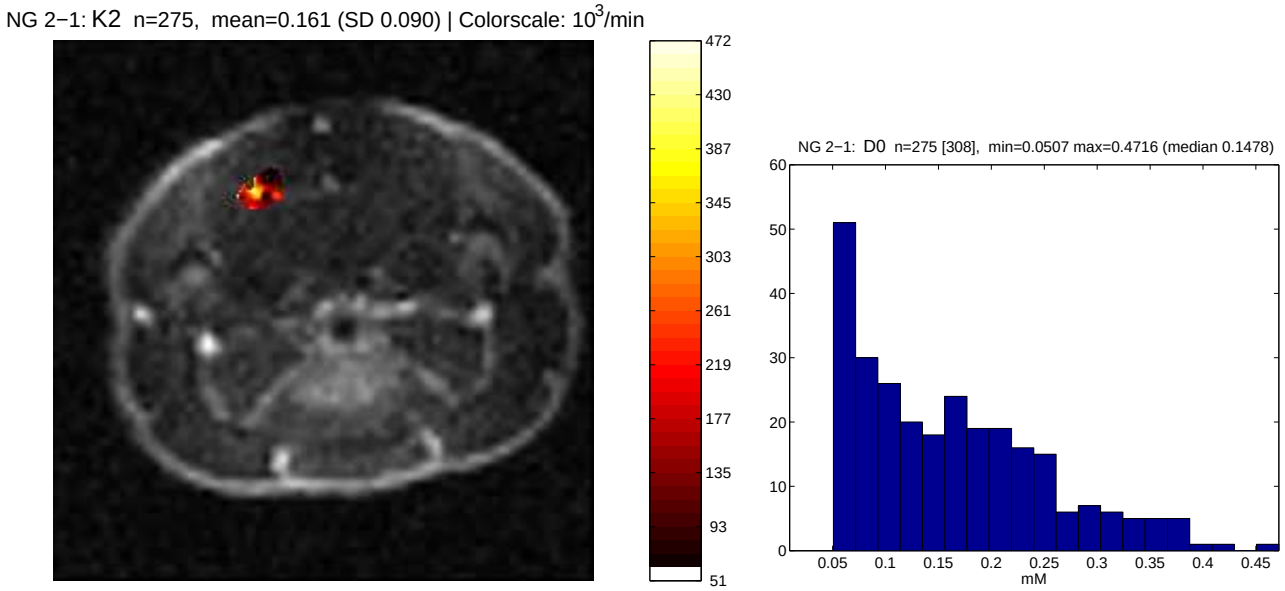

K_2 - second scanning:

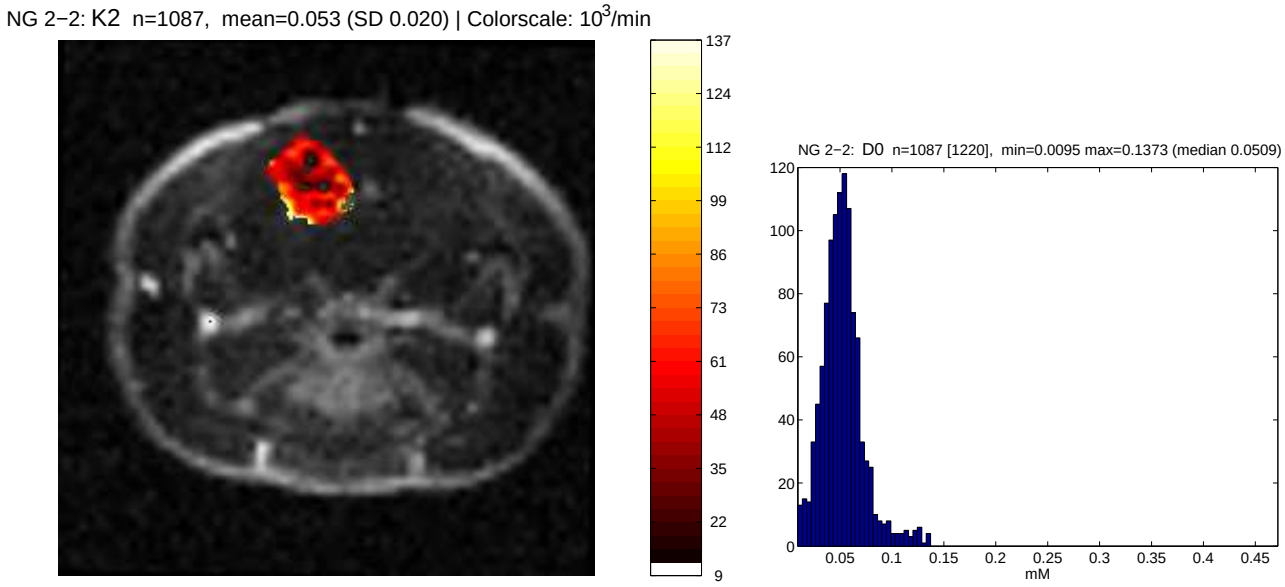

Figure 7.21.: Time development of Su parameter K_2 in animal NG 2; illustrating decreased wash-out rate at the second scan (represented by decrease in mean value). Histograms show noticeably less dispersion with time.

K^{trans} - first scanning:

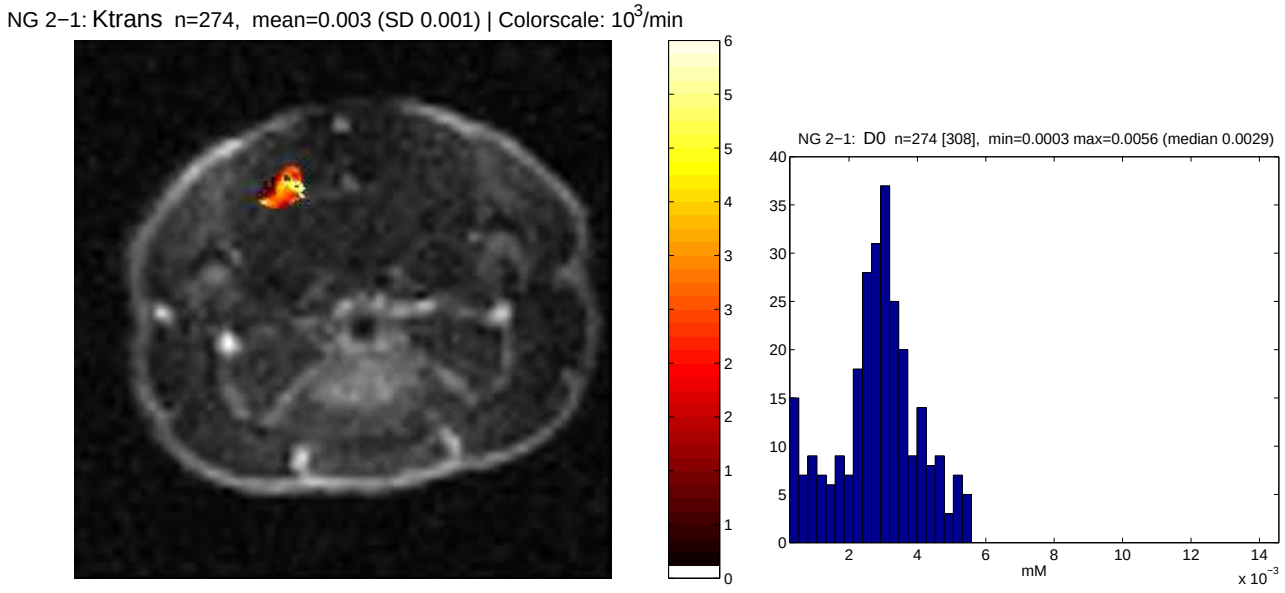

K^{trans} - second scanning:

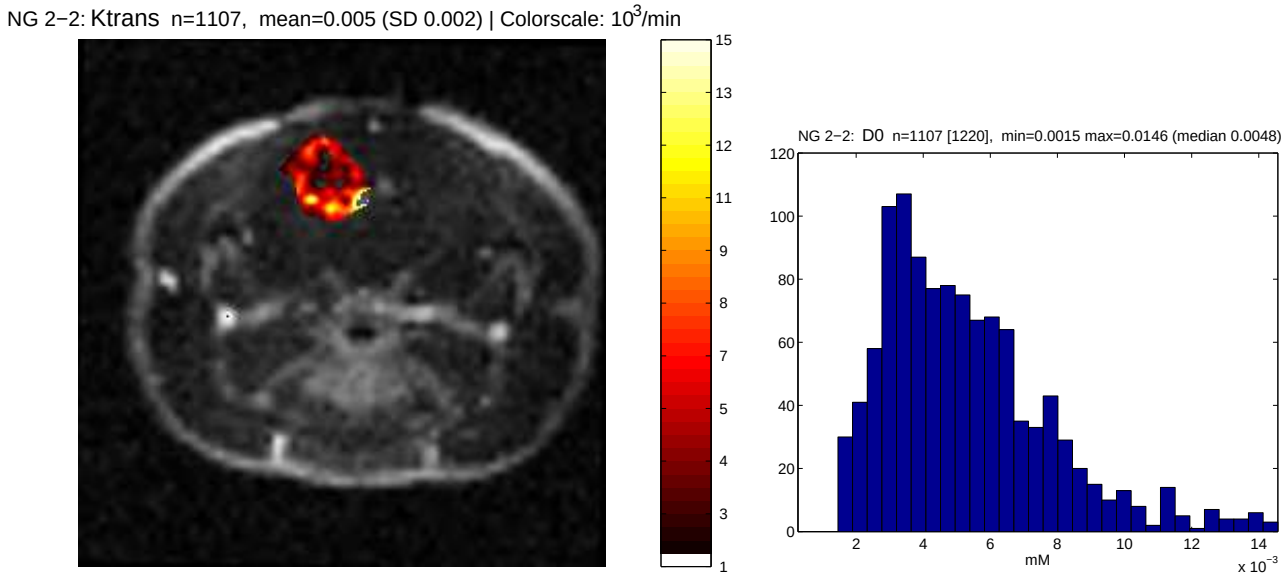

Figure 7.22.: Time development of Tofts parameter K^{trans} in animal NG 2; illustrating increased permeability at the second scan (represented by increased mean parameter value). Histograms show higher dispersion (i.e. a more heterogenous distribution of D_1) with time.

v_e - first scanning:

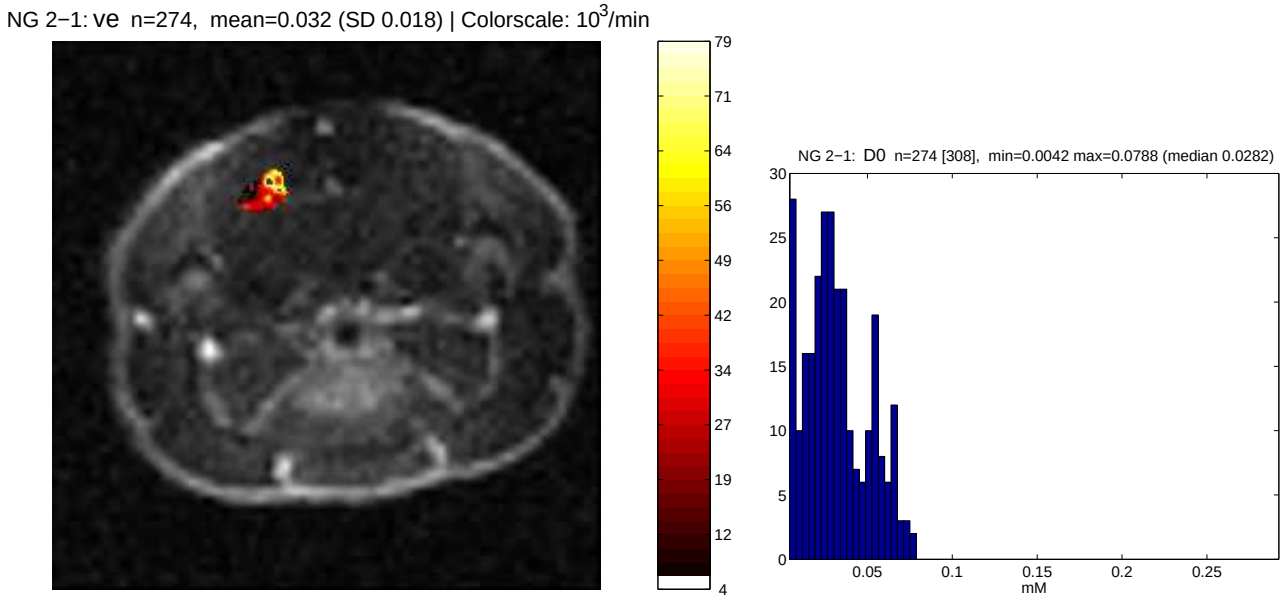

v_e - second scanning:

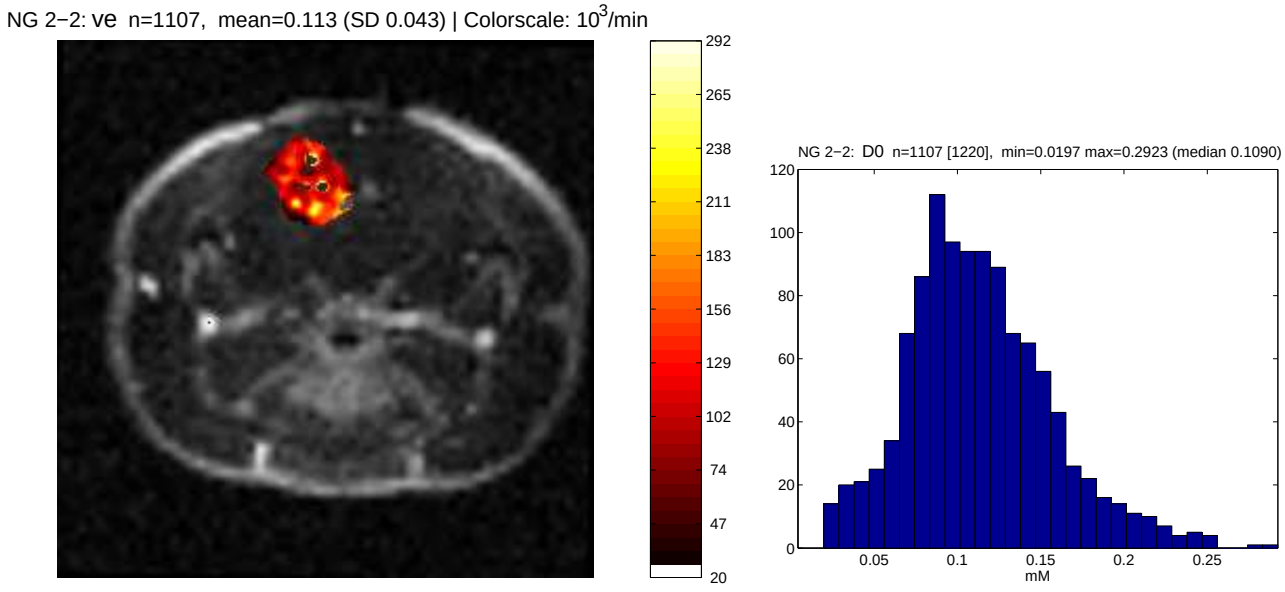

Figure 7.23.: Time development of Tofts parameter v_e in animal NG 2; illustrating increased fractional leakage volume at the second scan (represented by highly increased mean parameter value). Histograms show higher dispersion (i.e. a more heterogenous distribution of v_e) with time.

k_{ep} - first scanning:

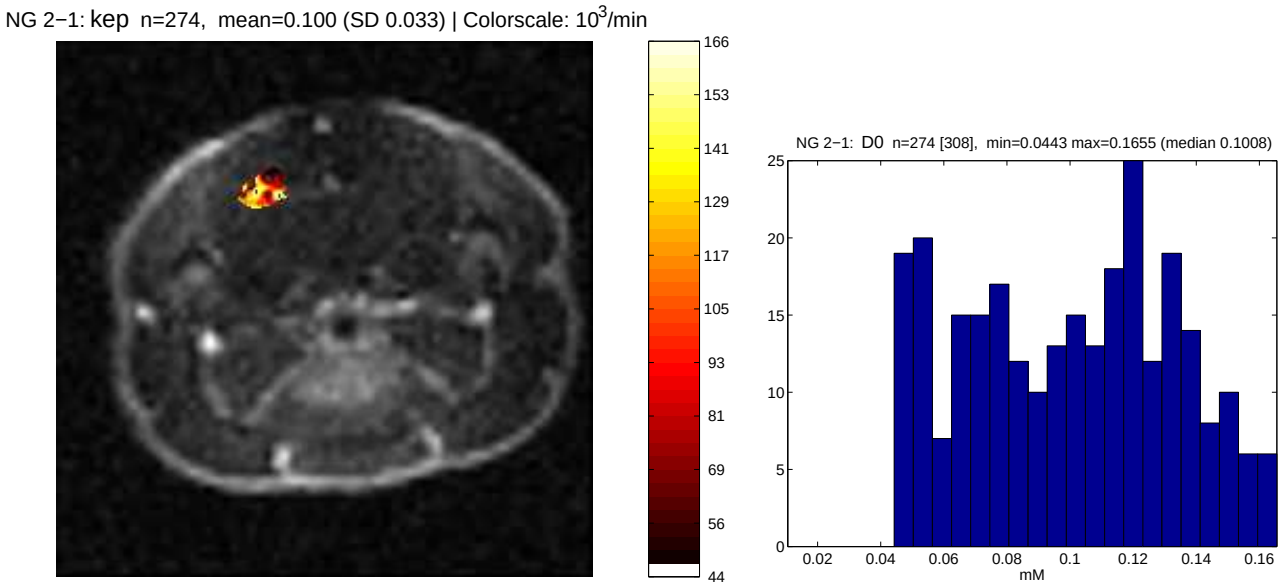

k_{ep} - second scanning:

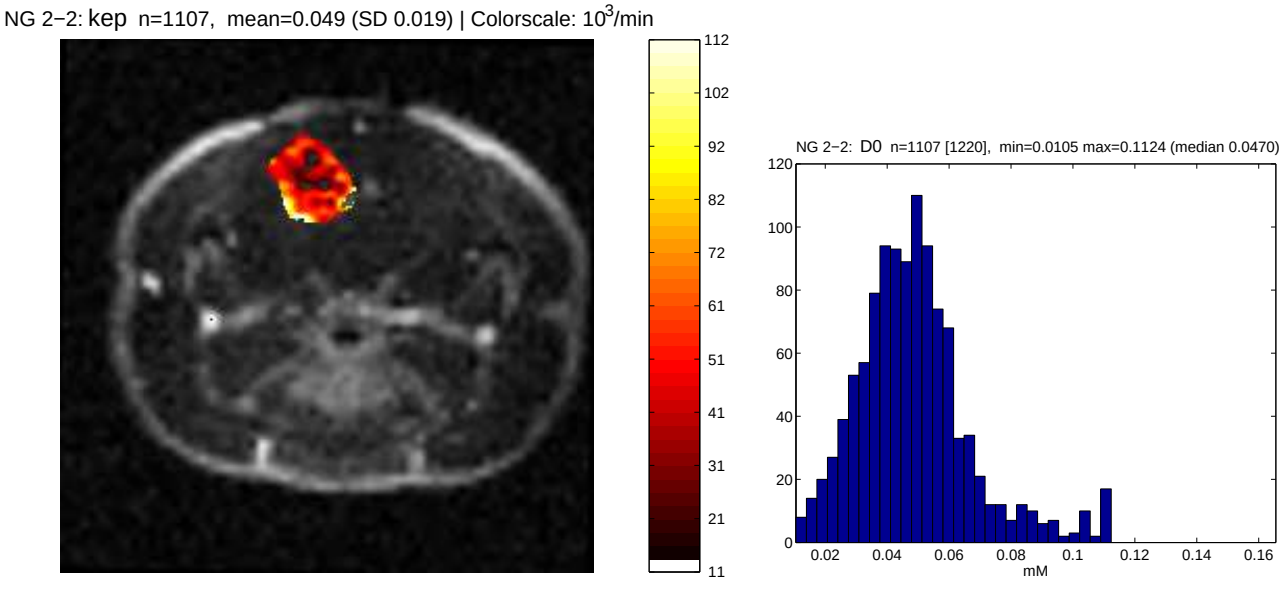

Figure 7.24.: Time development of Tofts parameter k_{ep} in animal NG 2; illustrating decreased wash-out rate at the second scan (represented by decrease in mean value). Histograms show less dispersion with time.

D_0 - first scanning:

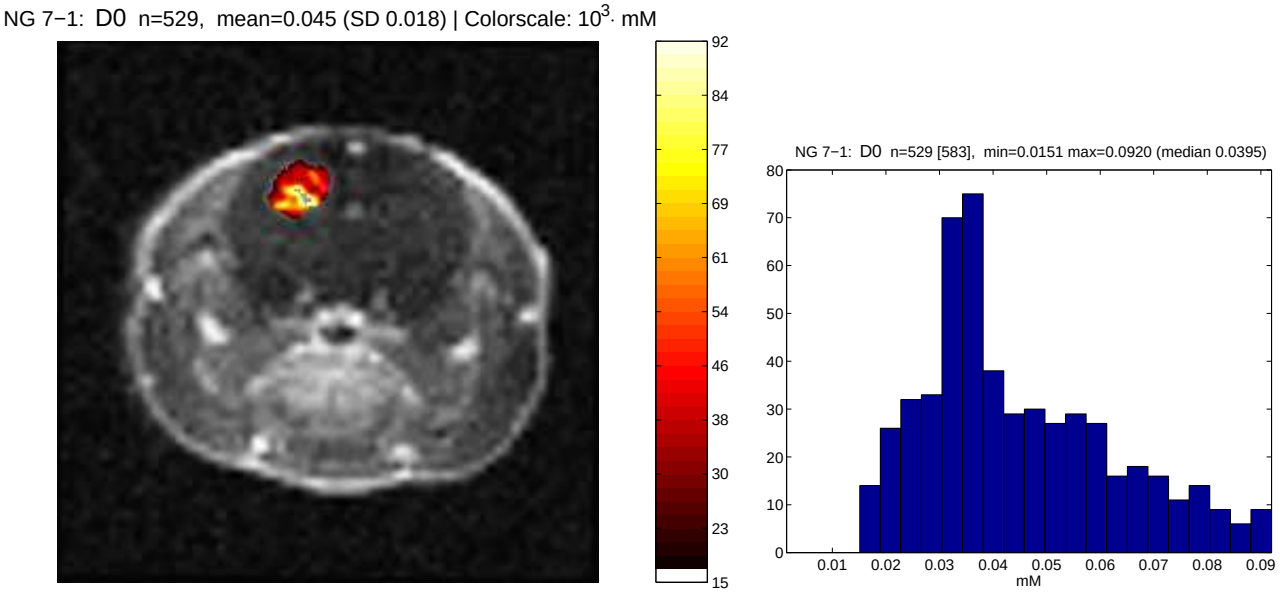

D_0 - second scanning:

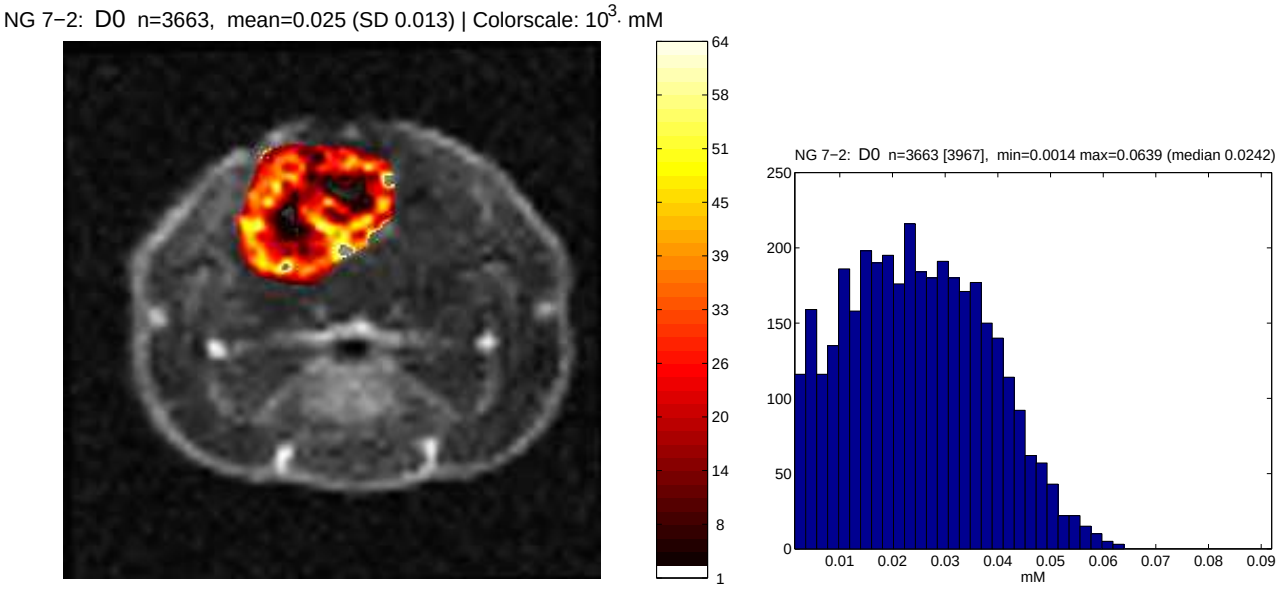

Figure 7.25.: Time development of Su parameter D_0 in animal NG 7; illustrating increased plasma volume fraction (represented by decrease in mean parameter value) with time. Histograms display a corresponding dispersion decrease.

D_1 - first scanning:

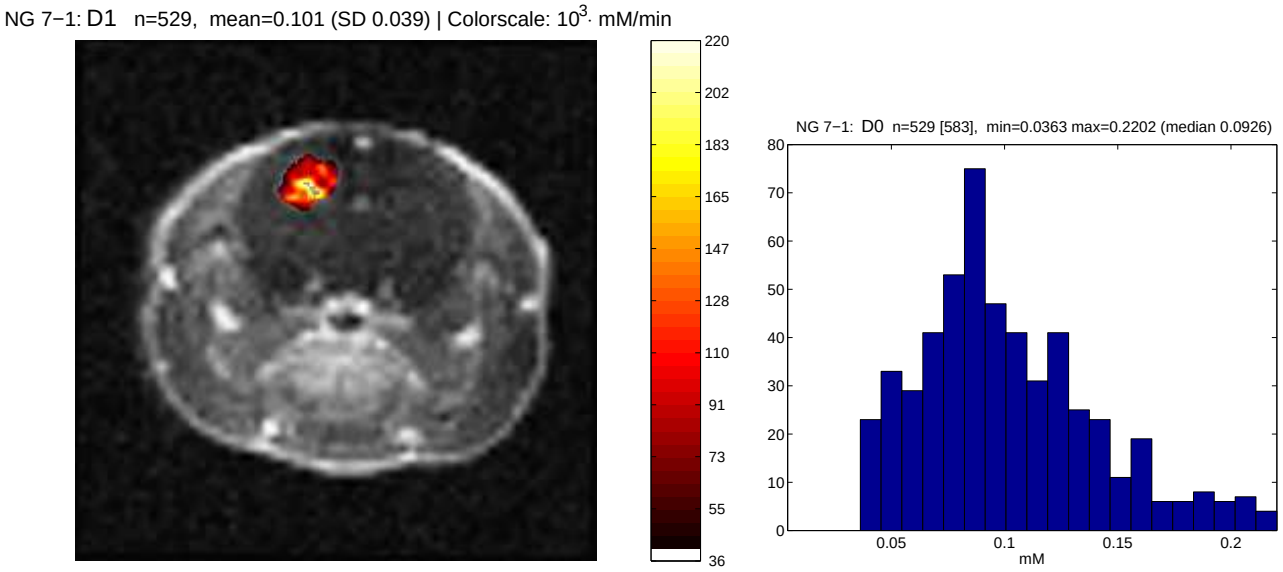

D_1 - second scanning:

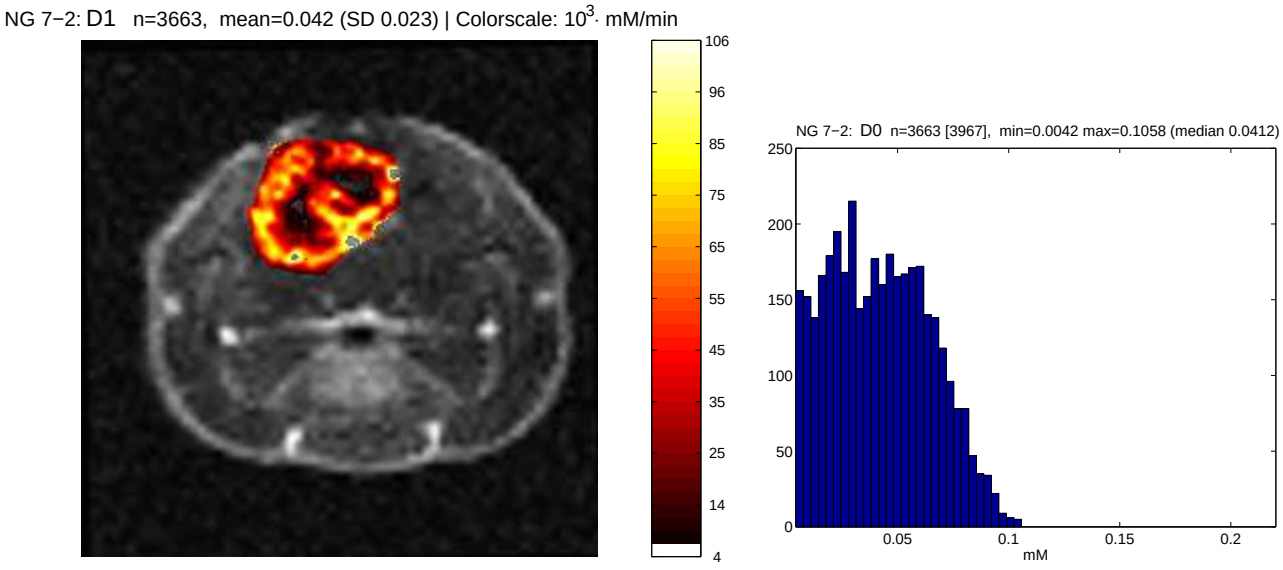

Figure 7.26.: Time development of Su parameter D_1 in animal NG 7; illustrating decreased permeability (represented by lower mean parameter value) with time. Histograms display decrease in dispersion.

K_2 - first scanning:

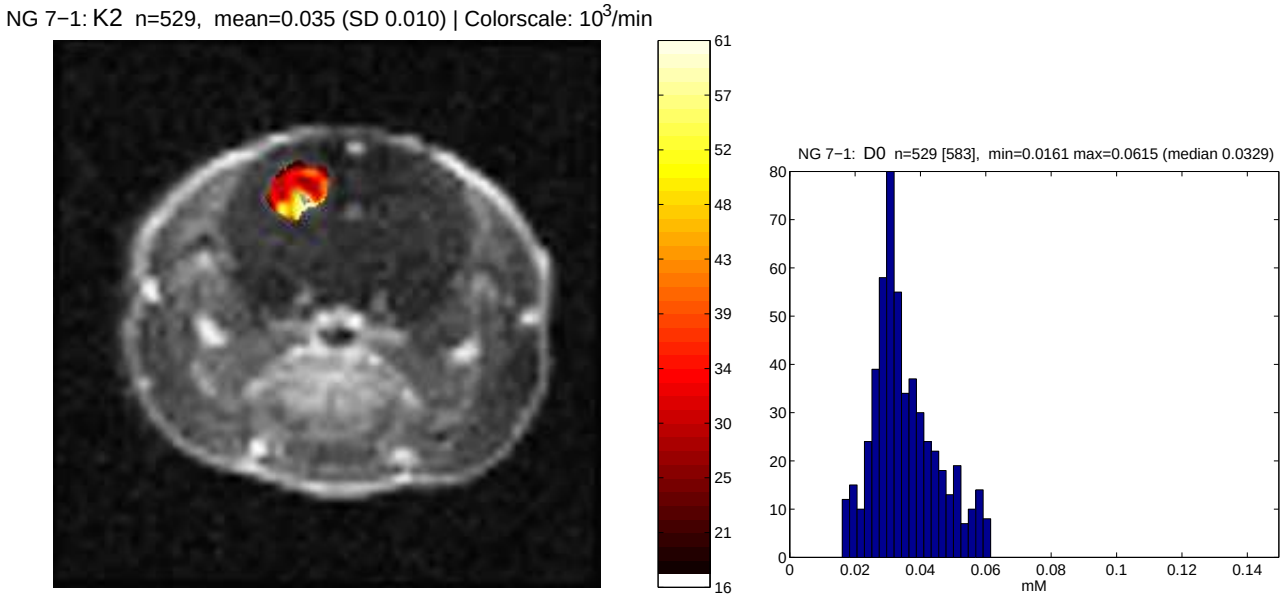

K_2 - second scanning:

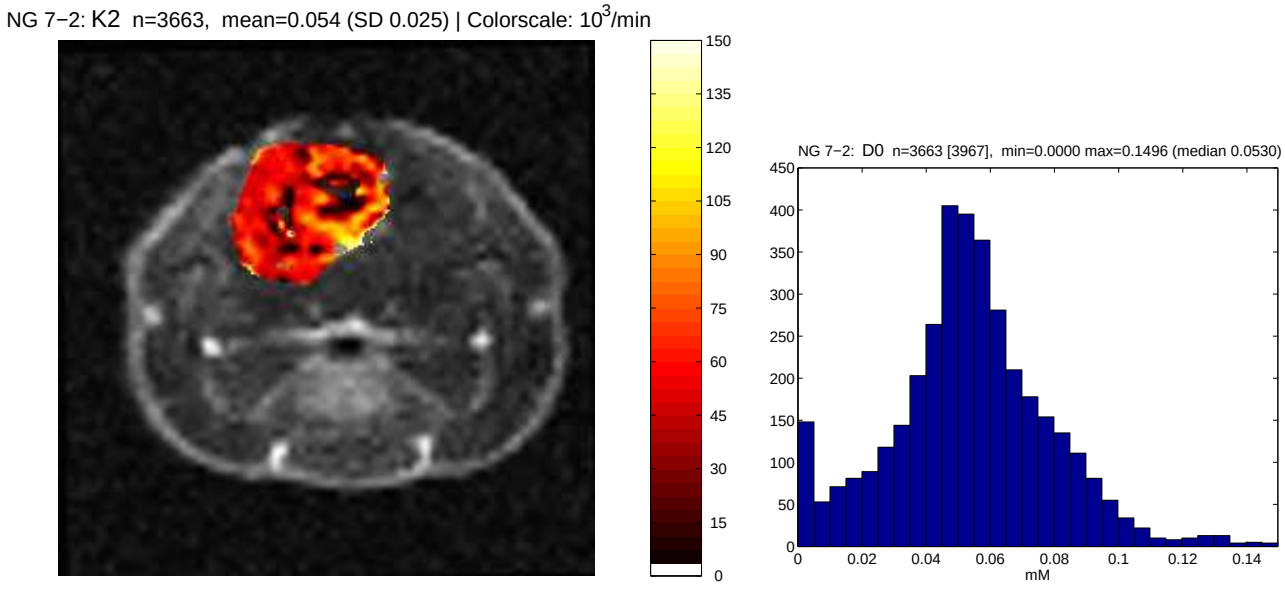

Figure 7.27.: Time development of Su parameter K_2 in animal NG 7; illustrating increased wash-out rate (represented by higher mean parameter value) at second scan. Histograms display increased dispersion.

K^{trans} - first scanning:

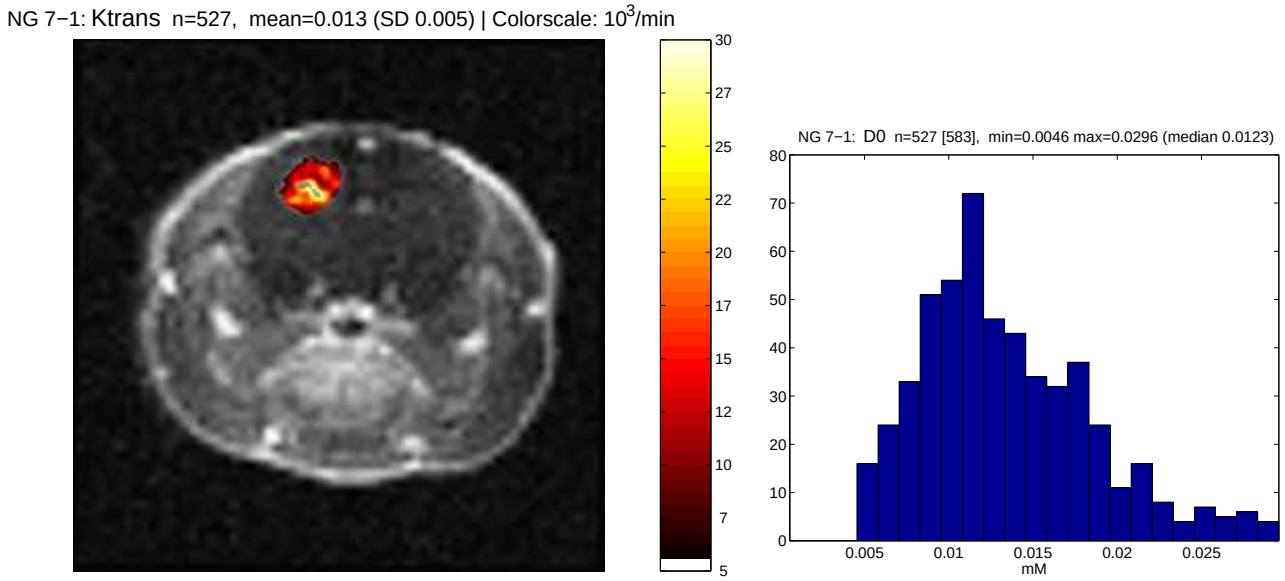

K^{trans} - second scanning:

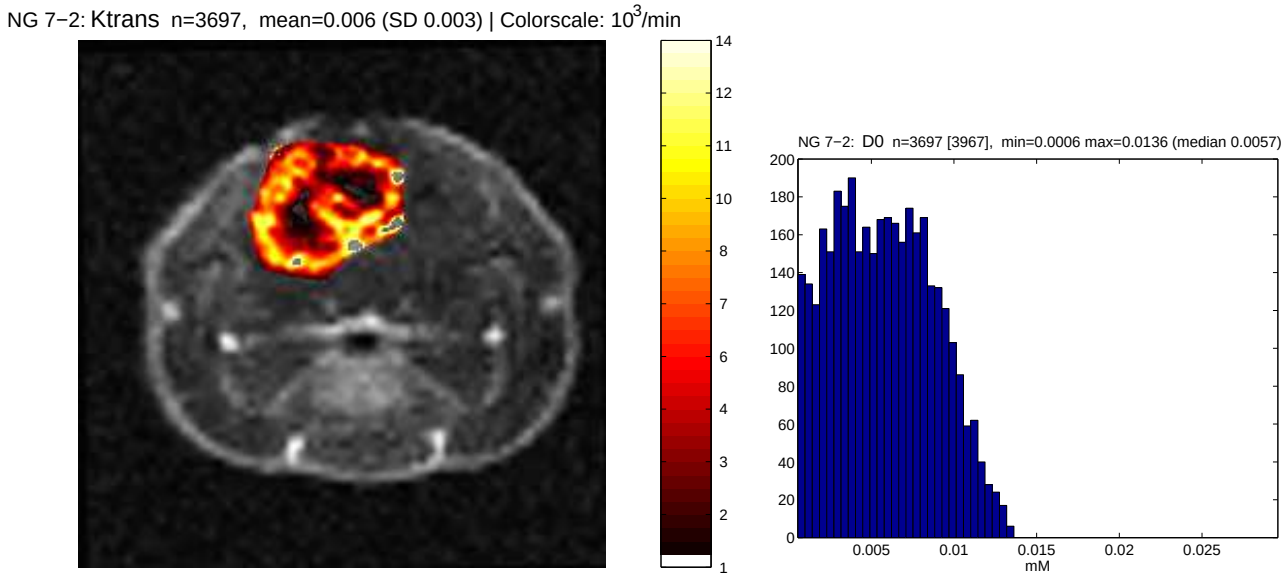

Figure 7.28.: Time development of Tofts parameter K^{trans} in animal NG 7; illustrating decreased permeability (mean parameter value is halved) at second scan. Histograms display decreased dispersion as well.

v_e - first scanning:

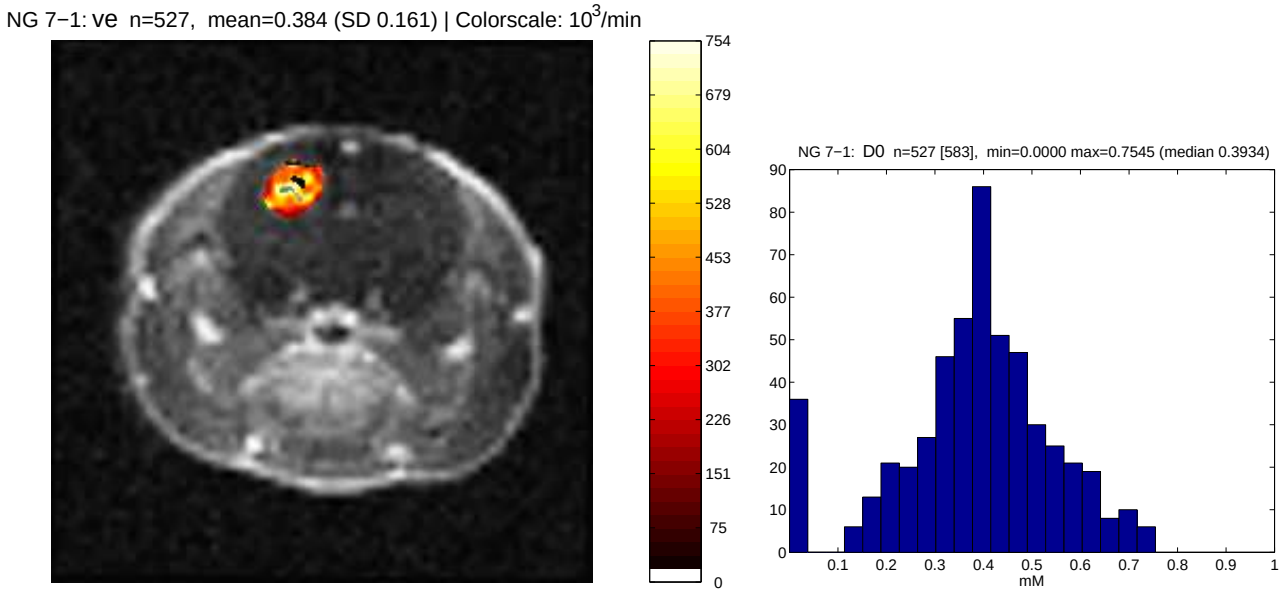

v_e - second scanning:

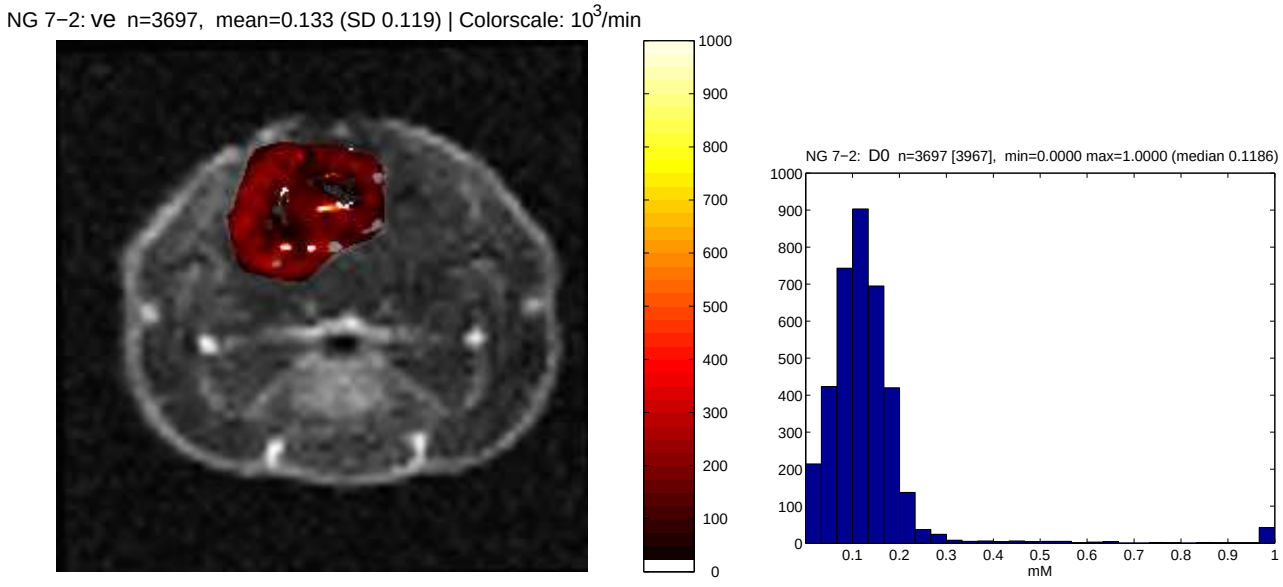

Figure 7.29.: Time development of Tofts parameter v_e in animal NG 7; illustrating largely decreased EES volume fraction (represented by huge decrease in mean parameter value) at second scan. Histograms display decreased parameter dispersion.

k_{ep} - first scanning:

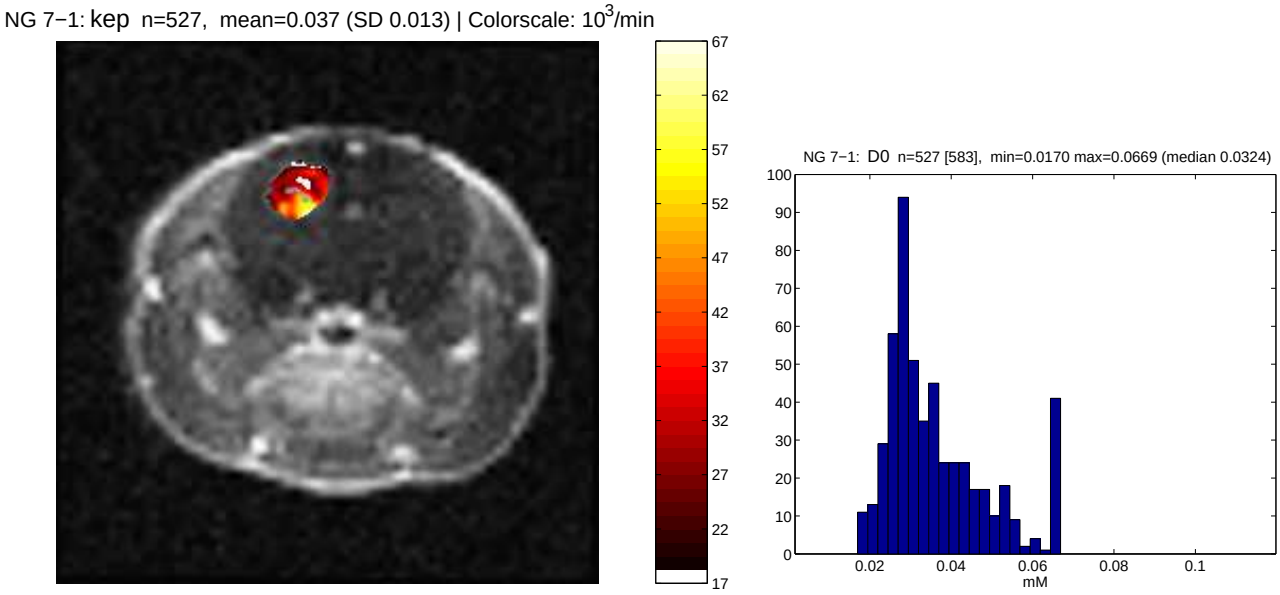

k_{ep} - second scanning:

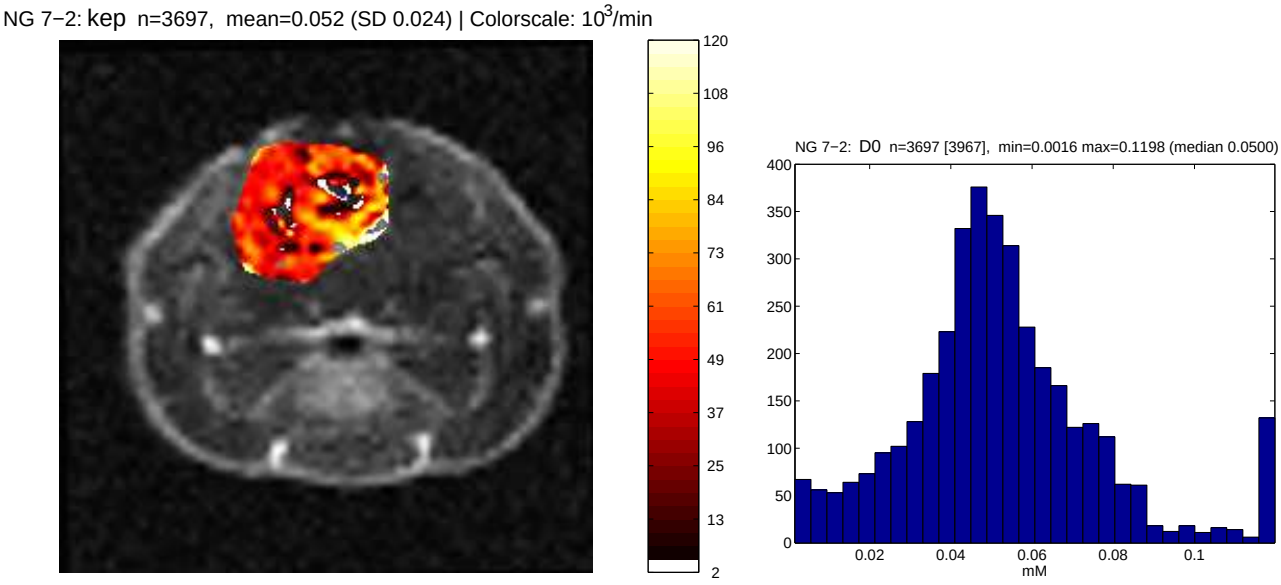

Figure 7.30.: Time development of Tofts parameter k_{ep} in animal NG 7; illustrating increased wash-out rate (represented by increase in mean parameter value) at second scan. Histograms display increase in dispersion with time.

7.3. Results from "goodness-of-fit"

To determine which model best fitted to the actual concentration data in both tumor tissue and healthy tissue data, three examinations were employed with *pixelwise* analysis of four ROIs each. The ROIs were chosen from viable tumor tissue, central necrotic tumor tissue, grey matter and striate muscle. All ROIs were manually chosen to include 30–50 pixels.

Figure 7.31, 7.32 and 7.33 demonstrates the four ROI-tracings and fitted curves from six selected pixels within each ROI for case NG 3-2, NG 7-2 and WT 3-2. Fitted concentration-time courses demonstrated difference in the two models for all illustrated pixels. Additionally, the fitted model-curves revealed following characteristics:

- Necrotic tumor regions revealed scattered/dispersed concentration data ("poorer" fit), slower uptake rates and slower wash-out rates than did viable tumor regions.
- Healthy tissue-regions revealed lower tissue tracer concentrations than observed in tumor tissue-regions.
- Model-fit from Su was better fitted to maximum concentration in tissues than model-fit by Tofts.
- Difference between fitted curves from the two models was larger in healthy tissues than in tumor tissue-regions.

A *pixel-wise*, numerical goodness-of-fit analysis in four ROIs were performed in these three examinations. "Goodness-of-fit" can be determined by SSE (sum of squares errors). However, since Tofts model is simpler than Su's model (i.e. involves fewer free parameters), comparison of the models were done using Akaike's information criterion (AIC, cf. Section 6.7.2). The calculations obtained were SSE-mean and SSE-range for both models, AIC_c-mean and AIC_c-range for both models, $\Delta AIC_c(Su - Tofts)$ mean, ΔAIC_c range, the probability and the evidence ratio.

Calculations for each ROI in the three tumors revealed a lower AIC_c score for Su's model, *implying that Su's model is most likely to be correct.* All calculations obtained are given in Table 7.4.

Summary of results; "goodness-of-fit"

I have elucidated that Su's model and Tofts' model employ slightly different curve-fit to observed concentration data. Variance between models seemed larger in healthy tissues.

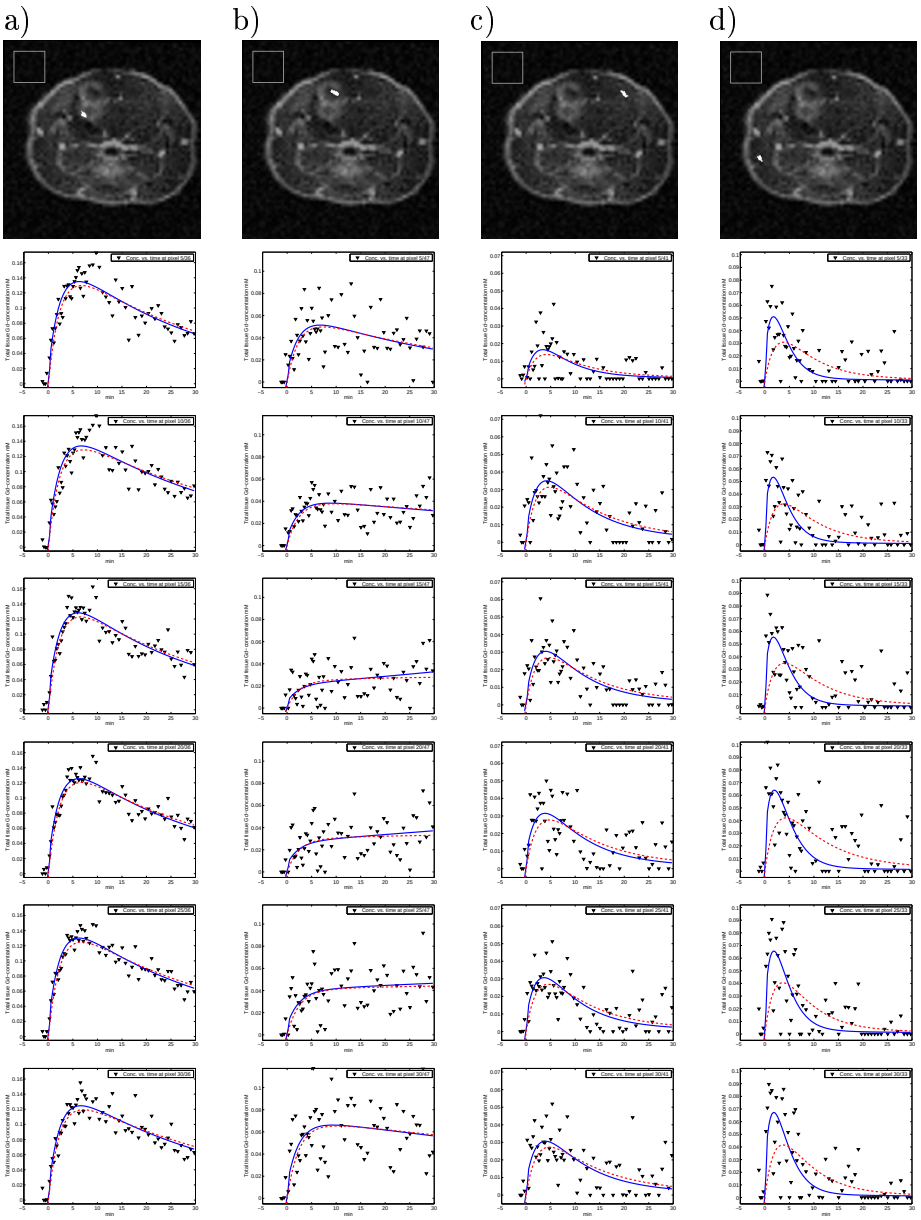

Figure 7.31.: Elucidation of "goodness-of-fit" for the two pharmacokinetic models. *Pixel-Wise* model fit (i.e.parameter estimation) for a NG positive tumor (NG 3-2) in ROIs covering; a) viable tumor (n=49); b) necrosis (n=40); c) grey matter (n=32); d) striate muscle (n=37). n denotes number of pixels included in each ROI. The fitted curves are shown for pixel number 5, 10, 15, 20, 25, and 30 within the ROIs. Su model is given with continuous lines (red), and Tofts model in broken lines (blue). The figure demonstrates a difference in the fit of the two models for all pixels in each ROI. However, difference between models was most pronounced in healthy tissues. Which model fits the actual data most accurately can not be determined visually. Notice the different concentration scales in tumor (column a) and b)) and health tissues (column c) and d)).

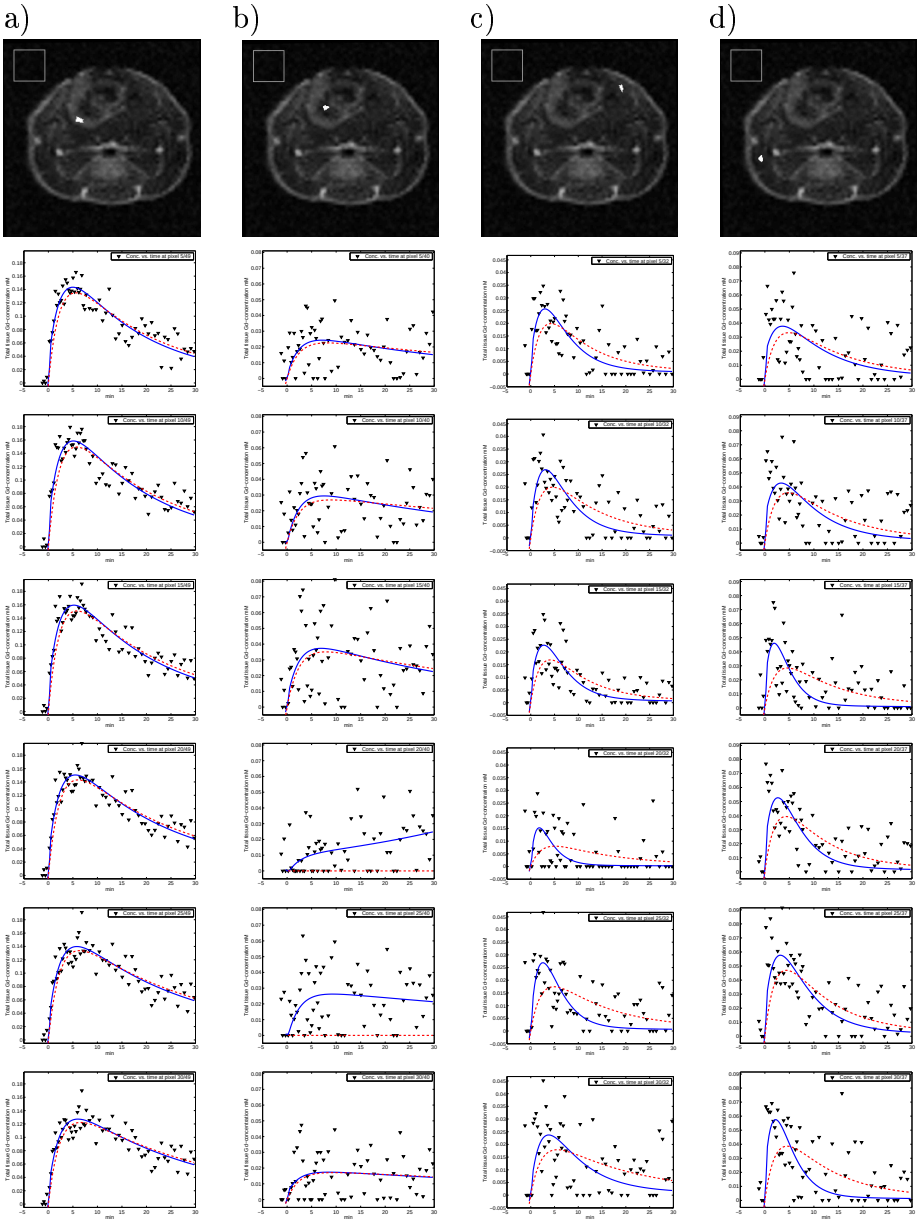

Figure 7.32.: Elucidation of "goodness-of-fit" for the two pharmacokinetic models. *Pixel-Wise* model fit (i.e.parameter estimation) given as example for a large NG tumor at seventh week (NG 7-2). Model fit were performed in four different ROIs covering; a) viable tumor (n=49); b) necrosis (n=40); c) grey matter (n=32); d) striate muscle (n=37). n denotes number of pixels included in each ROI. The fitted curves are shown for pixel number 5, 10, 15, 20, 25, and 30 within the ROIs. Su model is given with continuous lines (red), and Tofts model with broken lines (blue). The figure demonstrates a difference in the fit of the two models for all pixels in each ROI. However, difference between models was most pronounced in healthy tissues. Which model that fits the actual data most accurately can not be determined visually. Notice the different concentration scales in tumor (column a) and b)) and health tissues (column c) and d)).

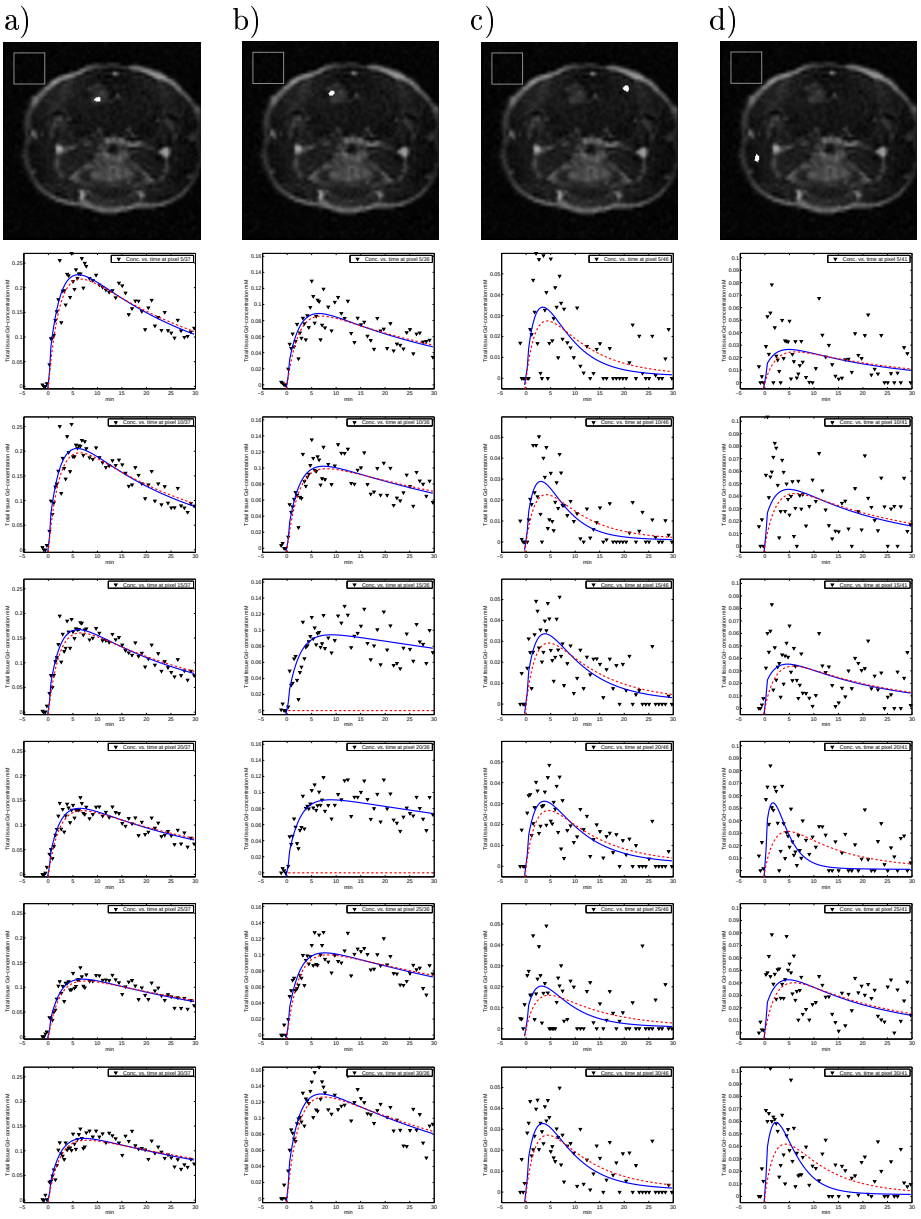

Figure 7.33.: Elucidation of "goodness-of-fit" for the two pharmacokinetic models. *Pixel-Wise* model fit (i.e.parameter estimation) for a wild type tumor (WT 3-2) in ROIs covering; WT 3-2; a) viable tumor (n=49); b) necrosis (n=40); c) grey matter (n=32); d) striate muscle (n=37). n denotes number of pixels included in each ROI. The fitted curves are shown for pixel number 5, 10, 15, 20, 25, and 30 within the ROIs. Su's model is given with continuous lines (red), and Tofts' model with broken lines (blue). The figure demonstrates a difference in the fit of the two models for all pixels in each ROI. However, difference between models was most pronounced in healthy tissues. Which model that fits the actual data most accurately can not be determined visually. Notice the different concentration scales in tumor (column a) and b)) and health tissues (column c) and d)).

	NG 3-2, vi, n=36		NG 7-2, vi, n=49		WT 3-2, vi, n=37	
	Su	Tofts	Su	Tofts	Su	Tofts
SSE	816.7	1991.0	2092.0	5677.5	2673.8	7919.1
AIC$_c$	162.9	216.3	209.2	270.5	211.5	267.5
Δ AIC$_c$ (S-T)	-53.4		-61.3		-56.0	
Probability (Su)	100%		100%		100%	
Evidence ratio (T/S)	0		0		0	
	NG 3-2, ne, n=47		**NG 7-2, ne, n=40**		**WT 3-2, ne, n=xx**	
	Su	Tofts	Su	Tofts	Su	Tofts
SSE	1471.1	1770.8	819.5	901.0	1956.4	3118.2
AIC$_c$	194.4	204.0	135.2	139.0	186.1	218.3
Δ AIC$_c$ (S-T)	-9.6		-3.8		-32.2	
Probability (Su)	92.9%		80.1%		96.3	
Evidence ratio (T/S)	0.090385		0.314998		0.201759	
	NG 3-2, GM, n=41		**NG 7-2, GM, n=32**		**WT 3-2, GM, n=46**	
	Su	Tofts	Su	Tofts	Su	Tofts
SSE	917.1	1120.7	242.4	356.4	398.9	553.9
AIC$_c$	164.4	175.2	80.9	103.9	117.2	134.5
Δ AIC$_c$ (S-T)	-10.8		-23.0		-17.4	
Probability (Su)	97.7%		99.6%		99.6%	
Evidence ratio (T/S)	0.025099		0.003620		0.003881	
	NG 3-2, mu, n=33		**NG 7-2, mu, n=37**		**WT 3-2, mu, n=41**	
	Su	Tofts	Su	Tofts	Su	Tofts
SSE	6958.1	10539.7	1460.2	1936.0	1247.5	1540.3
AIC$_c$	243.4	269.3	178.0	195.1	172.9	184.4
Δ AIC$_c$ (S-T)	-25.9		-17.1		-11.6	
Probability (Su)	100%		99.9%		98.0%	
Evidence ratio (T/S)	0.000059		0.001109		0.022042	

Table 7.4.: Tabulations for comparison of models by Akaike's information criterion (AIC). Outliers are excluded. For all cases: N=63 time-points. Numbers of parameters estimated (K) is three for Su's model, and two in case of Tofts' model. SSE is the sum of squares errors in mean of n pixels, and AIC$_c$ is the corrected AIC in mean of n pixels. The model scoring lowest AIC$_c$ is most likely to be correct. Su's model attained lowest AIC$_c$ score in all cases in this trial (i.e. four different ROIs in each of three tumors).

By MSE (mean of sum of squares errors) and AIC_c-score, Su' s model revealed the lowest values for all four ROIs in these three tumors (cf. table 7.4). Thus, the Su method was most likely to be correct to the data obtained According to this comparative AIC analysis, the probability that the Su model is most likely to be correct (among the two) is highest for viable tumor ROIs.

However, neither MSE nor AIC_c-score could be used as "goodness-of-fit-criteria" for comparison between tumor tissues and healthy tissues as they do not take the low tracer uptake in healthy tissues into account.

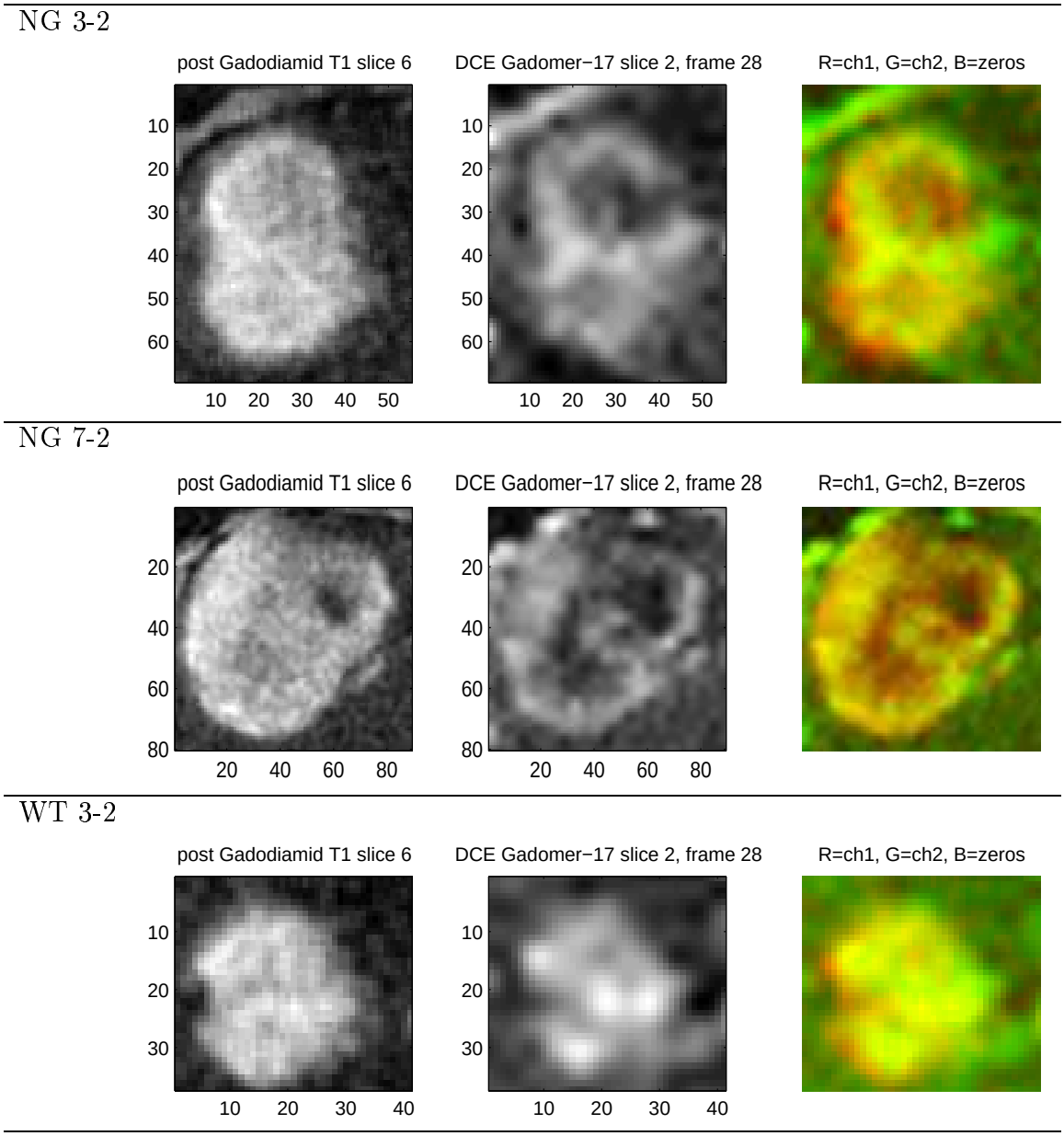

Figure 7.34.: Enhancement patterns of Omniscan and Gadomer-17. Omniscan (left panel) and Gadomer-17 (center) showed a different enhancement pattern, here demonstrated for three tumors (corresponding slices and time-points). The colored maps (right panel) demonstrate the overlaps and differences in enhancement, where Omniscan-enhancement (Gd-DTPA) is coded red, and Gadomer-17 enhancement is coded green. Thus, yellow coded areas represent enhancement of both contrast agent types. Black areas represent no contrast enhancement. Distinction between the two types of contrast agent is evident in reflection of both tumor boundaries and central areas. Dominant Gd-DTPA enhancement (red) is seen in the interfaces "tumor–surrounding tissue" and "tumor–central necrosis". Notice that slice thickness in dynamic and T_1 post-contrast scan were 3 mm and 1 mm, respectively. Thus, partial volume effects (caused by averaging of different structures or tissue types in voxels [77]) are more pronounced in dynamic images. However, using the dynamic mid-slice of tumor, this effect is smaller than if "peripheral slices" (involving both tumor tissue and healthy tissue) had been used.

8. Discussions and conclusions

As a large variety of MRI techniques have revealed microvascular structure and function, a meaningful comparison of results from different studies can be difficult, if not impossible. Differences are seen in imaging technique (equipment, sequences), in contrast administration (type of contrast agent, dose of injected agent, method of administration), and in the post-processing of dynamic data (generation of contrast-time curves, PK model applied etc). Some of these aspects have been elucidated in this thesis and will be discussed in this chapter. Aspects of DCE-MRI concerning acquisition technique is beyond the scope of this thesis[1] and will not be discussed.

8.1. *ROI-wise* analysis

The first step in DCE-MRI parameter estimation, is identification of the tumor region. This is however not always an easy task, especially if the cancer is a non-focal mass and/or if the neighboring normal parenchyma also exhibited some degree of enhancement [93].

Questions concerning i) variability of operator defined ROIs, ii) background information inherent in "Gadomer-17 enhanced" and "Gd-DTPA enhanced" images, iii) assessment of tumor heterogeneity by choosing smaller ROIs, and iv) regional differences were carried out by *ROI-wise* analysis. A mean signal intensity-time curve was computed for entire region of interest in each case. Generally, by *ROI-wise* pharmacokinetic analysis, physiological parameters can be estimated. However, more detailed spatial distribution (i.e. local heterogeneity) can not be assessed based on such ROI analysis.

8.1.1. Variability due to manual tracing of ROIs

The validity of a diagnostic tool depends not only on its accuracy, but also on its reliability [62]. In this study, identification of cancerous regions was done manually, i.e. operator-

[1] MRI acquisitions, including injection procedures, were not under experimental control in this work.

defined (irregular) ROIs were traced with a manually controlled cursor. In this part of my work, each ROI was outlined to include as much tumor tissue as possible (not excluding central tumor fibrosis or necrosis), although excluding fat and surrounding normal tissues. ROI depiction was repeated five times.

Descriptive statistics were calculated: within-tumor standard deviation and within-tumor coefficient of variation (i.e. variability). Results demonstrated variability in parameters due to manual outlining. Even though all parameters were within 95% confidence interval (in every trial), variability were shown to be inherent in subjective ROI analysis. Manual tracings of tumor boundaries are, as shown in this study, hard to reproduce. Therefore, one should be cautious using DCE-MRI derived parameters based on manual tracings in clinical contexts (such as in tumor characterization or assessment of therapy response).

A number of studies concerning manually versus automatic (or semi-automatic) methods of outlining ROIs have been carried out, e.g. [28, 53, 63]. It has been generally concluded that, in addition to differences in acquisition and quantification methods (scanning protocol and pharmacokinetic model used), variability in subjective ROI selection contribute to make the interpretation of estimated parameters more complex [63]. Variation in repetitive ROIs have been reported even when traced by the same experienced operator, as also demonstrated in this study. A solution to this problem can be to employ automated or semi-automated methods [62]. In a study, Liney et al. [53] found that semi-automated methods reduced variability compared to subjective ROI analyses. Liney et al. compared two semi-automated methods of ROI analysis with a user-defined method in a selection of breast tumors. User-defined ROIs were selected by an experienced radiologist. One semi-automated method used a 9-pixel square mask to select the area of greatest enhancement, while the third ROI was produced by determining pixels which were within 10% of the maximum signal intensity.

Although poor perfusion, contrast agents may gradually seep into necrotic regions. Automatic approaches taking into account the time it takes for each area (or pixel) to be enhanced should be considered when determining necrotic regions.

In conclusion, results demonstrated that manual tracings of ROIs is not an extremely reproducible and robust method for determining and reporting tissue specific parameters. Sensitivity to operator performance adds to the total variability in microvasculatory estimates. The smaller biological differences one want to discern, the more severe is this operator-derived “noise”.

8.1.2. Use of different background information for ROI determination

Additional manual ROI tracings were performed as discussed above (three trials, each repeated five times), however, using Gd-DTPA enhanced image as depiction template. In general, parameter variability was higher in Gd-DTPA depicted ROIs than in ROIs outlined on basis of Gadomer-17 enhancement. One tumor exhibited about twice as high CV using the Gd-DTPA template compared to the Gadomer-17 template (for all parameters in both models).

From the presented results (Table 7.1 and 7.2), it was evident that more reproducible parameter estimates were obtained when a Gadomer-17 enhanced template was used as background. This may be related to the fact that Gd-DTPA enhanced templates possess higher tracer leakage due to the agents smaller molecular-weight. Consequently, a Gd-DTPA enhanced tumor region may include parts or boundaries which are not enhanced using Gadomer-17. Pixels that are subject to this effect will influence the resulting parameter value.

As seen in Figure 6.6 dynamic (Gadomer-17 enhanced) and post-contrast (Gd-DTPA enhanced) images reveal enhancement differences for all three cases, especially concerning tumor peripheral- and central "boundaries". To explore the differences between them, enhancement for the two agents have been color coded in Figure 7.34. Substantial enhancement differences (between the two agents) are seen in viable tumor rims and central necrosis. Some central areas possessing no enhancement of Gadomer-17 did actually enhance using Gd-DTPA as contrast agent. Thus Gadomer-17 seem to display higher heterogeneity in its enhancement.

The different enhancement pattern in tumor, observed at comparable points in time (Figure 7.34), communicate different properties of physiology within tumor microenvironment. The results may imply that the tested pharmacokinetic models better apply to tumor-enhancement by a macromolecular tracer. However, slightly different results might have been obtained if central necrotic region were excluded from the ROIs. Non perfused regions affect the results [93]. In my study, however, necrotic areas were always included in the ROIs. Thus, variation, using either of the two contrast agents as template, is likely to reflect micro physiological differences inherent in the peripheral enhancement of tumors.

In the literature, manual ROIs has been reported to be identified from different image channels (e.g. from T_2-weighted anatomical images) [114]. In the multispectral image data used in this thesis, Gd-DTPA enhanced images provided the (visually) most distinct and well defined tumor margins. However, manual outlining of ROIs from these images gave larger variability in parameter estimates compared to tracings from dynamic measurements (using Gadomer-17). A possible explanation for this finding is that Gadomer-17 enhance only the "most" leaky areas. Enhancement with Gd-DTPA can extend beyond this areas,

towards central necrotic region and peripheral tumor boundaries. Gd-DTPA enhanced areas can thus include pixels where a Gadomer-17 based[2] pharmacokinetic model is less applicable. As stated in Kim et al. [46], agents such as Gd-DTPA have a 20% to 80% single-pass extraction fraction both in normal and malignant tissues. Contrary, Gadomer-17 have a small ($< 5\%$) single-pass extraction fraction in normal vessels. Additionally, as Gd-DTPA are smaller molecules, there are less diffusion hindrances within the tumor interstitium, resulting in larger areas of enhancement.

In conclusion, cancerous region were best identified from the Gd-DTPA enhanced images. However, as demonstrated in Figure 7.34 the two different contrast agent types possess different CA-enhancement disposition in the same tumor. Furthermore, pharmacokinetic models assuming a generalized blood-concentration course based on Gadomer-17 decay rates and concentration amplitudes, are likely to be more appropriate when ROIs are depicted from Gadomer-17 enhancement rather than Gd-DTPA enhancement. My findings of less parameter variability between repetitive ROI tracings using Gadomer-17 template compared to Gd-DTPA template support this theory.

8.1.3. Heterogeneity assessment by smaller ROIs

As mean values in ROI analysis do not take interior tumor heterogeneity into account, it might be preferable to select several smaller regions within a tumor rather than determine a mean value for the entire tumor [63].

By selecting several smaller ROIs from viable (enhanced) parts of tumor and some from "necrotic" (non-enhanced) areas, it was desired to demonstrate spatial parameter variation. Additionally, I wanted to investigate whether areas in tumor that seemed to possess the same degree of enhancement, were heterogenous in terms of the estimated parameters in the Su- and Tofts models. Spatial differences were confirmed.

Also the "necrotic" areas revealed differences (heterogeneity) in estimated parameters. This may imply that not all non-enhanced (Gadomer-17) areas are necessarily consistent with developed necrosis. Reduced perfusion (not fully developed necrosis) in areas may hinder leakage of Gadomer-17. Another explanation to non-enhanced areas can be that newly formed vessels mature and become less permeable to Gadomer-17 during time [14]. As seen in Section 6.6, some tumor regions which appear non-enhanced with Gadomer-17, appear enhanced with Omniscan. This should be taken into consideration when deciding that central necrotic/fibrotic tissues shall be excluded.

Although heterogeneity was found within both "enhanced" and "non-enhanced" regions, there was a trend concerning difference in time course between them. As would be ex-

[2]Both models (Su and Tofts, respectively) as used in this thesis are regarded as Gadomer-17 based because they employ concentration amplitudes and decay rates derived from Gadomer-17 kinetics in blood.

pected, enhanced regions generally showed a steeper up-slope, higher total concentration and a faster decay (wash-out) compared to non-enhanced regions (compare e.g. ROI 11 and 12 Figure 7.5). Concentration data from "non-enhanced" did not (visually) reveal a more dispersed distribution than those from "enhanced areas". However, the smaller ROIs obtained more dispersed data than the two "whole tumor" ROIs did (large ROIs improve SNR [70]).

Smaller "enhanced" ROIs showed variability in parameter out-comes. These areas possessed the same visual degree of enhancement (i.e. signal intensity). Within these "enhanced" regions, parameter variations were highest for K_2 and k_{ep}. If automated ROI selections (e.g. threshold segmentation [97]) are used, these findings of heterogeneity may indicate the need to differentiate between different ROI selection criteria even within the same tumor.

The variance in parameters estimated for ROIs that correspond to visual "non-enhanced" intra-tumor regions, may represent presence of low perfused areas, and not necessarily necrosis. On the other hand, the variation may also express a "non-validity" of the pharmacokinetic models in these low- or non-flow regions. Due to insufficient perfusion to necrotic and semi-necrotic areas, delivery of contrast agent is flow-limited rather than permeability-limited [94, 97]. In such areas, models that assume permeability-limited transport constants are thus not applicable. However, visual inspection of model curves fitted to the concentration time courses (Figure 7.5) did not reveal poor fit. Visually, "non-enhanced" ROIs may thus represent low perfusion/low permeability areas, and not necessarily necrosis.

8.1.4. Regional differences in four tissue ROIs

tissue-concentration curves derived from *healthy tissues* (*grey matter* regions and *muscle tissue* regions) revealed very low peak tissue concentration of contrast agents. Moreover, for both models (Su and Tofts), curve-fit seemed to be poor in healthy tissues compared to tumor tissues. However, concentration data in these areas were scattered, making it difficult to visually evaluate the quality of fit.

Evaluation of data-fitting revealed no conclusive visual difference between "whole-tumor" ROIs and "enhanced tumor-part" ROIs. Maximum tracer concentration was, however, slightly higher for enhanced ROI in all nine cases due to larger mean signal intensity in the ROIs restricted to enhanced regions only. Comparing "whole tumor" ROI analysis and "hotspot" (enhanced) analysis, Su et al. [93] reported a steeper up-slope, higher enhancement magnitude and a more rapid wash out phase for hotspots. In this study, the higher enhancement magnitude could be easily identified.

Difference between curve-fit by Su's model and by Tofts model was prominent for healthy tissue ROIs. Su's curve revealed higher maximum tissue concentrations and higher rate constants for tracer-flux back to blood (cf. Figures 7.7, 7.8 and 7.9). Both models showed

visually a "better" fit to tumor tissue than to healthy tissues, but it could not be decided from visual inspection alone which model provided the best fit.

Although the low Gadomer-17 tracer uptake in healthy tissues might indicate that the models are not applicable to these regions, they were nevertheless included for assessment of regional differences (cf. Figure 7.11) in permeability (D_1 and K^{trans}) and out-flux rate (K_2 and k_{ep}). In a study by Padhani et al. [70] it was proposed to use healthy tissue ROIs as reference to which the calculated DCE-parameters can be normalized to compensate for variations in physiological factors, such as cardiac output and blood pressure, that might affect parameter estimates. This assumes narrow ranges of kinetic parameter variability in healthy tissues.

In this study, permeability (K^{trans} or D_1) was shown to be highest in enhanced ROIs, and higher in tumor than in healthy tissues. Notice that both models (Su and Tofts) actually estimated some "permeability" in healthy tissue. This "permeability" is even seen in grey matter, in which the blood-brain barrier should not allow transvascular transport of macromolecules such as Gadomer-17. Remember, however, that permeability is not measured directly. Permeability is rather an assumption made in the models to describe the observed data. If the signal intensity raises for a short period of time, and then falls again, the models will consider this as permeability —regardless of the cause of the intensity change. In my experiments, it is likely to assume that such a short-durated signal intensity change may reflect "first pass" of contrast agent in highly vascularized normal tissues. Thus, permeability may have been incorrectly measured in areas without transcapillary leakage (i.e. healthy tissues).

Bi-variate scatter plot of parameters describing permeability in the two models (i.e. K^{trans} versus D_1) showed that they were highly correlated (Figure 7.12). This indicates that they reflect closely related physiological processes. K^{trans} (min^{-1}, Tofts) represents the permeability-surface area product per unit volume of tissue, while D_1 (mM/min, Su) is proportional to volume of extravascular extracellular space, the maximum plasma tracer concentration and the transport constant from blood to tissue (K_1). D_1 is described to reflect contrast agent accumulation in the intravascular space. K_1, reflecting the permeability-surface area product is not expressed explicitly by Su's model.

K_2 (Su) and k_{ep} (Tofts), expressing the out-flux rate of tracer from tissue, demonstrated higher values in normal tissues than in tumors tissues (cf. Figure 7.11) . This is not consistent with reports in the literature [97, 96], and may represent another indicator of the "non-validity" of the models in healthy tissues. A bi-variate plot of these parameters revealed a piecewise linear relationship (cf. Figure 7.12) with low values of K_2 and k_{ep} representing tumor, and higher values representing healthy tissues. Again, the high values (of K_2 and k_{ep}) estimated in grey matter and muscle are likely to reflect bolus passage in the microvasculature of these tissues, and not wash-out of tracer from tissue.

8.2. Pixel-Wise analysis

In ROI-wise analysis, the mean of the signal intensities within a selected ROI is calculated for each of the dynamic images, resulting in a single time-intensity curve which conceals tumor heterogeneity[63]. In pixel analysis however, time-intensity data curves are employed for each pixel within the selected ROI. Using pixel-wise quantitative analysis, results can be presented as parametric images[3], and corresponding histograms of calculated parameter can be plotted. Advantages of pixel mapping techniques include; 1) *improved assessment of the heterogeneity of tissue enhancement* and; 2) *elimination of the need for selective placement of user-defined ROIs* [8]. Furthermore, Tofts and Berkowitz [103] stated that even though the exact relationship between concentration and enhancement is known for a homogeneous region of tissue, it is not possible to estimate the exact relationship for a heterogenous region of tissue, unless the enhancement values within all parts of the region is known (i.e. *pixel-wise* analysis).

However, researchers present conflicting opinions about the value of *pixel-wise* estimation. Comparing *ROI-wise* whole tumor analysis with pixel-by-pixel analysis of whole tumor, Su et al. [93] found good correlation of the resulting parameters from the two methods. The researchers suggested that the correlation may be in part caused by use of computer assistance when defining ROIs, and that *pixel-wise* analysis does not provide any additional quantitative information (besides demonstrating the tumor heterogeneity) compared to *ROI-wise* analysis. The *pixel-wise* approach can be computationally heavy and is usually a very time consuming process. As a reward, the parametric maps may help improving diagnostic accuracy and revealing heterogeneity. Comparing manually selected (non-automatic) ROI estimation with whole tumor pixel estimation, generally favor *pixel-wise* information as the ROI-selection method affects the results.

The methodological problems with pixel-by-pixel parameter estimates includes the possibility of not being able to estimate parameters in a pixel, or that the estimate is not valid (the model assumptional requirements are not fulfilled). Such problems may be due to noise or movement artifacts. It may also be that the pixel in question is not enhanced. Alternatively, there can be numerical problems with the estimation algorithm. In this study, pixel estimates that were located outside the 2.5–97.5 percentile range, as defined from the *pixel-wise* distribution from the whole region of interest (cf. Figures 7.13– 7.30), were excluded to reduce such "artifacts" in the parametric images. In this way there might occur "voids" within the ROI, where the template image intensity is depicted instead, marking the occurrence of such outliers. The resulting parametric map will thus enable calculation of sample means and standard deviations as well as histogram plots, showing the heterogeneity of parameter distribution within the restricted ROI.

[3]Notice that for the parametric maps, the numerical range of each parameter is typically (pseudo-) color coded with the color scale shown beside the corresponding map.

Inspecting the generated parametric maps from *pixel-wise* analysis (Figures 7.13– 7.30), blood-tissue permeability maps (represented by D_1 and K^{trans}) indicate relatively large areas of low to medium permeability (red and orange color, respectively), surrounded by hotspots of high permeability (yellow) in small tumors ("week-five" scans). However, permeability maps of larger tumors ("week-seven" scans) exhibited large central areas of very low, or zero, permeability.

Possible explanations for such central low permeability are [5]:

- *Lack of perfusion (such as in necrotic regions),*
- *High interstitial pressure (as expected in central areas of tumors)* and/or
- *Presence of mature capillaries with very low permeability*

Both fractional blood volume, and permeability have been proposed as characteristic features of tumor aggressiveness [81]. Blood volume maps (D_0) and permeability maps (D_1) showed great similarities regarding location of areas with low values and the location of "hotspots". An example of this is seen when comparing D_0 and D_1 maps from seventh week scan of NG tumor one (cf. Figures 7.13 and 7.14. These maps show spatial relations (of D_0 and D_1) in the tumor. The highly heterogenous nature of blood volume (i.e. perfusion) is reflected in Figure 7.13. The chaotic structure of tumor vasculature is known to cause an unbalanced blood supply and thus tumor regions with transiently or chronically hypoxic. Further, a temporal and spatial heterogeneity of blood flow in tumors, is increased by the fact that only 20–80 % of the microvessels are perfused at a given time [29].

In small tumors, wash-out maps and permeability maps showed nearly a reciprocal relationship, i.e. high permeability areas correspond to low wash-out rate areas, and vice versa. One example of this is is seen when comparing K^{trans} and k_{ep} in fifth week scan for tumor NG one (cf. Figures 7.16 and 7.18) which show spatially a nearly inverse relation. Wash-out rate maps for the three large tumors (seventh week) demonstrated low wash-out for the largest tumor, and medium to high (although highly heterogenously distributed) wash-out rates for the two other tumors.

High permeability to contrast agent in small tumors could be related to angiogenic activity forming new, initially highly permeable micro-capillaries. The subsequent maturation of angiogenic vessels may decrease observed permeability due to extensive coverage with pericytes and smooth muscle cells. This progressive maturation of angiogenic vessels in tumors imply that young (and thereby small) tumors contain a higher fraction of immature and leaky vessels compared to larger tumors which have continued to grow and possess vessels with a decreased permeability [5, 48]. It is tempting to suggest that maturation of angiogenic vessels, and increased central interstitial pressure with corresponding edema formation, may contribute to the low parameter values observed in the largest tumor (NG 7-2). However, histological examination will be necessary to make more valid interpretation of the model based DCE-MRI findings.

8.2.1. Time development

To assess parameter changes in tumor during its development, mean parameter value for the entire tumor (all pixels) at both fifth and seventh week post-implantation were com-

puted for each of three tumors (three different animals). Two of these three cases showed parameter changes as would be expected with tumor growth. In these two tumors, the permeability-surface area product (D_1 and K^{trans}), the fractional blood volume (D_0) and the fractional leakage volume (v_e), accessible to Gadomer-17, *increased* during the two weeks between scans. In contrast, the flux rate of tracer returning to the vasculature (K_2 and k_{ep}) revealed a decrease. The findings indicating increased blood-tissue permeability, intravascular volume fraction[4] and tracer leakage volume was expected as these features represent characteristics of tumor aggressiveness [29]. Also, an increase in parameter dispersion, reflecting heterogeneity (which in turn reflects tumor aggressiveness), was demonstrated (cf. Section 7.2.1).

In their "NG-2 study", Brekke and Chekenya (at present time unpublished) also found reduced wash-out rates in NG-2 tumors at the second time-point. Such reduced wash-out rates are inconsistent with findings reported by Su et al. [97, 96, 98]. Brekke and Chekenya show their findings to be neither contrast agent dependent (reduced outflux was also observed using Gd-DTPA), nor model dependent (as both Su's and Tofts' model revealed a decrease in wash-out).

The development of reduced out-flux rates in NG-2 tumors analyzed in this thesis is *most likely caused by increased formation of low-perfused, or necrotic areas* as demonstrated in the parametric images. Contrast agent elimination from such low-exchange tissues is known to occur at slow rates [46, 58, 71]. A treatment implication of this phenomenon; high permeability and low wash-out properties of tumors, may be important for molecular drug-treatment. A high-molecular drug would easily leak from blood to tumor tissue and remain trapped there for a prolonged time.

Notice that "time-development" was studied using parameter mean of all the individual pixel (representing a single global value for the entire region). If used alone, parameter mean conceal heterogeneity. From Figures 7.13– 7.30 it is also seen that parameter histograms are not always unimodal and symmetric. In such cases of asymmetric skewed distribution, the sample mean (as in *ROI-wise* analysis) would not provide an appropriate statistical point estimate of the "typical" parameter value in the region of interest. Instead, their 25th, 50th and 75th percentiles could have been a better choice for representing parameter estimations at different time points, such as proposed by Galbraith et al. [28] and used by Bogin et al. [5]. And, obviously, it is not spatially or physiologically accurate to report a parameter mean of all the individual pixel values (i.e. a single global value for the entire region) as parametric images and histograms revealed a rather heterogenous tumor tissue response.

[4]Notice that intravascular volume fraction measured as Su's D_0 is related to blood flow by the fact that DCE-MRI can only detect functional vessels with flowing blood.

8.3. "Goodness-of-fit"; comparison of models

The visual difference in fit between the two models were largest in healthy tissues (Su seemed more appropriate than Tofts). However, in these cases there were extremely low tracer uptake with a large dispersion of data in the concentration time course. This dispersion might reflect the noise level in these time courses (i.e. bolus passage) so that the PK model will not be valid or enable reasonable parameter estimation. In tumor tissues, the difference in fit was less evident, but again, Su's model revealed a slightly better "goodness-of-fit" by visual inspection. Such difference in fit might be related to differences in model-assumptions, the derivations to obtain the final model equation, or simply the incorporation of one more free parameter in the Su model.

The quality of fitting the parametric models of Tofts and Su to the calculated concentration curves was first assessed through calculation of the sum of square errors (SSE). However, SSE does not provide a good measure for comparison of models which do not fit the same number of parameters. A model consisting of many parameters is usually more "expressive" and "adaptable" to data than a model with fewer parameters [110]. The curve generated by the most complicated model equation (i.e. more parameters) will nearly always have a lower sum-of-squares because it is more flexible [61]. On the other hand, we want as simple model (few parameters) as possible to account for the biological processes being involved.

Therefore, The Akaike's information criteria (AIC_c) was used to determine how well data supported each model. The Akaike's information criterion provides a numerical means to select an the most appropriate model from a set of competing models [110]. The approach takes both SSE and difference in number of fitting parameters into account. The model with lowest AIC_c score is most likely to be correct. The term ΔAIC_c tells how much more likely one model is compared to the other. In addition, Su and Tofts model were also compared with an AIC_c-based likelihood ratio. An advantage of using AIC is that the approach is less rigid than that of statistical hypothesis testing. Moreover, the AIC_c approach can be easily extended to compare more than two models [61]. However, Akaike's method is dependent on the magnitude of the observed data points [110]. Thus fit in "healthy tissue" regions could not be compared to fit in "tumor" regions using this criteria.

"Goodness-of-fit" analysis by AIC_c-score revealed numerically a better fit for Su's model (compared to Tofts model) in all four "tissues" (i.e. enhanced tumor, non-enhanced tumor, grey matter and muscle) in each of the three cases being assessed. Possibly this better adequacy of Su's model fit is caused by Su's two-part equation for describing contrast agent kinetics in blood compartment (Su's fitted curves seemed visually to better account for the early peak tissue contrast agent concentrations). The theoretical differences inherent in the two models, which may explain their different fitting properties, is further discussed in Section 8.4.1.

In conclusion it has been demonstrated that Su's model was most likely better than Tofts'

model to describe the observed concentration time courses in these experiments. This could be concluded from the AIC_c analysis, taken into account the "handicap" of Tofts model using only two parameters (compared to Su's three parameters). I could however, not numerically demonstrate that the models fitted poorly to data from healthy tissues compared to data from tumor tissues. Do do so, we would need a method that takes the low concentration in healthy tissues into account. Besides, numerical fit is not equivalent with with model validation.

Even though Su's model provided the best fit, future studies may prefer Tofts' model which provides more commonly unified parameters, possibly providing an easier biological interpretation (cf. consensus proposal by Tofts et al. [104]).

8.4. General methodological discussion

8.4.1. Theoretical differences in the two models

Several drawbacks concerning application of pharmacokinetic models have been addressed by different groups. The data obtained may not fit the model chosen. In addition, each model makes a number of assumptions that may not apply for every tissue or tumor type, to the type of contrast agent used, or to the actual MRI method applied [68]. Furthermore, the kinetics and physiological properties that may be extracted from the time course of tracer distribution depend upon an appropriate theoretical model and the related assumptions used to interpret data. The two models which were applied in this thesis (i.e. the Su-model and the Tofts-model) will be theoretically discussed here.

As described in Section 5.2, one difference between the Su model and the Tofts model lie in the mathematical formula determining the **generalized plasma concentration-time curve.** In contrast to Tofts et al., Su et al. assume plasma concentration to consist of two parts; first a linear increase to a maximum concentration and second a subsequent bi-exponential decay (cf. Figure 5.6). This linearity of plasma concentration during time t_0 may be a reasonable approximation since we are interested in tracer behavior on a much longer time scale ($\sim$ 30 min) than the brief period after the bolus injection ($\sim$ 30 s), needed for plasma concentration to peak. As already mentioned, the divided modeled plasma curve in Su's model may explain the better fit to maximum tissue tracer concentration compared to Tofts's model.

Secondly, Tofts model assumes **isodirectional flux.** This implies that diffusion is the major mechanism for transvascular transport of tracer. Contrary to Tofts model, Su et al. allow two **different transport constants** between the compartments and thus employ the possibility of convection as a transport mechanism. As described in Section 2.3, the exact

mechanisms for increased extravasation of tracer in tumor tissue remain unclear. However, both Gadomer-17 and Gd-DTPA are suggested to have diffusion as major mechanism of transport [43, 97, 96]. Thus, isodirectional transport may be a reasonable simplification for dynamic studies using Gadomer-17.

Finally, the Su model includes **intravascular signal contribution** and thus estimation of vascular volume fraction. Whether Tofts model, neglecting intravascular contribution and the possibility of two different transport rates, is too simple or not, is a returning, but yet not answered, question. Some have claimed the neglect of intravascular contribution to be incorrect and to cause false high levels of permeability (K^{trans}), especially when using a macromolecular tracer [41]. As one voxel generally contains both vasculature and tissue, perfused volume of these vessels may be an important factor governing the estimated parameters. Physiological specificity may be increased by including a plasma volume term (v_pC_p) as originally done by Su et al. [94], where contributions from blood vessels and extravascular components to the contrast uptake rate are separated (assuming a general arterial input function, AIF or$C(t)$). Tofts et al. [102] argue that neglecting vascular volume fraction contribution apply if perfusion is low, as in MS-lesions. Further, Su et al. claim that K_1 and K_2 can not be assumed equal in tumor tissue. Only in healthy tissues where vessels are non-leaky and diffusion is the main mechanism for tracer transport, it can be assumed that the transport rate for influx and efflux of tracer are equal [94]. Macromolecular agents have a smaller distribution volume than do low-molecular agents. Neglecting intravascular tracer might thus be less accurate using Gadomer-17 as a tracer rather than Gd-DTPA. Modifications of the Tofts's model to specifically include the intravascular signal contribution, and thus reduces errors due to false elevated K^{trans} have been proposed [10, 104]. Others have suggested that neglecting of vascular volume contribution (and permeability-limitation) is reasonable for many healthy tissues including fat and muscle, but probably not for pathological tissues [70].

The permeability-limitation ($F \gg PS$) assumed in both models, implies that perfusion must be high enough to replenish the amount of tracer leaking out of the microvasculature (i.e. local blood concentration is prevented from depletion). Although this assumption may not be satisfied for Gd-DTPA because of high leakage [94], Gadomer-17 most likely fulfill this requirement [109]. In malignant tumor tissues, K^{trans} is suggested to reflect a combination of permeability-surface area product and tissue perfusion (although vessels in general are more permeable than in normal tissues) because flow and permeability are highly heterogenous throughout the tumor. In healthy brain tissues however, with a tight blood-brain barrier and high perfusion, the rate at which contrast agents extravasate is limited by vessel permeability [28, 69].

Glioblastomas, are among the most vascularized solid tumors in humans [56]. It therefore likely to believe that viable tumor areas fulfill the requirement of permeability-limitation using Gadomer-17 as tracer. On the other hand, central areas of rapidly growing tumors commonly display inadequate blood flow due to reduced local perfusion pressure, resulting

from a combination of inadequate (angiogenic) vascularization and increased interstitial tumor pressure [49]. One can thus question whether these central areas of tumor fulfill requirements regarding sufficient flow. If blood flow is compromised, accumulation of tracer in the tissue would be flow-dependent and neither of the models would provide a good estimate of permeability (which may be the case in tumor central areas).

High permeability to Gd-DTPA has been observed in both normal vessels and tumor vessels [46]. Differentiation between malignant and benign tumors is therefore problematic. The selective hyperpermeability to macromolecules (in microvessels of cancers) does not extend to smaller molecular probes (less than 1 kDa) with exception of the brain [7]. As assessed by Verhoye [109], the diffusive transvascular transport of high-molecular contrast agents is slower than for low molecular weight agents, and may therefore be rate limiting in tracer-uptake (i.e. *permeability-limited*) rather than in blood perfusion. Higher molecular weight agents, such as Gadomer-17 would provide the most reliable measure of permeability as their transport is more likely to be permeability-limited than transvascular transport of low molecular contrast media.

The time varying plasma concentration is an important factor determining the contrast agent behavior in tissue and is determined mainly by four factors; dose, injection time, normal distribution within body and clearance from body [94]. Both the Tofts model and the Su model assume a time varying description of the blood concentration of contrast agent ($C_p(t)$, regarded as the arterial input function, AIF) generalized for all subjects in a study. As mentioned above, $C_p(t)$, or AIF, is assumed different in the two models. Rijpkema et al. [75] suggested that some kind of normalization concerning the AIF should be applied in order to minimize variations among patients and different measurements caused by variable systemic blood supply. This could be achieved by using signal enhancement of healthy tissue (e.g. in liver) as a reference, or by measuring concentration-time curves of the contrast agent in a feeding vessel within the imaging volume. The latter method would provide a more direct reference of the individual time course of tracer concentration in blood. However, both approaches involves additional time-consuming concerns.

Assuming a standardized blood curve, individual characteristics of capillary architecture and transit time have been neglected in the presented analysis.

8.4.2. Conversion to CA concentration

Both models depend on estimated contrast concentration. Conversion from signals, measured by dynamic MRI, assumes (i) an increase in T_1-relaxation rate which is proportional to tissue tracer concentration and (ii) a constant relaxivity Different studies solve these problems by assuming that their protocol (i.e. sequence, CA-dose) maintain the required proportionality [68]. Also, some works assume linearity between contrast agent dose and signal intensity [79], thus avoiding measurements of inherent (pre-contrast) tissue T_1-

relaxation times. The ability to measure R_{10} (i.e. $1/T_1$) in each individual subject (in each voxel within ROI) is important since the native T_1 vary widely. As is typical in DCE-MRI studies, methodological variations exists regarding measurement of the native T_1 and thus estimation of changes in contrast agent concentration transformed from signal intensity data. The accuracy of various methods to obtain T_1 maps differs [42]. Anyhow, although there may be methodological weaknesses in e.g. the T_1 estimation, this would be consistent between examinations being compared in a study.

Furthermore, the relation between the MRI measured signal intensity data and contrast concentration assumes that CA exerts minimal effect on tissue T_2 times. This has been proven true for doses below 0.2 mmol/kg [78].

Assuming a constant relaxivity, implies that contrast agent relaxation is a constant at the given field strength and temperature and is independent of tissue environment. However, in a study by Stanisz and Henkelman [91], it was found that GD-DTPA relaxivity depends on the environmental macromolecular content in the tissue.

In addition, conversion from signal intensity to concentration requires a fast water exchange. Both models assumes fast water exchange between intra- and extracellular space so that whole blood relaxes with one single T_1 value[5]. According to Donahue et al. [21] this is true for low contrast agent concentrations. The approximation is supported by the fact that the exchange between e.g. red blood cells and plasma (ms) is significantly faster than the relaxations times (s). An adequate model for brain tissues employ slow exchange between vascular and extravascular compartments and fast cellular water exchange [54].

8.4.3. Concluding remarks on the model assumptions

When analyzing DCE-MRI data by pharmacokinetic modeling one has to be aware of the assumptions that are made in the chosen model. Physiological interpretation of parameters estimated by such models may not always be trivial. As an example is the constant K^{trans} (Tofts model) not dependent on permeability alone, but may also be affected by other physiological parameters [75]. The Tofts model is simple, but provides complex parameters. K^{trans} express the features of blood flow, blood volume, endothelial permeability and endothelial surface area, but the specific contribution of each cannot be identified [41].

Despite the complexity lying in the parameters, pharmacokinetic analyses are theoretically attractive since they provide information connected to the underlying physiology of the tissues [42]. However, these complicated models are prone to errors that can compromise reproducibility. A simple strategy to solve these problems would be to derive parameters

[5]Even though contrast agents are excluded from certain compartments, they may affect water magnetization (i.e. relaxation times) in non-contrast compartments (i.e. cells) if water molecules move between compartments [21].

directly from the signal intensity curves, as usually done in clinical examinations (semi-quantitative analysis, cf. Section 5.1). However, such metrics extracted directly from intensity data hold the drawback of being sensitive to MRI scanning methods, so scanning procedure must be designed to minimize variations due to scanning and scaling parameters when utilizing semi-quantitative parameters [42]. However, Knopp et al [49] confirmed that the intensity of contrast enhancement in a lesion, which is often used as a clinical diagnostic tool, is not the best measure to differentiate malignant and benign lesions. Instead, the pharmacokinetic exchange rate (K^{trans}) showed significant differences between benign and malignant breast tumors. In addition, K^{trans} were mentioned as the quantitative parameter that most closely correlates with VEGF expression. In tumors without elevated expression of VEGF, a correlation between the parameter and microvessel density (MVD count) was detected.

Even though semi-quantitative methods have been proven clinically valuable, model based quantification methods are required to get a closer understanding concerning the micro-physiological basis of the enhancement curves.

Although one (or more) model assumptions is not valid, it can still be possible to directly compare parameters acquired serially in a given subject, and in different subjects examined at the same or different scanning sites. Such parameter comparison however, requires that the contrast agent concentration can be measured accurately, and that the type, volume and method of administration are consistent [68].

Regarding parameter assumptions in healthy tissues, Galbraith et al. [28] found when comparing Tofts parameters from tumors with parameters from muscle tissues (ROI analysis), that the mean values of all parameters were lower for muscle than for tumor. The study also demonstrated a slightly worse reproducibility for muscle than for tumors. Padhani et al. [70] estimated DCE-MRI parameters in normal pelvic tissues and found that fatty tissues and the femoral head were unreliable tissues from which to obtain kinetic parameter estimates because of their poor enhancement. Findings from normal tissues in this study may be consistent with the conclusion made by Padhani et al. Concentration data obtained from healthy tissues, were spread (and of low magnitude). The models adjustment to these data could therefore not be evaluated by visual inspection alone.

8.4.4. Concluding remarks on Gadomer-17 as "permeability-tracer"

Traditionally, the low molecular Gd-DTPA (<1 kDa) is used in DCE-MRI permeability assays. However, although Gd-DTPA provide the ability to differentiate permeable tumor vessels from normal vessels, only poor discrimination between tumors of different grades have been shown [95]. Additional differentiation have been seen using Albumin-GD-DTPA,

but biological concerns such as protein poisoning limits use of this agent in clinical scanning [96]. The novel contrast agent Gadomer-17 (30–35 kDa), chosen as tracer to assess microvascular characteristics in the "NG-2 project", can be cleared quickly via the kidneys, and have a high tolerance dose.

As they are more likely to possess a permeability-limited transport, macromolecular contrast media are suggested to reveal vascular properties (e.g. permeability) more accurately [7, 114, 98]. Moreover, permeability assessment using macromolecular contrast agents are shown to correlate with histological tumor grade [17]. Specifically, Gadomer-17 have been shown to detect changes in response to therapy at an earlier stage and with greater sensitivity than Gd-DTPA [97].

As stated by Verhoye [109], the choice of pharmacokinetic model for assessing Gadomer-17 uptake in tumor is not obvious due to the intermediate size of this agent. But its uptake in tissue is more likely to be diffusion (permeability) limited rather than flow-limited compared to Gd-DTPA. Although, determination of permeability limited perfusion requires a tracer which leak through capillaries at a rate slower than its flow [5], flow-limited situations, in which K^{trans} represents flow, are commonly found in parts of the tumor (e.g. in central necrosis). Neglecting the intravascular tracer concentration, as was done in Tofts' model, produces larger errors when using Gadomer-17 because this agent have a smaller distribution volume than Gd-DTPA.

While some studies (using low molecular agents) have shown correlation between tumor enhancement and microvessel density (cf. Section 1.1), others revealed no correlation [8, 17]. Furthermore, permeability (as estimated by DCE-MRI) is found to depend on VEGF expression (in addition to MVD counts) [49]. Although optimistic results regarding Gadomer-17 as a tracer (cf. Section 8.4.4), mediomolecular agents (i.e. 15–30 kDa) have been reported to show poor correlation with histological tumor grade [6]. Thus more studies are urged to provide an established DEC-MRI technique (concerning scanning method, contrast agent and PK-model) by which validation depends upon established surrogates of angiogenesis (i.e. MVD count and VEGF expression).

8.5. Conclusions

In this study it is demonstrated that variability in DCE-MRI outcome (i.e. physiological parameters) is partly caused by manual, subjective tracings of ROIs. Moreover, the macromolecular contrast agent Gadomer-17, used in the dynamic series (for which the pharmacokinetic models were fitted), seemed better suitable as "template" information for ROI delineations compared to post Gd-DTPA images. Smaller ROIs demonstrated spatial variations which may be related to the extremely heterogenous nature of tumors. Estimated parameter values were associated with tissue type and varied between different

tissue regions. There were also some tight correlations between parameters of the two models being tested. Furthermore, healthy tissue regions were characterized by very low (and relatively highly dispersed) contrast concentration during the dynamic scans. This latter finding might indicate that the pharmacokinetic models were less applicable to normal tissue compared to tumor tissue using Gadomer-17 as a tracer.

Pixel-wise analysis with resulting parametric maps and histograms, at fifth and seventh week post-implantation, demonstrated parameter changes, presumably reflecting microcirculatory changes (e.g. angiogenesis, leakage, compromised capillary flow). Finally, the Su model seemed to provide a better (numerical) fit to the calculated concentration curves in tumor regions than the Tofts model did.

The findings in this study (and other recent studies, e.g. [14, 65, 68, 71]) support the need for more standardized methods regarding imaging protocol (including T1-estimation and determination of contrast agent kinetics in blood), contrast agent type, contrast agent injection procedure and data analysis in the assessment of tumors using DCE-MRI.

Using several methods for presentation of data will provide more conclusive results when assessing tumor microcirculation from DCE-MRI measurements. However, further studies are needed in order to validate DCE-MRI findings using these post-processing tools. Only those methods (of MRI procedures and data presentation) that are shown to correlate with accepted surrogates of angiogenesis (e.g. VEGF expression and MVD counts) should be selected for clinical use.

A. The cardiovascular system

The heart and the blood vessels form the cardiovascular system which continuously provides fast transport of oxygen, nutrients, waste products and heat trough the body. As the heart pumps, oxygenated blood flows trough the aorta which progressively branch to form arteries —and later even narrower vessels, arterioles. The arterioles branch extensively to form the dense network of capillaries in tissues and organs. Capillaries reunite to form venules and veins leading back to the heart and pulmonary circulation to be re-oxygenated.

The general function of the circulation is to serve the metabolic needs of the tissue in order to ensure that the cells can perform their physiological tasks. The site of nutrient delivery to cells is across the thin walls of the capillaries, where also exchange between plasma and interstitial fluids takes place. These small exchange vessels constitute the major functional parts of the cardiovascular system, governing both volume of each compartment and the nutrient requirements of the cells [52].

A.1. Physiology of cerebral Circulation

Brain tissue has a high metabolic rate, extracts a large amount of oxygen from blood and has a limited ability to use anaerobic glycolysis for metabolism compared to other organs [74]. Thus, brain tissue is sensitive to alterations of blood flow, and the main task of the cerebral circulation is to maintain a constant delivery of oxygen and glucose to the brain.

The low capability of anaerobic metabolism is caused by the fact that neurons have high energy requirements due to transport of ions across their membrane[1]. Secondly, neurons only have a slight store of glycogen and oxygen within the tissue. The human brain is therefore extremely sensitive to lack of oxygen. A man will become unconscious after a few seconds of cerebral hypoxia, while minutes of oxygen deficit can cause irreversible cell damage and cell death.

Cerebral oxygen consumption in the brain accounts for about 20% of the total oxygen consumption in a normal resting human. The brain receives 14-15% of the resting cardiac output (5–7 liters/min in adults) although brain mass accounts for only about 2% of the total body mass. About 40% of the human brain consists of grey matter with mainly neuronal cell bodies. Grey matter receives a large amount of blood per unit time, about ten times the average for the whole body. White matter, which consist primarily of myelinated processes of neurons, is also well perfused, although less than grey matter.

[1]The high metabolic rate in neuronal cells is caused by continuous pumping of ions across their membrane in order to conduct signals [33].

Blood Supply

The brain is supplied with blood mainly by the internal carotid arteries and the vertebral arteries, the latter forming the basilar artery. The posterior and anterior circuits of cerebral circulation are interconnected by communicating arteries forming the circle of Willis [25]. The circle of Willis provides a safety factor by ensuring blood supply to the whole brain even if one of the main supplying arteries should become occluded.

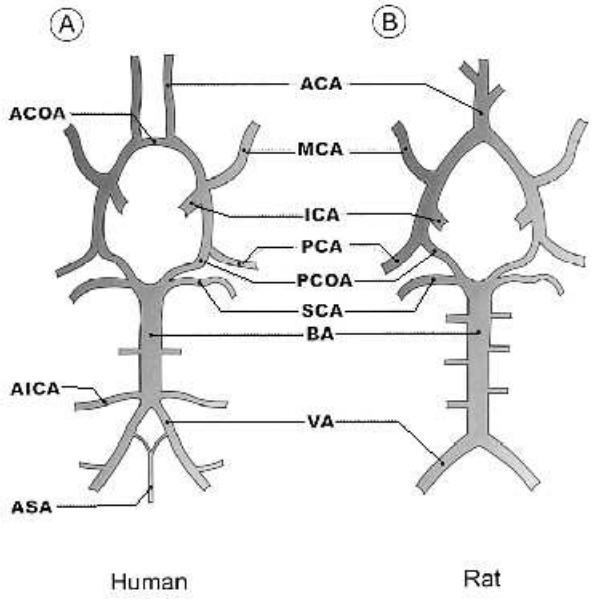

Figure A.1.: The circle of Willis supplies the brain with blood. From Farkas and Luiten, 2001 [25]. Anatomy of vessels in Willis circle in human (A) and rat (B) cerebral circulation. Abbreviations: ACA, anterior cerebral artery; ACOA, anterior communication artery; AICA, anterior inferior cerebellar artery; ASA, anterior spinal artery; BA, basilar artery; ICA, internal carotid artery; MCA, middle cerebral artery; PCA, posterior cerebral artery; PCOA, posterior communicating artery; SCA, superior cerebellar artery; VA, vertebral artery.

As described by Farkas & Luiten, 2001 [25], the finest branches of the vascular tree, the brain capillaries, form anastomoses and create a dense tree-dimensional vascular network. While arteries regulate blood pressure, the function of the brain capillaries is to maintain the blood-brain barrier (BBB) and sustain continuous exchange of nutrients, electrolytes and waste products between blood and neural tissue. The capillary bed has larger surface-exchange area than all other parts of the circulation, due to the extensive branching into a large number of thin vessels.

The dense capillary network provides large exchange area and minimizes the diffusion distance to ensure efficient transport of substances between blood and tissues. In general, grey matter has nearly three times higher density of capillaries than white matter [52]. Moreover, differences in density correlates with the energy demand and activity of a particular brain region. Sensory association centers are more heavily vascularized than motor centers, showing that capillary density is higher in metabolically active brain region [25]. Many mental and cognitive tasks are executed in well defined brain areas. Neuronal activity in a brain region raises the metabolic rate in the area. Cerebral circulation must therefore be capable of making regional adjustments of blood flow [52]. Berne & Levy, 1998 [4] stated that total cerebral blood

flow is constant, but that regional cortical blood flow is associated with regional neural activity.

Flow through a blood vessel is described as the quantity of blood that passes a given point in the vessel in a given period. Major determinators of blood flow is the pressure difference (or gradient) between the two ends of the vessel, and the vascular resistance to flow which occurs as a result of friction against the inside vessel wall [33]. Cerebral blood flow is tightly controlled by both systemic and local mechanisms. While vasoconstriction[2] mediated by autonomic fibers exerts a rough modulation, finer tuning of regional blood flow involves local (i.e. myogenic and metabolic) mechanisms.

A.2. Transendothelial transport

Transcapillary fluid balance aims to maintain constant fluid volume in the tissue interstitium, and thereby prevents edema. Balance is determined by three important factors:

1. The properties of the capillary membrane
2. The transcapillary hydrostatic pressure
3. The transcapillary colloid osmotic pressure

The relationship between these factors was first described by Ernest H. Starling (1896), and the factors are often referred to as Starling forces [52].

The transcapillary fluid flux (i.e. the net capillary fluid filtration, J_v) can be described quantitatively by following equation ("Starling hypothesis"):

$$J_v = K_f[(P_c - P_i) - \sigma(COP_c - COP_i)] = K_f \times \Delta P \tag{A.1}$$

where P_c and P_i are the hydrostatic pressures in capillary and interstitium, respectively. π_c and π_i are the corresponding colloid osmotic pressures in capillary and interstitium. σ is the reflection coefficient for proteins[3]. K_f[4] denotes the capillary filtration coefficient which includes the surface area (S) and the hydraulic conductivity ("water permeability", L_p). The net capillary filtration pressure (ΔP) is the pressure created from the imbalance between hydrostatic and osmotic pressures Thus the transcapillary fluid flux (J_v) can be determined by the product of capillary hydraulic conductivity and the net filtration pressure across the capillary wall [73, 113].

Material is rapidly transported *over large distances* by means of convection ("wash along") as the heart causes a stream of blood flowing through the vessels. The rapid transportation of molecules through the vasculature is governed by the vascular morphology and the blood flow rate; the first being influenced by the number, length, diameter, and geometric arrangement of various blood vessels [52]. Transport of material *across the vessel wall*, on the other hand, is mainly governed by diffusion. However, there is a minor contribution to transvascular transport of material from convection as well.

The intra- and extravascular exchange of fluid and solute molecules in a tissue is thus determined by two mechanisms; diffusion and convection[5] [52, 95].

[2] Vasoconstriction is provided by contraction of vascular smooth muscle cells (VSMC).
[3] $\sigma = 1$ for impermeable vessels, $\sigma = 0$ for freely permeable vessels.
[4] The capillary filtration coefficient, representing hydraulic conductivity, is denoted K_f by Wiig et al. [113]
[5] Convection, or wash along/solvent drag refers to mass movement of fluid [84].

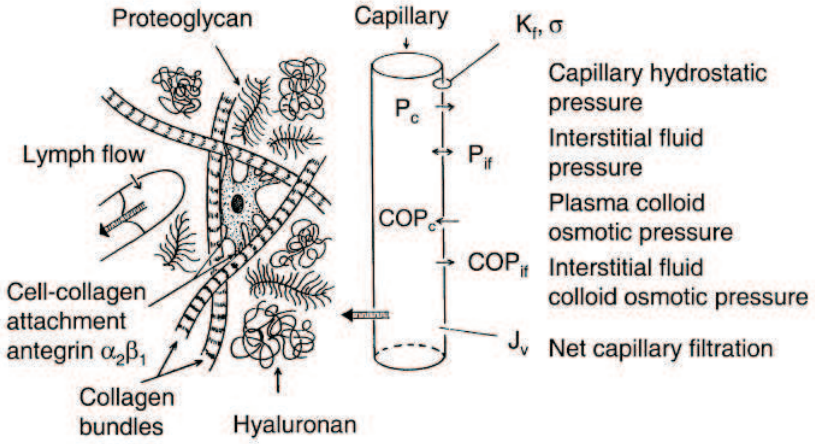

Figure A.2.: Transendothelial transport and fluid balance; the transcapillary-interstitial fluid exchange system as overviewed by Wiig et al [113]. The transcapillary hydrostatic (P) and colloid osmotic pressure (here: COP), in capillary and interstitium, determine capillary fluid flux. K_f and σ are capillary hydraulic conductivity and capillary reflection coefficient, respectively. Capillary net filtration pressure results in a net fluid filtration (J_v) which is removed by lymph flow. Collagen and hyaluronan are components of loose connective tissue.

In addition to the transluminal concentration- and pressure gradients (Starling forces, refer Eq. A.1) and the surface area available for exchange, three important parameters are responsible for the *transport of molecules* across the vessel wall;

1. vascular permeability (related to diffusion),
2. hydraulic conductivity (related to hydrostatic convection (J_v)), and
3. the reflection coefficient (related to osmotic convection).

These transport parameters depend on the number and width of endothelial junctions and trans-membrane channels of the vessel wall for a given size of molecule [95].

To summarize, the majority of solutes transported from blood to tissue is transferred by simple diffusion. Only a minor amount of solutes follow by bulk flow of fluid (solvent drag) [74]. The convection process can, however, be important for macromolecule transendothelial transport [52].

Diffusion

The rate of diffusion is described by Fickt's law, first presented in 1855t [52]:

$$J_s = -DS\frac{\Delta C}{\Delta x} \tag{A.2}$$

The mass of solute transported by diffusion per unit time (J_s), depends on the transluminal concentration difference (ΔC) and the diffusion distance (Δx). The ratio of these is referred to as the concentration gradient. In addition, diffusion rate depends on the surface area (S) and the diffusion coefficient (D). The

negative sign implies that diffusion is a "downhill" process along the concentration gradient. D represents the intrinsic velocity of the molecule and depends on temperature, viscosity and molecular size. For most solutes, D is inversely proportional to the cube root of the molecular weight [52]. Thus small molecules have higher diffusion velocity than does larger molecules.

Hydraulic conductivity

As mentioned, *fluid movement* across the vessel wall, depends on pressure gradients created by the heart and the hydraulic conductivity ("water permeability") of the membrane. The hydraulic conductivity is defined as the filtration rate (J_v), and depends on the porosity of the membrane.

Convection

Solute movement by convection depends on both the filtration rate (hydraulic conductivity) and on the reflection coefficient (osmotic conductivity). The reflection coefficient (σ) of a molecule refers to the selectivity and pore sizes of the membrane. If a solute diffuses through the membrane as freely as water, then (σ) equals 0. A molecule which have a (σ) of 1, is totally reflected by the pores and do not pass across the membrane. Plasma proteins usually have a (σ) value of 0.9 [74, 52]. The protein permeability ($\sigma < 1$) can be increased, for example in case of Histamine release, or in angiogenic vessels.

A.3. Features of the blood-brain barrier

The blood-brain barrier (BBB) is a specialization of the walls of brain capillaries which selectively isolates the extracellular space of brain tissue from the blood. Building blocks that execute BBB function include; endothelial cells, irregularly occuring pericytes and astrocytic end feet attached to the outside vessel wall. The endothelial cells form the inner layer around the capillary lumen. They are closely connected by tight junctions [25]. By means of tight junctions, specific transport proteins, absence of fenestrations and almost no transport via pinocyte vesicles, BBB vessel walls perform fine and ready control of the extracellular environment in the brain. The brain capillary endothelial forming blood-brain barrier possesses special characteristics. Additionally to tight junctions of extremely low permeability, these endothelial cells have low rates of fluid phase endocytosis and specific transport- and carrier molecules. Another feature of the endothelial cells is the high number of mitochondria which provide energy for the specific transporters of the blood brain barrier.

Figure A.3 illustrates the composition of a capillary wall. The extremely tight junctions effectively seal the paracellular transport pathway. While the inner side of the endothelial cells creates the vessel lumen, the outer side is surrounded by a basement membrane consistent of a tri-laminar extracellular matrix of collagen and proteins. The elements are produced by the cerebral capillary endothelial cells [25]. The basement membrane on the abluminal surface splits in places to enclose pericytes, which have contractile and phagocytotic properties. The outer portion of the basement membrane may be further expanded beyond the pericytes, especially in capillaries. This expansion forms a collagen-filled space containing "perivascular cells" and microglia (CNS macrophages) [1]. Astrocytic end feet are in close relation to the endothelial cells and perivascular cells by surrounding the basement membrane.

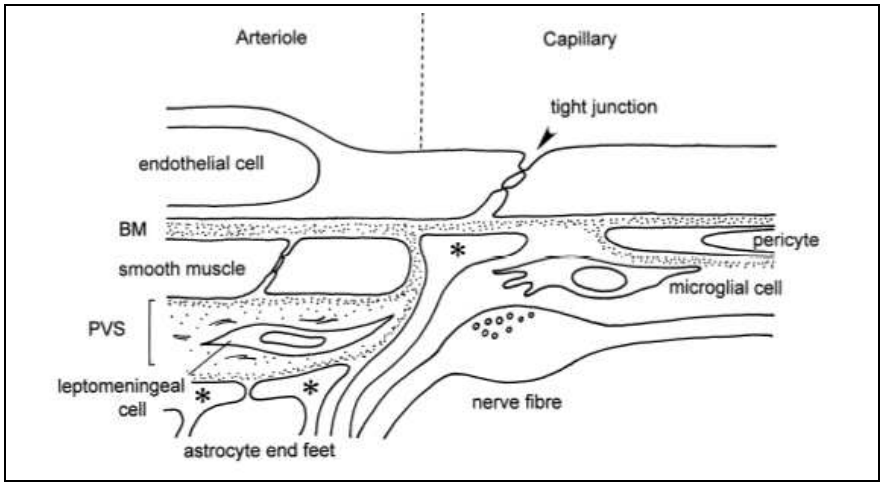

Figure A.3.: Cells in the microvessel wall (from Abbott et al. [1]). Cerebral arteriolar (left) and capillary (right) walls are formed by different cell types. The capillary blood-brain barrier is formed by the endothelial cells.

Gloor et al. [31] define BBB function as restriction of the non-specific flux of ions, proteins and other substances into the central nervous-system environment. The unique features of the blood-brain barrier serve to maintain homeostasis in the CNS by protecting the nervous environment from the harmful compositional fluctations occuring in the blood, and allow selective uptake of essential substances. Fluctations of a certain substance in the blood will therefore not be reflected in the extracellular brain tissue. This is important because the membrane potential of the nerve cells is sensitive to extracellular alterations of ionic composition (e.g. a raise in extracellular potassium will cause depolarization). Disruption or breakdown of the BBB is associated with a number of CNS disorder such as tumors, infarction or inflammation [31].

Injury to the brain, whether it is caused by disease, tumors, direct trauma, inflammatory substances or chemical toxins, which cause breakdown of the BBB, will allow free diffusion of large molecules and other blood components, such as toxic compounds and potassium, into the nervous tissue [87].

Routes across the brain endothelium

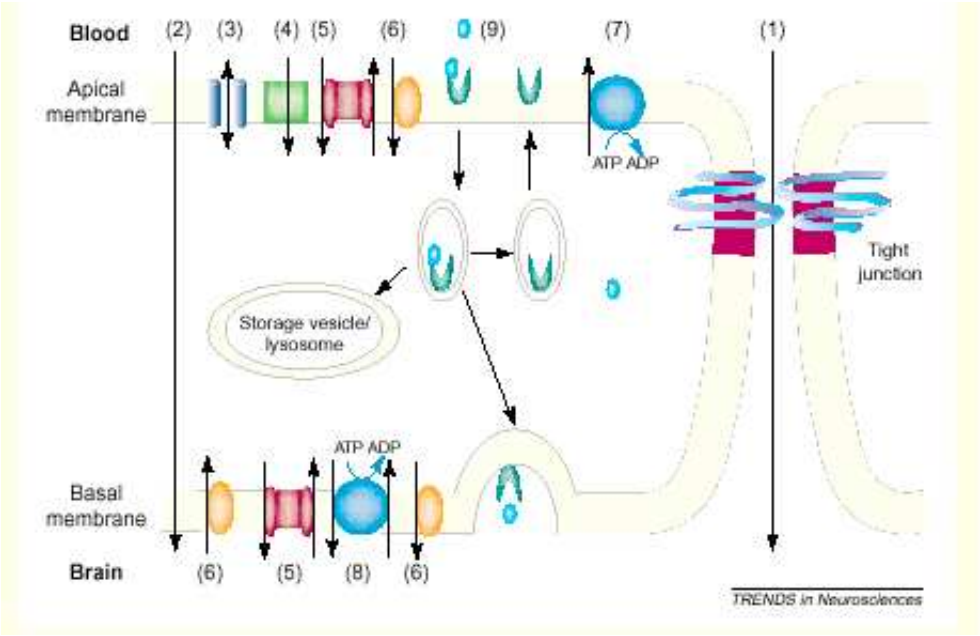

Figure A.4.: Routes across the blood-brain barrier (from Huber et al. [40]). Transport mechanisms and structures which provide BBB function; (1) paracellular diffusion, (2) trans-cellular diffusion, (3) cation channels, (4) ion symports, (5) ion antiports, (6) facilitated diffusion active transport, (7) active transport, (8) active antiport transport and (9) endocytosis (mediated by receptors).

Figure A.4 illustrates different pathways through the blood-brain barrier. Because of the tight junctions between adjacent endothelial cells, the paracellular pathway is impermeable to solutes. Even transport of ions and water is restricted. Only small lipophilic solutes (less than 600 Da), as well as gases such as oxygen and carbon dioxide, can generally pass through the BBB by passive diffusion. Nutrients are selectively transported into the brain via different surface transporters in the BBB (e.g. the insulin-independent GLUT-1 transporter provides transport of glucose across the BBB). BBB possesses only a small amount of pinocytic vesicles. Endocytosis is however important in transportation of e.g. some hormones [40].

Recent studies indicates that the tight junctions of the BBB have a dynamic structure which can be temporarily altered during pathological states. Modulation of the cytoarchitecture provides BBB protection of the CNS environment despite illness. A total disruption, or breakdown, of the blood brain barrier can, however, occur during extreme conditions or prolonged pathological states [40]. Generally tumor microvessels are unusually leaky to macromolecules. The structural basis of this leakiness remains unclear, but suggested possibilities will be discussed in section 2.3.

B. MRI contrast agents and tracer kinetics

Although inherent contrast in MR imaging is considered to be greater than in all other imaging modalities, some diagnostic questions require application of exogenous contrast agents (CA) [76]. Rinck [77] summarized the goals of MRI contrast agents as following:

- Improvement of tissue contrast, tissue characterization and overall sensitivity and specificity. These factors cause improvement of diagnosis and therapy.
- Monitoring of function, using functional imaging techniques (FMRI)
- Reduction of artifacts, imaging time and overall costs.

An important feature of MRI contrast agents compared to contrast agents used for other modalities, is that the agent itself is not visualized in MRI. Rather, the agents effect on the spinning protons behavior is detected. The agents used in MRI are therefore referred to as indirect contrast agents [86].

Changes in MRI signal-intensity depend on the effect that the contrast agents exert upon the magnetization of the water molecules in tissues. Contrast agents affect water magnetization, or proton spins, in two different ways; either by *direct relaxivity (T_1) effects* or by *indirect susceptibility (T_2) effects*. Although most agents exert both relaxivity and susceptibility effects, one effect usually dominates. Which effect dominates depend on contrast agent concentration, imaging technique and tissue distribution properties [21].

Generally, MRI contrast agents can also be classified from the compartments in which they are distributed: (1) intravascular ("blood-pool") agents, (2) intravascular, EES agents and (3) intravascular, EES, intracellular agents. All MRI agents clinically approved for humane use at present time, belong to the second class due to small molecular weights. Today, DCE-MRI is thus clinically performed using "class 2" agents which distribute in both intravascular space and extravascular extracellular space (EES). Macromolecular (weighted) agents which retain in the intravascular space for a prolonged time have been proven more effective in DCE-MRI [17]. However, such agents currently still remain at a pre-clinical stage [18].

B.1. Gadolinium Chelates

Clinically, paramagnetic contrast agents are the most frequently used in MR imaging. Most common is the lanthanide metal *Gadolinium (Gd^{3+})* chelated with a ligand to minimize its inherent toxicity. Diethylenetraminepentaacetic acid (DTPA) is such a compound. The complex of Gd-DTPA was the first

MR contrast agent approved for in clinical use. Gd-DTPA form a stable, low molecular water-soluble contrast agent, mainly excreted by the kidneys. The different contrast agents clinically approved for are Gadolinium chelated with derivates of either acyclic DTPA or the macrocyclic ligand DOTA [83, 116].

Positive (paramagnetic) MRI agents, such as Gd-DTPA, primarily shorten T_1-relaxation times and thereby *increase signal intensity on T_1-weighted images*, while negative (super-paramagnetic) agents decrease T_2-relaxation time and hence create a signal loss on T_2-weighted images in tissues in which the agent is accumulated [64, 77]. Due to seven unpaired 4f sub-orbital electrons, each Gadolinium molecule injected, creates a large dipole moment compared to that possessed by the proton [88]. In T_1-weighted images, a shorter T_1-relaxation time produces a stronger signal because a *larger population of protons relax in a given period of time*. Such concentration-dependent signal enhancement is favorable when imaging regions with little inherent contrast, or imaging deep regions that normally is shielded by the periphery (which causes decreased SNR) [83].

The effects the contrast agents exerts on tissue T_1- and T_2-relaxation times are actually similar, but since T_1 is much higher than T_2[1], the predominant effect at low doses (0.1–0.2 mmol/kg) is shorter T_1 and thus brighter area of interest in T_1-weighted images [76]. T_1 shortening caused by presence of CA is commonly referred to as the R1 effect.

As described, MRI contrast agents have two ways of action to increase contrast between tissues; direct relaxation effects and / or indirect susceptibility effects. At higher doses (above 0.2 mmol/kg), gadolinium chelates execute susceptibility effects. *Magnetic susceptibility* is described as the ability of a substance to become magnetized when influenced by an external magnetic field [77, 111]. This functional property of matter produces shortening of T_2 and T_2* times (R2 effect of the contrast agent). The R2 effect represents a loss of phase coherence of transverse magnetization resulting in a signal loss in areas in which the agent has accumulated. This R2 effect, created by the production of magnetic field gradients between the lumen of a vessel and the surrounding tissue, provides the basis for bolus contrast (T2-weighted) perfusion imaging [76].

Additionally to Gadolinium, other exogenous agents suited for perfusion imaging include dysprosium, macromolecular agents (e.g. Gd bound to albumin), superparamagnetic nanoparticles (e.g. iron oxide particles) and microbubbels. At present these are still under clinical trials, and not yet approved for clinical use. However, a formulation of iron oxide particles is available, but not approved for bolus use [88].

Pharmacokinetics of Gd-based agents

The pharmacokinetics and toxicity of paramagnetic contrast agents depend on their ligand (i.e. chelating agent). Free gadolinium has a biologic half live of several weeks and is excreted mainly through the kidneys and the liver. Chelation with e.g. DTPA alters the biodistribution and pharmacokinetic properties of the compound. A Gadolinium-complex will after chelation, exhibit an 500-fold increase in the rate of renal excretion [85].

In Norway, following Gadolinium-chelates are clinically validated for intravenous injection (per August, 2002): Even though these agents (cf. Table B.1 and B.2) have different chelating ligands, they have remarkably similar mechanisms of actions, pharmacokinetics and rates of side effects when administered as 0.5 M solution intravenously at doses of 0.1 mmol/kg. They are all water-soluble and have low molecular

[1]The percentage decrease in T_1 relaxation rate is larger than the percentage decrease in T_2 relaxation rate.

Agent	Generic name	Trade name	Producer
Gd-DTPA	dimeglumingadopentat	Magnevist	Schering A. G.
Gd-DOTA	meglumingadoterat	Dotarem	Guerbet S. A.
Gd-DTPA-BMA	**gadodiamide**	**Omniscan**	**Amersham Health**
Gd-HP-DO3A	gadoteridol	ProHance	Bracco International
Gd-DO3A-butriol	gadobutrol	Gadovist	Schering AG

Table B.1.: Intravascular class 2 agents. Gadolinium-based extracellular fluid space (ECS) contrast agents approved for clinical use at present time (August, 2002). Table is modified from Myhr et al [64]).

Agent	Enhancement pattern	Shape	Ionisity	Osmolarity
Gd-DTPA	positive	linear	ionic	high
Gd-DOTA	positive	macrocyclic	ionic	high
Gd-DTPA-BMA	**positive**	**linear**	**non-ionic**	**low**
Gd-HP-DO3A	positive	macrocyclic	non-ionic	low
Gd-DO3A-butriol	positive	macrocyclic	non-ionic	low

Table B.2.: Properties of gadolinium-based ECS agents. Table is modified from Myhr et al [64]).

weight (about 500 Da). In addition they have quite similar physical size and relaxivity[2]. Notice, however that Gadovist is marketed as 1.0 M solution as opposed to the other agents which is 0.5 M solutes. As a consequence, Gadovist has about twice the Osmolarity of the 0.5 M non-ionic solutes. However, in general, ionic ("charged") agents possess higher osmolality compared to the non-ionic ("neutral") chelates [64]. The osmolality of the agents range from 630 (Gd-HP-DO3A) to 1950 (Gd-DTPA) mmmol/kg of water. Studies on rat models have revealed that agents with higher osmolality have higher incidence of necrosis, hemorrhage and edema as a result of extravasion of the agent. This is not proven in humans [85]. The osmotic load injected for MRI imaging is however very low compared to that in for example an computer tomography (CT) imaging procedure.

The gadolinium agents presented in Table B.1 are all non-specific They do not function as markers of specific cells. Hence they do not accumulate in, or influence only certain tissues or organs. Following intravenous injection, the agents distribute rapidly within the extracellular fluid space and is eliminated by glomerular filtration in the kidneys. Gadolinium chelates have an elimination half-life of approximately 1.5–2 hours [85]. The distribution half-life is estimated to be about four minutes. Thus, concentration of agent in blood is half reduced after only four minutes. This explains the requirement for instrumentation and methods to perform rapid imaging.

Dissociation of the chelated Gadolinium complex represents a concern related to toxicity because free Gadolinium is quite toxic. Copper and zinc, which are normally present in the blood in small amounts, have a competing affinity for the chelate and will cause some dissociation. However, the total concentration of released free Gadolinium is very low and is cleared rapidly by the kidneys. Thus, normal renal function prevents accumulation of free Gadolinium. In general, macrocyclic agents release less free Gadolinium than the linearly DTPA derivates. The difference however, is found to be insignifficiant [83].

An advantage of the DOTA derivates is lower viscosities at physiological temperature. Lower viscosity make the agents diffuse more rapidly and pass through the needle more quickly. A more rapid diffusion

[2]The relaxivity of an agent represents the agents ability to affect proton relaxivity and is defined as relaxation rate enhancement per unit concentration of the agent.

reduces the burning sensation due to osmolality when the solution enters the blood stream [83].

All Gadolinium-based ECS agents (except Gadovist) are produced with a solute concentration of 500 mM for intravenous use. Recommended dose is 0.1 mmol/kg – 0.2 mmol/kg. Increasing the dose above the recommended may have both beneficial and unwanted effects. Depending on the field strength it may facilitate detection of some diseases, such as small CNS lesions with minimal BBB disruption. In other pathological states however, an increased dose can cause loss of contrast because T_2 (susceptibility) effects can be dominating at high concentrations of contrast agents [77].

B.2. Side effects

The side effects of Gd based contrast agents are few, relatively minor and rare [83].

The different Gadolinium chelates appear to have remarkably similar safety profiles as well as effectiveness. The total incidence of adverse reactions of all types for each of the agent ranges from approximately 2–4%[3]. However, the majority of adverse events occur at an incidence of less than 1% [86].

The most common reactions to MRI contrast agents include general symptoms such as nausea, headaches, emesis and hives, and local injection site symptoms such as pain, warmth, local edema and burning sensation. Other ocationally observed reactions are vomiting, allergic reactions, vasodilation, dizziness, chills, syncope and metallic taste in the mouth.

Anafylactic reactions are reported to have an incidence of about 1:100 000–1:500 000 [86]. The possibility of getting a life threatening anafylactic reaction is higher for patients with a clinical history of asthma or other respiratory disorders. Delayed reactions have been reported, and it is therefore important that patient disponated of reactions are observed for a time after injection. Contrast injection to pregnant patients is not recommended unless the potential benefit outweighs the potential risk [82, 85].

The LD_{50} values[4] reported for MRI contrast agents are quite high and are set in a range between 9 and 15 mmol/kg for most of them.

Future agents

Extracellular agents such as Gd chelates given as bolus injection (i.e. with injection time below 60 seconds) attain high initial first pass concentration which decreases instantaneously after the end of the injection. The agent is diluted with the total blood volume, it leaks from the capillaries to the extracellular space in most tissues, and it is eliminated from the body by the kidneys. Thus, vascular imaging using extracellular agents is limited to investigation of the first pass kinetics through the tissues.

An important goal in contrast agent development is intravascular agents or blood pool agents. These

[3] In a study done by Nelson et al. in 1995, it was found that the rate of adverse reactions show an injection rate dependency. The rate of reactions was estimated to 2.2% in slow injections, while the rate increased to 2.9% with bolus injection [82].

[4] LD_{50} is defined as the dose of a drug that when administrated to test animals, results in acute death of half of the population [85].

agents remain in the vascular space for a prolonged time and their tissue uptake is limited (e.g. by their shape and size) so that they can selectively display blood vessels. Intravascular agents therefore have a wider imaging window. If needed, the examination can even be repeated [77].

Blood pool agents as an application to MRI will be advantageous in imaging areas such as perfusion, determination of blood volume, determination of capillary leakage and determination of lymph node metastasis after interstitial injection [60].

Ideal intravascular agents should, in addition to sufficient retention in the vascular space and fast elimination, have high r_1 relaxivity[5] to make T_1 as short as possible, and simultaneously low $r_2$relaxivity since a high T_2 relaxation rate would avoid spin dephasing effects [77].

Several approaches for intravascular agents have been proposed; (i) liposome encapsuled Gd-chelates, (ii) low-molecular paramagnetic chelates with strong affinity to plasma proteins and (iii) ultra-small superparamagnetic iron oxide particles. Another proposal presented is macromolecular compounds which due to their molecular size show no or only little extravasion; Gd labeled BSA, polylysine derivates, dextranes and dendrimers [60].

In addition to research to find the ideal contrast agent specific for the intravascular space, other organ- or tissue-specific contrast agents are developed. Some are already approved for clinical routine use, and other are still under trial. Three different liver specific contrast agent are currently approved for clinical use in Norway, one being paramagnetic positive, and two being superparamagnetic negative. The first is taken up in hepatocytic cells and enhance T_1 relaxation. Non-pathological liver tissue will thus show high intensity compared to pathological areas. The negative, liver-specific agents are superparamagnetic iron oxide particles. After intravenous injection, these nanoparticles will be taken up with phagocytosis in Kupffercells in liver, in spleen and in bone marrow. Normal tissues will show negative contrast i.e. low signal while pathological areas exhibit normal signal intensities [64].

Still, one of the ultimate goals in MRI contrast agent research is the development of pathology-seeking compounds which would actively target pathological sites such as tumors (e.g. antiangiogenic markers). Many new development of specific tumor targeting contrast agents are promising, but none have yet reached the clinical stage. As example, both gadolinium mesoporphyrin (Gd-MP) and manganese tetraphenylporphyrin (Mn-TPP) show non-specific tumor enhancement during early imaging phase and excellent enhancement of non-viable tumor parts in delayed imaging phase. Additionally, tumor-specific monoclonal antibodies labeled with gadolinium have been tested in animal trials. These enhance specific tumors and antibody sites after infarction and infectious diseases [77].

Dendrimers

As early as in the late 1970s, researchers took interest in synthesis of molecular compounds with long branches radiating from a central macromolecule. The success of this early research led to synthesis of dendrimers. A polyamidoamine (PAMAM) series of dendrimers was synthesized, and named starburst after star branched polymers and the Greek word dendra for tree. Today, the term dendrimers is used to describe highly branched spherical polymers. Two types of polymers are commercially available; polyamidoamine (PAMAM) and diaminobutane (DAB). The dendrimers (both PAMAM and DAB dendrimers) are highly soluble in aqueous solutions and have an unique surface covered by primary amino groups. These surface

[5] The r_1 relaxivity describes the ability of the contrast agent to affect the tissue T_1-relaxivity (cf. section 4.3).

amino groups make the dendrimers useful in binding large numbers of chelating agents to a single core [50, 51]. Dendrimers as MRI contrast agents (e.g. Gadomer-17) are not yet approved for clinical settings.

C. Functional MRI

A brief description of some of the methods which may be included in the term functional MR imaging (FMRI) is given in this chapter to introduce their general principles and their applications in imaging of the brain.

FMRI

Dynamic contrast enhanced MRI, as used in this thesis, is one of several MRI techniques which belongs to the group termed functional Magnetic Resonance Imaging (FMRI). Functional imaging using MRI has been a significant scientific discipline in the last decade [39]. The evolution of the method have been of large interest in different research fields such as neuro-science, physiology, psychology and psychiatry as it reveals different aspects of brain function. Functional brain MRI has been defined as following:

> *Functional MRI brain imaging is the application of MRI techniques to investigate cerebral physiology while preserving anatomic specificity [89].*

A number of different techniques and imaging parameters can be used in FMRI. The choice of which method to use is based upon the specific requirements for each experiment. FMRI based evaluation of physiological processes includes molecular mobility of water (diffusion), microvascular hemodynamics (tissue perfusion), brain activation (neuronal activity), and blood-brain barrier permeability [90].

Generally, cerebral FMRI is used to demonstrate brain function by visualizing changes in chemical composition of brain areas, or changes in the flow of fluids that occur in the brain. Because blood perfusion and energy metabolism in the brain is closely related to neural activity, FMRI can provide information about how the brain is working [57]. Until recently, information concerning brain functioning were limited to electrical recording methods or methods using radio nucleides, which all provides less spatial resolution than FMRI [3]. FMRI appears to have excellent spatial sensitivity compared to any other method for visualizing functional parameters such as PET, SPECT, EEG[1].

As in many other MRI methods, functional imaging has revealed critical dependence upon both signal-to-noise ratio (SNR) and contrast-to-noise ratio (CNR). The latter is, in MRI, associated with detection of differences in signal intensity and is thus closely connected to the problem of exact localization of signal origin, spatial resolution.

[1]PET = positron emission tomography, SPECT = single photon emission computed tomography, and EEG = electro enchephalogram.

The rapid development of FMRI techniques can in part be related to the accelerated development and improvement of instrumentation and techniques (imaging techniques as post-processing methods). Especially has the establishment of echo planar imaging (EPI) and other fast imaging techniques been of major impact since speed (temporal resolution) is a requirement for functional imaging. In FMRI, the experimental setup may be designed to "sacrifice" spatial resolution for the sake of temporal resolution [106].

BOLD-fMRI

The term *f*MRI most traditionally refers to the blood-oxygen-level-dependent (BOLD)-fMRI method, which over the past few years has become one of the major experimental tools for analyzing cognitive processes in the human brain [39]. The method is widely used for mapping of brain regions by imaging of functional activation during sensory or motor tasks or with cognitive processing. As BOLD-fMRI provides information concerning oxygenation, itt may also be important for imaging of tumor physiology by monitoring changes in tissue concentration of deoxyhemoglobin [29].

In general, the MRI signal intensity reflects the concentration of water within a sample and is also dependent on the chemical and physical environment in which the water molecules are situated. In BOLD-MRI, parameters are optimized to make signal intensity and image contrast dependent on concentration of deoxyhemoglobin in a sample [39]. The oxygen required for brain metabolism is supplied by the hemoglobin component of the blood. The BOLD method is based on the fact that the susceptibility effects of hemoglobin depends upon whereas it carries oxygen or not. Deoxyhemoglobin have shorter rate of signal decay (i.e. shorter T_2*-relaxation time) than oxyhemoglobin. Thus, changes in oxygenation of the blood can be visualized as signal change in T_2* weighted images. Upon neural activity in an area, the cerebral blood flow to the active areas increases remarkable and brings more oxyhemoglobin. This reduces the fraction of regional deoxyhemoglobin, and the increase in blood flow to regions with neural activity can thereby be observed as increase in signal [15].

Diffusion-weighted imaging

Diffusion-weighted imaging (DWI) methods utilizes the signal loss associated with the random thermal motion of water molecules in the presence of magnetic field gradients to derive a parameter: the apparent diffusion coefficient (ADC). ADC directly reflects the translational mobility of water molecules in the tissues. This non-invasive method thus measures self diffusion of water within body tissue. The diffusion coefficient is known to be altered in some pathological states. Clinically, DWI is especially promising in early detection and assessment of stroke. The method can also be seen as a valuable tool in tumor characterization, monitoring of terapy changes and evaluation of for example multiple sclerosis [30, 55].

Dynamic perfusion-weighted imaging

Dynamic perfusion MRI is performed using a combination of rapid imaging techniques and bolus injection of Gadolinium chelates. Such bolus tracking methods are classified into two groups; T_2*-weighted dynamic susceptibility contrast MRI *(DSC-MRI)* [88] and T_1-weighted Dynamic Contrast Enhanced MRI *(DCE-MRI)* [32]. The first is the method most often referred to when using the term perfusion imaging. The latter, DCE-imaging, is used as imaging method in this thesis.

DSC-MRI: T_2*-weighted dynamic susceptibility contrast imaging

This method of dynamic perfusion imaging employ bolus injection of exogenous contrast that remain restricted to the vascular compartment so that rapid T_2*-weighted imaging of the first pass kinetics reflect cerebral perfusion. The method is often denoted Perfusion imaging (PWI). PWI is not an enhancement technique. Instead it depends upon the negative, susceptibility effects of the Gadolinium agent, and is thus less applicable if the blood-brain-barrier is absent or disrupted. BBB leakage would reduce compartmentalization of the agent and thus diminish the susceptibility effect. Because of dilution of the bolus when circulating through the body, circulation characteristics have to be evaluated from the "first pass" of the agent through the brain.

Perfusion MRI is commonly used complementary to diffusion MRI as a diagnostic tool in e.g. stroke assessment. Because microvascular blood flow is altered in early stage of most pathological states, perfusion MRI is a particularly clinically important method [88].

DCE-MRI; dynamic contrast enhanced T_1-weighted MRI

Contrary to the dynamic T_2-weighted perfusion imaging, this method do not provide assessment of the first pass of the bolus injection, but rather the agents distribution within the first minutes after injection.

The method is based on the fact that injected exogenous contrast agents freely diffuse across the blood-brain barrier and distribute in proportion to delivery rates or perfusion. A rapid T_1-weighted imaging sequence "detect" the kinetics of the contrast agent over time. By application of a compartmental analysis model, parameters related to permeability and vascular volume fraction can be estimated [1]. This method, highly applicaple for understanding tumor microcirculation and drug access to tumor, is often denoted pharmacokinetic MRI when used in conjunction with such theoretical models. Aspects of pharmacokinetic MRI, or DCE-MRI, have been revealed in this thesis.

D. MR Imaging protocol

Following chapter includes information about the imaging sequences acquired in the "NG-2 study"; why they were included in the study, and which sequence parameters they were obtained with.

T_2 weighted (RARE) sequence

T_2-weighted images display differences in the transverse decay characteristics. Most pathological states reveal an elongation of T_2. T_2 is found sensitive to pathology because the T_2 decay (milliseconds) is much more rapid than the T_1-relaxation (second). Thus a small change in T_2 would cause a larger prosentage difference than would the same change in T_1 [34]. To avoid T_1 contribution, TR is chosen to be long enough for the longitudinal magnetization in all tissues to be recovered.

In the "NG-2 project" a sequence of T_2 weighted images were performed with spin echo (SE) technique in axial slice orientation. T_2 weighting is known to achieve good visualization of tumor separated from normal brain tissue. The contrast in a T_2-weighted image is mainly determined by differences in T_2 relaxation times between fat and water [77]. A TE long enough for both fat and water to receive T_2 decay will reveal these differences in T_2 contrast [77]. As tumors have high water content, they can be well demonstrated in T_2 sequences. The sequence had a turbofactor of eight echoes. Consequently TE could not be too long (eight echoes must be collected for each TR) even though long TE causes better contrast (but weaker signal).

FLAIR

A fluid attenuated inversion recovery (FLAIR) sequence was performed with same geometry as the T_2 (RARE) sequence. The saturation method allows suppression of fluid, in particular cerebro spinal fluid (CSF) to display lesions otherwise obscured by CSF (which is normally producing high signal). FLAIR is a valuable complementary sequence to the standard T_2 weighted sequence because in the latter, bright CSF can obscure tissue and hide pathology [77]. The inversion time (TI) in CSF of rats had been tested in pilot trials. The preparation pulse blocks signal from CNS so that edematous tissue (tumor tissue) and CFS can be distinguished. Pathological states with only minor elevation in water content can thus be distinguished from normal tissue. High signal (bright) in both sequences shows edema. However, areas which appears bright in T_2 and dark in FLAIR, is not edema but free liquid (CSF).

Parameter	T_2	FLAIR
FOV	3 cm	3 cm
Matrix	128	128
No slices	11	11
Slice thickness	1 mm	1 mm
NEX	4	2
Gap	1,2 mm	1,2 mm
TE	60 ms	60 ms
TR	6000 ms	6000 ms
TI		2500 ms
Turbofactor	8	

Table D.1.: Scan parameters, RARE and FLAIR

T_1 Maps

Pre-contrast T_1-weighted SE measurements were obtained from five sequences of axial slices with the exact same geometric slice placement and orientation. All acquisition parameters remained the same in the five series, except TR which had following values; 2000 ms, 1500 ms,500 ms, 300 ms and 100 ms. The purpose of these five sequences was to estimate T_1 relaxation times; for assessment of the time course of contrast agent in blood, and for tissue characterization. The other scan parameters for T_1 maps were; FOV = 3, matrix = 64x64, no slices = 3, slice thickness = 3, NEX =1, slice gap = 3.5 TE(eff) = 8.8.

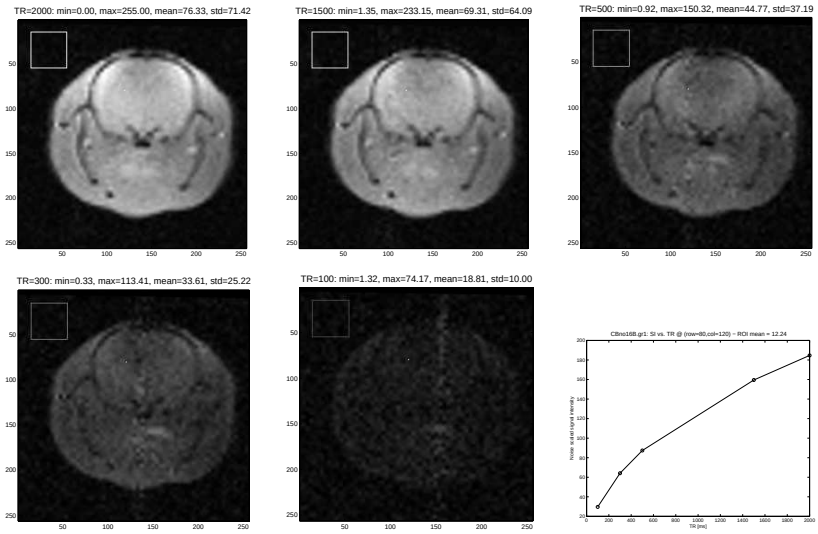

Figure D.1.: Example of (noise scaled) SE acquisitions (study `ng2_1and2_4_2`) with TE = 8.8 ms and TR = 2000, 1500, 500, 300, 100 ms, respectively. The lower right figure shows noise-corrected signal intensity versus TR time in pixel (80,120). This pixel is also labeled (white) in the SE images. This series of images is used for pixel-wise nonlinear least squares estimation of T1 relaxation times. Further description of these calculations were beyond the scope of this thesis.

T_1 weighted dynamic contrast enhanced sequence (DCE)

A dynamic T_1 weighted series of images with time resolution of 16.7 s (increased to 43 s after acquisition of frame 30) seconds was acquired. Contrast agent (0.2 mmol/kg Gadomer-17) was given as a short bolus (duration about 12 sec) after four baseline precontrast images. With TR/TE of 122.5/5 ms, a set of contrast enhanced images at 59 frames was acquired. Total acquisition time of each frame was 15.7 sec. Total sequence time was 32 minutes. By planning geometry on the basis of the T_2 sequence, mid-slice of the sequence was set to correlate with center of tumor (i.e. the slice showing the largest appearance of tumor in the T_2 weighted sequence). Injection had a duration of about 12 seconds with start five seconds

FOV	3 cm
Matrix	64x64
No slices	3
Slice thickness	3 mm
NEX	2
Gap	3.5 mm
TE	5 ms
TR	122.5 ms

Table D.2.: Scanning parameters dynamic sequence.

prior to start of scan #5 (t_0). The first image of slice two after bolus injection will therefore be acquired 12.84 seconds after start of injection (7.84 sec + 5 sec). For exact time resolution of the dynamic scanning, see section 6.3

T_1 Post contrast

Following the dynamic scanning, a bolus injection of 0.5 mmol/kg conventional Gd-DTPA (Omniscan, Amerham Health) was given about two minutes prior to acquisition of a T_1 weighted imaging sequence. The sequence was acquired to provide good delineation of tumor. Sequence slices had the same geometry as slices in the RARE and FLAIR sequences.

Normal soft tissue T_1 values are markedly different from each other and can thus provide good contrast between different tissues. To achieve T_1-weighting, T_2 effects have to be minimized by choosing a short TE. TR should be shorter than T_1 to reveal differences between tissues. Tissues with lower T_1, show higher signal. The contrast agents additionally reduce T_1 time in tissues in which it is distributed, providing higher signal from these areas. This increase in T_1-relaxation after T_1 shortening, is directly proportional to the concentration of the contrast agent in that tissue. The contrast agents have an additional effect in shortening in T_2 which tend to counterbalance the wanted effect on T_1. However, the T_2 reduction is of minor magnitude compared to the T_1 shortening which is determined to be the predominant effect of the contrast agents used.

FOV	3 cm
Matrix	256x256
No slices	11
Slice thickness	1 mm
NEX	4
Gap	1.2 mm
TE	13 ms
TR	407 ms

Table D.3.: Scanning parameters post contrastT_1 sequence.

Contrast agent doses

For the dynamic imaging, Gadomer-17 (Schering AG; 0.5 mmol/ml) were given at a dose of 0.2 mmol/ml as intravenous bolus injection at the immediate start of the dynamic scanning (though after four baseline images were acquired). Omniscan (Amersham Health; 0.5 mmol/ml) at a dose of 0.5mmol/kg were given 2 minutes before start of the post-contrast T_1 sequence. Injection volumes of both contrast agents are given in table D.4, and D.5, D.6 and D.7.

The doses of Gadomer-17 and Omniscan was given to each animal, decided as following: i.e. animal with weight of 117 g. **Gadomer-17** was given at a dose of 0.2 mmol/kg. Weight of 0.117 g gives: 0.2 mmol/kg · 0.117 kg = 0.024 mmol. Further: 0.024 mmol / 0.5 mmol/ml = 0.048 ml = 48 µl. In addition, 200 *micro*l of dead space volume must be injected due to the length of the catheter. The injection dose in this case was therefore 250 µl Gadomer-17. **Omniscan** was injected at a dose of 0.5 mmol/kg. For an animal weighing 117 g this means an volume of 117 µl in addition to 200 µl in dead space volume. The total injection volume was therefore 320 µl. Due to the length of the catheter, there was a dead space volume (dsv) of 200 µliter. Hence, a saline flush after bolus injection could not be done.

Rat	Weight kg	Volume, Gad-17 in ml	Injected Volume incl 0.2 ml dsv	Volume, Omn in ml	Injected volume incl 0.2 ml dsv
1	0.196	0.087	0.280	0.196	0.400
2	0.195	0.078	0,.280	0.195	0.395
3	0.198	0.079	0.280	0.198	0.400
4	0.170	0.068	0.280	0.170	0.370
5	0.125	0.050	0.250	0.125	0.325
8	0.153	0.061	0.260	0.153	0.350
9	0.126	0.050	0.250	0.126	0.325
10	0.103	0.041	0.240	0.103	0.300
11	0.102	0.041	0.240	0.102	0.300

Table D.4.: Doses and injected volumes, WT tumor animals, fifth-week scans.

Rat	Weight kg	Volume, Gad-17 in ml	Injected Volume incl .,2 ml dsv	Volume, Omn in ml	Injected volume incl 0.2 ml dsv
13	0.192	0.077	0.280	0.192	0.390
14	0.188	0.075	0.280	0.188	0.390
15	0.121	0.048	0.250	0.121	0.320
16	0.133	0.053	0.255	0.133	0.335
17	0.117	0.047	0.250	0.117	0.320
18	0.120	0.048	0.250	0.118	0.320
20	0.105	0.042	0.240	0.105	0.305
23	0.143	0.057	0.260	0.143	0.345

Table D.5.: Doses and injected volumes, NG-2 tumor animals, fifth-week scans.

Rat	Weight kg	Volume, Gad-17 in ml	Injected Volume incl 0.2 ml dsv	Volume, Omn in ml	Injected volume incl 0.2 ml dsv
1	0.203	0.081	0.280	0.203	0.405
2	0.209	0.084	0.285	0.209	0.410
3	0.209	0.084	0.285	0.209	0.410
4	0.182	0.073	0.270	0.182	0.380
5	0.144	0.058	0.260	0.144	0.340
8	0.171	0.068	0.270	0.171	0.370
9	0.137	0.055	0.255	0.137	0.335
10	0.121	0.048	0.250	0.121	0.320
11	0.102	0.041	0.240	0.102	0.300

Table D.6.: Doses and injected volumes, WT tumor animals, seventh-week scans.

Rat	Weight kg	Volume, Gad-17 in ml	Injected Volume incl 0.2 ml dsv	Volume, Omn in ml	Injected volume incl 0.2 ml dsv
13	0.193	0.077	0.280	0.193	0.395
14	0.204	0.082	0.280	0.204	0.405
15	0.149	0.059	0.260	0.149	0.350
16	0.135	0.054	0.255	0.135	0.335
17	0.135	0.054	0.255	0.135	0.335
18	0.150	0.060	0.260	0.150	0.350
20	0.111	0.045	0.245	0.111	0.310
21	0.140	0.056	0.260	0.140	0.340

Table D.7.: Doses and injected volumes, NG-2 tumor animals seventh week scans.

Following animals have been included as subject in this theseis:

- The animals number 13, 14 and 20 in Table D.5 correspond to examinations NG 1-1, NG 2-1 and NG 7-1 respectively.
- Rat no three (Table D.6) corresponds to examination WT 3-2.
- The rats numbered 13, 14, 15, 19 and 20 in Table D.7 corresponds to the selected examinations NG 1-2, NG 2-2, NG 3-2, NG 6-2 and NG 7-2 respectively.

Relaxivity data, Gadomer-17

Following data was received from Bernd Mizzelwitz on request (by mail). By further correspondence he suggested to assume a T_1relaxivity (r_1) of 14.7 $mM^{-1}s^{-1}$ (bovine plasma at 40°C and 2 T) in pharmacokinetic analyses of the dynamic data.

Medium	Temperature	Field Strength	r_1 L/(mmol×s)	r_2 L/(mmol×s)
Water	40C	0,47 T	17,3	22,2
Bovine plasma	40C	0,47 T	18,7	21,3
Water	20C	1,5 T	13,7	
Bovine plasma	20C	1,5 T	15,7	
Dog blood	37C	1,5 T	16,9	22,1
Dog plasma	37C	1,5 T	17,8	21,4
Water	40C	2 T	13,4	
Bovine plasma	40C	2 T	14,7	

Table D.8.: Relaxivity data: Gadomer-17

E. Implemented Matlab codes

For each pixel time-course in each of these regions we first fitted the pharmacokinetic parameters defined in the model by Su et al. (i.e. D_0, D_1, and K_2) and in the model by Tofts et al. (i.e. K^{trans} and v_e) using nonlinear least-squares data fitting by the Gauss-Newton method.

In the Su et al. model (denoted S) we have implemented
`[BETA,R,J] = nlinfit(t, C, @tissue_cons_fixed_my_t0, BETA0_fixed_t0);` where the initial parameters are:

```
D0_init = 0.11;  %  0.11 [mM]
D1_init = 0.57;  %  0.57 [mM/min]
K2_init = 0.30;  %  0.30 [1/min]
BETA0_fixed_t0 = [D0_init, D1_init, K2_init];
```

and the function
`[C] = tissue_cons_fixed_my_t0(beta, t)`
is defined by:

```
t0 = 0.5;  % fixed value from Su et al.
D0 = beta(1);
D1 = beta(2);
K2 = beta(3);
% if t <= t0
I1 = find(t <= t0);
a1_le = D0 * (t(I1)/t0);
a2_le = (D1 / (K2*K2*t0)) * (exp(-K2*t(I1)) - 1);
a3_le = (D1/K2) * (t(I1)/t0);
C_le(I1) = a1_le + a2_le + a3_le;

% if t >= t0
I2 = find(t > t0);
alpha1 = 0.417;
alpha2 = 0.027;
x = 49.2;   (A1 = 38.38 kg/l;  A2 = 0.79 kg/l)

f1 = ( D0 + (D1 / (K2 - alpha1)) ) * ( x / (1+x) );
a1_gt = f1 * exp(-alpha1*(t(I2)-t0));
```

```
f2 = ( D0 + (D1 / (K2 - alpha2)) ) * ( 1 / (1+x) );
a2_gt = f2 * exp(-alpha2*(t(I2)-t0));
f3 = (D1/(K2*K2*t0)) * ...
    (exp(-K2*t0) - 1) + (D1/K2) - (D1/(K2-alpha1))*(x/(1+x)) - ...
    (D1/(K2-alpha2))*(1/(1+x));
a3_gt = f3 * exp(-K2*(t(I2)-t0));

C_gt(I2) = a1_gt + a2_gt + a3_gt;
C = C_le + C_gt;
```

In the Tofts et al. model (denoted T) we have implemented
`[BETA,R,J] = nlinfit(t, C, @tofts_tissue_conc_func, BETA0);`
where the initial parameters are:

```
Ktrans_0 = 0.1; [1/min]\\
(Verhoye et al (2002) found 0.18 \pm 0.05 in tumor)
ve_0 = 0.5;
BETA0 = [Ktrans_0, ve_0];
```

and the function
`[C] = tofts_tissue_conc_func(beta, t)`
is defined by:

```
k = beta(1);   % k = Ktrans: volume transfer constant  [min^-1]
ve = beta(2);  % extravascular volume fraction per volume tissue 0 < ve < 1
kep = k/ve;    % derived rate constant

D = 0.2;     % [mmol*kg^-1]  injected CA dose
m1 = 0.417;  % [min^-1]  rate constant for biexponential plasma conc decrease
m2 = 0.027;  % [min^-1]  rate constant from the litterature ...
a1 = 38.38;  % [kg*l^-1] concentration amplitude
a2 = 0.79;  % [kg*l^-1] concentration amplitude
% Tofts & Kermode (1991) Eqs. (6a) and (6b)
m3 = kep;
b1 = k*a1 / (m3-m1);
b2 = k*a2 / (m3-m2);
b3 = -(b1+b2);
C = D*(b1*exp(-m1*t) + b2*exp(-m2*t) + b3*exp(-m3*t));
```

Goodness-of-fit criteria (AIC) were coomputed using the following Matlab code:

```
% N = number of samples in time (63)
% J = number of pixels within ROI (varies)
M_su = 3;     %  D0, D1, K2
M_tofts = 2;  %  Ktrans, ve
K_su = M_su+1;
K_tofts = M_tofts+1;
mm = 1000; % i.e. conc. unit in micromol
```

```
for j=1:J
    SSE_su(j) = mm*res_su(:,j)' * mm*res_su(:,j);
    SSE_tofts(j) = mm*res_tofts(:,j)' * mm*res_tofts(:,j);
    AICc_su(j) = N * log(SSE_su(j)/N) + ...
              2*K_su + (2*K_su*(K_su+1))/(N-K_su-1);
    AICc_tofts(j) = N * log(SSE_tofts(j)/N) + ...
              2*K_tofts + (2*K_tofts*(K_tofts+1))/(N-K_tofts-1);
    delta_AICc(j) = AICc_su(j) - AICc_tofts(j);
    evidence_ratio(j) = 1.0/exp(-0.5*delta_AICc(j));
    prob(j) = exp(-0.5*delta_AICc(j))/(1+ exp(-0.5*delta_AICc(j)));
end
```

References

[1] Abbott, N. J., Chugani, D. C., Zaharchuk, G., Rosen, B. R., and Lo, E. H. 1999. Delivery of imaging agents into brain. *Adv Drug Deliv Rev* 37(1-3):253–277.

[2] Aref, M., Brechbiel, M., and Wiener, E. C. 2002. Identifying tumor vascular permeability heterogeneity with magnetic resonance imaging contrast agents. *Invest Radiol* 37(4):178–92.

[3] Belliveau, J. W., Cohen, M. S., Weisskoff, R. M., Buchbinder, B. R., and Rosen, B. R. 1991. Functional studies of the human brain using high-speed magnetic resonance imaging. *J Neuroimaging* 1(1):36–41.

[4] Berne, R. M. and Levy, M. N. 1998. *Physiology*, chap. 30, pp. 319–512. Mosby, fourth edn.

[5] Bogin, L., Margalit, R., Mispelter, J., and Degani, H. 2002. Parametric imaging of tumor perfusion using flow- and permeability-limited tracers. *J Magn Reson Imaging* 16(3):289–99.

[6] Brasch, R., Pham, C., Shames, D., Roberts, T., van Dijke, K., van Bruggen, N., Mann, J., Ostrowitzki, S., and Melnyk, O. 1997. Assessing tumor angiogenesis using macromolecular MR imaging contrast media. *J Magn Reson Imaging* 7(1):68–74.

[7] Brasch, R. and Turetschek, K. 2000. MRI characterization of tumors and grading angiogenesis using macromolecular contrast media: status report. *Eur J Radiol* 34(3):148–55.

[8] Brasch, R. C., Li, K. C., Husband, J. E., Keogan, M. T., Neeman, M., Padhani, A. R., Shames, D., and Turetschek, K. 2000. In vivo monitoring of tumor angiogenesis with MR imaging. *Acad Radiol* 7(10):812–23.

[9] Brown, J. M. and Giaccia, A. J. 1998. The unique physiology of solid tumors: opportunities (and problems) for cancer therapy. *Cancer Res* 58(7):1408–16.

[10] Buckley, D. L. 2002. Uncertainty in the analysis of tracer kinetics using dynamic contrast-enhanced T1-weighted MRI. *Magn Reson Med* 47(3):601–6.

[11] Carmeliet, P. 2003. Angiogenesis in health and disease. *Nat Med* 9(6):653–60.

[12] Carmeliet, P. and Jain, R. K. 2000. Angiogenesis in cancer and other diseases. *Nature* 407(6801):249–57.

[13] Chekenya, M., Hjelstuen, M., Enger, P. O., Thorsen, F., Jacob, A. L., Probst, B., Haraldseth, O., Pilkington, G., Butt, A., Levine, J. M., and Bjerkvig, R. 2002. NG2 proteoglycan promotes angiogenesis-dependent tumor growth in CNS by sequestering angiostatin. *Faseb J* 16(6):586–8.

[14] Choyke, P. L., Dwyer, A. J., and Knopp, M. V. 2003. Functional tumor imaging with dynamic contrast-enhanced magnetic resonance imaging. *J Magn Reson Imaging* 17(5):509–20.

[15] Clare, S. 1997. *Functional Magnetic Resonance Imaging: Methods and Applications.* Ph.D. thesis, University of Nottingham.

[16] Cohen, M. 1998. Theory of Echo-Planar Imaging. In: *Echo-Planar Imaging Theory, Technique and Application*, R. Schmitt, M. K. Stehling, and R. Turner, editors, vol. 1, pp. 11–30, Springer-Verlag, Heidelberg Berlin, Germany, First edn.

[17] Daldrup, H., Shames, D. M., Wendland, M., Okuhata, Y., Link, T. M., Rosenau, W., Lu, Y., and Brasch, R. C. 1998. Correlation of dynamic contrast-enhanced MR imaging with histologic tumor grade: comparison of macromolecular and small-molecular contrast media. *AJR Am J Roentgenol* 171(4):941–9.

[18] Daldrup-Link, H. E. and Brasch, R. C. 2003. Macromolecular contrast agents for MR mammography: current status. *Eur Radiol* 13(2):354–65.

[19] Degani, H., Chetrit-Dadiani, M., Bogin, L., and Furman-Haran, E. 2003. Magnetic resonance imaging of tumor vasculature. *Thromb Haemost* 89(1):25–33.

[20] Delorme, S. and Knopp, M. V. 1998. Non-invasive vascular imaging: assessing tumour vascularity. *Eur Radiol* 8(4):517–27.

[21] Donahue, K. M., Weisskoff, R. M., and Burstein, D. 1997. Water diffusion and exchange as they influence contrast enhancement. *J Magn Reson Imaging* 7(1):102–10.

[22] Dvorak, A. M. and Feng, D. 2001. The vesiculo-vacuolar organelle (VVO). A new endothelial cell permeability organelle. *J Histochem Cytochem* 49(4):419–32.

[23] Dvorak, H. F., Brown, L. F., Detmar, M., and Dvorak, A. M. 1995. Vascular permeability factor/vascular endothelial growth factor, microvascular hyperpermeability, and angiogenesis. *Am J Pathol* 146(5):1029–39.

[24] El-Haddad, K. S. and Padhani, A. R. 2003. Recent advances in oncological imaging. *Clin Med* 3(4):318–22.

[25] Farkas, E. and Luiten, P. G. 2001. Cerebral microvascular pathology in aging and Alzheimer's disease. *Prog Neurobiol* 64(6):575–611.

[26] Feng, D., Nagy, J. A., Dvorak, A. M., and Dvorak, H. F. 2000. Different pathways of macromolecule extravasation from hyperpermeable tumor vessels. *Microvasc Res* 59(1):24–37.

[27] Folkman, J. 2000. Incipient angiogenesis. *J Natl Cancer Inst* 92(2):94–5.

[28] Galbraith, S. M., Lodge, M. A., Taylor, N. J., Rustin, G. J., Bentzen, S., Stirling, J. J., and Padhani, A. R. 2002. Reproducibility of dynamic contrast-enhanced MRI in human muscle and tumours: comparison of quantitative and semi-quantitative analysis. *NMR Biomed* 15(2):132–42.

[29] Gillies, R. J., Bhujwalla, Z. M., Evelhoch, J., Garwood, M., Neeman, M., Robinson, S. P., Sotak, C. H., and Van Der Sanden, B. 2000. Applications of magnetic resonance in model systems: tumor biology and physiology. *Neoplasia* 2(1-2):139–51.

[30] Gillies, R. J., Raghunand, N., Karczmar, G. S., and Bhujwalla, Z. M. 2002. MRI of the tumor microenvironment. *J Magn Reson Imaging* 16(4):430–50.

[31] Gloor, S. M., Wachtel, M., Bolliger, M. F., Ishihara, H., Landmann, R., and Frei, K. 2001. Molecular and cellular permeability control at the blood-brain barrier. *Brain Res Brain Res Rev* 36(2-3):258–64.

[32] Griebel, J., Mayr, N. A., de Vries, A., Knopp, M. V., Gneiting, T., Kremser, C., Essig, M., Hawighorst, H., Lukas, P. H., and Yuh, W. T. 1997. Assessment of tumor microcirculation: a new role of dynamic contrast MR imaging. *J Magn Reson Imaging* 7(1):111–9.

[33] Guyton, A. C. and Hall, J. E. 2000. *Textbook of medical physiology*, chap. 14-18,24. W. B. Saunders Company, tenth edn.

[34] Haacke, E. M., Robert, W. B., Thompson, M. R., and Venkatesan, R. 1999. *Magnetic Resonance Imaging Physical Priciples and Sequence Design*, chap. 15 & 22. Wiley-Liss, A John Wiley & Sons, inc., publication.

[35] Hashemi, R. H. and Bradley, W. G. 1997. *MRI the basics*. William and Wilkins.

[36] Hashizume, H., Baluk, P., Morikawa, S., McLean, J. W., Thurston, G., Roberge, S., Jain, R. K., and McDonald, D. M. 2000. Openings between defective endothelial cells explain tumor vessel leakiness. *Am J Pathol* 156(4):1363–80.

[37] Henderson, E., Sykes, J., Drost, D., Weinmann, H. J., Rutt, B. K., and Lee, T. Y. 2000. Simultaneous MRI measurement of blood flow, blood volume, and capillary permeability in mammary tumors using two different contrast agents. *J Magn Reson Imaging* 12(6):991–1003.

[38] Hobbs, S. K., Monsky, W. L., Yuan, F., Roberts, W. G., Griffith, L., Torchilin, V. P., and Jain, R. K. 1998. Regulation of transport pathways in tumor vessels: role of tumor type and microenvironment. *Proc Natl Acad Sci U S A* 95(8):4607–12.

[39] Howseman, A. M. and Bowtell, R. W. 1999. Functional magnetic resonance imaging: imaging techniques and contrast mechanisms. *Philos Trans R Soc Lond B Biol Sci* 354(1387):1179–94.

[40] Huber, J. D., Egleton, R. D., and Davis, T. P. 2001. Molecular physiology and pathophysiology of tight junctions in the blood-brain barrier. *Trends Neurosci* 24(12):719–25.

[41] Jackson, A. 2003. Quantitative characterization of tumor microvasculature using dynamic contrast-enhanced MRI. *MEDICAMUNDI* 47(1):40–46.

[42] Jackson, A., Jayson, G. C., Li, K. L., Zhu, X. P., Checkley, D. R., Tessier, J. J., and Waterton, J. C. 2003. Reproducibility of quantitative dynamic contrast-enhanced MRI in newly presenting glioma. *Br J Radiol* 76(903):153–62.

[43] Jain, R. K. 1987. Transport of molecules across tumor vasculature. *Cancer Metastasis Rev* 6(4):559–93.

[44] Jain, R. K. 1996. Delivery of molecular medicine to solid tumors. *Science* 271(5252):1079–80.

[45] Jain, R. K. 2001. Delivery of molecular and cellular medicine to solid tumors. *Adv Drug Deliv Rev* 46(1-3):149–68.

[46] Kim, Y. H., Choi, B. I., Cho, W. H., Lim, S., Moon, W. K., Han, J. K., Weinmann, H. J., and Chang, K. H. 2003. Dynamic contrast-enhanced MR imaging of VX2 carcinomas after X-irradiation in rabbits: comparison of gadopentetate dimeglumine and a macromolecular contrast agent. *Invest Radiol* 38(9):539–49.

[47] Knopp, M. V., Giesel, F. L., Marcos, H., von Tengg-Kobligk, H., and Choyke, P. 2001. Dynamic contrast-enhanced magnetic resonance imaging in oncology. *Top Magn Reson Imaging* 12(4):301–8.

[48] Knopp, M. V., Von Tengg-Kobligk, H., and Choyke, P. L. 2003. Functional magnetic resonance imaging in oncology for diagnosis and therapy monitoring. *Mol Cancer Ther* 2(4):419–26.

[49] Knopp, M. V., Weiss, E., Sinn, H. P., Mattern, J., Junkermann, H., Radeleff, J., Magener, A., Brix, G., Delorme, S., Zuna, I., and van Kaick, G. 1999. Pathophysiologic basis of contrast enhancement in breast tumors. *J Magn Reson Imaging* 10(3):260–6.

[50] Kobayashi, H., Kawamoto, S., Saga, T., Sato, N., Hiraga, A., Ishimori, T., Akita, Y., Mamede, M. H., Konishi, J., Togashi, K., and Brechbiel, M. W. 2001. Novel liver macromolecular MR contrast agent with a polypropylenimine diaminobutyl dendrimer core: comparison to the vascular MR contrast agent with the polyamidoamine dendrimer core. *Magn Reson Med* 46(4):795–802.

[51] Kobayashi, H., Kawamoto, S., Saga, T., Sato, N., Hiraga, A., Ishimori, T., Konishi, J., Togashi, K., and Brechbiel, M. W. 2001. Positive effects of polyethylene glycol conjugation to generation-4 polyamidoamine dendrimers as macromolecular MR contrast agents. *Magn Reson Med* 46(4):781–8.

[52] Levick, J. R. 2000. *An Introduction to Cardiovascular Physiology*, chap. 8-15. Arnold, third edn.

[53] Liney, G. P., Gibbs, P., Hayes, C., Leach, M. O., and Turnbull, L. W. 1999. Dynamic contrast-enhanced MRI in the differentiation of breast tumors: user-defined versus semi-automated region-of-interest analysis. *J Magn Reson Imaging* 10(6):945–9.

[54] Ludemann, L., Wurm, R., and Zimmer, C. 2002. Pharmacokinetic modeling of Gd-DTPA extravasation in brain tumors. *Invest Radiol* 37(10):562–70.

[55] Luypaert, R., Boujraf, S., Sourbron, S., and Osteaux, M. 2001. Diffusion and perfusion MRI: basic physics. *Eur J Radiol* 38(1):19–27.

[56] Machein, M. R. and Plate, K. H. 2000. VEGF in brain tumors. *J Neurooncol* 50(1-2):109–20.

[57] Magistretti, P. J. and Pellerin, L. 1999. Cellular mechanisms of brain energy metabolism and their relevance to functional brain imaging. *Philos Trans R Soc Lond B Biol Sci* 354(1387):1155–63.

[58] Matsubayashi, R., Matsuo, Y., Edakuni, G., Satoh, T., Tokunaga, O., and Kudo, S. 2000. Breast masses with peripheral rim enhancement on dynamic contrast-enhanced MR images: correlation of MR findings with histologic features and expression of growth factors. *Radiology* 217(3):841–8.

[59] McNamara, D. A., Harmey, J. H., Walsh, T. N., Redmond, H. P., and Bouchier-Hayes, D. J. 1998. Significance of angiogenesis in cancer therapy. *Br J Surg* 85(8):1044–55.

[60] Misselwitz, B., Schmitt-Willich, H., Ebert, W., Frenzel, T., and Weinmann, H. J. 2001. Pharmacokinetics of Gadomer-17, a new dendritic magnetic resonance contrast agent. *Magma* 12(2-3):128–34.

[61] Molutsky, H. and Cristopoulos, A. 2003. *Fitting Models to Biological Data using Linear and Nonlinear Regression*, chap. F. Comparing models. GraphPad Software, Inc.

[62] Mussurakis, S., Buckley, D. L., Coady, A. M., Turnbull, L. W., and Horsman, A. 1996. Observer variability in the interpretation of contrast enhanced MRI of the breast. *Br J Radiol* 69(827):1009–16.

[63] Mussurakis, S., Buckley, D. L., and Horsman, A. 1997. Dynamic MRI of invasive breast cancer: assessment of three region-of-interest analysis methods. *J Comput Assist Tomogr* 21(3):431–8.

[64] Myhr, G., Nordlid, K., Bjornerud, A., and Lihaug, E. G. 2002. *Fokus på MRI og bruk av kontrastmidler*. Amersham Health, Oslo, Norway, 4th edn.

[65] Neeman, M., Provenzale, J. M., and Dewhirst, M. W. 2001. Magnetic resonance imaging applications in the evaluation of tumor angiogenesis. *Semin Radiat Oncol* 11(1):70–82.

[66] Nicolle, G. M., Toth, E., Eisenwiener, K. P., Macke, H. R., and Merbach, A. E. 2002. From monomers to micelles: investigation of the parameters influencing proton relaxivity. *J Biol Inorg Chem* 7(7-8):757–69.

[67] Nicolle, G. M., Toth, E., Schmitt-Willich, H., Raduchel, B., and Merbach, A. E. 2002. The impact of rigidity and water exchange on the relaxivity of a dendritic MRI contrast agent. *Chemistry* 8(5):1040–8.

[68] Padhani, A. R. 2002. Dynamic contrast-enhanced MRI in clinical oncology: current status and future directions. *J Magn Reson Imaging* 16(4):407–22.

[69] Padhani, A. R. 2002. Functional MRI for anticancer therapy assessment. *Eur J Cancer* 38(16):2116–27.

[70] Padhani, A. R., Hayes, C., Landau, S., and Leach, M. O. 2002. Reproducibility of quantitative dynamic MRI of normal human tissues. *NMR Biomed* 15(2):143–53.

[71] Padhani, A. R. and Husband, J. E. 2001. Dynamic contrast-enhanced MRI studies in oncology with an emphasis on quantification, validation and human studies. *Clin Radiol* 56(8):607–20.

[72] Padhani, A. R. and Neeman, M. 2001. Challenges for imaging angiogenesis. *Br J Radiol* 74(886):886–90.

[73] Reed, R. K., Woie, K., and Rubin, K. 1997. Integrins and control of interstitial fluid pressure. *News Physiol Sci* 12:42–48.

[74] Rhoades, R. A. and Tanner, R. A., editors 1995. *Medical Physiology*, chap. 17. Little, Brown and Company.

[75] Rijpkema, M., Kaanders, J. H., Joosten, F. B., van der Kogel, A. J., and Heerschap, A. 2001. Method for quantitative mapping of dynamic MRI contrast agent uptake in human tumors. *J Magn Reson Imaging* 14(4):457–63.

[76] Rinck, P. A. 1993. *Magnetic Resonance in Medicine.* Blackwell Scientific Publications.

[77] Rinck, P. A. 2001. *Magnetic Resonance in Medicine.* Blackwell Scientific Publications, 4th edn.

[78] Rinck, P. A. and Muller, R. N. 1999. Field strength and dose dependence of contrast enhancement by gadolinium-based MR contrast agents. *Eur Radiol* 9(5):998–1004.

[79] Roberts, H. C., Roberts, T. P., Bollen, A. W., Ley, S., Brasch, R. C., and Dillon, W. P. 2001. Correlation of microvascular permeability derived from dynamic contrast-enhanced MR imaging with histologic grade and tumor labeling index: a study in human brain tumors. *Acad Radiol* 8(5):384–91.

[80] Roberts, H. C., Roberts, T. P., Brasch, R. C., and Dillon, W. P. 2000. Quantitative measurement of microvascular permeability in human brain tumors achieved using dynamic contrast-enhanced MR imaging: correlation with histologic grade. *AJNR Am J Neuroradiol* 21(5):891–9.

[81] Roberts, T. P., Turetschek, K., Preda, A., Novikov, V., Moeglich, M., Shames, D. M., Brasch, R. C., and Weinmann, H. J. 2002. Tumor microvascular changes to anti-angiogenic treatment assessed by MR contrast media of different molecular weights. *Acad Radiol* 9 Suppl 2:S511–3.

[82] Runge, V. M. 2000. Safety of approved MR contrast media for intravenous injection. *J Magn Reson Imaging* 12(2):205–13.

[83] Schiffler, M. A. 2001. Scope and Applications of Gadolinium(III) MRI Contrast Agents. In: *Biomaterials Seminar*, vol. 1.

[84] Schmidt-Nielsen, K. 1997. *Animal Physiology. Adaption and environment.* Cambridge University Press.

[85] Shellock, F. G. and Kanal, E. 1999. Safety of magnetic resonance imaging contrast agents. *J Magn Reson Imaging* 10(3):477–84.

[86] Shellock, F. G., Kanal, E., and Moscatel, M. 1996. Bioeffects and Safety Conciderations. In: *Magnetic Resonance Imaging of the Brain and Spine*, S. Atlas, editor, vol. 1, pp. 109–148, Lippincott-Raven, Philadelphia, Second edn.

[87] Snell, R. S. 2001. *Clinical Neuroanatomy.* Lippincott Williams & Wilkins, third edn.

[88] Sorensen, A. G. and Reimer, P. 2000. *Cerebral MR Perfusion Imaging. Principles and Current Applications.* Georg Thieme Verlag.

[89] Sorensen, A. G. and Rosen, B. R. 1996. Functional MRI of the Brain. In: *Magnetic Resonance Imaging of the Brain and Spine*, S. Atlas, editor, vol. 1, pp. 1501–1546, Lippincott-Raven, Philadelphia, Second edn.

[90] Sorensen, A. G., Tievsky, A. L., Ostergaard, L., Weisskoff, R. M., and Rosen, B. R. 1997. Contrast agents in functional MR imaging. *J Magn Reson Imaging* 7(1):47–55.

[91] Stanisz, G. J. and Henkelman, R. M. 2000. Gd-DTPA relaxivity depends on macromolecular content. *Magn Reson Med* 44(5):665–7.

[92] Stubbs, M. 1999. Application of magnetic resonance techniques for imaging tumour physiology. *Acta Oncol* 38(7):845–53.

[93] Su, M. Y., Cheung, Y. C., Fruehauf, J. P., Yu, H., Nalcioglu, O., Mechetner, E., Kyshtoobayeva, A., Chen, S. C., Hsueh, S., McLaren, C. E., and Wan, Y. L. 2003. Correlation of dynamic contrast enhancement MRI parameters with microvessel density and VEGF for assessment of angiogenesis in breast cancer. *J Magn Reson Imaging* 18(4):467–77.

[94] Su, M. Y., Jao, J. C., and Nalcioglu, O. 1994. Measurement of vascular volume fraction and blood-tissue permeability constants with a pharmacokinetic model: studies in rat muscle tumors with dynamic Gd-DTPA enhanced MRI. *Magn Reson Med* 32(6):714–24.

[95] Su, M. Y., Muhler, A., Lao, X., and Nalcioglu, O. 1998. Tumor characterization with dynamic contrast-enhanced MRI using MR contrast agents of various molecular weights. *Magn Reson Med* 39(2):259–69.

[96] Su, M. Y., Wang, Z., Carpenter, P. M., Lao, X., Muhler, A., and Nalcioglu, O. 1999. Characterization of N-ethyl-N-nitrosourea-induced malignant and benign breast tumors in rats by using three MR contrast agents. *J Magn Reson Imaging* 9(2):177–86.

[97] Su, M. Y., Wang, Z., and Nalcioglu, O. 1999. Investigation of longitudinal vascular changes in control and chemotherapy-treated tumors to serve as therapeutic efficacy predictors. *J Magn Reson Imaging* 9(1):128–37.

[98] Su, M. Y., Yu, H., Chiou, J. Y., Wang, J., Nalcioglu, O., Fruehauf, J. P., Mehta, R. S., and Baick, C. H. 2002. Measurement of volumetric and vascular changes with dynamic contrast enhanced MRI for cancer therapy monitoring. *Technol Cancer Res Treat* 1(6):479–88.

[99] Taylor, J. S. and Reddick, W. E. 2000. Evolution from empirical dynamic contrast-enhanced magnetic resonance imaging to pharmacokinetic MRI. *Adv Drug Deliv Rev* 41(1):91–110.

[100] Taylor, J. S., Tofts, P. S., Port, R., Evelhoch, J. L., Knopp, M., Reddick, W. E., Runge, V. M., and Mayr, N. 1999. MR imaging of tumor microcirculation: promise for the new millennium. *J Magn Reson Imaging* 10(6):903–7.

[101] Tinoco, I., Sauer, K., Wang, J. C., and Puglisi, J. D., editors 2002. *Physical Chemistry, Principles and Applications in Biological Sciences*, chap. 7. Prentice Hall, Upper Saddle River, New Jersey, fourth edn.

[102] Tofts, P. S. 1997. Modeling tracer kinetics in dynamic Gd-DTPA MR imaging. *J Magn Reson Imaging* 7(1):91–101.

[103] Tofts, P. S. and Berkowitz, B. A. 1994. Measurement of capillary permeability from the Gd enhancement curve: a comparison of bolus and constant infusion injection methods. *Magn Reson Imaging* 12(1):81–91.

[104] Tofts, P. S., Brix, G., Buckley, D. L., Evelhoch, J. L., Henderson, E., Knopp, M. V., Larsson, H. B., Lee, T. Y., Mayr, N. A., Parker, G. J., Port, R. E., Taylor, J., and Weisskoff, R. M. 1999. Estimating kinetic parameters from dynamic contrast-enhanced T(1)-weighted MRI of a diffusable tracer: standardized quantities and symbols. *J Magn Reson Imaging* 10(3):223–32.

[105] Tofts, P. S. and Kermode, A. G. 1991. Measurement of the blood-brain barrier permeability and leakage space using dynamic MR imaging. 1. Fundamental concepts. *Magn Reson Med* 17(2):357–67.

[106] Toga, A. W. and Maziotta, J. C., editors 2002. *Brain Mapping the methods*. Academic Press, California, USA, second edn.

[107] Vajkoczy, P. and Menger, M. D. 2000. Vascular microenvironment in gliomas. *J Neurooncol* 50(1-2):99–108.

[108] Vaupel, P. 1998. *Blood Perfusion and Microenvironment of Human Tumores*. Springer-Verlag, Berlin.

[109] Verhoye, M., van der Sanden, B. P., Rijken, P. F., Peters, H. P., Van der Kogel, A. J., Pee, G., Vanhoutte, G., Heerschap, A., and Van der Linden, A. 2002. Assessment of the neovascular permeability in glioma xenografts by dynamic T(1) MRI with Gadomer-17. *Magn Reson Med* 47(2):305–13.

[110] Wen, Y. H., Kalff, J., and Peters, R. H. 1999. Pharmacokinetic modeling in toxology: a critical perspective. *Environ Rev* 7:1–18.

[111] Westbrook, C. and Kaut, C. 1993. *MRI in practice*. Blackwell Science Ltd.

[112] Westbrook, C. and Kaut, C. 1998. *MRI in practice*. Blakwell Science, second edn.

[113] Wiig, H., Rubin, K., and Reed, R. K. 2003. New and active role of the interstitium in control of interstitial fluid pressure: potential therapeutic consequences. *Acta Anaesthesiol Scand* 47(2):111–21.

[114] Yu, H., Su, M. Y., Wang, Z., and Nalcioglu, O. 2002. A longitudinal study of radiation-induced changes in tumor vasculature by contrast-enhanced magnetic resonance imaging. *Radiat Res* 158(2):152–8.

[115] Zheng, J., Venkatesan, R., Haacke, E. M., Cavagna, F. M., Finn, P. J., and Li, D. 1999. Accuracy of T1 measurements at high temporal resolution: feasibility of dynamic measurement of blood T1 after contrast administration. *J Magn Reson Imaging* 10(4):576–81.

[116] Zitha-Bobens, E., Elst, L. V., Muller, R. N., and et al. 2001. Relaxivity Studies on a Gadolinium(III) Complex of a Macrocyclic DTPA Derivate. *Eur J Inorg Chem* pp. 3101–3105.